SURFACE AND INTERFACE EFFECTS ON THE PHOTOEXCITED PROCESS OF SILVER

NANOCLUSTERS, AND LEAD & CADMIUM CHALCOGENIDE NANOCRYSTALS

A Dissertation
Submitted to the Graduate Faculty
of the
North Dakota State University
of Agriculture and Applied Science

By

Mohammed Abu Jabed

In Partial Fulfillment of the Requirements
for the Degree of
DOCTOR OF PHILOSOPHY

Major Department:
Chemistry and Biochemistry

September 2020

Fargo, North Dakota

# North Dakota State University
## Graduate School

**Title**

SURFACE AND INTERFACE EFFECTS ON THE PHOTOEXCITED
PROCESS OF SILVER NANOCLUSTERS, AND LEAD & CADMIUM
CHALCOGENIDE NANOCRYSTALS

**By**

Mohammed Abu Jabed

The Supervisory Committee certifies that this ***disquisition*** complies with North Dakota

State University's regulations and meets the accepted standards for the degree of

**DOCTOR OF PHILOSOPHY**

SUPERVISORY COMMITTEE:

Dr. Svetlana V. Kilina
Chair

Dr. Wenfang Sun

Dr. Erik K. Hobbie

Dr. Dmitri S. Kilin

Approved:

November 16, 2020                     Dr. Gregory Cook
Date                                                 Department Chair

**ABSTRACT**

The surface and interface of the metal nanoclusters and semiconducting nanomaterials play a key role in determining the electronic structure and overall photophysical properties. A single strand DNA stabilizes the metal nanoclusters, but it also influences the structural change, solvation free energy, and photophysical properties. On the other hand, surface and interface states in Pb and Cd chalcogenide nanomaterials affect the phonon mediated hot carrier relaxation. We applied DFT and DFT based non-adiabatic dynamics methods to study the surface and interface's effects on the photoexcited processes. In the first part, we have studied the Ag nanoclusters' photophysical properties that are affected by the structural isomers, redox potential, nucleobase passivation, and cluster size. Ag nanoclusters are shown alternative reduction potential, which makes nanoclusters of singlet spin multiplicity thermodynamically favorable. Besides, the optically bright transition in the range of 2.5-3.5 eV is shown metal to ligand charge transfer. It is modulated by the $s+p+d$ orbital mixing in the hole and electron states. We also simulate the charge transfer from the photoexcited PbS QD to organic dye (PDI) attached to the QD surface. Depending on the linker group and the dipole moment of neighboring passivating ligands, the PDI-QD conformations are varies. In response to structural change, the total dipole moment is modulated, changing its electronic structure and hence the photoexcited electron transfer rate from the PbS QD to PDI. We also investigate the inorganic-inorganic interactions in the $PbCl_2$ bridged PbSe NPL and PbSe|CdSe Janus heterostructure. The energy dissipation rate of hot electrons is slower in NPL than the hot hole, while hot $e$-$h$ relaxed to the band-edge by $\approx$1.0ps in the QD. The slower relaxation rate is rationalized by a large average intraband energy difference and smaller coupling term. Besides, the hot carriers in the NPL are spatially separated by $\approx$1.00 ps, which is a favorable condition for the carrier

iii

multiplication process. In Janus QD, (100) interfacial layer creates a structural mismatch in the

CdSe part. Besides, the energy offset between the valance localized on PbSe and CdSe part is

minimum in the PbSe Janus QD of an interface of (111) facet.

# ACKNOWLEDGMENTS

I have dedicated this achievement to my parents. We live in the distance for a long time, but I am lucky enough to get their support in every step in my life so far. Growing up in a middle-class family and achieving my goal would not be possible without their selfless help and sacrifices. I think the completion of this degree is the sign that your life-long struggle to give us a better life had not gone in vain. Hearing your proud voice over the phone on the day of my Ph.D. defense is one of the happiest moments in my life. Many thanks to both of you for everything you have done for me.

I have dedicated this dissertation to Late Xulhaz Mannan too. Xulhaz vaia, you are not with us today, but I am sure that you would be very happy and proud of my achievement. I got courage and guidance from you when I was struggling in my life. I have learned so many things from you, and that helped me to keep myself on track. Thank you very much for showing me how to live a life.

I know that completion of the Ph.D. will be considered as my achievement. However, I made it possible by getting help from many people throughout this journey. I started loving science and maths in primary school. Tough but supportive Fajlun Nahar mam's explanation of science with relatable scenarios created the interest of science in me. Her math problem-solving techniques made it fun and rewarding for me. Thank you mam, for shaping my first impression of science. Mohammad Hossain sir, I still remember the day when you asked me to stand up in front of the class. Then you and the whole class had convinced me to join the school competition on general knowledge. Yes! I finished the second position in that competition. Your such confidence in me became an everlasting inspiration to an introvert-shy high school student. Kamrul Islam sir, I decided to make my career in science when I was in high school, and mostly by your influence. Thank you very much for your appreciation of my curiosity in math and

# DEDICATION

To

**My beloved parents**

For their endless support and love

And

**In memory of Xulhaz Mannan**

Taught me how to live a life

"আকাশে ছড়ানো মেঘের কাছাকাছি
দেখা যায় তোমাদের বাড়ি,

তার নীল দেয়ালে যেন স্বপ্ন বেলোয়ারি

তার কাঁচ দেয়ালে যেন স্বপ্ন বেলোয়ারি।"

# TABLE OF CONTENTS

# LIST OF TABLES

# LIST OF FIGURES

# LIST OF SCHEMES

# LIST OF ABBREVIATIONS

0-D/1-D/2-D/3-D ............................................Zero/One/two/three dimensions

2-PDI.............................................................N,N'-bis(di propanoic) perylene dicarboxamide

5-PDI.............................................................N,N'-bis(di pentatonic) perylene dicarboxamide

A...................................................................Adenine

AgNC ...........................................................Ag nanoclusters

aq..................................................................Aqueous

BO................................................................Born-Oppenheimer

C...................................................................Cytosine

CB ................................................................Conduction band

CFCA ...........................................................4-(trifluoro methyl) cinnamic acid

CM  ..............................................................Carrier multiplication

CPCM ...........................................................Conductor polarized continuum model

CT ................................................................Charge transfer

DFCA............................................................2,6-di-fluro cinnamic acid

DFCA35.........................................................3,5-di-fluro cinnamic acid

DFT  .............................................................Density functional theory

DNA..............................................................Deoxyribonucleic acid

DOS...............................................................Density of states

$e$-$h$  ...............................................................Electron-hole

$E_h$...................................................................Hole state energy

$E_e$...................................................................Electron state energy

eV..................................................................Electron Volt

F ...................................................................Faraday constant

FFT................................................................Fast Fourier transform

nm ...............................................................nanometer

NPL .........................................................Nanoplatelets

NR ............................................................Nanorods

NTOs.........................................................Natural transitions orbitals

OA.............................................................Oleic acid

PCA ..........................................................Principal component analysis

PCM...........................................................Polarized continuum model

PDI.............................................................Perylene dicarboximide

PDOS .........................................................Projected density of states

PL...............................................................Photoluminescence

ps................................................................Picosecond

PV ..............................................................Photovoltaic

PVC.............................................................Photovoltaic cell

QDs .............................................................Quantum dots

R/r ...............................................................Radius

RMSD ..........................................................Root-mean square deviation

s..................................................................second

SHE..............................................................Standard hydrogen electrode

SMD.............................................................Solvation model based on density

Soln Geom ....................................................Geometry optimized including solvent

ss-DNA .........................................................Single stand DNA

STOs ............................................................Slater-type orbitals

T ..................................................................Thymine

TDDFT ........................................................Time dependent DFT

TDKS............................................................Time-dependent Kohn-Sham

VASP ............................................................Vienna ab-initio simulation package

*w*....................................................................Wurtzite

VB ................................................................Valence band

# LIST OF SYMBOLS

Å.................................................................Angstrom

$E_b$.................................................................Binding energy

$e^-/e$ .................................................................Electron

$h$.................................................................Hole

$r$.................................................................Radius

$\hbar$.................................................................Reduced Planck's constant

$k_{cool}$ .................................................................Intra-band cooling rate

$\tau_{CM}$ .................................................................Time-scale for single CM

$E_{i,th}$ .................................................................Energy of $i^{th}$ state

$r$ .................................................................QD radius.

$m_e$ .................................................................Effective mass of the conduction band.

$m_h$ .................................................................Effective mass of the valence

$m_0$ .................................................................Mass of a freely moving electron.

$\hat{H}$ .................................................................Hamiltonian operator.

$\Psi(r_1,\ldots r_M, R_1,\ldots,R_N)$ .................................................................Many-body wavefunction.

$E$ .................................................................Eigenvalues

$E_F$.................................................................Fermi energy

$r_n$ .................................................................Coordinate of the $n^{th}$ electron.

$R_n$ .................................................................Coordinate of the $n^{th}$ nuclei.

$\hat{H}_e$ .................................................................Electronic Hamiltonian operator.

$\psi(r_i; \{R_I\})$ .................................................................Electronic wavefunction.

$\zeta$.................................................................Width of an orbital

$\Omega$.................................................................Volume (define basis set)

$G$ .................................................................Cut-off energy

$\Delta t$.................................................Time-step

$E_{tot}$.................................................Total energy

$E_{HOMO}$.................................................Energy of HOMO

$E_{LUMO}$.................................................Energy of LUMO

$\varepsilon_k$.................................................Excited occupied state energy

$\varepsilon_l$.................................................Excited unoccupied state energy

$E_g$.................................................Bandgap

$\alpha/\beta$.................................................Axis angle

$E_{abs}^0(O|R)$.................................................Reduction potential

$\Delta G_{red(aq)}$.................................................Gibbs free energy of redox reaction

$\Delta G_{therm}$.................................................Thermal correction to enthalpy change

$\Delta G_{solv}$.................................................Solvation free energy

$S$.................................................Overlap matrix

$P_{n,frag}$.................................................Projected density to a fragment

$D_m$.................................................Degree of charge transfer

$P_e$.................................................Population of electron

$P_h$.................................................Population of hole

$N$.................................................Gaussian normalization factor.

$\sigma$.................................................Linewidth of the Gaussian.

# 1. INTRODUCTION

Particles with a dimension in the nanometer ($10^{-9}$ m) scale are usually referred to as nanoparticles. Although extensive studies are done in the recent few decades on synthesizing and applications of nanoparticles, naturally found nanoparticles had been used in different applications since the ancient era. Naturally found nanoparticles include inorganic compounds (metals, iron oxides, copper compounds) and organic (proteins, viruses, polysaccharides, etc.). The most prominent use of nanoparticle was the Au metal nanoparticles as a pigment on the glass surfaces (Figure 1.1). Double layers of dispersed Ag and Cu nanoparticles were used to create a lustering glaze on the glass surface.[1] Ancient Chinese, Egyptian, and Romans knew the application of metal clusters for decorative applications.[2] People in Indian civilization knew the application of metal nanoparticles to cure diseases like arthritis.



**Figure 1.1**: Stained glass in Roman Cathedral and Lycurgus glass from the 4th century AD roman era. Courtesy: www.britishmuseum.org and Freestone et al., Gold Bulletin, **40,** 270–277 (**2007**)

## 1.1. Common Properties of the Metal and Semiconductor Nanoparticles

The significant scientific step was taken about 150 years ago when Michael Faraday synthesizes the Ruby color Au nanoparticles, although the chemistry behind this feature was unknown. In the middle of the 20th century, American physicist Richard Feynman's famous

lecture entitled "there is Plenty of Room at the Bottom" opened the door of tuning properties of a

material by controlling the size instead of altering the compositions. Faraday's Gold

nanoparticles size was 6±2 nm.[3-4] The emission of bulk metals is very weak, but quantum yield

drastically increases due to metal clusters size reduction to the nanometer scale. Therefore,

Faraday's gold nanoclusters' bright ruby color emission was a result of the strong surface

plasmon of metal nanoclusters. The plasmon energy from the collective electron oscillation can

be treated by classical electrodynamics.[5-6]

$$\hbar\omega_p = \sqrt{\frac{ne^2}{m\varepsilon_0}} \qquad (1.1)$$

Where, $\omega_p$ is the plasmon frequency, $n$ is the electron density, $\varepsilon_0$ is the free electron mass.
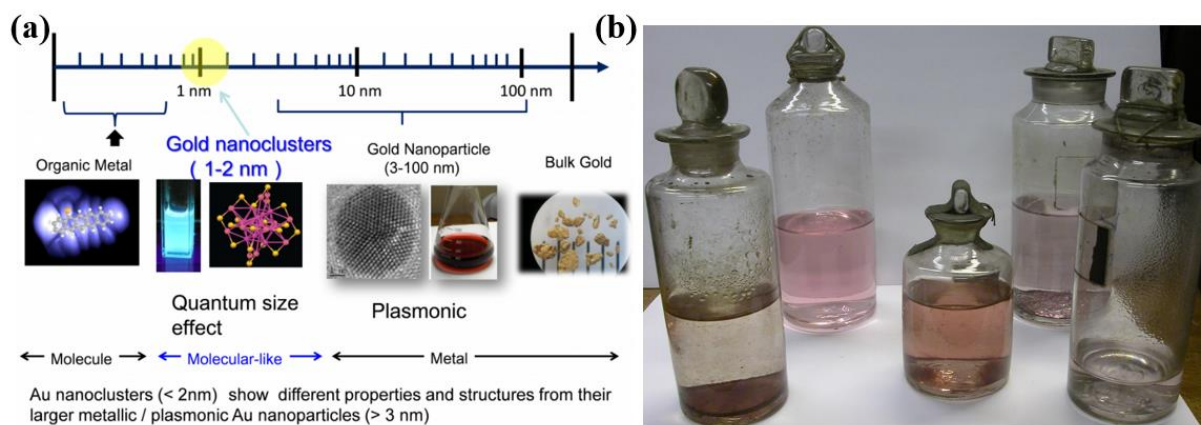


**Figure 1.2**: (a) Evaluation and the Au nanoclusters' different properties with decreasing the nanoparticle size. Au metal shows the plasmon emission as an organic molecule like bright emission based on the clusters' size. (b) The original ruby color nanoclusters of Au; synthesized by Michael Faraday in the 1850s.

However, bandgap energy becomes large, and emission energy becomes a single

electronic state excitation dependent when the nanocluster's size is reduced to nm to the sub-nm

range. **Figure 1.2** is showing the evaluation of optical properties with the nanoparticle size. In

the case of gold nanoclusters, the broad plasmon absorption spectra turn to discrete absorption

spectra in clusters smaller than 1.1 nm, one of such examples is thiol passivated $Au_{25}$.[7-8]

Similarly, Ag and Au metal nanoclusters of smaller than 25 atoms show characteristics optoelectronic properties dominated by the precise size and geometry.

Small metal nanoclusters are fundamentally different from the spherical semiconductor nanoparticles. If semiconductor nanoparticles size is smaller than the exciton Bohr radius, quantum confinement plays a dominating role in determining the optoelectronic properties due to their isoelectronic feature.[9-10] In contrast, the electronic structure and optical properties of small metal clusters are dependent on the detailed structure of the nanocluster. Therefore, few atom size metal nanoclusters are considered as molecular metals.[10-11] As such, metal nanoclusters are prepared by passivating large organic molecules or macromolecule templates, like single-strand DNA (ss-DNA). On the other hand, a semiconductor nanoparticle or nanocrystal is a small crystal fragment of materials with the bulk crystals structure of the materials — a typical size ranges from 1-10 nm. After Feynman's prediction in 1959, A.I. Ekimov of the Soviet Union and Louis Brus, Michael Steigerwald from Bell Labs, first realized that the fundamental optoelectronic properties of semiconductors change at the small size regimes.[12-13] Although semiconductor nanocrystals have bulk crystal lattice, it has significant surface reorganization due to the quantum confinement. Therefore, surface passivation by organic and inorganic molecules is used to stabilize and prevent the colloidal nanocrystals' dangling surface bond.

Despite the fact that the ligands are used for passivating both metal and semiconductor nanoparticles, it also used to tune and functionalized the nanoparticles. Silver nanoclusters behave as fluorescent emitters when coordinated and stabilized by a single strand DNA.[14] Oligonucleotides typically with 10−30 bases locally concentrate $Ag^+$ cations[15] and facilitate the assembling of chemically reduced silver in the form of nanoclusters encapsulated in DNA (DNA–AgNCs).[11, 16-21] Such DNA–AgNCs demonstrate emission at the range from visible to

near-infrared (n-IR) wavelength with high quantum yields[15, 22] up to 90 %, and lifetimes[14, 23-26] of 1−5 ns. These data demonstrate that DNA–AgNCs have excellent optical properties while possessing high photostability and low toxicity, making them more appealing in biological applications than organic dyes and semiconductor quantum dots.[27-31] Such applications include DNA–AgNCs use as highly sensitive sensors,[32-34] fluorophores in bio-imaging[35-36] (especially beneficial at high background interferences[37]), and *in vitro* and *in vivo* nanothermometry.[38] Similarly, semiconductor QDs are tuned and functionalized for high quantum yield[39], broader absorption energy range[40-41], narrow emission[42-43], carrier multiplications[44-46], and many other applications.

Single strand DNA (ss-DNA) works as templated in Ag nanoclusters, but it also dominates the structural and electronic properties. Electrostatic dipole and surface interaction of ss-DNA with metal nanoclusters are used to tune optoelectronic properties. Similarly, the dipole of the organic ligand and the surface states determine the electron transfer dynamics in the electron acceptor-donor system, e.g., PbS QD- PDI model. Besides, $PbCl_2$ molecules are used as a bridging molecule between the PbSe QDs to synthesize thickness controlled nanoplatelets. Both ss-DNA and $PbCl_2$ work as templates for the metal and semiconductor nanoparticle synthesis, but its effects on overall photophysics are different. Ss-DNA influences the overall nanoclusters' geometry and optical transitions. On the other hand, $PbCl_2$ creates an interface in PbSe lattice, which influences the excited carrier dynamics. Considering the importance of ligand and templates molecule, we have studied both surface and interface effects on the photoexcited process in Ag metal nanoclusters and Pb and Cd chalcogenide nanomaterials.

### 1.1.1. Electronic Properties of the Confined Nanomaterials

When the particle size is smaller than the Bohr radius, confined materials are comparable with the famous example from quantum mechanics – "a particle in a box." Solving the Schrodinger equation for the wavefunction, which is confined in a deep potential, would result in quantized and widely separated discrete energy states as molecular orbitals in molecules. Since an electronic wavefunction is confined in a small volume, electronic states' energy significantly changes in response to changing the confined volume. Metal nanoclusters can be considered metal molecules with size and structure-dependent electronic and optical properties. Inspired by the continuous electronic state of bulk metal, Kubo suggested that energy level spacing in a metal cluster of N atom can be determined by –

$$\delta = \frac{E_F}{N^{\frac{1}{3}}} \tag{1.2}$$

Where $E_F$ is the Fermi energy of the bulk metal. Later, Na clusters electronic states explained by Jellium electronic model of metal.[47] Ag and Au nanoclusters are synthesized by stabilizing using thiolate[48] or macromolecules like polymers,[49-50] single-strand DNA (ss-DNA),[11, 14, 51] proteins[52-53]. Because of metals' molecular features, discrete electronic levels are perturbed by the ligand passivation. The base sequence of the ss-DNA dominates the nanoclusters' structural symmetry, hence the electronic properties.

Similarly, the electronic properties of confined materials can be tuned by the size of the nanomaterials. Semiconducting materials with a large exciton Bohr radius permits a wide range of tunability of electronic states and bandgap energy; for example, the Bohr exciton radius of PbS is 18.0nm[54], PbSe is 46 nm[55], GaAg is 14.90nm[56], and CdSe is 5.4nm[57]. Bohr exciton radius is the maximum distance where an excited electron and hole feel Coulombic attraction. As such,

5

the composition and the volume dominate the photophysical properties of nanomaterials. Therefore, Pb chalcogenide nanomaterials (PbS, PbSe, PbTe) emerged as a promising material for photovoltaic applications [58-59], light-emitting diodes,[60-61] lasers[62-63], field-effect transistors[64] etc.

Due to the small volume of spherical QDs, the surface-volume ratio is large in a low dimensional nanomaterial, especially in 3D confined QD and metal nanoclusters.[65] Although the core of QD retained bulk lattice crystal, surface and interfaces are deformed from the bulk lattice and result in a reactive surface. In the experimental case, the relatively reactive surface of the nanomaterials is passivated by the different organic and inorganic ligands to improve stability, solubility and to remove dangling bond[66-67]. Despite the positive impact of surface ligands, improper ligand passivation could cause the surface trap states,[68-69] dangling bonds, which reduced the device efficiency.[69] Besides, the electronic energy of a QDs would alter in the presence of surface ligand dipole.[70] These effects open the door to tune the occupied and unoccupied state's energy, as such the bandgap.[70-71] The electronic band and energy alignments engineering would facilitate the hot carrier and energy transfer between the nanomaterials and functional chemical group, which would increase the efficiencies of optoelectronic processes.[71] Overall QD-dye structural feature dominates the frontier band alignment, as such electron transfer. In chapter 4, we have shown the effects of ligand dipole and structural features on the electronic structure of the perylene diimide (PDI) functionalized PbS QDs.

## 1.1.2. Structural Variation of Nanoclusters

Because of the quantum confinement, the structure and composition of nanoclusters dominate the photophysical properties. Thiolate, polymer, or DNA encapsulated Ag clusters are formed by the agglomeration of chemically reduces Ag ions. Adsorbing thiolate on the

6

nanocluster surface prevents the nanoclusters' growth and stabilize the nanoclusters. In the case

of DNA passivation, tertiary structure and nucleobase sequence dominates the Ag nanoclusters'

structural feature. Because of the few atom sizes, structural symmetry determines the sparse

electronic states, and it is perturbed by the nucleobase. Hence, the electronic and photophysical

properties of the encapsulated nanoclusters are mostly dependent on the nucleobase and Ag

nanoclusters interactions.

The other most common nanomaterials are ligand passivated spherical semiconductor

QDs. Cd and Pb chalcogenide QDs are synthesized using long-chain aliphatic ligand- oleate

acid[72], hydrophilic ligands like thiolate ligands[66], or inorganic Pb halide ligand[73-74] and many

others. Although ligand passivation minimizes the surface dangling bond, to achieve the ideal

passivation in the colloidal solution medium is almost impossible. Instead of organic or inorganic

ligand, semiconductor QDs can be covered with a non-identical semiconducting material layer.[75]

Usually, this type of QDs known as core-shell QDs[76]. Core-shell structure substantially improves

the photoluminescence efficiency[77] by confining the hot carrier in a small core volume[78-79] and

minimize the surface dangling bond results of the rigid shell surface. [79] The interface also

dominates the optoelectronic properties of the core-shell structure.[80] Interfacial trap state[81],

spatial localization of *e-h* states[82], and the potential interfacial barrier[83-84] would determine the

overall efficiency. Although it is reported that the quantum yield of the Cd and Pb chalcogenide

is improved, the realization of a practical photovoltaic device from the core-shell structure would

be challenging because the shell is acting as a barrier of core localized hole transport. Recently a

cation exchange synthesis method is reported for the Janus type PbSe|CdSe spherical QDs.[85]

Using the Femtosecond transient absorption, Kroupa et al. hypothesize that the Janus type

architecture of PbSe|CdSe QDs would improve the multiexciton generation efficiency in

compared to PbSe QDs.[86] The dielectric field in spherical QDs are homogeneous, but increasing the spatial dimension of nanocrystal would create the asymmetric dielectric field. NPL should have a higher dielectric constant than spherical QD but lower than bulk semiconductor. So, thickness control would use as a tool to control the exciton Coulomb interaction in the NPL.

**1.2. The Key Role of Surface and Interface in the Application of Nanomaterials**

**1.2.1. Effects of Surface Passivation of Metal Nanoclusters Electronic Properties**

The structural and optical properties of DNA-AgNCs have proven to be challenging to control, as they can adopt a wide variety of shapes, sizes, charges, and conformations, which change with the DNA sequence,[14] as well as its secondary structure.[24, 87-91] The molecule-like (discrete) electronic structure of DNA-AgNCs is very sensitive to variations in their conformations, oxidation state, and binding sites interacting with DNA bases leading to significantly different optical and catalytic properties of specific clusters.[92-93] In particular, DNA-AgNCs usually exhibit multiple absorptions and emission peaks that do not correlate to structured continuum feature.[87, 94] The variations in emission wavelength upon changes in the excitation wavelength together with the increase of the average decay time as a function of wavelength in DNA-AgNCs[95] have been related to different emitters, due to inhomogeneous changes of the conformation of the AgNC or the DNA scaffold.[96-97] Nonetheless, it was also found that certain shapes and sizes of AgNCs are more stable at the given DNA length,[51, 98-99] sequence, [14-15, 17, 22, 25, 87, 89, 100-101] and synthesis conditions, including variations in Ag$^+$ concentrations,[16, 102] pH,[102-103] and types of oxidizing-reducing agents.[14, 104] As such, the stoichiometry of AgNC and, consequently, their electronic structure and optical spectra can be controlled to some degree by altering the DNA sequences.

**1.2.2. Effect of Surface Passivation of NC**

Discrete energy levels are expected to reduce the intraband relaxation rate of an excited carrier due to the energy mismatch between the longitudinal optical phonon (LO) and intraband energy difference[105]. Electronic absorption spectra analysis of the various QDs had shown that the splitting is about ten times larger than phonon frequencies.[106] These well-separated discrete intraband energy relaxation occurs only when an excited electron (*hot-e*) is coupled with multiple phonons[107]. This multi-phonon process is required to meet energy balance and resonance with multiple phonon[107], which significantly reduces the hot carrier relaxation rate[108]; thus, this phenomenon is known as the phonon-bottleneck.[109] Despite the expectation of slower relaxation due to the phonon-bottleneck, time-resolved spectroscopies of Pb and Cd chalcogenide nanomaterials show the fast relaxation in the range sub-picosecond to picosecond.[110-114] These theoretical and experimental results suggested that hot electron and hole dissipate the excess energy mainly via two mechanisms - through a non-radiative decay via surface originated states.[113, 115-116], and the Auger scattering-type process.[110, 117] An off-stoichiometric surface passivation increases the relaxation via intermediate states, while the optimal number of surface ligands ensures the semiconducting behavior of the QDs without no midgap.[118] Crystal mismatch and surface passivation of the nanomaterials creates a dangling bond of overlapping between the surface and core state.[118-120] It increases the coupling between hot carrier states in core and the higher frequency surface phonon mode.[115, 120] Overall, phonon bottleneck breaks by energy dissipation of the high energy state through phonon and via the multi-phonon process in the frontier orbitals.[120-121] The fast intraband relaxation would be beneficial for making the device like light-emitting diodes (LED). But if ligand or surface layer generates trap states, hot carriers are trapped in surface originated trap states.[122] QD start

9

blinking due to the charging and discharging of the trap state,[123-124] which reduces the

photoluminescence yield of the QDs.[122]

### 1.2.3. Properties Governed by an Interface in Semiconductor NC

In the core-shell QDs, an interfacial strain is formed due to the lattice mismatch, which

results in an interfacial "trap state"[122]. A thick shell and interfacial alloying layer eliminate the

interfacial trap spate.[79, 125] Besides the surface originated states, the Auger scattering process

dominates the hot carrier relaxation process in QDs.[126] Spatial separation of hot electron and hole

is an efficient process to reduce the Auger decay rate.[45] In core-shell QDs, an interfacial layer

determines the hole and electron wavefunction overlap. Time-domain spectroscopic of the

CdSe/CdS QDs show that core localized hole has a minimum overlapping with the whole QD

localized electrons, and which suppress the Auger decay rate by reducing the e-h overlap. [127] But

the overall Auger decay time depends on the characteristics of the interfacial layers. A thin shell

or sharp interface would have a sharp potential difference between core and shell localized

states. Smoothening the confinement potential by creating an interfacial alloy could reduce the

overlap between initial and final states for the hot carrier.[83] a thick shell of CdS with a smaller

core of CdSe create an interfacial alloy $CdSe_xS_{1-x}$ layer at the interface and smoothen the

confined potential between CdSe and CdS.[83] The alloyed layer suppresses the biexciton Auger

recombination rate and improves the overall emission efficiency.

The interfacial layer has a different role in the Janus type heterostructure. Kroupa et al.

hypothesize using the spectroscopic result that the higher energy hole can be trapped at the

interfacial state, which slows the relaxation process significantly.[85-86] Reduced intraband

relaxation rate, higher exciton Coulomb interaction due to an asymmetric structure would

increase the carrier multiplication[85] (Detail discussion in sub-section 1.3). But the formation of

interfacial states and its dependence on lattice symmetry is still unknown. ab initio study on the effects of PbSe and CdSe lattice and interfacial lattice plane on the electronic properties of Janus PbSe|CdSe QDs will help to understand the role of the interfacial states in the photophysical process. In chapter 6, we have shown the effects of lattice parameter on the electronic properties of the Janus QDs.

## 1.3. Role of Intraband Relaxation in Application of Nanocrystals

**1.3.1. Effects of Phonon Mediated Hot Carrier Relaxation**

The hot carrier cooling process, especially in QDs, studied extensively both experimentally and theoretically. Despite discrete widen electronic states in 3D confined nanoclusters, electron-phonon coupling mediated energy dissipation play an important role in non-adiabatic energy relaxation of the hot carrier. Bulk semiconducting materials have strong electron-phonon coupling, especially with the longitudinal optical phonon, compared to the confined NC. Kilina et al. predicted that the multiphoton relaxation through the strong coupling with acoustic phonon.[128] A pump-probe spectroscopy suggested that the hot electron relaxation depends mainly on the degree of surface passivation while hole relaxed through the intrinsic QD state or intrinsic surface state[110,129]. Acoustic phonons are lower in energy phonon mode, which is mainly correspond to surface originated state. It is confirmed by the Huang-Rhys factor dependence on the surface-volume ratio in the PbSe and CdSe QDs. As a result, surface localized excited state originated from the dangling bond or off-stoichiometric surface increase the electron-phonon coupling in QD. Theoretical calculations of the PbSe and PbSe QDs show that the energy dissipation dynamics of both electron and hole are dominated by electron-phonon coupling of the acoustic phonon mode along with the smaller coupling with optical phonon mode in the energy range of 150-300 cm$^{-1}$. A Raman spectroscopy suggested that the optical phonon

modes are the results of thermal fluctuations. Other effects of higher acoustic phonon coupling are that it accelerates the dephasing rate. Theoretical studies show that dephasing time is elongated due to increasing the QD size, which results from lowering the acoustic phonon coupling.

Two-dimensional CdSe nanoplatelets have narrow emission linewidth, which indicates the low longitudinal optical phonon interactions. The computational study predicts the low dephasing rate due to the lower acoustic phonon coupling.[130] But the considered model was anatomically ideal flat NPL. On the other hand, thickness controlled NPL synthesis is reported by $PbCl_2$ bridging between the PbSe QDs. It incorporates Pb halide molecules in the NPL lattice, which would create a surface or interface localized states. In chapter 5, we have shown the effects of the confinement and incorporated $PbCl_2$ molecules in NPL.

## 1.3.2. Effect of Hot Carrier Relaxation: Auger Recombination vs. Carrier Multiplication

The second energy dissipation process is an Auger type process, where efficient *e-h* energy transfer takes place in quantum-confined nanomaterials due to the strong Coulomb interaction between the excited carrier (*e,h*).[108,110,126] The valance band's density of states is denser due to the heavier hole effective mass and degeneracy in the valance band states.[108, 110] In results of that, energy from the excited electron (*hot-e*) can transfer to the hole, and excited holes (*hot-h*) energy can dissipate very fast through the phonon coupling, which overcomes the phonon bottleneck. Another multicarrier process is Auger recombination in which *e-h* in the frontier bands are recombined and transfer the energy to the third carrier and excite to the higher energy state. [84, 131] Auger recombination process is inefficient in the bulk semiconductor materials because it requires translational momentum conservation along with energy conservation.[132] But due to the small dimension of the confined nanomaterials, the Bloch states are in defined

12

momentum, which relaxed the momentum conservation constrain[133,134] and increases the Auger scattering rate. Although the fast intraband relaxation and Auger scattering process could be beneficial for the applications like light induce diode[60, 115] and lasing[61,135], it has adverse effects on the photovoltaic applications.[136-137]

Although Auger scattering is reported in Pb chalcogenide nanomaterials, Pb chalcogenide nanoclusters (NC) become a promising material for application in a photovoltaic cell (PVC) because of the higher carrier multiplication (CM) rate.[133,134,138] CM is an inverse process of Auger scattering where an electron excites to the frontier conduction band by absorbing the excess energy of a hot carrier and created multiple pairs of hot carriers. Since more than one pair of hot carriers are generated by absorbing a single photon, intrinsic quantum yield in the photovoltaic application could exceed 100%. Because of a similar mechanism, CM is also referred to as inverse Auger scattering,[139] multi-exciton generations (MEG),[140-141] impact ionization.[142]

Similarly, both the Auger process and CM rate of semiconducting materials are governed by the same Coulomb matrix element[143] while the rates are not equal as the densities of the initial and final states in either process are not identical. Overall, the CM rate competing with the rate of the phonon mediated relaxation and the Auger scattering rate.[126, 143] Several quantum chemical-based models are proposed to determine the CM, but spectroscopic results inspired the window-of-opportunity model to describe the CM rate satisfactorily where CM treats a competition between the impact ionization and non-CM process.[143] The CM rate, $\eta_i$ is defined as $\eta_i \propto (E_i - E_{i,th})/(k_{cool}\tau_{CM})$, where $\tau_{CM}$ is the time scale for a single CM process, and $k_{cool}$ is the intra-band cooling rate, $E_i$ is the carrier energy and $E_{i,th}$ is the minimum energy to initiate a CM process. Therefore, the CM rate be modified by tuning $k_{cool}$ or $\tau_{CM}$ or both. Although, a

single CM time $\tau_{CM}$ decreases with decreasing nanoclusters size,[144] spectroscopic study of PbSe QD suggested that cooling rate is inversely proportional to the nanoclusters volume $k_{cool} \propto R^{-3}$.[110,114,145] Considering the effects of the CM time scale and intraband cooling rate on overall multiexciton yield, one can design a nanocluster of high CM yield with slower intraband relaxation engineering.

In the case of CdSe QDs, a hot hole is much more massive than the hot electron, as such hot-electron energy efficiently transfers to the hole and hot hole relaxed through the denser valance band state.[146-147] In contrast, PbSe has almost symmetric valance and conduction band density, which makes hot-electron to hole energy transfer inefficient. Besides, intraband relaxation in PbSe is less susceptible to being affected by the surface state in comparison to CdSe QDs.[121, 148] Overall, Auger type cooling dominates in CdSe QDs while PbSe QDs shows size-dependent activation of the cooling channel.[114]

### 1.3.3. Effects of Confinement and Spatial Separation of *e-h* on Carrier Relaxation

Core-shell type QD with a thick shell is an example of engineering the hot carrier cooling mechanism. An electron of this quasi type II QD is delocalized over the whole volume while the ground state hole wave function is strongly confined in the smaller PbSe core, which results in a larger energetic gap between the hole state immediately below the band edge. Wider energy gap reduces the hole relaxation due to the phonon bottleneck and further decreases due to the limited wavefunction overlap between the shell localized and core localized frontier hole states. In addition, core localized valence band carriers ($1S_h$) experience stronger Coulomb coupling due to smaller spatial separation, which increases the overall CM rate.[45]

Modification of nanoclusters shape (0D, 1D, or 2D) is another efficient method of tuning charge carriers' intraband relaxation. Elongation in 1 dimension (1D nanorod-NR) let quantum

confinement in two directions and reported different carrier-carrier interaction and carrier

cooling rates. Due to elongation in one dimension (1-D NR), NR is expected to have a denser

density of states. Moreover, due to the structural anisotropy, NR has an asymmetric dielectric

field in surrounding in comparison to the colloidal spherical QDs. NR has a lower dielectric

constant, and it results in stronger carrier-carrier Coulomb interaction. The dielectric constant of

the PbSe semiconductor is in order of magnitude higher in comparison of solvent or organic

ligands. Despite the enhancement of the Coulomb interactions in the PbSe NR, Padilha et al.

reported that the Auger recombination rate is decreased in 1D PbSe NR than QDs, but it was

found that CM rate is higher in 1D NR.[44] This contradictory result is rationalized by considering

the opposite initial and final state in these two processes. Due to the stronger Coulomb coupling

between the relaxed *e-h* pair, Auger recombination is not a three-particle collision process in NR

as it is in QDs. Auger recombination in NR is a neutral biexciton process and, as such, decreases

the Auger recombination rate.[133] Besides, CM rate is optimal in a particular aspect ratio of the

length and diameter of the NR.[44] Increasing the dimension from the spherical QD shape

increases the Coulomb interaction, but bulk like momentum conservation becomes a dominating

factor after a certain aspect ratio.

Similarly, NPL also should have higher Coulombic effects from structural anisotropy,

and higher density of states in addition to momentum constrain.[149-150] However, structural

anisotropy and momentum conservation can be tuned by tuning the lateral dimension and

thickness ratio.[151-152] In addition, a larger volume along the planner surface would be beneficial

for tuning spatial separation of the hot carrier. Higher than bulk CM efficiency and lowering the

threshold energy compared to bulk are reported in PbS NPL.[153] In another method, PbSe NPL

synthesized by oriental attachment of PbSe QD by Cl-Pb-Cl bridging on (110) facet and grown

in (100) lattice direction.[152] The effects of the $PbCl_2$ bridging molecules on the hot carrier relaxation process is still unknown, although later method gives more control on the orientation of the lateral dimension and thickness.

### 1.4. Tuning the Photoluminescence of DNA Templated Ag Clusters

It is reported that Watson-Creak type pairing through $Ag^+$ bridging can stabilize the double-strand DNA and form elongated nanorod clusters.[87, 154-155] Single-strand DNA typically results in brighter DNA-AgNCs by forming a loop around the cluster.[14, 156] It was recently detected that different lengths of repeated $C_2A$ and $C_2T$ strands identify a minimal $(C_2X)_6$ (X=G, A, T) scaffold that stabilizes the $(Ag_{10})^{6+}$ chromophore absorbing between 400−450 nm.[157] This points out that AgNCs of a certain stable stoichiometry can be coordinated via multiple nucleobases.

In the case of homo-oligonucleotide, cytosine (C)[25, 102, 158], and guanine (G)[158] strands have been reported to form highly emissive DNA-AgNCs. Clusters formed with thymine (T) strands emit only at the controlled oxidation state,[104, 158], while adenine (A) strands do not result in emissive clusters.[51, 158] Therefore, adenine (A) is typically used as a spacer between nucleotide sequences. Computational calculations also support these results predicting higher affinity of the cationic silver to $C^{159}$ and $G^{160}$ nucleotides forming coordinated bonds with their nitrogens.[161] Similar to the emission energies, the intensity of the emission also depends on cluster-based interactions. Due to the highest reduction potential among nucleotide bases, G-Ag interaction could increase the hybridized charge transfer character of the lowest energy transitions, which is expected to increase the intensity of the emission.[51, 162] Despite these extensive studies, identification and controllable manipulation of the structure, size, and shape of DNA-AgNCs are

16

still in dispute. Overall, the rigorous relationship between structural conformations and the optical response of DNA-AgNCs is still unclear.

## 1.5. The Objectives of this Thesis

This dissertation is focused on studying surface and interface effects on the ground and excited state photophysical process of the metal and semiconductor nanoclusters. As we have discussed in the above section, surface and interfacial state have a dominating role in the photophysics and excited-state dynamics. It is required to understand the surface and interface effects to tune the photophysical process. We have used ab initio computational methodology to study the relationship between the passivating ligand, structure, lattice symmetry, interfacial layer, and photophysical process of the Ag nanoclusters and Cd and Pb chalcogenide.

Ag clusters are synthesized in a bottom-up process, where reduced Ag cation agglomeration and form small clusters. Photophysical properties are dominated by charge, size, structure, oxidation state, Ag-N interactions, and many others. Complementing experiments, quantum chemistry calculations can provide important insights into the interaction mechanisms between the DNA bases and AgNCs and their effect on the electronic structure and the optical response. However, literature reports on such calculations are still limited. Reported studies are mainly focused on the impact of a charge and/or size of small AgNCs (of 2 to 6 atoms in size) on the interaction with a specific DNA base (either C[159] or G[160, 163]). The effect of a base type on the interaction with AgNCs has also been studied computationally.[159, 160] In all cases, however, the stability and optical spectra of DNA-AgNC have been modeled for clusters bound to only one type or a pair of bases in a vacuum, rather than clusters completely encapsulated by different bases in a polar media, as it takes place in experiments. Moreover, core Ag metal clusters' symmetry could be modified significantly in the polar solvent conditions, as such electronic

structure cannot be described adequately by simple electronic shell stabilization model.[164]

Samanta et al. previously reported the importance of inclusion of complete nucleobases model[165]. A single strand DNA was used in the calculation but strand of only identical nucleobases. In addition, absorption spectra are predicted by the imaginary part of the dielectric constant obtained from the ground state density matrix. This simplistic approach is not enough when the exciton binding energy is large in small metal clusters.[166]

Motivated by the idea of improving the DNA-AgNCs models to better suit realistic structures, here we present calculations based on Density Functional Theory (DFT) and Time-Dependent DFT (TDDFT) of AgNCs fully passivated by various DNA bases, including their mixtures, reduction potential, size dependency, in a polar environment and compare results to the vacuum calculations.

The overall charge and formation of the clusters should depend on the redox potential of the Ag clusters. It was reported that the Ag nanoclusters have negative Redox potential when nanoclusters formed, and it varies significantly based on the size and charge. Accurate calculation of redox potential also depends on the structural feature and solvation methodology adopted. In chapter 3, we have answered the effects of the solvation method on redox potential calculation and the most probable oxidation state in a reaction medium. We also elucidate the effect of conformations, charges, and a polar solvent on the optical spectra of DNA-AgNCs. Besides, the evaluation of photophysical properties with the Ag NC size is also investigated. In the last section the chapter 3, we have answered that what are the required descriptor to predict or making a QSAR model predict the lowest transition oscillator strength.

In chapter 4, we have studied the electronic properties of the cinnamic acid derivative passivated PbS QD – PDI model. Perylene diimide (PDI) and its' derivatives are promising for

18

optoelectronic devices for their high absorption cross-section, strong electron acceptor, and good conductor in solid. Efficient electron transfer from Pb chalcogenide QD to PDI derivatives would be beneficial for the application in PVC. Electron transfer from PbS QD to PDI largely depends on QD and PDI localized state. We have investigated how the PDI linker group and PDI-QD surface-interaction tuned and optimized the photoexcited electron transfer process.

Higher efficiency PVC is already made from PbSe NCs. The CM efficiency would be even higher in the PbSe nanoplatelets. Koh et al. reported the synthesis of thickness controlled PbSe NPL from the $PbCl_2$ passivated PbSe QDs.[152] But what are the effects of $PbCl_2$ incorporation in the NPL lattice on the excited state carrier relaxation is not understood yet. In chapter 5, we have studied the effects of $PbCl_2$ in the NPL interface and the effects of confinement on hot carrier dynamics. We use the Fewest Switching surface hopping method to simulate the phonon mediated excited electron and hole relaxation process.

The next interface type we considered is the interface between PbSe and CdSe lattice in PbSe|CdSe Janus type QDs. Due to smaller offset between the PbSe and CdSe localized unoccupied band, PbSe|CdSe can form either type I or type II structure based on the interfacial layer. Hot carrier relaxation and overall dynamics are dominated by the characteristics of the interfacial layer in Janus QDs. In Chapter 5, we have studied the lattice structure variation of the Janus QDs and its' effects on the interfacial electronic states. These results will help to design and control the Janus QDs' photophysical properties.

## 1.6. References

1.      Sciau, P.; Mirguet, C.; Roucau, C.; Chabanne, D.; Schvoerer, M., Double nanoparticle layer in a 12th century lustreware decoration: Accident or technological mastery? *Journal of Nano Research* **2009,** *8*, 133-139.

2.      Freestone, I.; Meeks, N.; Sax, M.; Higgitt, C., The Lycurgus Cup — A Roman nanotechnology. *Gold Bulletin* **2007,** *40* (4), 270-277.

3.  Faraday, M., X. The Bakerian Lecture.2014; Experimental relations of gold (and other metals) to light. *Philosophical Transactions of the Royal Society of London* **1857,** *147*, 145-181.

4.  Thompson, D., Michael Faraday's recognition of ruby gold: the birth of modern nanotechnology. *Gold Bulletin* **2007,** *40* (4), 267-269.

5.  Reiners, T.; Ellert, C.; Schmidt, M.; Haberland, H., Size Dependence of the Optical Response of Spherical Sodium Clusters. *Phys. Rev. Lett.* **1995,** *74* (9), 1558-1561.

6.  Ashcroft, N. W.; Mermin, N. D., *Solid state physics*. Saunders college: Philadelphia, Pa., 1976.

7.  Sakanaga, I.; Inada, M.; Saitoh, T.; Kawasaki, H.; Iwasaki, Y.; Yamada, T.; Umezu, I.; Sugimura, A., Photoluminescence from Excited Energy Bands in $Au_{25}$ Nanoclusters. *Applied Physics Express* **2011,** *4* (9), 095001.

8.  Varnavski, O.; Ramakrishna, G.; Kim, J.; Lee, D.; Goodson, T., Critical Size for the Observation of Quantum Confinement in Optically Excited Gold Clusters. *J. Am. Chem. Soc.* **2010,** *132* (1), 16-17.

9.  Brus, L. E., Electron–electron and electron-hole interactions in small semiconductor crystallites: The size dependence of the lowest excited electronic state. *J. Chem. Phys.* **1984,** *80* (9), 4403-4409.

10. Ashenfelter, B. A.; Desireddy, A.; Yau, S. H.; Goodson, T.; Bigioni, T. P., Fluorescence from Molecular Silver Nanoparticles. *J. Phys. Chem. C* **2015,** *119* (35), 20728-20734.

11. Petty, J. T.; Story, S. P.; Hsiang, J.-C.; Dickson, R. M., DNA-Templated Molecular Silver Fluorophores. *J. Phys. Chem. Lett.* **2013,** *4* (7), 1148-1155.

12. Rossetti, R.; Nakahara, S.; Brus, L. E., Quantum size effects in the redox potentials, resonance Raman spectra, and electronic spectra of CdS crystallites in aqueous solution. *J. Chem. Phys.* **1983,** *79* (2), 1086-1088.

13. Pinheiro, A. V.; Han, D.; Shih, W. M.; Yan, H., Challenges and opportunities for structural DNA nanotechnology. *Nat. Nanotechnol.* **2011,** *6* (12), 763-772.

14. Petty, J. T.; Zheng, J.; Hud, N. V.; Dickson, R. M., DNA-Templated Ag Nanocluster Formation. *J. Am. Chem. Soc.* **2004,** *126* (16), 5207-5212.

15. Schultz, D.; Gardner, K.; Oemrawsingh, S. S.; Markesevic, N.; Olsson, K.; Debord, M.; Bouwmeester, D.; Gwinn, E., Evidence for rod-shaped DNA-stabilized silver nanocluster emitters. *Adv. Mater.* **2013,** *25* (20), 2797-803.

16. Liu, J., DNA-stabilized, fluorescent, metal nanoclusters for biosensor development. *TrAC, Trends Anal. Chem.* **2014,** *58*, 99-111.

17.  Gwinn, E.; Schultz, D.; Copp, S. M.; Swasey, S., DNA-Protected Silver Clusters for Nanophotonics. *Nanomaterials (Basel)* **2015,** *5* (1), 180-207.

18.  Han, B.; Wang, E., DNA-templated fluorescent silver nanoclusters. *Anal. Bioanal. Chem.* **2012,** *402* (1), 129-138.

19.  Latorre, A.; Somoza, A., DNA-mediated silver nanoclusters: synthesis, properties and applications. *ChemBioChem* **2012,** *13* (7), 951-958.

20.  Obliosca, M. J.; Liu, C.; Batson, A. R.; Babin, C. M.; Werner, H. J.; Yeh, H.-C., DNA/RNA Detection Using DNA-Templated Few-Atom Silver Nanoclusters. *Biosensors* **2013,** *3* (2).

21.  Goswami, N.; Zheng, K.; Xie, J., Bio-NCs – the marriage of ultrasmall metal nanoclusters with biomolecules. *Nanoscale* **2014,** *6* (22), 13328-13347.

22.  Richards, C. I.; Choi, S.; Hsiang, J.-C.; Antoku, Y.; Vosch, T.; Bongiorno, A.; Tzeng, Y.-L.; Dickson, R. M., Oligonucleotide-Stabilized Ag Nanocluster Fluorophores. *J. Am. Chem. Soc.* **2008,** *130* (15), 5038-5039.

23.  Berti, L.; Burley, G. A., Nucleic acid and nucleotide-mediated synthesis of inorganic nanoparticles. *Nat. Nanotechnol.* **2008,** *3* (2), 81.

24.  Díez, I.; Ras, R. H. A.; Kanyuk, M. I.; Demchenko, A. P., On heterogeneity in fluorescent few-atom silver nanoclusters. *Phys. Chem. Chem. Phys.* **2013,** *15* (3), 979-985.

25.  Ritchie, C. M.; Johnsen, K. R.; Kiser, J. R.; Antoku, Y.; Dickson, R. M.; Petty, J. T., Ag Nanocluster Formation Using a Cytosine Oligonucleotide Template. *J. Phys. Chem. C* **2007,** *111* (1), 175-181.

26.  Shang, L.; Dong, S., Facile preparation of water-soluble fluorescent silver nanoclusters using a polyelectrolyte template. *Chem. Commun.* **2008,** (9), 1088-1090.

27.  Yang, C.; Shi, K.; Dou, B.; Xiang, Y.; Chai, Y.; Yuan, R., In Situ DNA-Templated Synthesis of Silver Nanoclusters for Ultrasensitive and Label-Free Electrochemical Detection of MicroRNA. *ACS Appl. Mater. Interfaces* **2015,** *7* (2), 1188-1193.

28.  Shen, C.; Xia, X.; Hu, S.; Yang, M.; Wang, J., Silver Nanoclusters-Based Fluorescence Assay of Protein Kinase Activity and Inhibition. *Anal. Chem.* **2015,** *87* (1), 693-698.

29.  Wang, Y.; Dai, C.; Yan, X.-P., Fabrication of folate bioconjugated near-infrared fluorescent silver nanoclusters for targeted in vitro and in vivo bioimaging. *Chem. Commun.* **2014,** *50* (92), 14341-14344.

30.  Li, J.; You, J.; Dai, Y.; Shi, M.; Han, C.; Xu, K., Gadolinium Oxide Nanoparticles and Aptamer-Functionalized Silver Nanoclusters-Based Multimodal Molecular Imaging

Nanoprobe for Optical/Magnetic Resonance Cancer Cell Imaging. *Anal. Chem.* **2014,** *86* (22), 11306-11311.

31. Supran, G. J.; Song, K. W.; Hwang, G. W.; Correa, R. E.; Scherer, J.; Dauler, E. A.; Shirasaki, Y.; Bawendi, M. G.; Bulović, V., High-Performance Shortwave-Infrared Light-Emitting Devices Using Core-Shell (PbS-CdS) Colloidal Quantum Dots. *Adv. Mater.* **2015,** *27* (8), 1437-1442.

32. Su, Y.-T.; Lan, G.-Y.; Chen, W.-Y.; Chang, H.-T., Detection of Copper Ions Through Recovery of the Fluorescence of DNA-Templated Copper/Silver Nanoclusters in the Presence of Mercaptopropionic Acid. *Anal. Chem.* **2010,** *82* (20), 8566-8572.

33. Chen, W.-Y.; Lan, G.-Y.; Chang, H.-T., Use of Fluorescent DNA-Templated Gold/Silver Nanoclusters for the Detection of Sulfide Ions. *Anal. Chem.* **2011,** *83* (24), 9450-9455.

34. Chen, Y.-A.; Obliosca, J. M.; Liu, Y.-L.; Liu, C.; Gwozdz, M. L.; Yeh, T., Nanocluster Beacons for Detection of a Single N6-Methyladenine Epigenetic Modification. *Biophys. J.* **2016,** *110* (3, Supplement 1), 519a.

35. Jain, P. K.; Huang, X.; El-Sayed, I. H.; El-Sayed, M. A., Noble Metals on the Nanoscale: Optical and Photothermal Properties and Some Applications in Imaging, Sensing, Biology, and Medicine. *Acc. Chem. Res.* **2008,** *41* (12), 1578-1586.

36. Lohse, S. E.; Murphy, C. J., Applications of Colloidal Inorganic Nanoparticles: From Medicine to Energy. *J. Am. Chem. Soc.* **2012,** *134* (38), 15607-15620.

37. Richards, C. I.; Hsiang, J.-C.; Senapati, D.; Patel, S.; Yu, J.; Vosch, T.; Dickson, R. M., Optically Modulated Fluorophores for Selective Fluorescence Signal Recovery. *J. Am. Chem. Soc.* **2009,** *131* (13), 4619-4621.

38. Cerretani, C.; Carro-Temboury, M. R.; Krause, S.; Bogh, S. A.; Vosch, T., Temperature dependent excited state relaxation of a red emitting DNA-templated silver nanocluster. *Chem Commun (Camb)* **2017,** *53* (93), 12556-12559.

39. Doose, S.; Tsay, J. M.; Pinaud, F.; Weiss, S., Comparison of photophysical and colloidal properties of biocompatible semiconductor nanocrystals using fluorescence correlation spectroscopy. *Anal. Chem.* **2005,** *77* (7), 2235-42.

40. Shrestha, A.; Batmunkh, M.; Tricoli, A.; Qiao, S. Z.; Dai, S., Near-Infrared Active Lead Chalcogenide Quantum Dots: Preparation, Post-Synthesis Ligand Exchange, and Applications in Solar Cells. *Angew. Chem. Int. Ed. Engl.* **2019,** *58* (16), 5202-5224.

41. Wise, F. W., Lead Salt Quantum Dots: the Limit of Strong Quantum Confinement. *Acc. Chem. Res.* **2000,** *33* (11), 773-780.

42. Moreels, I.; Lambert, K.; Smeets, D.; De Muynck, D.; Nollet, T.; Martins, J. C.; Vanhaecke, F.; Vantomme, A.; Delerue, C.; Allan, G.; Hens, Z., Size-dependent optical properties of colloidal PbS quantum dots. *ACS Nano* **2009,** *3* (10), 3023-30.

43. Moreels, I.; Lambert, K.; De Muynck, D.; Vanhaecke, F.; Poelman, D.; Martins, J. C.; Allan, G.; Hens, Z., Composition and Size-Dependent Extinction Coefficient of Colloidal PbSe Quantum Dots. *Chem. Mater.* **2007,** *19* (25), 6101-6106.

44. Padilha, L. A.; Stewart, J. T.; Sandberg, R. L.; Bae, W. K.; Koh, W.-K.; Pietryga, J. M.; Klimov, V. I., Aspect Ratio Dependence of Auger Recombination and Carrier Multiplication in PbSe Nanorods. *Nano Lett.* **2013,** *13* (3), 1092-1099.

45. Cirloganu, C. M.; Padilha, L. A.; Lin, Q.; Makarov, N. S.; Velizhanin, K. A.; Luo, H.; Robel, I.; Pietryga, J. M.; Klimov, V. I., Enhanced carrier multiplication in engineered quasi-type-II quantum dots. *Nat. Commun.* **2014,** *5* (1).

46. Aerts, M.; Suchand Sandeep, C. S.; Gao, Y.; Savenije, T. J.; Schins, J. M.; Houtepen, A. J.; Kinge, S.; Siebbeles, L. D., Free charges produced by carrier multiplication in strongly coupled PbSe quantum dot films. *Nano Lett.* **2011,** *11* (10), 4485-9.

47. Knight, W. D.; Clemenger, K.; de Heer, W. A.; Saunders, W. A.; Chou, M. Y.; Cohen, M. L., Electronic Shell Structure and Abundances of Sodium Clusters. *Phys. Rev. Lett.* **1984,** *52* (24), 2141-2143.

48. Cao, Y.; Guo, J.; Shi, R.; Waterhouse, G. I. N.; Pan, J.; Du, Z.; Yao, Q.; Wu, L.-Z.; Tung, C.-H.; Xie, J.; Zhang, T., Evolution of thiolate-stabilized Ag nanoclusters from Ag-thiolate cluster intermediates. *Nat. Commun.* **2018,** *9* (1), 2379.

49. Shen, Z.; Duan, H.; Frey, H., Water-Soluble Fluorescent Ag Nanoclusters Obtained from Multiarm Star Poly(acrylic acid) as "Molecular Hydrogel" Templates. *Adv. Mater.* **2007,** *19* (3), 349-352.

50. Xu, H.; Suslick, K. S., Sonochemical Synthesis of Highly Fluorescent Ag Nanoclusters. *ACS Nano* **2010,** *4* (6), 3209-3214.

51. Yeh, H.-C.; Sharma, J.; Han, J. J.; Martinez, J. S.; Werner, J. H., A DNA−Silver Nanocluster Probe That Fluoresces upon Hybridization. *Nano Lett.* **2010,** *10* (8), 3106-3110.

52. Narayanan, S. S.; Pal, S. K., Structural and Functional Characterization of Luminescent Silver−Protein Nanobioconjugates. *J. Phys. Chem. C* **2008,** *112* (13), 4874-4879.

53. Guo, C.; Irudayaraj, J., Fluorescent Ag Clusters via a Protein-Directed Approach as a Hg(II) Ion Sensor. *Anal. Chem.* **2011,** *83* (8), 2883-2889.

54. Pal, C.; Sosa-Vargas, L.; Ojeda, J. J.; Sharma, A. K.; Cammidge, A. N.; Cook, M. J.; Ray, A. K., Charge transport in lead sulfide quantum dots/phthalocyanines hybrid nanocomposites. *Org. Electron.* **2017,** *44*, 132-143.

55. Al, E.; Efros, A., Interband absorption of light in a semiconductor sphere. *Soviet Physics Semiconductors* **1982,** *16*, 772-775.

56. Tong, H.; Wu, M. W., Theory of excitons in cubic III-V semiconductor GaAs, InAs and GaN quantum dots: Fine structure and spin relaxation. *Phys. Rev. B.* **2011,** *83* (23), 235323.

57. Mao, H.; Chen, J.; Wang, J.; Li, Z.; Dai, N.; Zhu, Z., Photoluminescence investigation of CdSe quantum dots and the surface state effect. *Physica E: Low-dimensional Systems and Nanostructures* **2005,** *27* (1), 124-128.

58. Tang, J.; Kemp, K. W.; Hoogland, S.; Jeong, K. S.; Liu, H.; Levina, L.; Furukawa, M.; Wang, X.; Debnath, R.; Cha, D.; Chou, K. W.; Fischer, A.; Amassian, A.; Asbury, J. B.; Sargent, E. H., Colloidal-quantum-dot photovoltaics using atomic-ligand passivation. *Nat Mater* **2011,** *10* (10), 765-71.

59. McDonald, S. A.; Konstantatos, G.; Zhang, S.; Cyr, P. W.; Klem, E. J.; Levina, L.; Sargent, E. H., Solution-processed PbS quantum dot infrared photodetectors and photovoltaics. *Nat Mater* **2005,** *4* (2), 138-42.

60. Anikeeva, P. O.; Halpert, J. E.; Bawendi, M. G.; Bulović, V., Electroluminescence from a Mixed Red−Green−Blue Colloidal Quantum Dot Monolayer. *Nano Lett.* **2007,** *7* (8), 2196-2200.

61. Klimov, V. I.; Mikhailovsky, A. A.; Xu, S.; Malko, A.; Hollingsworth, J. A.; Leatherdale, C. A.; Eisler, H.-J.; Bawendi, M. G., Optical Gain and Stimulated Emission in Nanocrystal Quantum Dots. *Science* **2000,** *290* (5490), 314-317.

62. Konstantatos, G.; Howard, I.; Fischer, A.; Hoogland, S.; Clifford, J.; Klem, E.; Levina, L.; Sargent, E. H., Ultrasensitive solution-cast quantum dot photodetectors. *Nature* **2006,** *442* (7099), 180-183.

63. Klimov, V. I., Mechanisms for Photogeneration and Recombination of Multiexcitons in Semiconductor Nanocrystals:  Implications for Lasing and Solar Energy Conversion. *J. Phys. Chem. B* **2006,** *110* (34), 16827-16845.

64. Hetsch, F.; Zhao, N.; Kershaw, S. V.; Rogach, A. L., Quantum dot field effect transistors. *Mater. Today* **2013,** *16* (9), 312-325.

65. Kilina, S.; Ivanov, S.; Tretiak, S., Effect of Surface Ligands on Optical and Electronic Spectra of Semiconductor Nanoclusters. *J. Am. Chem. Soc.* **2009,** *131* (22), 7717-7726.

66. Jeong, S.; Achermann, M.; Nanda, J.; Ivanov, S.; Klimov, V. I.; Hollingsworth, J. A., Effect of the Thiol−Thiolate Equilibrium on the Photophysical Properties of Aqueous CdSe/ZnS Nanocrystal Quantum Dots. *J. Am. Chem. Soc.* **2005,** *127* (29), 10126-10127.

67. Thomas, D.; Lee, H. O.; Santiago, K. C.; Pelzer, M.; Kuti, A.; Jenrette, E.; Bahoura, M., Rapid Microwave Synthesis of Tunable Cadmium Selenide (CdSe) Quantum Dots for Optoelectronic Applications. *Journal of Nanomaterials* **2020,** *2020*, 5056875.

68. Puzder, A.; Williamson, A. J.; Gygi, F.; Galli, G., Self-Healing of CdSe Nanocrystals: First-Principles Calculations. *Phys. Rev. Lett.* **2004,** *92* (21), 217401.

69. Kilina, S. V.; Tamukong, P. K.; Kilin, D. S., Surface Chemistry of Semiconducting Quantum Dots: Theoretical Perspectives. *Acc. Chem. Res.* **2016,** *49* (10), 2127-2135.

70. Kroupa, D. M.; Vörös, M.; Brawand, N. P.; McNichols, B. W.; Miller, E. M.; Gu, J.; Nozik, A. J.; Sellinger, A.; Galli, G.; Beard, M. C., Tuning colloidal quantum dot band edge positions through solution-phase surface chemistry modification. *Nat. Commun.* **2017,** *8* (1), 15257.

71. Yang, S.; Prendergast, D.; Neaton, J. B., Tuning Semiconductor Band Edge Energies for Solar Photocatalysis via Surface Ligand Passivation. *Nano Lett.* **2012,** *12* (1), 383-388.

72. Munro, A. M.; Chandler, C.; Garling, M.; Chai, D.; Popovich, V.; Lystrom, L.; Kilina, S., Phenyldithiocarbamate Ligands Decompose During Nanocrystal Ligand Exchange. *J. Phys. Chem. C* **2016,** *120* (51), 29455-29462.

73. Pan, Y.; Sohel, M. A.; Pan, L.; Wei, Z.; Bai, H.; Tamargo, M. C.; John, R., Synthesis of Air-stable PbSe Quantum Dots Using PbCl2-oleylamine System. *Materials Today: Proceedings* **2015,** *2* (1), 281-286.

74. Bae, W. K.; Joo, J.; Padilha, L. A.; Won, J.; Lee, D. C.; Lin, Q.; Koh, W.-k.; Luo, H.; Klimov, V. I.; Pietryga, J. M., Highly Effective Surface Passivation of PbSe Quantum Dots through Reaction with Molecular Chlorine. *J. Am. Chem. Soc.* **2012,** *134* (49), 20160-20168.

75. Kim, H.; Achermann, M.; Balet, L. P.; Hollingsworth, J. A.; Klimov, V. I., Synthesis and Characterization of Co/CdSe Core/Shell Nanocomposites:  Bifunctional Magnetic-Optical Nanocrystals. *J. Am. Chem. Soc.* **2005,** *127* (2), 544-546.

76. Hanson, C. J.; Hartmann, N. F.; Singh, A.; Ma, X.; DeBenedetti, W. J. I.; Casson, J. L.; Grey, J. K.; Chabal, Y. J.; Malko, A. V.; Sykora, M.; Piryatinski, A.; Htoon, H.; Hollingsworth, J. A., Giant PbSe/CdSe/CdSe Quantum Dots: Crystal-Structure-Defined Ultrastable Near-Infrared Photoluminescence from Single Nanocrystals. *J. Am. Chem. Soc.* **2017,** *139* (32), 11081-11088.

77. Htoon, H.; Malko, A. V.; Bussian, D.; Vela, J.; Chen, Y.; Hollingsworth, J. A.; Klimov, V. I., Highly Emissive Multiexcitons in Steady-State Photoluminescence of Individual "Giant" CdSe/CdS Core/Shell Nanocrystals. *Nano Lett.* **2010,** *10* (7), 2401-2407.

78. Park, Y. S.; Malko, A. V.; Vela, J.; Chen, Y.; Ghosh, Y.; García-Santamaría, F.; Hollingsworth, J. A.; Klimov, V. I.; Htoon, H., Near-Unity Quantum Yields of Biexciton Emission from CdSe/CdS Nanocrystals Measured Using Single-Particle Spectroscopy. *Phys. Rev. Lett.* **2011,** *106* (18), 187401.

79. Lin, Q.; Makarov, N. S.; Koh, W.-k.; Velizhanin, K. A.; Cirloganu, C. M.; Luo, H.; Klimov, V. I.; Pietryga, J. M., Design and Synthesis of Heterostructured Quantum Dots with Dual Emission in the Visible and Infrared. *ACS Nano* **2015,** *9* (1), 539-547.

80. García-Santamaría, F.; Brovelli, S.; Viswanatha, R.; Hollingsworth, J. A.; Htoon, H.; Crooker, S. A.; Klimov, V. I., Breakdown of Volume Scaling in Auger Recombination in CdSe/CdS Heteronanocrystals: The Role of the Core−Shell Interface. *Nano Lett.* **2011,** *11* (2), 687-693.

81. Jones, M.; Lo, S. S.; Scholes, G. D., Quantitative modeling of the role of surface traps in CdSe/CdS/ZnS nanocrystal photoluminescence decay dynamics. *Proceedings of the National Academy of Sciences* **2009,** *106* (9), 3011-3016.

82. Chen, O.; Zhao, J.; Chauhan, V. P.; Cui, J.; Wong, C.; Harris, D. K.; Wei, H.; Han, H.-S.; Fukumura, D.; Jain, R. K.; Bawendi, M. G., Compact high-quality CdSe–CdS core–shell nanocrystals with narrow emission linewidths and suppressed blinking. *Nat. Mater.* **2013,** *12* (5), 445-451.

83. Bae, W. K.; Padilha, L. A.; Park, Y.-S.; McDaniel, H.; Robel, I.; Pietryga, J. M.; Klimov, V. I., Controlled Alloying of the Core–Shell Interface in CdSe/CdS Quantum Dots for Suppression of Auger Recombination. *ACS Nano* **2013,** *7* (4), 3411-3419.

84. Park, Y.-S.; Bae, W. K.; Padilha, L. A.; Pietryga, J. M.; Klimov, V. I., Effect of the Core/Shell Interface on Auger Recombination Evaluated by Single-Quantum-Dot Spectroscopy. *Nano Lett.* **2014,** *14* (2), 396-402.

85. Kroupa, D. M.; Pach, G. F.; Vörös, M.; Giberti, F.; Chernomordik, B. D.; Crisp, R. W.; Nozik, A. J.; Johnson, J. C.; Singh, R.; Klimov, V. I.; Galli, G.; Beard, M. C., Enhanced Multiple Exciton Generation in PbS|CdS Janus-like Heterostructured Nanocrystals. *ACS Nano* **2018**.

86. Zhang, J.; Chernomordik, B. D.; Crisp, R. W.; Kroupa, D. M.; Luther, J. M.; Miller, E. M.; Gao, J.; Beard, M. C., Preparation of Cd/Pb Chalcogenide Heterostructured Janus Particles via Controllable Cation Exchange. *ACS Nano* **2015,** *9* (7), 7151-7163.

87. Gwinn, E. G.; O'Neill, P.; Guerrero, A. J.; Bouwmeester, D.; Fygenson, D. K., Sequence-Dependent Fluorescence of DNA-Hosted Silver Nanoclusters. *Adv. Mater.* **2008,** *20* (2), 279-283.

88. Li, Y.; Wang, X.; Xu, S.; Xu, W., The solvent effect on the luminescence of silver nanoclusters. *Phys. Chem. Chem. Phys.* **2013,** *15* (8), 2665-2668.

89. Copp, S. M.; Schultz, D.; Swasey, S. M.; Faris, A.; Gwinn, E. G., Cluster Plasmonics: Dielectric and Shape Effects on DNA-Stabilized Silver Clusters. *Nano Lett.* **2016,** *16* (6), 3594-3599.

90. Schultz, D.; Gwinn, E. G., Silver atom and strand numbers in fluorescent and dark Ag:DNAs. *Chem. Commun.* **2012,** *48* (46), 5748-5750.

91.     Copp, S. M.; Schultz, D.; Swasey, S.; Pavlovich, J.; Debord, M.; Chiu, A.; Olsson, K.; Gwinn, E., Magic Numbers in DNA-Stabilized Fluorescent Silver Clusters Lead to Magic Colors. *J. Phys. Chem. Lett.* **2014,** *5* (6), 959-963.

92.     Zheng, J.; Nicovich, P. R.; Dickson, R. M., Highly fluorescent noble-metal quantum dots. *Annu. Rev. Phys. Chem.* **2007,** *58*, 409-431.

93.     Schmid, G., Large clusters and colloids. Metals in the embryonic state. *Chem. Rev.* **1992,** *92* (8), 1709-1727.

94.     Aikens, C. M., Electronic Structure of Ligand-Passivated Gold and Silver Nanoclusters. *J. Phys. Chem. Lett.* **2011,** *2* (2), 99-104.

95.     Bogh, S. A.; Cerretani, C.; Kacenauskaite, L.; Carro-Temboury, M. R.; Vosch, T., Excited-State Relaxation and Förster Resonance Energy Transfer in an Organic Fluorophore/Silver Nanocluster Dyad. *ACS Omega* **2017,** *2* (8), 4657-4664.

96.     Wang, K.-H.; Chang, C.-W., The spectral relaxation dynamics and the molecular crowding effect of silver nanoclusters synthesized in the polymer scaffold. *Phys. Chem. Chem. Phys.* **2015,** *17* (35), 23140-23146.

97.     Hooley, E. N.; Carro-Temboury, M. R.; Vosch, T., Probing the Absorption and Emission Transition Dipole Moment of DNA Stabilized Silver Nanoclusters. *J. Phys. Chem. A* **2017,** *121* (5), 963-968.

98.     Ganguly, M.; Bradsher, C.; Goodwin, P.; Petty, J. T., DNA-Directed Fluorescence Switching of Silver Clusters. *J. Phys. Chem. C* **2015,** *119* (49), 27829-27837.

99.     Driehorst, T.; O'Neill, P.; Goodwin, P. M.; Pennathur, S.; Fygenson, D. K., Distinct Conformations of DNA-Stabilized Fluorescent Silver Nanoclusters Revealed by Electrophoretic Mobility and Diffusivity Measurements. *Langmuir* **2011,** *27* (14), 8923-8933.

100.    Link, S.; Wang, Z. L.; El-Sayed, M. A., Alloy Formation of Gold−Silver Nanoparticles and the Dependence of the Plasmon Absorption on Their Composition. *J. Phys. Chem. B* **1999,** *103* (18), 3529-3533.

101.    Petty, J. T.; Nicholson, D. A.; Sergev, O. O.; Graham, S. K., Near-Infrared Silver Cluster Optically Signaling Oligonucleotide Hybridization and Assembling Two DNA Hosts. *Anal. Chem.* **2014,** *86* (18), 9220-9228.

102.    Choi, S.; Yu, J.; A. Patel, S.; Tzeng, Y.-L.; M. Dickson, R., Tailoring silver nanodots for intracellular staining. *Photochem. Photobiol. Sci.* **2011,** *10* (1), 109-115.

103.    Morishita, K.; L. MacLean, J.; Liu, B.; Jiang, H.; Liu, J., Correlation of photobleaching, oxidation and metal induced fluorescence quenching of DNA-templated silver nanoclusters. *Nanoscale* **2013,** *5* (7), 2840-2849.

104. Sengupta, B.; Springer, K.; Buckman, J. G.; Story, S. P.; Abe, O. H.; Hasan, Z. W.; Prudowsky, Z. D.; Rudisill, S. E.; Degtyareva, N. N.; Petty, J. T., DNA templates for fluorescent silver clusters and i-motif folding. *J. Phys. Chem. C* **2009,** *113* (45), 19518-19524.

105. Bockelmann, U.; Bastard, G., Phonon scattering and energy relaxation in two-, one-, and zero-dimensional electron gases. *Phys Rev B Condens Matter* **1990,** *42* (14), 8947-8951.

106. Schaller, R. D.; Petruska, M. A.; Klimov, V. I., Effect of electronic structure on carrier multiplication efficiency: Comparative study of PbSe and CdSe nanocrystals. *Appl. Phys. Lett.* **2005,** *87* (25), 253102.

107. Inoshita, T.; Sakaki, H., Electron relaxation in a quantum dot: Significance of multiphonon processes. *Phys Rev B Condens Matter* **1992,** *46* (11), 7260-7263.

108. Efros, A. L.; Kharchenko, V. A.; Rosen, M., Breaking the phonon bottleneck in nanometer quantum dots: Role of Auger-like processes. *Solid State Commun.* **1995,** *93* (4), 281-284.

109. Benisty, H.; Sotomayor-Torres, C. M.; Weisbuch, C., Intrinsic mechanism for the poor luminescence properties of quantum-box systems. *Phys Rev B Condens Matter* **1991,** *44* (19), 10945-10948.

110. Klimov, V. I.; McBranch, D. W.; Leatherdale, C. A.; Bawendi, M. G., Electron and hole relaxation pathways in semiconductor quantum dots. *Phys. Rev. B.* **1999,** *60* (19), 13740-13749.

111. El-Ballouli, A. a. O.; Alarousu, E.; Usman, A.; Pan, J.; Bakr, O. M.; Mohammed, O. F., Real-Time Observation of Ultrafast Intraband Relaxation and Exciton Multiplication in PbS Quantum Dots. *ACS Photonics* **2014,** *1* (3), 285-292.

112. An, J. M.; Califano, M.; Franceschetti, A.; Zunger, A., Excited-state relaxation in PbSe quantum dots. *J. Chem. Phys.* **2008,** *128* (16), 164720.

113. Cooney, R. R.; Sewall, S. L.; Anderson, K. E. H.; Dias, E. A.; Kambhampati, P., Breaking the Phonon Bottleneck for Holes in Semiconductor Quantum Dots. *Phys. Rev. Lett.* **2007,** *98* (17).

114. Schaller, R. D.; Pietryga, J. M.; Goupalov, S. V.; Petruska, M. A.; Ivanov, S. A.; Klimov, V. I., Breaking the phonon bottleneck in semiconductor nanocrystals via multiphonon emission induced by intrinsic nonadiabatic interactions. *Phys. Rev. Lett.* **2005,** *95* (19), 196401.

115. Richter, A. F.; Binder, M.; Bohn, B. J.; Grumbach, N.; Neyshtadt, S.; Urban, A. S.; Feldmann, J., Fast Electron and Slow Hole Relaxation in InP-Based Colloidal Quantum Dots. *ACS Nano* **2019,** *13* (12), 14408-14415.

116.    Guyot-Sionnest, P.; Wehrenberg, B.; Yu, D., Intraband relaxation in CdSe nanocrystals and the strong influence of the surface ligands. *J. Chem. Phys.* **2005,** *123* (7), 074709.

117.    Klimov, V. I.; Mikhailovsky, A. A.; McBranch, D. W.; Leatherdale, C. A.; Bawendi, M. G., Mechanisms for intraband energy relaxation in semiconductor quantum dots: The role of electron-hole interactions. *Phys. Rev. B.* **2000,** *61* (20), R13349-R13352.

118.    Kim, D.; Kim, D.-H.; Lee, J.-H.; Grossman, J. C., Impact of stoichiometry on the electronic structure of PbS quantum dots. *Phys. Rev. Lett.* **2013,** *110* (19), 196802.

119.    Peterson, M. D.; Cass, L. C.; Harris, R. D.; Edme, K.; Sung, K.; Weiss, E. A., The Role of Ligands in Determining the Exciton Relaxation Dynamics in Semiconductor Quantum Dots. *Annu. Rev. Phys. Chem.* **2014,** *65* (1), 317-339.

120.    Kilina, S.; Velizhanin, K. A.; Ivanov, S.; Prezhdo, O. V.; Tretiak, S., Surface Ligands Increase Photoexcitation Relaxation Rates in CdSe Quantum Dots. *ACS Nano* **2012,** *6* (7), 6515-6524.

121.    Kilina, S.; Kilin, D.; Prezhdo, O., Breaking the Phonon Bottleneck in PbSe and CdSe Quantum Dots: Time-Domain Density Functional Theory of Charge Carrier Relaxation. *ACS Nano* **2009,** *3* (1), 93-99.

122.    Chen, Y.; Vela, J.; Htoon, H.; Casson, J. L.; Werder, D. J.; Bussian, D. A.; Klimov, V. I.; Hollingsworth, J. A., "Giant" Multishell CdSe Nanocrystal Quantum Dots with Suppressed Blinking. *J. Am. Chem. Soc.* **2008,** *130* (15), 5026-5027.

123.    Fernée, M. J.; Tamarat, P.; Lounis, B., Spectroscopy of single nanocrystals. *Chem. Soc. Rev.* **2014,** *43* (4), 1311-1337.

124.    Orfield, N. J.; Majumder, S.; McBride, J. R.; Yik-Ching Koh, F.; Singh, A.; Bouquin, S. J.; Casson, J. L.; Johnson, A. D.; Sun, L.; Li, X.; Shih, C.-K.; Rosenthal, S. J.; Hollingsworth, J. A.; Htoon, H., Photophysics of Thermally-Assisted Photobleaching in "Giant" Quantum Dots Revealed in Single Nanocrystals. *ACS Nano* **2018,** *12* (5), 4206-4217.

125.    Lystrom, L.; Tamukong, P.; Mihaylov, D.; Kilina, S., Phonon-Driven Energy Relaxation in PbS/CdS and PbSe/CdSe Core/Shell Quantum Dots. *J. Phys. Chem. Lett.* **2020,** *11* (11), 4269-4278.

126.    Klimov, V. I., Multicarrier Interactions in Semiconductor Nanocrystals in Relation to the Phenomena of Auger Recombination and Carrier Multiplication. *Annu. Rev. Condens. Matter Phys.* **2014,** *5* (1), 285-316.

127.    Padilha, L. A.; Bae, W. K.; Klimov, V. I.; Pietryga, J. M.; Schaller, R. D., Response of Semiconductor Nanocrystals to Extremely Energetic Excitation. *Nano Lett.* **2013,** *13* (3), 925-932.

128. Kilina, S. V.; Craig, C. F.; Kilin, D. S.; Prezhdo, O. V., Ab Initio Time-Domain Study of Phonon-Assisted Relaxation of Charge Carriers in a PbSe Quantum Dot. *J. Phys. Chem. C* **2007,** *111* (12), 4871-4878.

129. Klimov, V. I.; Schwarz, C. J.; McBranch, D. W.; Leatherdale, C. A.; Bawendi, M. G., Ultrafast dynamics of inter- and intraband transitions in semiconductor nanocrystals: Implications for quantum-dot lasers. *Phys. Rev. B.* **1999,** *60* (4), R2177-R2180.

130. Achtstein, A. W.; Schliwa, A.; Prudnikau, A.; Hardzei, M.; Artemyev, M. V.; Thomsen, C.; Woggon, U., Electronic Structure and Exciton–Phonon Interaction in Two-Dimensional Colloidal CdSe Nanosheets. *Nano Lett.* **2012,** *12* (6), 3151-3157.

131. Klimov, V. I.; Mikhailovsky, A. A.; McBranch, D. W.; Leatherdale, C. A.; Bawendi, M. G., Quantization of Multiparticle Auger Rates in Semiconductor Quantum Dots. *Science* **2000,** *287* (5455), 1011-1013.

132. Landsberg, P. T., *Recombination in Semiconductors*. Cambridge University Press: Cambridge, 1992.

133. Padilha, L. A.; Stewart, J. T.; Sandberg, R. L.; Bae, W. K.; Koh, W. K.; Pietryga, J. M.; Klimov, V. I., Carrier multiplication in semiconductor nanocrystals: influence of size, shape, and composition. *Acc. Chem. Res.* **2013,** *46* (6), 1261-9.

134. Beard, M. C.; Midgett, A. G.; Hanna, M. C.; Luther, J. M.; Hughes, B. K.; Nozik, A. J., Comparing Multiple Exciton Generation in Quantum Dots To Impact Ionization in Bulk Semiconductors: Implications for Enhancement of Solar Energy Conversion. *Nano Lett.* **2010,** *10* (8), 3019-3027.

135. Klimov, V. I.; Ivanov, S. A.; Nanda, J.; Achermann, M.; Bezel, I.; McGuire, J. A.; Piryatinski, A., Single-exciton optical gain in semiconductor nanocrystals. *Nature* **2007,** *447* (7143), 441-446.

136. Richter, A.; Hermle, M.; Glunz, S. W., Reassessment of the Limiting Efficiency for Crystalline Silicon Solar Cells. *IEEE Journal of Photovoltaics* **2013,** *3* (4), 1184-1191.

137. Richter, A.; Glunz, S. W.; Werner, F.; Schmidt, J.; Cuevas, A., Improved quantitative description of Auger recombination in crystalline silicon. *Phys. Rev. B.* **2012,** *86* (16), 165202.

138. ten Cate, S.; Sandeep, C. S. S.; Liu, Y.; Law, M.; Kinge, S.; Houtepen, A. J.; Schins, J. M.; Siebbeles, L. D. A., Generating Free Charges by Carrier Multiplication in Quantum Dots for Highly Efficient Photovoltaics. *Acc. Chem. Res.* **2015,** *48* (2), 174-181.

139. Califano, M.; Zunger, A.; Franceschetti, A., Efficient Inverse Auger Recombination at Threshold in CdSe Nanocrystals. *Nano Lett.* **2004,** *4* (3), 525-531.

140. Murphy, J. E.; Beard, M. C.; Norman, A. G.; Ahrenkiel, S. P.; Johnson, J. C.; Yu, P.; Mićić, O. I.; Ellingson, R. J.; Nozik, A. J., PbTe Colloidal Nanocrystals:  Synthesis,

Characterization, and Multiple Exciton Generation. *J. Am. Chem. Soc.* **2006,** *128* (10), 3241-3247.

141. Nozik, A. J., Quantum dot solar cells. *Physica E: Low-dimensional Systems and Nanostructures* **2002,** *14* (1), 115-120.

142. Nozik, A. J., Spectroscopy and Hot Electron Relaxation Dynamics in Semiconductor Quantum Wells and Quantum Dots. *Annu. Rev. Phys. Chem.* **2001,** *52* (1), 193-231.

143. Stewart, J. T.; Padilha, L. A.; Bae, W. K.; Koh, W.-K.; Pietryga, J. M.; Klimov, V. I., Carrier Multiplication in Quantum Dots within the Framework of Two Competing Energy Relaxation Mechanisms. *J. Phys. Chem. Lett.* **2013,** *4* (12), 2061-2068.

144. Midgett, A. G.; Luther, J. M.; Stewart, J. T.; Smith, D. K.; Padilha, L. A.; Klimov, V. I.; Nozik, A. J.; Beard, M. C., Size and Composition Dependent Multiple Exciton Generation Efficiency in PbS, PbSe, and PbSxSe1–x Alloyed Quantum Dots. *Nano Lett.* **2013,** *13* (7), 3078-3085.

145. Klimov, V. I.; McBranch, D. W., Femtosecond *1P*-to-*1S* Electron Relaxation in Strongly Confined Semiconductor Nanocrystals. *Phys. Rev. Lett.* **1998,** *80* (18), 4028-4031.

146. Neukirch, A. J.; Prezhdo, O. V., Charge and Exciton Dynamics in Semiconductor Quantum Dots: A Time Domain, ab Initio View. In *Solar Energy Conversion*, 2013; pp 37-76.

147. Kilina, S. V.; Kilin, D. S.; Prezhdo, V. V.; Prezhdo, O. V., Theoretical Study of Electron–Phonon Relaxation in PbSe and CdSe Quantum Dots: Evidence for Phonon Memory. *J. Phys. Chem. C* **2011,** *115* (44), 21641-21651.

148. Wise, F. W., Lead Salt Quantum Dots: the Limit of Strong Quantum Confinement. *Acc. Chem. Res.* **2000,** *33* (11), 773-780.

149. Shabaev, A.; Efros, A. L.; Nozik, A. J., Multiexciton Generation by a Single Photon in Nanocrystals. *Nano Lett.* **2006,** *6* (12), 2856-2863.

150. Sills, A.; Califano, M., Origins of improved carrier multiplication efficiency in elongated semiconductor nanostructures. *Phys. Chem. Chem. Phys.* **2015,** *17* (4), 2573-2581.

151. Kershaw, S. V.; Rogach, A. L., Carrier Multiplication Mechanisms and Competing Processes in Colloidal Semiconductor Nanostructures. *Materials (Basel)* **2017,** *10* (9), 1095.

152. Koh, W.-k.; Dandu, N. K.; Fidler, A. F.; Klimov, V. I.; Pietryga, J. M.; Kilina, S. V., Thickness-Controlled Quasi-Two-Dimensional Colloidal PbSe Nanoplatelets. *J. Am. Chem. Soc.* **2017,** *139* (6), 2152-2155.

153. Aerts, M.; Bielewicz, T.; Klinke, C.; Grozema, F. C.; Houtepen, A. J.; Schins, J. M.; Siebbeles, L. D. A., Highly efficient carrier multiplication in PbS nanosheets. *Nat. Commun.* **2014,** *5*, 3789.

154. Ma, K.; Shao, Y.; Cui, Q.; Wu, F.; Xu, S.; Liu, G., Base-Stacking-Determined Fluorescence Emission of DNA Abasic Site-Templated Silver Nanoclusters. *Langmuir* **2012,** *28* (43), 15313-15322.

155. Ramazanov, R. R.; Sych, T. S.; Reveguk, Z. V.; Maksimov, D. A.; Vdovichev, A. A.; Kononov, A. I., Ag–DNA Emitter: Metal Nanorod or Supramolecular Complex? *J. Phys. Chem. Lett.* **2016,** *7* (18), 3560-3566.

156. Petty, J. T.; Sergev, O. O.; Ganguly, M.; Rankine, I. J.; Chevrier, D. M.; Zhang, P., A Segregated, Partially Oxidized, and Compact Ag10 Cluster within an Encapsulating DNA Host. *J. Am. Chem. Soc.* **2016,** *138* (10), 3469-3477.

157. Petty, J. T.; Ganguly, M.; Rankine, I. J.; Baucum, E. J.; Gillan, M. J.; Eddy, L. E.; Léon, J. C.; Müller, J., Repeated and Folded DNA Sequences and Their Modular Ag106+ Cluster. *J. Phys. Chem. C* **2018,** *122* (8), 4670-4680.

158. Schultz, D.; Gwinn, E., Stabilization of fluorescent silver clusters by RNA homopolymers and their DNA analogs: C, G versus A, T (U) dichotomy. *Chem. Commun.* **2011,** *47* (16), 4715-4717.

159. Soto-Verdugo, V.; Metiu, H.; Gwinn, E., The properties of small Ag clusters bound to DNA bases. *J. Chem. Phys.* **2010,** *132* (19), 195102.

160. Swasey, S. M.; Leal, L. E.; Lopez-Acevedo, O.; Pavlovich, J.; Gwinn, E. G., Silver (I) as DNA glue: Ag+mediated guanine pairing revealed by removing Watson-Crick constraints. *Sci. Rep.* **2015,** *5*, 10163.

161. Dale, B. B.; Senanayake, R. D.; Aikens, C. M., Research Update: Density functional theory investigation of the interactions of silver nanoclusters with guanine. *APL Materials* **2017,** *5* (5), 053102.

162. Chen, T.-T.; Chen, Q.-Y.; Liu, M.-Y., GAG-containing nucleotides as mediators of DNA-silver clusters and iron-DNA interplay. *Chin. Chem. Lett.* **2016,** *27* (3), 395-398.

163. Brown, S. L.; Hobbie, E. K.; Tretiak, S.; Kilin, D. S., First-Principles Study of Fluorescence in Silver Nanoclusters. *J. Phys. Chem. C* **2017,** *121* (43), 23875-23885.

164. Fernández, E. M.; Soler, J. M.; Garzón, I. L.; Balbás, L. C., Trends in the structure and bonding of noble metal clusters. *Phys. Rev. B.* **2004,** *70* (16), 165403.

165. K. Samanta, P.; Periyasamy, G.; K. Manna, A.; K. Pati, S., Computational studies on structural and optical properties of single-stranded DNA encapsulated silver/gold clusters. *J. Mater. Chem.* **2012,** *22* (14), 6774-6781.

166. Tsuneda, T., Theoretical investigations on geometrical and electronic structures of silver clusters. *J. Comput. Chem.* **2019,** *40* (1), 206-211.

## 2. THEORY AND METHODOLOGY

Accurate electronic structure prediction is the first and most important step to predict physical and optoelectronic observable of a material. We have used different ab initio and statistical methods in this disquisition to compute the structural and photophysical observables. It is important to take these theories and approximations into consideration to analyze and correlate the predicted observable with the experimental results. As such, all the considered methodology and approximations are discussed in this chapter.

### 2.1. Ground State Optimization of a Many Electron System

### 2.1.1. Solving a Many Electrons System

The big goal of the computational chemist community is to solve the Schrodinger equation for a many-electron system –

$$\widehat{H}\mathbf{\Psi} \; = \; E\mathbf{\Psi} \tag{2.1}$$

where $\Psi$ is a total wavefunction of $n$ electrons. The wave function $\Psi$ can be written in terms of $n$ single-electron antisymmetric wavefunctions –

$$\boldsymbol{\Psi} = \psi_1.\psi_2.\psi_3 \dots \dots \psi_n \tag{2.2}$$

$\psi_n$ is the single electron wavefunction and orthogonal. H is the Hamiltonian operator which can be expressed as follow which consist of both kinetic and potential operator –

$$\widehat{H} = -\frac{\hbar^2}{2}\sum_{i=1}^{N}\frac{\nabla_k^2}{m_e} - \frac{\hbar^2}{2}\sum_{k=1}^{M}\frac{\nabla_k^2}{M_k} + \frac{1}{2}\sum_{i\neq j}^{N}\frac{e^2}{|r_i - r_j|} + \frac{1}{2}\sum_{k\neq l}^{M}\frac{Z_k Z_l e^2}{|r_i - r_j|} - \sum_{k,i}^{M,N}\frac{Z_k e^2}{|r_i - R_k|} \tag{2.3}$$

The first and second terms are the kinetic energy term for the electron and nuclei; the third and fourth terms are the Coulomb interaction of the electron-electron and nuclei-nuclei, respectively, and the firth terms are the electron-nuclei interaction. The Hamiltonian is very complex for the many-electron system that solving the eq (2.1) for the eigenvalues is numerically

impossible. Therefore, several approximations have been considered to calculate a many

electrons system.

The first approximation is electron and nuclei motion of a many-electron system that can

be treated separately due to their significant mass difference known as Born-Oppenheimer

approximation (BOA). This approximation allows us to simplify the Hamiltonian by ignoring the

nuclei kinetic energy. And simplify the wavefunction by decoupling the nuclei wavefunction

from the electron wavefunction.[1]

$$\hat{H} = -\frac{\hbar^2}{2} \sum_{i=1}^{N} \frac{\nabla_k^2}{m_e} + \frac{1}{2} \sum_{i \neq j}^{N} \frac{e^2}{|r_j - r_j|} - \sum_{k,i}^{M,N} \frac{Z_k e^2}{|r_i - R_k|}$$

$$\hat{H} = \hat{T}(r) + \hat{U}(r) + \hat{V}_{ext}(r, R_0) \tag{2.4}$$

And,

$$\Psi(r_i, R_k) = \Psi(r_i, \{R\}) \tag{2.5}$$

The next approximation is that $\Psi$ is defined as a product of single-electron orthonormal

wavefunction, which simplifies the computation and restricts the overlapping between the

wavefunction. The third approximation is the Pauli exclusion principle. Electron degenerate

wavefunction is restricted by electron spin; as such, it reduces the number of wavefunctions

required to calculate the electronic structure of a compound.

**2.1.2. Hartree-Fock Method**

One of the simplified computational methods to solve the eq-2.1 is the Hartree-Fock (HF)

method, where the Fock operator of a single determinantal wavefunction $\psi_i$ is defined by a

single electron Hamiltonian with an electron Coulomb and exchange operator.

$$F(\psi_{ij}) = H_{ij} + \sum (2J_{ij} - K_{ij}) \tag{2.6}$$

In the eq-2.6 $J_{ij}$ capture the electron-electron Coulomb interaction between the $i^{th}$ and $j^{th}$ electron, and $K_{ij}$ calculate the electron exchange interaction. However, the Fock operator does not include the full correlation interactions; as such HF cannot reproduce very accurate electronic properties.

### 2.1.3. Hohenberg-Kohn Theorem

Considering the density of a many-electron system instead of a single-electron simplify the calculation and increase the accuracy. Density Functional Theory (DFT) used ground state density to describe the electron wavefunction and hence observable. DFT is based on two main postulations. The First Hohenberg-Kohn theorem is that *the ground state density ($\rho_0$) of a many-electron system can be used to calculate the corresponding ground state wavefunction,* $\psi_0(r_1, r_2, .... r_n)$.[2] The second Hohenberg-Kohn theorem stated how one density term would produce a wavefunction of *n* variable. It stated that *a ground state density map to a wavefunction* $\psi_0$ *which should have the universal lowest energy.*[2]

Ground state density of an electron system can be represented by -

$$\rho_0(r) = \iint ... \int |\psi_0(r_1, r_2, .... r_n)|^2 dr_1 dr_2 ... dr_n \tag{2.7}$$

And the ground state energy of the system is –

$$E_{v,0} = \min_{\psi \to \rho_0} \langle \psi_0 | \hat{T}(r) + \hat{U}(r) + \hat{V}_{ext}(r, R_0) | \psi_0 \rangle \tag{2.8}$$

Where $E_{v,0}$ is the ground state energy in the potential $\hat{V}_{ext}$ which has ground state wavefunction $\psi_0$ and ground-state density is $\rho_0$. Equation 2.8 can be written for an arbitrary density $\rho$ –

$$E_v[\rho] = \min_{\psi \to \rho} \langle \psi | \hat{T}(r) + \hat{U}(r) | \psi \rangle + \int d^3 r \rho(r) v(r) \tag{2.9}$$

The density in $\rho$ in equation 2.9 is some arbitrary electron density. Equation 2.9 has variational properties. If $\psi$ is not ground state wavefunction,

$$E_{v,0}[\rho_0] \leq E_v[\rho] \qquad (2.10)$$

### 2.1.4. Density Functional Theory (DFT): The Kohn-Sham Method[3]

The Kohn-Sham method transforms a many-body electron wavefunction to a single electron wavefunction.[3] Let $\varphi_i$ is a single-particle electron wavefunction, then Schrodinger equation is –

$$\left(-\frac{\hbar^2}{2}\frac{\nabla_k^2}{m_e} + v_{KS}\right)\varphi_i(r_i;\{R_I\}) = \varepsilon_i\varphi_i(r_i;\{R_I\}) \qquad (2.11)$$

$v_{KS}$ is the effective Kohn-Sham (KS) potential –

$$v_{KS} = v_{ext}(r) + \int dr' \frac{\rho r'}{|r-r'|} + v_{xc}(r) \qquad (2.12)$$

$v_{xc}$ is the exchange-correlation potential. The exact prediction of $v_{xc}$ would produce the exact solution for the Kohn-Sham potential, hence $\rho_0$. The predictability of the DFT method depends on the accurate prediction of $v_{xc}$ and it should contain all the many-body aspect of calculations.[4] The exchange-correlation potential can be defined as –

$$v_{xc}(r) = \frac{\delta E_{xc}[\rho(r)]}{\delta\rho(r)} \qquad (2.13)$$

### 2.1.5. Local Functional: LDA

Historically, the most important approximation of the functional is the Local-Density Approximation (LDA).[5] The correlation of electron of a many-electron system approximates as a homogenous interacting electron density. The exchange-correlation energy in LDA is

$$E_{xc}[\rho] \approx E_{xc}^{LDA}[\rho] = \int d^3r e_{xc}^{hom}(\rho(r)) \qquad (2.14)$$

Where $e_{xc}^{hom} = e_x^{hom}e_c^{hom}$ and the corresponding XC potential is –

$$v_{xc}^{LDA}[\rho](r) = \left.\frac{\partial e_{xc}^{hom}(\rho)}{\partial\rho}\right|_{\rho\to\rho(r)} \qquad (2.15)$$

LDA is known for systematic error cancellation. Usually, LDA underestimate the correlation potential ($v_c$) but overestimates the exchange potential ($v_e$). Overall, it produces acceptable results in some cases.

**2.1.6. Semi-Local Functional and Beyond**

LDA functional describes the density at a point **r,** but any real system is inhomogeneous in spatial density distribution. The next approximation is gradient-expansion approximations (GEA),[6] it is based on the gradient of the electron density gradient, in the form of $|\nabla\rho(r)|$, $|\nabla\rho(r)|^2$ etc. to the LDA. Later, the potential was defined on the general gradient form known as Generalized-gradient approximation (GGA).[7]

$$E_{xc}^{GGA}[\rho] = \int d^3r \, f\big(\rho(r), \nabla\rho(r)\big) \tag{2.16}$$

Since the potential is described as a function of $f\big(\rho(r), \nabla\rho(r)\big)$, different GGA functionals can be designed by fitting the parameter to the test set molecules. The most popular GGA type functional is PBE[7-8] and BLYP[9] functionals. The next type of functional is the hybrid functional, where HF exchange is mixed with DFT exchange. The weight of the HF and DFT exchange is proposed from some type of benchmarking using empirical results. The two well-known hybrids functional is PBE0[10-11] and B3LYP[12] functional, where 25% and 20% exchange parts are HF type exchange potential, respectively. PBE and PBE0 functional are used in the ground state calculations of all semiconductor QDs and NPL of this dissertation. The exchange potential correction can be screened as a function of range **r**, and the range-correction term added functional is known as long-range corrected functional. The long-range orbital-orbitals exchange interaction is described with the HF exchange integral. We have used the long-range corrected CAM-B3LYP functional[13] in the disquisition to study the metal nucleobase passivated metal clusters.

### 2.1.7. Basis Set

Computational application of the DFT is also dependent on designing the appropriate wavefunction $\varphi_i(r_i; \{R_I\})$. A basis set is a linear combination of the atomic basis (local basis) or the plane-wave basis (non-local basis). Atomic centered basis function can be written in terms of Gaussian and Slater type orbitals.[14]

A Slater type orbital (STO) define -

$$\varphi_{n,l,m,\zeta}^{STO}(r,\theta,\phi) = NY_{lm}(\theta,\phi)r^{(n-l)}e^{-\zeta r} \tag{2.17}$$

And Gaussian type orbitals define as -

$$\varphi_{n,l,m,\zeta}^{GTO}(r,\theta,\phi) = NY_{lm}(\theta,\phi)r^{(2n-2-l)}e^{-\zeta r^2} \tag{2.18}$$

N is the normalized constant, $Y_{lm}(\theta,\phi)$ are spherical harmonic, $l$, $m$, and $n$ are angular momentum component, and $\zeta$ is the radius of the orbital. For example, 6-31G*[15] is used in the all geometry optimization calculation of materials consist of the first two rows of the periodic table. To minimize the number of the wavefunction in a basis set, the core electrons of heavier atoms are treated with pseudopotential.[16] Core electron of semiconductor elements like Pb, Se, Cd is treated with pseudopotential basis like LANL2Dz. [16]

On the other hand, the Plane waves basis set define as following where $\Omega$ is the volume, and G is defined based on the cut-off energy.

$$\varphi_i(r) = \frac{1}{\sqrt{\Omega}}e^{(iG.r)} \tag{2.19}$$

## 2.2. Reduction Potential Calculation

### 2.2.1. Methodology to Calculate Redox Potential

Actual or formal electron transfer is a typical process that leads to oxidation or reduction of a reactant. Reduction potential is the key tool in electrochemistry to describe the reactant's potential to be oxidized or reduced. However, direct measurement of the reduction potential is sometimes difficult or unfeasible in practice due to their high reactivity or irreversible half-reaction.[17] Standard reduction potential can be calculated in the solution phase by using the Gibbs free energy of a corresponding half-reaction, based on the thermodynamics cycle, which includes the free energy of reactants and products in the gas phase and solution phase.

Consider the following reduction half-reaction –

$$O(aq) + ne^- \xrightarrow{\Delta G_{red(aq)}} R(aq) \tag{2.20}$$

Absolute reduction potential in equation (2) can be calculated by using the following formula –

$$E_{abs}^0(O|R) = {-\Delta G_{red(aq)}}\big/{nF} \tag{2.21}$$

Where, $\Delta G_{red(aq)}$ is the Gibbs free energy of the reduction half-reaction, $n$ is the number of the electron transfer, and F is the Faraday constant.

The standard reduction potential of the above reaction is -

$$E_{std}^0(O|R) = E_{abs}^0(O|R) - E_{abs}^0(SHE) \tag{2.22}$$

Where $E_{std}^0(O|R)$ is standard reduction potential and $E_{abs}^0(O|R)$ is the calculated absolute reduction potential of the reaction (1) and $E_{abs}^0(SHE)$ is the standard hydrogen cell reduction potential, which is 4.28 V.[18-19]

$$[Ag_nCyt_n]_g^+ + e^- \xrightarrow{\Delta G_{red\,(g)}} [Ag_nCyt_n]_g^0$$

$$\Delta G_{Solv}^+ \Big\downarrow \qquad \Big\downarrow \Delta G^0 = 0 \qquad \Big\downarrow \Delta G_{Solv}^0$$

$$[Ag_nCyt_n]_{water}^+ + e^- \xrightarrow{\Delta G_{red\,(water)}} [Ag_nCyt_n]_{water}^0$$
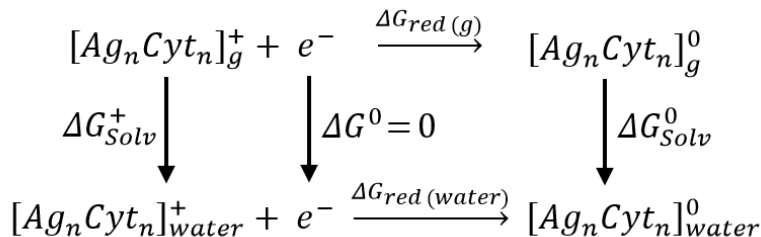
**Scheme 2.1**: Born-Haber thermochemical cycle to calculate Gibbs free energy ΔG(red(water)) of *a* reaction in water by using the standard free energy of the gas phase reaction, solvation free energy of reactant and product. Water indicates reaction in the water medium and g in the gaseous medium.

Gibbs free energy of the reduction reaction is calculated by using the Born-Haber cycle (Scheme 2.1). So absolute Gibbs energy of reducing or oxidizing agent is -

$$G_g = U_g + \Delta G_{therm} \tag{2.23}$$

Gibbs free energy of the reduction half-reaction in the gaseous phase is -

$$\Delta G_{red(g)} = G_g^0 - G_g^+ - G_g^0(e^-) \tag{2.24}$$

Gibbs free energy of the electron is also needed to consider in our calculation according to the scheme in Scheme 2.1. There have two thermochemical conventions to calculate the formation enthalpy of the electron. In the electron convention, where reference standard enthalpy change of electron is considered as element and enthalpy of formation is considered as zero in all temperatures. And in the ion convention, the formation enthalpy of the electron is equal to the integrated heat capacity overall temperatures. The difference between the two methods is the heat capacity of an electron, and the actual value depends on the statistical thermodynamics model to treat an electron. If we consider an electron in the gas phase and treat with Boltzmann statistics at room temperature, Gibbs free energy of an electron is zero, $G_g^0(e^-) = 0.00\,V$. Since the electron is a Fermion, Gibbs free energy of an electron at 298K in Fermi-Dirac distribution is -3.6Kj/mole, which is close to zero. As a result–

$$\Delta G_{red(g)} = G_g^0 - G_g^+ \tag{2.25}$$

### 2.2.2. Calculation of Solvation Free Energy

The continuum model has been reported for accurate prediction of solvation enthalpy. Using gas-phase energy of a system, solvation enthalpy can be determined by using the following equation –

$$\Delta G_{solv} = G_g - G_{solv} \tag{2.26}$$

If a thermal correction to the Gibbs free energy in the gas and solvent phase are comparable, equation 2.6 would be

$$\Delta G_{solv} = U_g - U_{solv} \tag{2.27}$$

$U$ is the Born-Oppenheimer equilibrium potential energy, where vibrational energy is canceled out each other in the equation 2.26 and 2.27

In the PCM solvation model[20], a solvent's true electrostatic terms are calculated from the bulk dielectric constant of the solvent. The non-bulk electrostatic term is adjusted according to the requested solvent cavity boundary, but the bulk electrostatic term is sensitive to the cavity size. It is reported that the SMD solvation method[21] is more accurate[21-22] than the continuum model like CPCM model[23-24]. Moreover, a gas phase geometry and a solvent phase geometry reorganization energy affect the solvation enthalpy. Ho et al. suggest the solvation enthalpy correction if the conformational change is significantly different from gaseous phase geometry.[25]

$$\Delta G_{solv} \cong \Delta G_{solv}(soln\ geom) + U_g(soln\ geom) - U_g(gas\ geom)) \tag{2.28}$$

In the sub-chapter 3.3, besides redox potential calculation of Ag nanoclusters, the geometry and solvation models' effects are investigated.

### 2.3. Analysis of Charge Transfer Character of Optical Transitions

The ground state molecular orbital (MO) decomposition on the basis of atomic orbitals reads

$$\varphi_n = \sum_{i=1}^{N} C_i^n \psi_i \tag{2.29}$$

Here, $N$ stands for the total number of atomic orbitals involved in the description of the system. The MOs obey normalization properties as following

$$\langle \varphi_n | S | \varphi_n \rangle = 1 \tag{2.30}$$

Here, S is the overlap matrix of atomic orbitals defined as

$$S_{ij} = \langle \psi_i | \psi_j \rangle \tag{2.31}$$

We approximate that $S_{i \neq j} = 0$, so that

$$\langle \varphi_n | S | \varphi_n \rangle = \sum_{i=j=1}^{N} C_i^{n*} C_j^n = \langle \Sigma_{i=1}^{N} C_i^{n*} \psi_i^* | S | \Sigma_{j=1}^{N} C_j^n \psi_j \rangle = \sum_{i=1}^{N} C_i^{n*} C_i^n \langle \psi_i^* | S | \psi_i \rangle \tag{2.32}$$

The MOs are projected onto atomic orbitals originating from different fragments of the system (*frag*): the Ag clusters (*frag=Ag*), cytosine (*frag=C*), Guanine (*frag=G*) and Thymine (*frag =T*) ligands. In this representation, the normalized projection reads:

$$P_{n,frag} = \frac{1}{\sum_{i=j=1}^{N} C_i^{n*} C_j^n} \sum_{k}^{N_k} C_k^{n*} C_k^n \tag{2.33}$$

$$\sum_{k_{frag,i}}^{frag= Ag,C,G,T} k_{frag,i} = N \tag{2.34}$$

In TDDFT calculations of the excited state, each optical transition with the energy $E_m$ is defined as a linear combination of MO pairs $i$ (occupied) and $j$ (unoccupied) contributing with weight coefficients $A_{m,i,j}$. The spatial electronic density distribution of occupied orbitals (holes) may be significantly different from those of unoccupied orbitals (electrons), contributing to the optical transition so that electrons are mainly localized on one spatial fragment of the system (e.g., on the silver cluster). In contrast, the hole is localized on the other fragment (e.g., on the

passivated bases). The excited states having a different character of the electron and hole spatial distribution are called charge transfer (CT) states. The degree of charge transfer, $D_m$, for each optical transition $m$ can be defined as a difference between projections of unoccupied (electron) and occupied (hole) orbitals, $D_m = P_e - P_h$, projected to each fragment and represented as following

$$D_{m,frag} = A^2_{m,i,j}\left(P_{i,frag} - P_{j,frag}\right) \tag{2.35}$$

where $P_{i,frag}$ is defined by Eq. (vi).

The degree of charge transfer $D_m$ is plotted in Chapter 3. Negative $D_m$ indicates the charge transfer from the fragment, and positive $D_m$ indicates the charge transfer to the fragment. As a result, all vertical sticks in related figures are a mirror image of positive and negative values. A very small $|D_m|$ indicates that transitions have negligible CT character and metal-to-metal or base-to-base ($\pi$-$\pi^*$) are dominating features in this transition.

## 2.4. Excited State Calculations: Linear Response Time-Dependent DFT (TDDFT)

Calculating the excited state energy is an essential tool to predict excited-state phenomena like luminescence, phosphorescence, and many others. The electronic density changes in the response of the external potential ($v'(t)$), and the new density by the perturbation of small external potential is calculated by the linear response time-dependent DFT (TD-DFT) method. Runge-Gross theorem[26] is the basis of Time-dependent DFT (TD-DFT). The Runge-Gross theorem stated that *two different external potentials cannot produce the same probability density function if the initial states are similar.* [26]
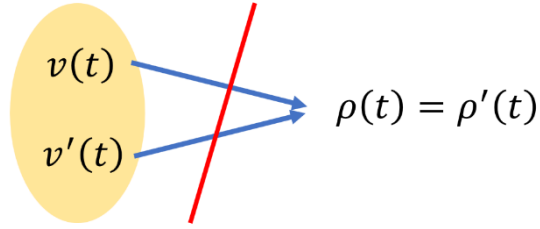
**Figure 2.1**: Two different potential cannot give an identical density of an electronic system with identical ground state density.

Time independent ground-state electron density determined using the variational principle, and the Runge-Gross theorem can be used to determine the electron density after external potential. But instead of ground-state density $\rho_0$, action integral is used to determine the density under an external potential[27]

$$\mathcal{A}[\phi] = \int_{t_2}^{t_1} dt \left\langle \phi(r,t) \left| \frac{i\partial}{\partial t} - \hat{H}(r,t) \right| \phi(r,t) \right\rangle \tag{2.36}$$

$\phi(r,t)$ is the time-dependent wavefunction, So the time-dependent Schrodinger equation is –

$$\frac{i\partial}{\partial t}\phi(r,t) = \hat{H}(r,t)\phi(r,t) \tag{3.37}$$

Similar to the ground state density in the DFT method, equation 2.29 and 2.30 shows that the action integral need to converge to the zero in the variation method to find the solution of the wavefunction under the external potential. As the Runge-Gross theorem stated, converging the action integral will give an exact probability density function.

If a ground state electronic system is perturbed by an external electromagnetic field, the new Hamiltonian is[28] –

$$\hat{H}(r,t) = \hat{H}_{gs}(r) + \hat{H}_1(r,t) \tag{2.38}$$

and time-dependent density will be –

$$\rho(r_i,t) = \rho_{gs} + \rho_1 \tag{2.39}$$

$\hat{H}_{gs}(r)$ and $\rho^{GS}$ are the ground state Hamiltonian and density, respectively. $\hat{H}_1(r,t)$ is the time-dependent perturbation on the ground state Hamiltonian and $\rho(r_i, t)$ is the time-dependent electronic density. This perturbation arises from the effects of an oscillating electric field with the electric dipole moment ($\mu_z$) of an electronic system, which is –

$$\hat{H}_1(r,t) = -\mu_z E \cos(\omega t) \qquad (2.40)$$

and,

$$\rho_1 = \rho(r_i, \omega) \cos(\omega t) \qquad (2.41)$$

The change of the density from $\rho_{gs}$ to $\rho(r_i, t)$, which is known as transition densities, is a result of electron excitation from an occupied orbital to the unoccupied orbitals. The change in the electron density upon the excitation is –

$$\delta\rho(r_i, \omega) = \sum_{a,b} C_{a,b}(\omega)\theta_a\theta_b^* + \sum_{b,a} C_{b,a}(\omega)\theta_a^*\theta_b \qquad (2.42)$$

$C_{a,b}$ and $C_{b,a}$ are the expansion coefficient, $\theta_a$ and $\theta_b$ are the occupied and unoccupied orbitals of electronic transitions. The expansion coefficient of this density change can be calculated by diagonalizing the Casida equation[27] –

$$\begin{bmatrix} A & B \\ B & A \end{bmatrix} \begin{bmatrix} X \\ Y \end{bmatrix} = \omega_I \begin{bmatrix} 1 & 0 \\ 0 & -1 \end{bmatrix} \begin{bmatrix} X \\ Y \end{bmatrix} \qquad (2.43)$$

## 2.5. Simulation of Phonon-Mediated Relaxation

One of the main objectives of computational modeling is to predict the experimental observation. Excited carrier dynamics govern the optoelectronic process in a photovoltaic cell, light-emitting diode, and others. We used the DFT based time-domain Kohn-Sham (TDKS)[29] and Fewest Switching Surface Hopping (FSSH) method[30-31] to study the excited hot carrier (hot electron and hot hole) dynamics in PbSe NPL and QDs. TDKS based FSSH method provides the phonon mediated carrier relaxation using a non-adiabatic coupling. We use FSSH on an

ensemble of trajectories, which ensure the trajectory branching[30] and detailed balance.[32] Trajectory branching describing the phonon correlation with different electronic states.

### 2.5.1. Time-Dependent Kohn-Sham Theory (TDKS)

The electron density of a many electrons system can be determined by equation 2.7 under the DFT method, and the electron density in Kohn-Sham[29] representation is –

$$\rho(r,t) = \sum_{n=1}^{N_e} |\varphi_n(r,t)|^2 \tag{2.44}$$

$N_e$ is the total number of electrons and $\varphi_n(r,t)$ are the single-electron Kohn-Sham (KS) orbitals, which are determined by the application of the time-dependent variational principle to the KS energy –

$$E[\varphi_p] = \sum_{n=1}^{N_e} \langle \varphi_p | K | \varphi_p \rangle + \sum_{n=1}^{N_e} \langle \varphi_p | V | \varphi_p \rangle + \frac{e^2}{2} \iint \frac{\rho(r',t)\rho(x,t)}{|r-r'|} d^3x d^3r' + E_{xc}[\rho] \tag{2.45}$$

The first term in the right hand is the kinetic energy of the non-interacting system, the second term is the potential due to the nucleus, and the next term is the electron-electron Coulomb interaction, the $E_{xc}$ cover the exchange-correlation part of the electrons. A single electron can be obtained using the variational principle where Hamiltonian depends on the wavefunction of the system–

$$i\hbar \frac{\partial \varphi_n(x,t)}{\partial t} = H\big(\varphi_n(x,t)\big)\varphi_n(x,t), \quad where \; p = 1, \dots . N_e \tag{2.46}$$

The above time-dependent wavefunction $\varphi_n(x,t)$ can be written in a linear combination of the adiabatic KS orbitals –

$$\varphi_n(x,t) = \sum_{k=N_1}^{N} c_{nk}(t)|\tilde{\varphi}_k(r,R)\rangle \tag{2.47}$$

N is the number of electrons, so $N^{th}$ orbital is the highest occupied molecular orbitals (HOMO), and $N^{th}+1$ indicates the lowest unoccupied molecular orbitals (LUMO). Using the eq- 2.46, eq 2.47 is transformed into the equation of motion as a function of linear coefficient $c_{nk}(t)$ –

$$i\hbar \frac{\partial c_{nk}(t)}{\partial t} = \sum_m^N c_{nk}(t)\left(\varepsilon_m \delta_{km} + d_{km}.\dot{R}\right)$$ (2.48)

$d_{km}.\dot{R}$ is the non-adiabatic (NA) term of the non-adiabatic wavefunction, where –

$$d_{km}.\dot{R} = -i\hbar\langle\tilde{\varphi}_k(r,R)|\nabla_R|\tilde{\varphi}_m(r,R)\rangle$$ (2.49)

and

$$\dot{R} = -i\hbar\left\langle\tilde{\varphi}_k\left|\frac{\partial}{\partial t}\right|\tilde{\varphi}_m\right\rangle$$ (2.50)

Ionic motion in adiabatic dynamics gives the time dependency on the TDKS for the electron-nuclear dynamics. NA coupling terms are dependent on the adiabatic KS orbitals, which can be computed using minimum computational resources by equation 2.13.

## 2.5.2. Hot Carrier Dynamics in Confined Semiconductor Nanomaterials

The methodology designed in section 2.4.1 is based on the ground state adiabatic molecular dynamics trajectories, and we have treated electron by single-particle wavefunction derived from the many-electron basis. This approximation is valid in the compound of heavier elements which has a rigid bond and higher density of states (DOS).[33-34] We have studied the hot carrier dynamics in the Pb and Cd chalcogenide nanomaterials. These nanomaterials have strong confinement and a small spherical homogeneous dielectric field. In the case of NC, confinement energy and Coulomb energy between the particle are scaled as $(r_B/R)^2$ and $r_B/R$ respectively where $r_B$ is the Bohr radius, and R is the radius of NC. As such, quadratic confinement term dominates the excited state carrier interaction, and excite electron and hole wavefunction can be

decoupled. This feature of the NC validates using the zeroth-order approximation in excited hot carrier dynamics.[35]

$$\varphi(e, h) = \varphi(e)\varphi(h) \tag{2.51}$$

The trajectory surface hopping (TSH) method predicts a probability of hopping between electronic states.[36] Correlation between the hopping probability with the motion of ion makes it time-dependent. The hopping probability from $k$ to $m$ is[35] –

$$dP_{km} = e^{\left[-\frac{\Delta\epsilon_{km}}{K_b T}\right]} \frac{b_{km}}{a_{km}} dt \tag{2.52}$$

Where, $b_{km} = -2Re\left(a^*_{km} d_{km} \cdot \dot{R}\right)$ and $a_{km} = c_k c^*_m$

Here, $c_k$ and $c_m$ are the linear coefficient in equation 2.40. $dP_{km}$ is the hopping probability, which is a function of the NA coupling term $d_{km}.\dot{R}$. We have applied some constrained which ensure the electron transition to the frontier orbitals. If $dP_{km}$ is negative, the hopping probability is set to zero. The exponential part is the Boltzmann distribution, which accounts for the detail balance[32] and prevents the quantum back excitation. It also maintains the constrain particle always hopped to lower density states.

## 2.6. References

1.      Born, M.; Oppenheimer, R., Zur Quantentheorie der Molekeln. *Annalen der Physik* **1927,** *389* (20), 457-484.

2.      Hohenberg, P.; Kohn, W., Inhomogeneous Electron Gas. *Phys. Rev.* **1964,** *136* (3B), B864-B871.

3.      Kohn, W.; Sham, L. J., Self-Consistent Equations Including Exchange and Correlation Effects. *Phys. Rev.* **1965,** *140* (4A), A1133-A1138.

4.      Garrick, R.; Natan, A.; Gould, T.; Kronik, L., Exact Generalized Kohn-Sham Theory for Hybrid Functionals. *Physical Review X* **2020,** *10* (2), 021040.

5.      Vosko, S. H.; Wilk, L.; Nusair, M., Accurate spin-dependent electron liquid correlation energies for local spin density calculations: a critical analysis. *Can. J. Phys.* **1980,** *58* (8), 1200-1211.

6. Perdew, J., Electronic structure of solids 91, edited by Ziesche, P. and Eschrig, H.(berlin: Akademie-verlag) p. 11; Perdew, JP and Wang, Y., 1992. *Phys. Rev. B* **1991,** *45* (13), 244.

7. Perdew, J. P.; Burke, K.; Ernzerhof, M., Generalized Gradient Approximation Made Simple. *Phys. Rev. Lett.* **1996,** *77* (18), 3865-3868.

8. Perdew, J. P.; Burke, K.; Ernzerhof, M., Generalized Gradient Approximation Made Simple [Phys. Rev. Lett. 77, 3865 (1996)]. *Phys. Rev. Lett.* **1997,** *78* (7), 1396-1396.

9. Becke, A. D., Density-functional exchange-energy approximation with correct asymptotic behavior. *Physical Review A* **1988,** *38* (6), 3098-3100.

10. Ernzerhof, M.; Scuseria, G. E., Assessment of the Perdew–Burke–Ernzerhof exchange-correlation functional. *J. Chem. Phys.* **1999,** *110* (11), 5029-5036.

11. Adamo, C.; Barone, V., Toward reliable density functional methods without adjustable parameters: The PBE0 model. *J. Chem. Phys.* **1999,** *110* (13), 6158-6170.

12. Stephens, P. J.; Devlin, F. J.; Chabalowski, C. F.; Frisch, M. J., Ab initio calculation of vibrational absorption and circular dichroism spectra using density functional force fields. *J. Phys. Chem.* **1994,** *98* (45), 11623-11627.

13. Yanai, T.; Tew, D. P.; Handy, N. C., A new hybrid exchange–correlation functional using the Coulomb-attenuating method (CAM-B3LYP). *Chem. Phys. Lett.* **2004,** *393* (1-3), 51-57.

14. Ditchfield, R.; Hehre, W. J.; Pople, J. A., Self-Consistent Molecular-Orbital Methods. IX. An Extended Gaussian-Type Basis for Molecular-Orbital Studies of Organic Molecules. *J. Chem. Phys.* **1971,** *54*, 724-728.

15. Schlegel, H. B.; Frisch, M. J., Transformation between Cartesian and pure spherical harmonic Gaussians. *Int. J. Quantum Chem* **1995,** *54* (2), 83-87.

16. Hay, P. J.; Wadt, W. R., Ab initio effective core potentials for molecular calculations. Potentials for K to Au including the outermost core orbitals. *J. Chem. Phys.* **1985,** *82* (1), 299-310.

17. Marenich, A. V.; Ho, J.; Coote, M. L.; Cramer, C. J.; Truhlar, D. G., Computational electrochemistry: prediction of liquid-phase reduction potentials. *Phys. Chem. Chem. Phys.* **2014,** *16* (29), 15068-15106.

18. Ribeiro, R. F.; Marenich, A. V.; Cramer, C. J.; Truhlar, D. G., Use of Solution-Phase Vibrational Frequencies in Continuum Models for the Free Energy of Solvation. *J. Phys. Chem. B* **2011,** *115* (49), 14556-14562.

19. Ho, J.; Ertem, M. Z., Calculating Free Energy Changes in Continuum Solvation Models. *J. Phys. Chem. B* **2016,** *120* (7), 1319-1329.

20. Cancès, E.; Mennucci, B.; Tomasi, J., A new integral equation formalism for the polarizable continuum model: Theoretical background and applications to isotropic and anisotropic dielectrics. *J. Chem. Phys.* **1997,** *107* (8), 3032-3041.

21. Marenich, A. V.; Cramer, C. J.; Truhlar, D. G., Universal Solvation Model Based on Solute Electron Density and on a Continuum Model of the Solvent Defined by the Bulk Dielectric Constant and Atomic Surface Tensions. *J. Phys. Chem. B* **2009,** *113* (18), 6378-6396.

22. Cramer, C. J.; Truhlar, D. G., A Universal Approach to Solvation Modeling. *Acc. Chem. Res.* **2008,** *41* (6), 760-768.

23. Cossi, M.; Rega, N.; Scalmani, G.; Barone, V., Energies, structures, and electronic properties of molecules in solution with the C-PCM solvation model. *J. Comput. Chem.* **2003,** *24* (6), 669-681.

24. Barone, V.; Cossi, M.; Tomasi, J., Geometry optimization of molecular structures in solution by the polarizable continuum model. *J. Comput. Chem.* **1998,** *19* (4), 404-417.

25. Ho, J.; Coote, M. L.; Cramer, C.; Truhlar, D. G., Theoretical calculation of reduction potentials. In *Organic Electrochemistry, Fifth Edition*, CRC Press: **2015**; pp 229-260.

26. Runge, E.; Gross, E. K. U., Density-Functional Theory for Time-Dependent Systems. *Phys. Rev. Lett.* **1984,** *52* (12), 997-1000.

27. Casida, M. E.; Jamorski, C.; Casida, K. C.; Salahub, D. R., Molecular excitation energies to high-lying bound states from time-dependent density-functional response theory: Characterization and correction of the time-dependent local density approximation ionization threshold. *J. Chem. Phys.* **1998,** *108* (11), 4439-4449.

28. Petersilka, M.; Gossmann, U. J.; Gross, E. K. U., Excitation Energies from Time-Dependent Density-Functional Theory. *Phys. Rev. Lett.* **1996,** *76* (8), 1212-1215.

29. Marques, M. A.; Gross, E. K., Time-dependent density functional theory. *Annu. Rev. Phys. Chem.* **2004,** *55*, 427-55.

30. Tully, J. C., Molecular-Dynamics with Electronic-Transitions. *J. Chem. Phys.* **1990,** *93* (2), 1061-1071.

31. Hammes-Schiffer, S.; Tully, J. C., Proton-Transfer in Solution - Molecular-Dynamics with Quantum Transitions. *J. Chem. Phys.* **1994,** *101* (6), 4657-4667.

32. Parandekar, P. V.; Tully, J. C., Mixed quantum-classical equilibrium. *J. Chem. Phys.* **2005,** *122* (9), 094102.

33. Kilina, S.; Kilin, D.; Prezhdo, O., Breaking the Phonon Bottleneck in PbSe and CdSe Quantum Dots: Time-Domain Density Functional Theory of Charge Carrier Relaxation. *ACS Nano* **2009,** *3* (1), 93-99.

34. Kilina, S. V.; Kilin, D. S.; Prezhdo, V. V.; Prezhdo, O. V., Theoretical Study of Electron-Phonon Relaxation in PbSe and CdSe Quantum Dots: Evidence for Phonon Memory. *J. Phys. Chem. C* **2011,** *115* (44), 21641-21651.

35. Craig, C. F.; Duncan, W. R.; Prezhdo, O. V., Trajectory surface hopping in the time-dependent Kohn-Sham approach for electron-nuclear dynamics. *Phys. Rev. Lett.* **2005,** *95* (16), 163001.

36. Tully, J. C.; Preston, R. K., Trajectory surface hopping approach to nonadiabatic molecular collisions: the reaction of H+ with D2. *J. Chem. Phys.* **1971,** *55* (2), 562-572.

# 3. SIMULATIONS PHOTOPHYSICAL PROPERTIES OF THE NUCLEOBASE PASSIVATED AG CLUSTER[*]

## 3.1. Computational Methodology Details

### 3.1.1. Ground State Geometry Optimization

Initial geometries of our DNA-AgNCs are created using the lowest energy conformations of the $Ag_4$-$Ag_{21}$ NC, including several low energy conformations of bare $Ag_5$ and $Ag_6$ clusters reported in the literature.[1] The lowest energy conformations of bare AgNCs smaller than 7 atoms in size have been proven to have planar geometries.[1-3] To check the effect of the planarity of DNA-AgNCs, we also model non-planar low energy conformations of $Ag_6$ and $Ag_5$ as initial structures (Table 3.1). Since all Ag atoms in such clusters can be considered surface atoms, the DNA bases are then added to each Ag atom of the cluster and optimized with (+1 e) and without charge (neutral). Using this approach, we have constructed clusters passivated by only C, G, or T (**5X**-$Ag_5$ and **6X**-$Ag_6$, with X = C, G, or T) and by their combinations of **(n-2)C2X**-$Ag_n$ and **2C(n-2)T**-$Ag_n$, where n = 5 or 6 and X = G or T. DFT (Details in sub-chapter 2.1 ) is applied for geometry optimization of all considered DNA-AgNCs, and TDDFT[4-5] (Detail in sub-chapter 2.3) is used for all excited-state calculations, as implemented in Gaussian16 software package.[6] Long-range corrected exchange-correlation functional CAM-B3LYP[7] and mixed basis set LANL2DZ[8] (for Ag atoms) / 6-31G*[9] (for N, O, C, and H atoms) are used for both the ground and excited-state calculations. Long-range corrected CAM-B3LYP functional have shown a more accurate

---

[*] Section 3.2 of this chapter reproduced in part with permission from *J. Phys. Chem. A* 2020, 124, 43, 8931–8942 Copyright 2020 American Chemical Society.  The material in section 3.2 was co-authored by Dr. Naveen Dandu and Dr. Sergei Tretiak. Dr. Naveen Dandu calculated the electronic structure of the 6C-$Ag_6$ geometry. Dr. Sergei Tretiak contributed by helpful suggestions and reviewed the methodology and conclusion of the calculations. Mohammed A. Jabed was the primary contributor of the methodology design, performed all the calculations and conclusion that are advanced in this sub-chapter. Dr. Svetlana Kilina served as a supervisor of the project conducted by Mohammed A Jabed and Dr. Naveen Dandu.

description of charge transfer transitions in DNA-AgNCs, compared to pure GGA or hybrid functionals, despite blue-shifts in optical transitions.[10-12] These findings define our choice of the functionals and basis sets. In addition to vacuum calculations, we also have performed calculations in water utilizing conductor-like polarizable continuum model (CPCM)[13] for simulating solvent environment for the ground and excited state calculations.

### 3.1.2. Calculation of Transition Energy

Ninety optical transitions are obtained from TDDFT calculations to reproduce the absorption spectra at the range of 1.00-5.50 eV. The profile of the spectra is modeled using the Gaussian function with a width of 0.08 eV to reproduce a thermal broadening of spectral bands. To visualize the charge density distribution of the excited state, Natural Transition Orbitals (NTOs)[14] are calculated for photoexcited electron-hole pair based on transition densities obtained from TDDFT, as implemented in Gaussian09[15]/Gaussian16[6] software. VMD[16] software has been used for visualization of NTOs. To better understand the nature of the transitions, we have decomposed the excited state wavefunction contributed from the Ag and the base parts of the DNA-AgNCs, and plotted it as a difference between the electron and hole states, using the equation 2.33 and 2.34.

### 3.1.3. Reduction Potential Calculations

Reduction potential is calculated by using the theory given in section 2.2 of Chapter 2. Solvation Gibbs free energy plays a dominating role in determining the reduction potential. Zero-point energy correction and correction to Gibbs free energy obtained from the frequency calculation with simple harmonic approximation in Gaussian software packages.[6] A mixed basis set of LANL2DZ[8] and 6-31G* basis[9] are used in all calculations for the Ag and all other elements, respectively. Despite accurate ground state geometry prediction by continuum solvent

54

methods, SMD is reported for better accuracy. We have considered both CPCM[13] and SMD

solvation methods and investigate the effects of geometry and solvation continuum method

consideration on the overall reduction potential of the cytosine passivated Ag nanoclusters.

### 3.1.4. Binding Energy Calculations

To elucidate the strength of an interaction between the specific type of the base ($L1$=C,

G, or T) and the AgNC, the binding energy is calculated using the following formula:

$$E_{b,L1} = \frac{E_{Ag_nL1_pL2_q} - \left(E_{Ag_nL2_q} + p * E_{L1}\right)}{p} \tag{3.1}$$

where $n$ is the number of the silver atoms, $p$ and $q$ are the number of the base types $L_1$ and $L_2$,

respectively, with $n = p + q$. The energy $E_{Ag_nL2_p}$ is calculated for optimized DNA-AgNCs

fragment with the bases of type $L_1$ removed from the AgNC. The energy $E_{L1}$ is calculated for the

isolated optimized base of the type $L_1$. For clusters passivated only by cytosines, the average

cluster-base binding energy, $\langle Ag - N \rangle$, is calculated as the difference between the total energies

of the passivated cluster and its pristine counterparts – the bare silver cluster and the pristine

cytosine multiplied by the number of cytosines at the cluster – with all structures optimized to

their minimal energies. The result is divided by the total number of cytosines passivating the

cluster to get the average binding energy per base.

$$E_{\langle Ag - N \rangle} = \frac{E_{Ag_nL_p} - (E_{Ag_n} + p * E_L)}{p} \tag{3.2}$$

Where $p$ is the number ligand type $L$, and $n$ is the cluster size.

### 3.1.5. Principal Component Analysis (PCA) of the Structural Descriptor in Ag₅ and Ag₆

We have utilized the principal component analysis to better understand the geometrical

descriptor and its effects on the brightness of the lowest energy transitions. Due to the single

strand DNA sequences' tertiary structure, Ag nanoclusters have non-equilibrium geometry and

higher energy geometry than ground state conformers. In the first step, 500 random geometries of the nanocluster size 5 and 6 atoms were created by imposing the constrained – 1. The number of Ag atom and cytosine ratio is 1:1, 2. Cytosine interacts with Ag atom by 3-N of the cytosine ring. The 500 initial geometries of each cluster are optimized as neutral and charge clusters. Water was used as a solvent and implemented with the CPCM solvation method in gaussian16 software.

## 3.2. Structural Isomer and Solvent Polarity on Cytosine Passivated $Ag_5$ and $Ag_6$ Nanoclusters

### 3.2.1. Structural Conformation of Cytosine Passivated $Ag_5$ and $Ag_6$ Nanoclusters

Due to a high degree of flexibility of the nucleotides passivating DNA-AgNCs, different structural conformations of clusters likely coexist in experimental samples. To address the diversity in DNA-AgNC conformations, we consider a planer and non-planar geometries of $Ag_5$ and $Ag_6$ clusters that have been shown as one of the most stable conformations of bare silver clusters of these sizes.[1, 17] DNA-AgNCs of **5**C-$Ag_5$ and **6**C-$Ag_6$ initially constructed from these bare clusters are used to study the effect of a polar solvent, charge, and passivating bases on the structural conformations of clusters, with results presented in Table 3.1. In the vacuum, coordination of Ag atoms by cytosines noticeably changes the geometry of non-planar neutral clusters (Geom-2 and Geom-3), while only slightly distorts the initially planar conformation (Geom-1). The cluster **6**C-$Ag_6$ stays planar, preserving its $^1D_{3h}$ symmetry resulting in the lowest energy conformation among its isomers. However, a slight distortion results in breaking perfect planarity of the cluster **5**C-$Ag_5$, raising its energy by ~0.3 eV, compared to its initially non-planar isomer (Geom-2). In a vacuum, charging the clusters results in significant stabilization of

56

the nearly planar Geom-1 isomer of **5C**-Ag$_5^+$, while breaks initial planarity and the symmetry of

Geom-1 **6C**-Ag$_6^+$ destabilizing this structure, compared to other charged isomers.

**Table 3.1**: The most stable Ag$_6$ and Ag$_5$ clusters used as initial structures for related isomers of 6C-Ag$_6$ and 5C-Ag$_5$ DNA-AgNCs optimized in vacuum and water with no charge (neutral) and +1 charge. Zero energy is assigned to structures with the lowest energy of their bare AgNC counterparts. The red font depicts the optimized final structures with the lowest energies among considered isomers.
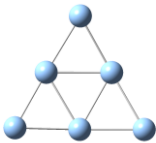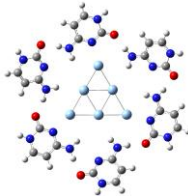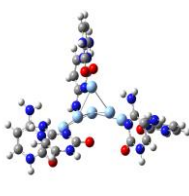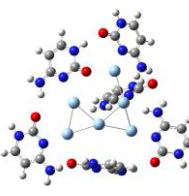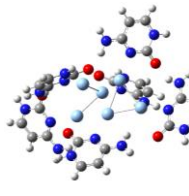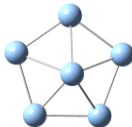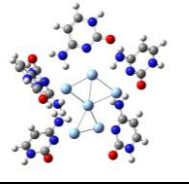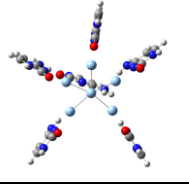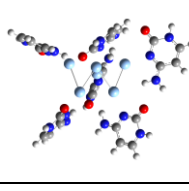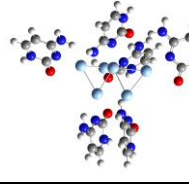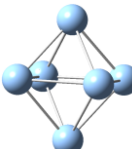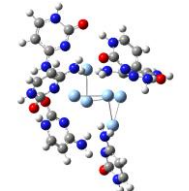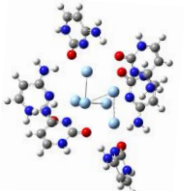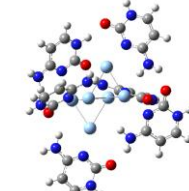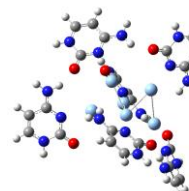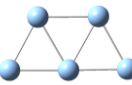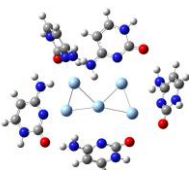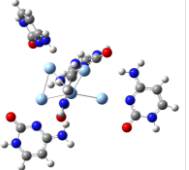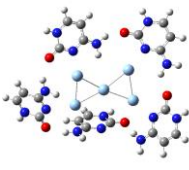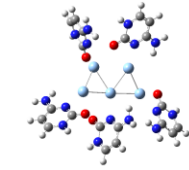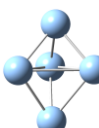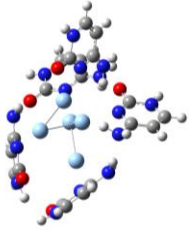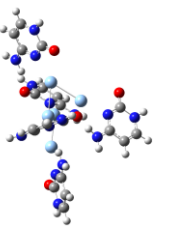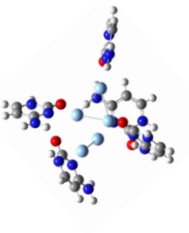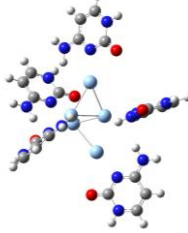
| | Initial AgNC structure | Optimized Neutral | | Optimized Charged | |
|---|---|---|---|---|---|
| | | Vacuum | Water | Vacuum | Water |
| **Ag$_6$ clusters** | Geom-1 | | | | |
| | **0.00 eV** | **0.00 eV** | 0.00 eV | 0.00 eV | 0.00 eV |
| | Geom-2 | | | | |
| | 0.20 eV | 0.88 eV | 0.13 eV | 0.01 eV | 0.26 eV |
| | Geom-3 | | | | |
| | 0.84 eV | 1.29 eV | **-0.12 eV** | -0.18 eV | **-0.11 eV** |
| **Ag$_5$ clusters** | Geom-1 | | | | |
| | **0.00 eV** | 0.00 eV | 0.00 eV | **0.00 eV** | **0.00 eV** |
| | Geom-2 | | | | |
| | 0.99 eV | **-0.31 eV** | **-0.13 eV** | 0.41 eV | 0.01eV |

**Table 3.2:** Structural parameters of neutral and charged 5C-Ag$_5$ clusters. For the average Ag-Ag bond length, $\langle Ag - Ag \rangle$, only Ag-Ag bonds with a length of less than 3 Å are considered. The cluster-based binding energies (E$_{bind}$) are calculated using Eq. 3.1, where L$_1$ is the cytosine with either the shortest or the longest Ag-N bond length and p=1. The values of the total energy, E$_{tot}$, marked in red, highlight the most stable isomers with the lowest energy.

| | | **5C**-Ag$_5$ isomers | Vacuum | | Solvent | |
|---|---|---|---|---|---|---|
| | | | Geom-1 | Geom-2 | Geom-1 | Geom-2 |
| Neutral | Bond length, Å | $\langle$Ag-$Ag\rangle$ | 2.75±0.06 | 2.77±0.09 | 2.82±0.10 | 2.84±0.12 |
| | | $\langle$Ag-$N\rangle$ | 2.50±0.29 | 2.36±0.01 | 2.40±0.04 | 2.40±0.03 |
| | | (Ag-N)$_{Short}$ | 2.23 | 2.34 | 2.36 | 2.35 |
| | | (Ag-N)$_{Long}$ | 3.04 | 2.37 | 2.47 | 2.43 |
| | E$_{bind}$, eV | $\langle E_{Ag-N} \rangle$ | 0.63 | -0.69 | -0.34 | -0.37 |
| | | $E_{Ag-N,Short}$ | -0.82 | -0.55 | -0.07 | -0.27 |
| | | $E_{Ag-N,Long}$ | -0.55 | -1.14 | -0.18 | -0.18 |
| | | E$_{tot}$, eV | 0.00 | -0.31 | 0.00 | -0.13 |
| Charged (+1) | Bond length, Å | $\langle$Ag-$Ag\rangle$ | 2.75±0.07 | 2.84±0.16 | 2.76±0.07 | 2.81±0.14 |
| | | $\langle$Ag-$N\rangle$ | 2.63±0.52 | 2.36±0.03 | 2.38±0.13 | 2.33±0.02 |
| | | (Ag-N)$_{Short}$ | 2.27 | 2.31 | 2.27 | 2.30 |
| | | (Ag-N)$_{Long}$ | 3.64 | 2.42 | 2.57 | 2.35 |
| | E$_{bind}$, eV | $\langle E_{Ag-N} \rangle$ | -1.34 | -1.26 | -1.17 | -0.59 |
| | | $E_{Ag-N,Short}$ | -1.33 | -0.96 | -0.39 | -0.61 |
| | | $E_{Ag-N,Long}$ | -1.10 | -0.43 | -0.14 | -0.30 |
| | | E$_{tot}$, eV | 0.00 | 0.41 | 0.00 | 0.01 |

Several competing factors influence the overall stability of the cluster. It was shown that closed-shell small metal clusters are more stable in their symmetric planar structure.[3, 18] This agrees with our findings that the planar geometries of the **6C**-Ag$_6$ and **5C**-Ag$_5^+$ are more stable compared to their non-planar 3D isomers, Table 3.1. However, for all structures in a vacuum, cytosines are not equally coordinated with Ag atoms, as evidenced from the significant variations in the Ag-N bond lengths mainly correlated to the strength of the binding energy between the base and the cluster, as presented in Table 3.2 for **5C**-Ag$_5$ and Table 3.3 for **6C**-Ag$_6$ clusters.

**Table 3.3**: Structural parameters of the **6C-**$Ag_6$ cluster. For the average silver-silver bond length, $\langle Ag\text{-}Ag\rangle$, only Ag-Ag bond lengths less than 3Å are considered. For the average Ag-N bond length between the cluster and the base, $\langle Ag\text{-}N\rangle$, all six bonds are considered. The bond between the oxygen and hydrogen of two adjacent cytosines shorter than 2 Å is considered the hydrogen bond (H-bond). The cluster-base binding energies ($E_{bind}$) are calculated using Eq. 3.1, where $L_1$ is the cytosine with either the shortest or the longest Ag-N bond length and p=1.

| 6C-$Ag_6$ isomers | | Vacuum | | | Solvent | | |
|---|---|---|---|---|---|---|---|
| | | Geom-1 | Geom-2 | Geom-3 | Geom-1 | Geom-2 | Geom-3 |
| **Neutral** — Bond length, Å | $\langle Ag\text{-}Ag\rangle$ | 2.78±0.02 | 2.77±0.03 | 2.86±0.17 | 2.81±0.05 | 2.82±0.12 | 2.85±0.12 |
| | $\langle Ag\text{-}N\rangle$ | 3.45±1.17 | 2.97±0.81 | 2.71±0.60 | 2.45±0.07 | 2.61±0.55 | 2.44±0.03 |
| | (Ag-N)$_{Long}$ | 4.52 | 4.03 | 3.92 | 2.57 | 3.75 | 2.48 |
| | (Ag-N)$_{Short}$ | 2.38 | 2.33 | 2.42 | 2.39 | 2.36 | 2.39 |
| # Bonds | Ag-N | 3 | 4 | 5 | 6 | 5 | 6 |
| | H-bond | 6 | 2 | 4 | 1 | 1 | 4 |
| $E_{bind}$, eV | $\langle E_{Ag-N}\rangle$ | -0.81 | -0.77 | -0.80 | -0.31 | -0.98 | -0.55 |
| | $E_{Ag-N,Short}$ | -1.21 | -1.28 | -0.45 | -0.19 | -0.81 | -0.29 |
| | $E_{Ag-N,Long}$ | -1.21 | -0.75 | -0.33 | -0.16 | -1.074 | -0.28 |
| **Charged (+1)** — Bond length, Å | $\langle Ag\text{-}Ag\rangle$ | 2.77±0.06 | 2.86±0.10 | 2.84±0.09 | 2.85±0.09 | 2.83±0.11 | 2.87±0.10 |
| | $\langle Ag\text{-}N\rangle$ | 2.63±0.55 | 2.40±0.08 | 2.36±0.02 | 2.39±0. 09 | 2.35±0.03 | 2.37±0.04 |
| | (Ag-N)$_{Long}$ | 3.74 | 2.56 | 2.39 | 2.55 | 2.40 | 2.43 |
| | (Ag-N)$_{Short}$ | 2.30 | 2.32 | 2.34 | 2.30 | 2.33 | 2.32 |
| # Bonds | Ag-N | 5 | 6 | 6 | 6 | 6 | 6 |
| | H-bond | 4 | 4 | 5 | 3 | 2 | 4 |
| $E_{bind}$, eV | $\langle E_{Ag-N}\rangle$ | -1.19 | -1.21 | -1.22 | -0.57 | -1.11 | -0.61 |
| | $E_{Ag-N,Short}$ | -0.52 | -0.92 | -0.97 | -0.35 | -0.63 | -0.56 |
| | $E_{Ag-N,Long}$ | -1.20 | -0.85 | -0.56 | -0.21 | -0.76 | -0.34 |

This behavior is the most pronounced for **6C-**$Ag_6$ isomers in a vacuum. For instance, only three bases create strong coordinate bonds with Ag at the edges of the planar Geom-1 structure, while the other three bases are much weaker coordinated with Ag at the sides (see Table 3.1 and 3.3). However, weakly coordinated bases form the hydrogen bond (H-bond) with the oxygen from the nearest base, thus, encapsulating the cluster minimizing the total energy of Geom-1 isomer of **6C-**$Ag_6$. Non-planar geometry breaks some of the hydrogen bonds, raising the

total energy of 3-D **6C**-Ag$_6$ isomers in the vacuum. In contrast, the energy of 3-D **6C**-Ag$_6^+$ is reduced for Geom-3 due to a larger number of hydrogen bonds and also decreased Ag-N bond length for all capping bases associated with the strongest base-cluster interactions. Similar trends are observed for Ag$_5$ in the vacuum, where **5C**-Ag$_5$ non-planar structure (Geom-2) and nearly planar structure (Geom-1) of **5C**-Ag$_5^+$ poses both maximum number of hydrogen bonds and the strongest base-cluster interactions resulting in the most stable conformations, Table 3.2.

As a result of significantly different geometries of isomers, the average Ag-Ag bond length varies at the range of 2.75–2.87 Å for both **5C**-Ag$_5$ and **6C**-Ag$_6$ neutral and charged clusters, as shown in Table 3.2 and Table 3.3. In all cases, the average Ag-Ag bond length of the Geom-1 isomers is the shortest in the vacuum (2.75–2.78 Å) and the most affected towards elongation by the solvent because of the planner (**6C**-Ag$_6$) or nearly planar (**5C**-Ag$_5$) geometry transfers to non-planar 3-D structure in water. In contrast, Geom-3 demonstrates the least effect on its Ag-Ag bond by both charge and solvent. Among all isomers, Geom-3 has the longest Ag-Ag bond of 2.84–2.87 Å for neutral **6C**-Ag$_6$ and charged **6C**-Ag$_6^+$ clusters insignificantly varying in vacuum and solvent.

The bond length between the cluster and the covalently coordinated base, (Ag-N)$_{short}$, varies at the range of 2.23–2.45 Å. This excludes Ag-N bond length larger than 3 Å, which is an outcome of the very weak interaction between the cytosine and the cluster. Note that this weak cluster-base interaction is partially compensated by the hydrogen bonding between O and H from the NH$_2$ group of the adjacent cytosines, as discussed in the main text. The Ag-N bond length for weakly coordinated bases, (Ag-N)$_{Long}$, significantly decreases in water for all clusters approaching the (Ag-N)$_{Short}$ bond length of strongly coordinated bases, which is also accompanied by reducing the number of hydrogen bonds.

In both neutral and charged clusters, average binding energies between the cluster and the bases are weaker in water than in a vacuum. This decrease in the cluster-base binding strength originates from the dipole-dipole screening effect of the polar media. Due to the Ag core's cationic nature, the binding energy between the cluster and the cytosine with the longest Ag-N bond length is stronger in the charged clusters relative to their neutral counterparts. It is important to note, however, that the trend in the cluster-base binding energies do not always follow the trend in the Ag-N bond lengths so that the binding energy between the cluster and the base with the longest Ag-N bond length does not always end up to the largest value of $E_{bind}$, as expected for the weakest cluster-base interactions. This discrepancy originates from strong changes in the optimized conformations when a particular base is removed from the DNA-AgNC, used for calculations of the binding energy according to equation 3.1 in the main text. For example, removal of one of the cytosines – either strongly coordinated one with the shortest Ag-N bond length or weakly interacting one with the longest Ag-N bond length – from the neutral planar Geom-1 of **6C**-Ag$_6$ results in the same **5C**-Ag$_6$ structure with additional interaction between the cluster and the base via Ag-O coordination, as illustrated in Figure 3.1. For simplicity, equation 3.1 can be rewritten as $E^{opt}$(**6C**-Ag$_6$) - $E^{opt}$(**5C**-Ag$_6$) - $E^{opt}$(**C**), where each term represents the total energy of the optimized structures of Geom-1 **6C**-Ag$_6$, **5C**-Ag$_6$, and pristine cytosine, respectively. Since for both strongly and weakly interacting bases, all the terms in this equation are identical. One gets exactly the same value of the binding energies for both weakly and strongly interacting bases, Table 3.3. Similar effects are also found in Geom-2 isomers, which also result in discrepancies between the trends in the cluster-base binding energies and trends in the Ag-N bond length.

**(a)** 6C-Ag$_6$        **(b)** Initial 5C-Ag$_6$        **(c)** Final 5C-Ag$_6$
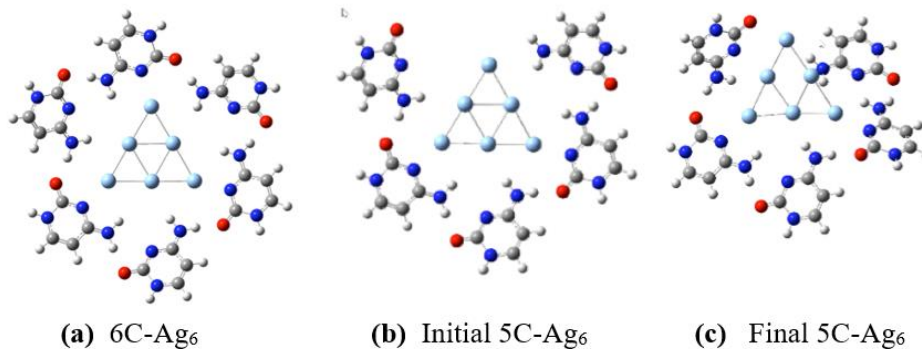
**Figure 3.1:** Initial and final structures used for calculations of the base-cluster binding energy using Eq.1. (a) Neutral **6C**-Ag$_6$ cluster optimized from the initial planar Geom-1 structure in the vacuum. (b) One cytosine at the edge of the cluster is removed from the Geom-1 **6C**-Ag$_6$ resulting in a **5C**-Ag$_6$ cluster. (c) Optimized geometry of the **5C**-Ag$_6$ cluster in a vacuum. After removal of cytosine, vacant Ag atom is involved in the coordinated bond with oxygen from the adjacent cytosine at the side, while this cytosine is much stronger coordinated to the side Ag atom, compared to those in the **6C**-Ag$_6$ cluster.

It is important to note that the shortest Ag-N bond does not always correspond to the strongest binding energy between the base and the cluster, Table 3.3. This discrepancy originates from a strong reconstruction of the cluster after removal of the base when used in calculations of the binding energy according to equation 3.1. For instance, losing one of the bases from the planar Geom-1 isomer of **6C**-Ag$_6$ results in a new **5C**-Ag$_6$ structure, where the weakly interacting base is strongly coordinated to the side Ag atom via the nitrogen and also to the edge Ag atom via the oxygen, Figure 3.1. As such, the obtained base-cluster binding energy is 'contaminated' by the additional interaction via the oxygen that is not presented in the initial structure. Due to strong structural variations upon removing one of the cytosines, trends in the base-cluster binding energies are not well correlated with the trends in the Ag-N bond lengths for some isomers. On the other hand, the obtained **5C**-Ag$_6$ structure demonstrates that cytosines can be coordinated to AgNC via either nitrogen or oxygen or both if there is a limiting number of bases available for the cluster capping. This result agrees with computational findings for Ag$_{12}$ clusters encapsulated in single-strand DNA scaffold consisted of 12 nucleobases.[19]

A polar solvent, such as water, significantly reduces the number of hydrogen bonds in the DNA-AgNCs due to the dipole-dipole screening effect. As a result, all optimized structures in water are not planar, and their initial structural symmetry is also significantly distorted in Table 3.1. Similar to the vacuum calculations, the most stable isomer is preserving the largest number of hydrogen bonds and the strongest base-cluster interactions associated with nearly similar Ag-N bond length for all bases. In water, these conditions are satisfied for Geom-3 isomer of **6C**-Ag$_6$ and **6C**-Ag$_6^+$ (Table 3.1 and 3.3) and Geom-1 isomer of **5C**-Ag$_5$ and **5C**-Ag$_5^+$ (Table 3.2).

Calculated structures point to three main trends. First, our results well agree with the previous studies of larger clusters (> 10 atoms) confirming non-planar 3-D structures of DNA-AgNCs in polar solvents.[20-22] Moreover, our results reveal that a polar solvent governs the planar to non-planar 3-D structural stabilization even for DNA-AgNC isomers with less than 7 atoms in sizes. Second, the inclusion of a polar solvent significantly changes the conformation of the DNA-AgNCs by reducing the number of hydrogen bonds between neighboring bases and making all bases nearly equally interacting with Ag atoms. Both of these conditions play a key role in the stabilization of a particular isomer. Third, several isomers of DNA-AgNCs are likely to coexist in polar solvents due to the relatively small energy differences between their conformations (0.1 – 0.2 eV). In contrast, closed shell **6C**-Ag$_6$ and **5C**-Ag$_5^+$ clusters in the vacuum (or non-polar solvents) have a more distinct tendency for preferential planar conformations, with a larger difference in their total energies (up to ~1 eV) compared to non-planar isomers, which agrees with computational predictions for the bare Ag clusters.[3, 18,23]

**3.2.2. Dependence of Optical Properties on Conformations of Clusters Passivated by Cytosines.**

Absorption spectra of all considered isomers calculated in vacuum and water are shown in Figure 3.3 for **6C**-Ag$_6$ and in Figure 3.2 for **5C**-Ag$_5$ clusters. The oscillator strength of the lowest energy transition of **6C**-Ag$_6$ clusters is the most impacted by the isomer conformation, resulting in the completely optically inactive (dark) first transition of the Geom-1 isomer and optically allowed (bright) the first transition of other neutral isomers both in vacuum and water, Figure 3.3a and b. Interestingly, Geom-3 that is the most stable neutral isomer in water, has the optically bright lowest energy transition, which is expected to provide favorite conditions for high emission of **6C**-Ag$_6$ clusters in water. In contrast, the Geom-3 isomer of the charged **6C**-Ag$_6^+$ cluster with the most stable structure has an optically inactive first transition in water, while the Geom-1 isomer provides the bright first transition both in vacuum and water, Figure 3.3c and d. These results suggest that emissive **6C**-Ag$_6$ clusters in polar solvents are likely not charged. Contrary, both isomers of the charged **5C**-Ag$_5^+$ cluster demonstrate the narrow and highly intensive lowest peak with optically active first transitions in water, compared to broader and much less intensive first peak of neutral **5C**-Ag$_5$ clusters, Figure 3.2b and 3.2d. This suggests that charged **5C**-Ag$_5^+$ clusters (with the closed shell electronic structure) are expected to be more emissive in polar solvents than their neutral counterparts (open shell structures).

However, the overall shape of the absorption spectra of clusters is not very sensitive to the geometry of isomers, with less pronounced changes in spectral features for both charged and neutral **6C**-Ag$_6$ and **5C**-Ag$_5$ isomers in water, compared to those in the vacuum. Despite some variations in energies and intensities of spectral peaks of different isomers, the overall number of peaks and the spectrum profile are quite similar for all isomers in water. This is evidenced by the

shape of the spectrum averaged over considered isomers, which well coincides with each

individual spectrum of an isomer (dashed magenta lines in figure 3.3b and d). As such, the

absorption spectrum of various DNA-AgNC conformations unlikely results in distinct spectral

fingerprints of a specific isomer. On the other hand, the presence of different DNA-AgNC

isomers in experimental samples is expected to only increase the inhomogeneous broadening of

the absorption spectra while the main absorption bands stay nearly the same.
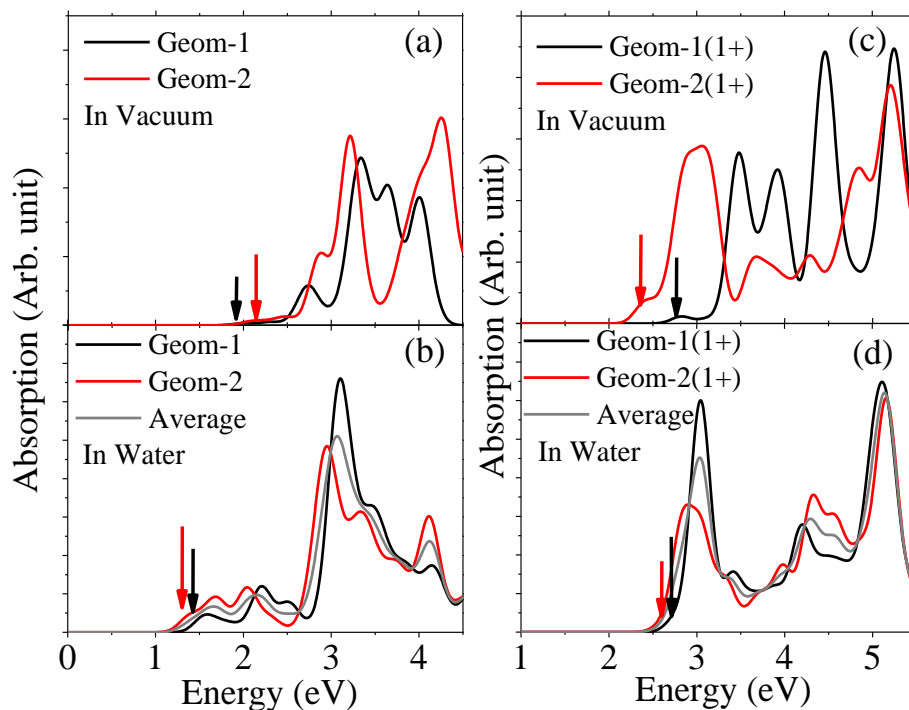


**Figure 3.2:** Absorption spectra of two isomers of **5C-**$Ag_5$ and **5C-**$Ag_5^+$ clusters calculated in vacuum and water. **(a)** and **(b)** Spectra of neutral clusters in vacuum and water, respectively. **(c)** and **(d)** Spectra of charged clusters in vacuum and water, respectively. Names of the isomers correspond to those in Table 1 in the main text. Grey lines correspond to the absorption spectra averaged over both conformations. The vertical arrows denote the energy of the fist optical transition of Geom-1 (black lines) and Geom-2 (red lines) isomers. While the spectral profile and the energy of the first optical band are noticeably different between Geom-1 and Geom-2 isomers in a vacuum, they are less distinct in water. As such, the spectra averaged over both isomers (the grey line) follow the same shape and optical features as those of Geom-1 (the black line) and Geom-2 (the red line) isomers in water for both neutral **5C-**$Ag_5$ (b) and charged **5C-**$Ag_5^+$ (d) clusters.
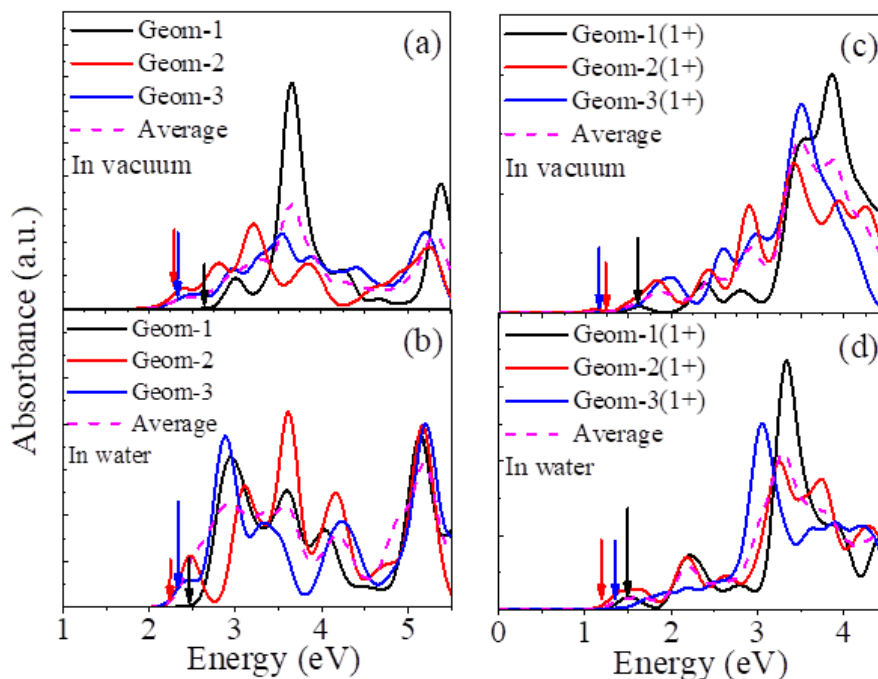
**Figure 3.3**: Absorption spectra of **6C-**$Ag_6$ isomers. Neutral **6C-**$Ag_6$ in the vacuum **(a)** and water **(b)**. Charged **6C-**$Ag_6^+$ in the vacuum **(c)** and water **(d)**. The names of the isomers correspond to those in Table 1. Absorption spectra averaged over three isomers are represented by dashed magenta lines. Vertical arrows correspond to the first optical transition with the lowest energy for each isomer.

### 3.3. Electrochemical Properties of the Ag Nanoclusters
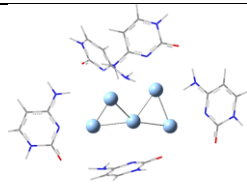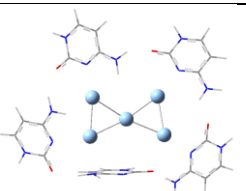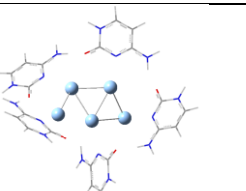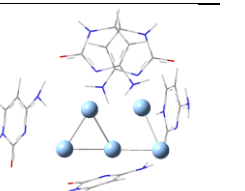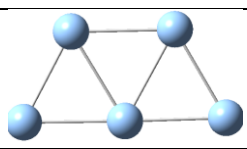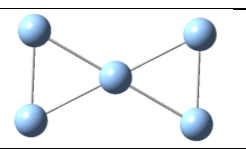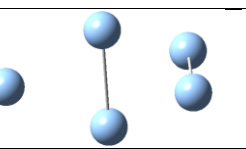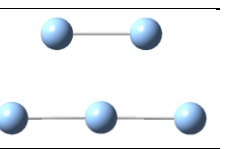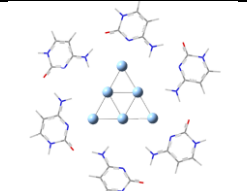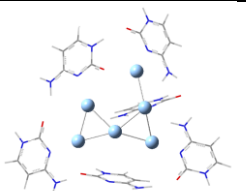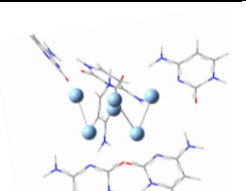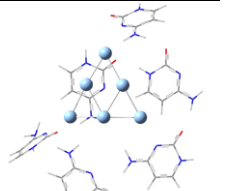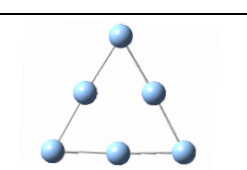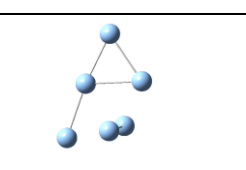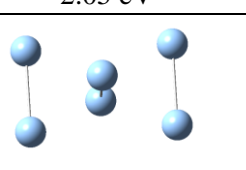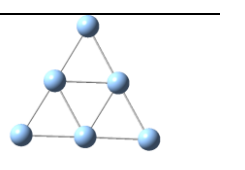
As we have discussed in chapter 1, Ag nanoclusters are promising for the bight and structure dependent emission, especially where background noise is significant.[24] Size and oxidation state are among the dominating factors in determining fluorescence yield. The oxidation state of the nanoclusters is not predictable because bulk Ag has positive reduction potential, but Ag nanocluster can have negative reduction potentials.[25-27]Moreover, emission in some metal clusters can't be assessed accurately due to the oxidation reaction.[28] Similarly, one of the common synthesis processes of Ag nanocluster is a surface redox reaction. Ag nanoclusters formed by free radical induced reduction of $AgNO_3$, which shown higher $Ag_{ion}/Ag_{cluster}$ reduction potential.[29] In metal clusters, the effective electron transfer is only possible if the metal clusters' relative reduction potential is positive compared to the electron donor. The higher difference of

66

redox potential is utilized in catalytic water splitting reaction.[29] But Ag nanoclusters show reduction potential alternation by odd-even number of Ag atoms in clusters up to 20 atom size.[30] Accurate prediction of reduction potential is essential to predict the cluster size and oxidation states of the Ag clusters, and its electronic properties. Therefore, we have examined the computational methodology to calculate the redox potential of the cytosine passivated Ag clusters.

**3.3.1. Oxidation and Size Dependent Structure of Cytosine Passivated Ag Nanoclusters**

In the solution phase, the nature of surface passivation dominates the electron transfer process between the redox species. The effect of oxidation state is studied in this section. All cytosine passivated $Ag_n$ geometries are prepared from Chen et al.[1], as given in detail in section 3.4. The initial geometries are optimized in the different oxidation states. Table 3.4 is showing the 5 and 6 Ag atom size cluster geometries after optimization in cytosine passivated and bare clusters. Initial geometry of the five and six cytosines passivated $Ag_5$, and $Ag_6$ clusters are planner. $Ag_5$ has five of $5S^1$ electron, which fit with the Jellium model, where it filled $1S^2$ and $1P_x^2$ and $1P_y^1$ and formed planner geometry.[31] It also agrees with optimizing the passivated clusters in the vacuum, which has shown the hydrogen bond network between the nucleobase cytosine and retained the planner structure of the core Ag. It is noticed that the cytosine passivated clusters become non-planner due to the cytosine-Ag interaction, while bare clusters maintain the symmetry. Although the geometry of the two clusters is shown in Table 3.4 as an example, it was noticed in the all considered Ag nanoclusters that the anionic and neutral nanocluster has similar structural symmetry.

**Table 3.4:** The relaxed geometry of $(AgC)_n^z$ where n=4, 5, 6, and z= 0, 1, 2, and -1, along with average Ag-cytosine binding energy and shape of the core Ag cluster. Binding energy is calculated as the average binding of all ligands.

| No. of atom & ligation | | Neutral | +1 | +2 | -1 |
|---|---|---|---|---|---|
| 5 | Ligated | -0.63 eV | -1.35 eV | -2.33 eV | -0.71 eV |
| | Bare | | | | |
| 6 | Ligated | -0.81 eV | -1.19 eV | -2.05 eV | -0.70 eV |
| | Bare | | | | |

### 3.3.2. Reduction Potential of the Different Size Ag Nanoclusters

Ag nanoclusters are passivated by bond formation with electronegative N atom of nucleobase cytosine. So, electronegative cytosine should have a stronger bond with the electropositive metalcore. The average cytosine binding energy in the different oxidation states is calculated using equation-3.2 and shown in Figure 3.4. Due to increasing the volume of the nanoclusters, the overall charge density decreases with increasing the nanoclusters' size. Therefore, the strength of the bond between electronegative cytosine and electropositive metal nanoclusters decreases with increasing the nanocluster size from 4 to 17. Due to the similar effects, cytosine binding energy is the minimum in the reduced $Ag_4^{-1}$ nanoclusters.
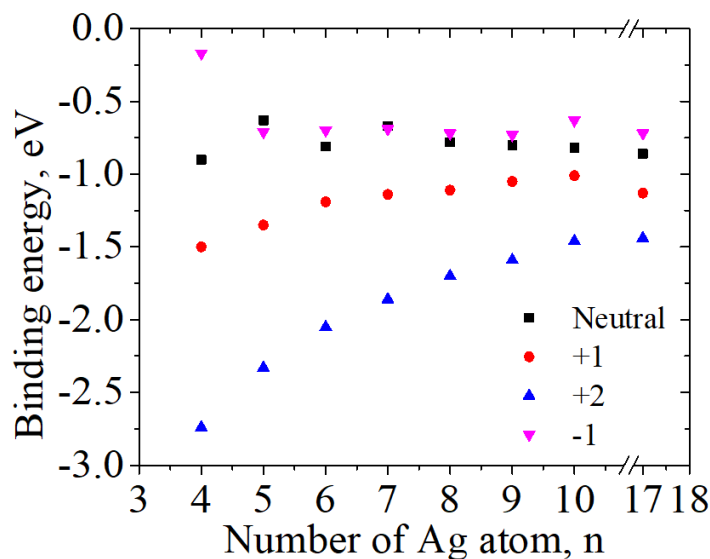
**Figure 3.4**: Average Binding energy of the cytosine in the Ag nanoclusters of the $Ag_4$ to $Ag_{17}$ atom size, calculated by using the equation (3.2).

All the geometries are optimized in the vacuum. The zero-point energy and the thermal correction of the Gibbs free energy of the vacuum optimized geometries are calculated by vibration frequency calculation. Solvation energy is calculated by running a single point calculation of the vacuum optimized geometry using the Conductor polarized model CPCM.[13] The theory of the reduction potential calculations is in the sub-chapter 2.2. The calculated reduction potentials are shown in figure 3.5. First, all considered clusters have negative reduction potential for the +1, +2, and neutral clusters despite reduction potential in bulk silver are positive.[25, 32] Previous theoretical calculation predicted that the smaller nanoclusters' redox potential shows alternative potentials.[31] The odd and even number of Ag in a cluster has alternatively singlet and multiple spins depending on their oxidation states. Since we have calculated the reduction potential of a single electron transfer reaction, all reductions are subjected to spin change from singlet to doublet and vice versa. The overall trend is that all clusters have oxidation potential (negative reduction potential), and it is maximum when a cluster spin changes from doublet to singlet spin. Due to the stronger confinement in smaller

size QDs, an electron transfer reaction has significant effects due to the larger energy splitting.

As a result, the potential difference between the successive oxidation states is higher in the

smaller clusters. So, by increasing the QD size, the energy difference is decreases, which is

minimum in the $Ag_{17}$ clusters.
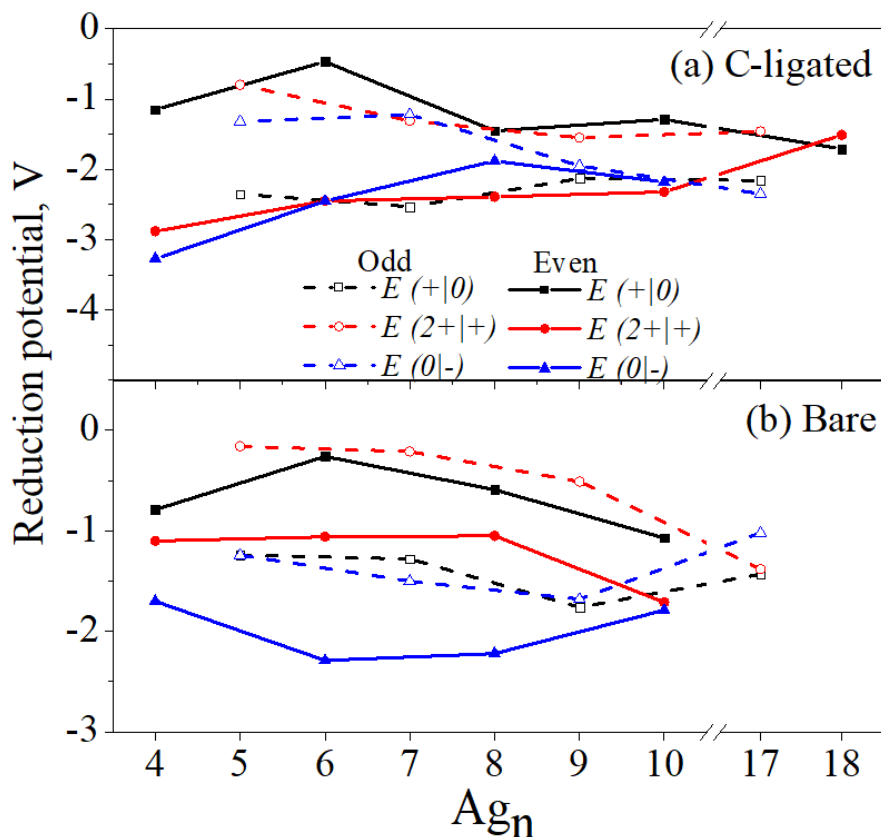


**Figure 3.5**: Calculated reduction potential of the cytosine passivated Ag4-10 and Ag17 clusters (top) and bare Ag4-Ag10 cluster (bottom) in 3 different oxidation states. the black, red, and blue represent reduction half reaction of 1+ to neutral, 2+ to 1+ and neutral to 1- oxidation state respectively. Solid and dash line represents the Ag clusters of the even and odd number of the atom, respectively. **Panel (a)** is a cytosine passivated Ag cluster system, and **panel (b)** is a bare Ag cluster system.

The reduction potential of the bare silver clusters follows a similar trend except for the

negative oxidation states, $E(0|-1)$. In the cytosine passivated Ag clusters, metal core is

electropositive, and cytosines are electronegative nucleobase. Because of electropositive bare Ag

core and absence of electronegative cytosine, the reduction potential of neutral to negative

oxidation state is considerably lower, $E(0|-1)$ (Higher oxidation potential).

### 3.3.3. Effects of Solvation Methods in Redox Potential Calculations

The solvation free energy depends on the Gibbs free energy change of the solute in the

solvent medium and vacuum. Free energy change in solvation can be calculated by using the

equation-2.26. In the case of a charged system, a free energy change should include the surface

potential.[33] In most cases, it was considered that geometry reorganization is minimum, and

therefore solvation free energy can be calculated by equation 2.26. In this section, we have

considered geometry change in the solvent. On the other hand, continuum solvation models are

accurate to predict the solute's electronic structure, and it cannot predict solvation free energy

accurately.[34] It is reported that the continuum solvation model underestimates the anion's

solvation free energy.[33] The cluster-continuum solvation model would able to calculate accurate

solvation energy like explicit solvation in the calculations. The previous report suggested that

free energy calculations are by using the solvation method like SMD-M062X[35] would predict

solvation free energy more accurately than PCM solvation.[36-37]
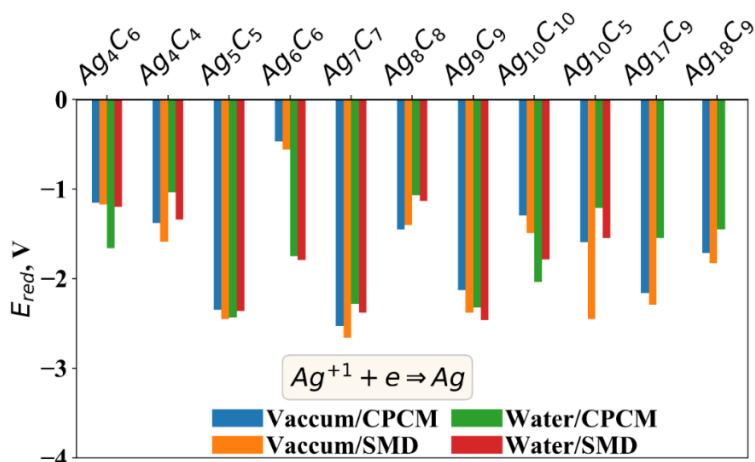


**Figure 3.6**: Reduction potential of the first oxidation ($Ag_n^{+1}|Ag_n$) of the all considered Ag NC,
calculated by four different calculation methods.

71
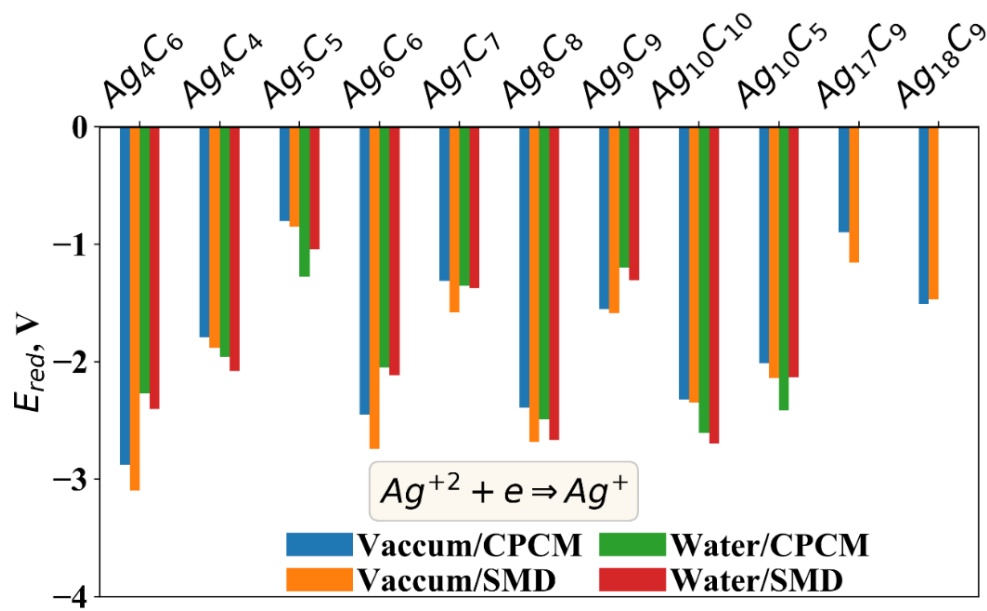
**Figure 3.7**: Reduction potential of the first oxidation ($Ag_n^{+2}|Ag_n^{+1}$) of the all considered Ag NC, calculated by four different calculation methods.
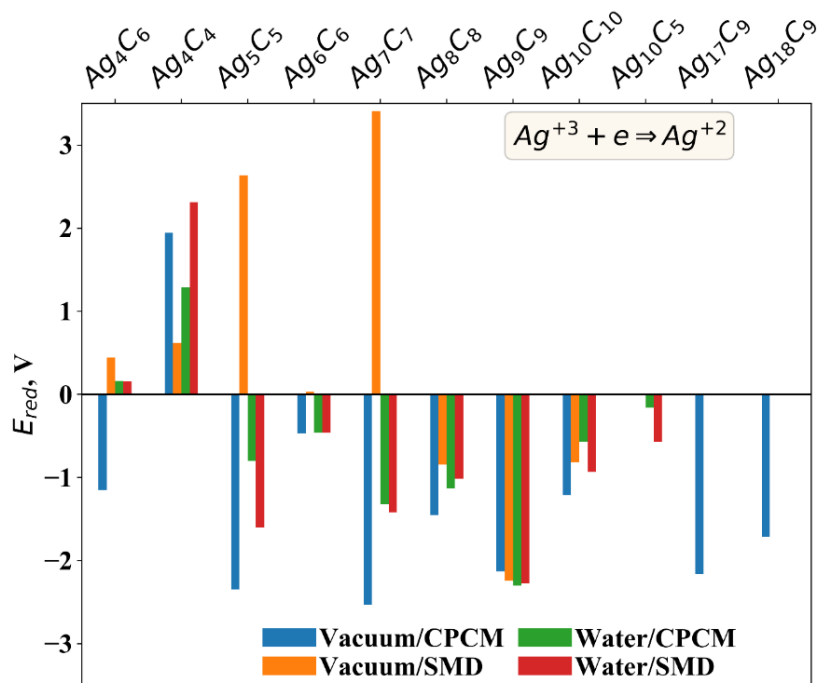


**Figure 3.8**: Reduction potential of the first oxidation ($Ag_n^{+3}|Ag_n^{+2}$) of the all considered Ag NC, calculated by four different calculation methods.
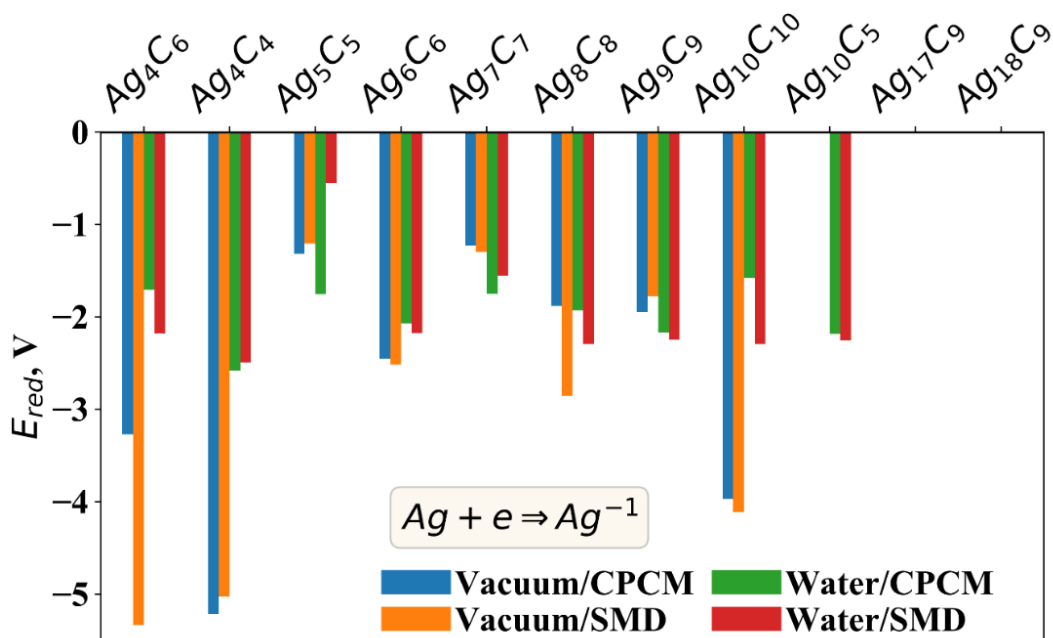
**Figure 3.9**: Reduction potential of the first oxidation ($Ag_n|Ag_n^{+1}$) of the all considered Ag NC, calculated by four different calculation methods.
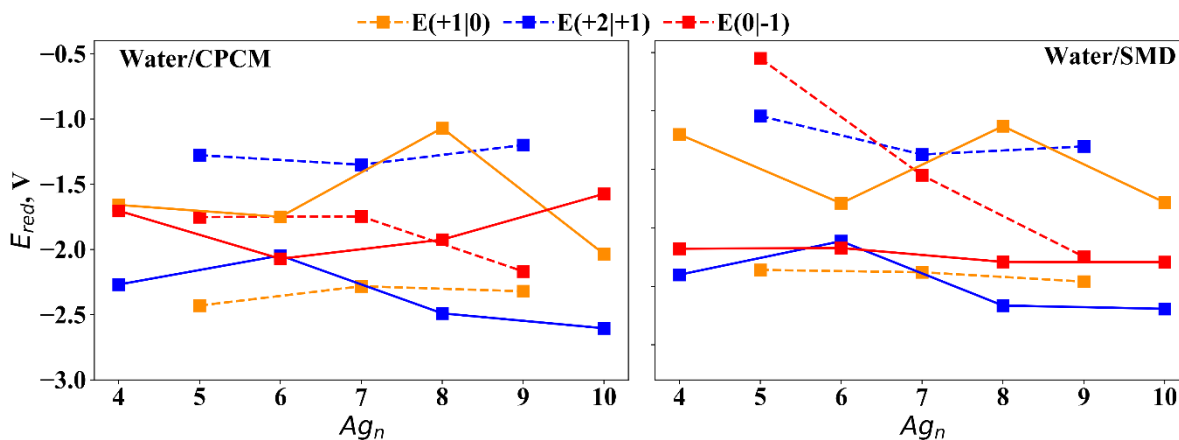


**Figure 3.10**: Calculated reduction potential of the cytosine passivated Ag4-10 from the water optimized geometry and using the CPCM and SMD solvation model. Orange, blue and red represent the reduction half reaction of 1+ to neutral, 2+ to 1+, and neutral to 1- oxidation state. Solid and dash line represents the Ag clusters of the even and the odd number of atoms, respectively.

We have calculated the redox geometry in four different methodologies based on the geometry and solvation free energy. The calculated redox potential calculated in these four different methods is shown in figure 3.6-3.3.9. The first series of redox potential is calculated by

73

optimizing the geometry in the vacuum, and solvation energy calculated by using the CPCM

theory and SMD in the second series. The remaining two sets of the redox potential are

calculated using the optimized geometry with the CPCM method and optimized in the SMD

solvation theory. Comparing these four methods of calculation would provide information on

how a solvation method affects the overall redox potential of the cytosine passivated Ag

nanoclusters.

The significant deviations of the redox potential between the geometry optimized in

vacuum and water are shown in the smaller nanoclusters – $Ag_4$, and in the $Ag_{10}C_5$, where surface

passivation in minimum. The highest deviation in redox potential between the SMD and CPCM

optimized structures are noticed where the stronger cytosine-cytosine hydrogen bond networks

are present ($Ag_5C_5$, $Ag_{10}C_{10}$). On the other hand, Geometry from the optimization in the vacuum

produces comparable or underestimated reduction potential in comparison to optimized geometry

in water. Due to strong confinement and higher surface volume ratio, reorganization energy due

to solvation is significantly higher. Consequently, the solvation energy and free energy change

are overestimated in the vacuum. The redox potential of the higher oxidation state ($Ag_N^{3+}$) is also

negative (positive oxidation potential), except $Ag_4$, $Ag_5$, and $Ag_6$ (Figure 3.8). But in the case of

the $Ag_5$ and $Ag_6$, only the vacuum/SMD method has positive reduction potential. This the

outcome of the unreliable optimized structure of the $Ag_{5,6}^{3+}$ in the vacuum. Due to the higher

positive charge in the small metal cluster, $Ag_4^{3+}$ has positive reduction potential.

**3.3.4. Redox Potential of an Ag Nanocluster Formation and Predicted Conformations**

Using the reduction potential of the nanoclusters, the redox potential of a reaction

between different oxidation states can be determined. If we consider that the synthesis media is a

mixture Ag cluster in different oxidation states, the most favorable oxidation state should have a

higher yield compared to the counterpart. We are considered the following two redox reaction –

$$2Ag_n^0 \rightarrow Ag_n^+ + Ag_n^-$$ (a)
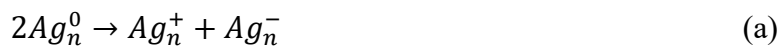
$$2Ag_n^+ \rightarrow Ag_n^{2+} + Ag_n^0$$ (b)

**Table 3.5**: Redox potential of the two model reactions. Net positive redox potential would indicate a spontaneous reaction. $Ag_n$, **n** indicates the number of Ag atom in Ag cluster.

| $Ag_n$ | Redox potential of the model full reaction | |
| | $2Ag_n^0 \rightarrow Ag_n^+ + Ag_n^-$ V/mole | $2Ag_n^+ \rightarrow Ag_n^{2+} + Ag_n^0$ V/mole |
| --- | --- | --- |
| 4 | -2.12 | 1.73 |
| 6 | -1.98 | 1.98 |
| 8 | -0.43 | 0.94 |
| 10 | -2.68 | 1.03 |
| 18 | -- | -0.21 |
| 5 | 1.03 | -1.55 |
| 7 | 1.31 | -1.22 |
| 9 | 0.18 | -0.58 |
| 17 | -0.19 | -1.26 |

The overall redox potential of the reaction of each cluster is shown in Table 3.5. Negative

and positive redox potential is indicating that the backward and forward reaction respectively, is

thermodynamically favorable. Let assume a reaction mixture has 2 moles neutral and 2 moles of

+1 oxidation state Ag nanoclusters. If the size of the nanoclusters is even in number, $Ag_n^{+1}$

converts to the neutral and $Ag_n^{+2}$ by a redox reaction, and the final composition will be 3:1 of the

neutral and +2 nanoclusters. Similar, in the case of odd number clusters, the final composition

will be +1 and -1 oxidation states with the composition of 3:1.

## 3.4. Tuning Charge Transfer Characters by Nucleobase Passivation in Optically Active Transitions of Ag Nanoclusters

We focus on small AgNCs models of 5 and 6 atoms in size, which have been already computationally studied[2], but we include complete encapsulation of clusters with different combinations of C, G, and T passivation, as illustrated in Figure. 1. We also elucidate the effect of conformations, charges, and a polar solvent on the optical spectra of DNA-AgNCs. Our calculations demonstrate that the inclusion of polar media, such as water, drastically changes the shape of clusters and optical spectra of DNA-AgNCs. The lowest optical transitions mainly have charge transfer (CT) character with the main contribution from C bases to AgNCs, while the transitions of CT to the T are relatively dark. On the hand G and T bases increase the average transfer character per C bases in the mixed nucleobase passivated AgNCs. Overall, our results from the extensive analysis of the hole and excited electron state would help to better understand the intrinsic properties of these hybrid DNA-AgNCs chromophores and will complement of experimental data.
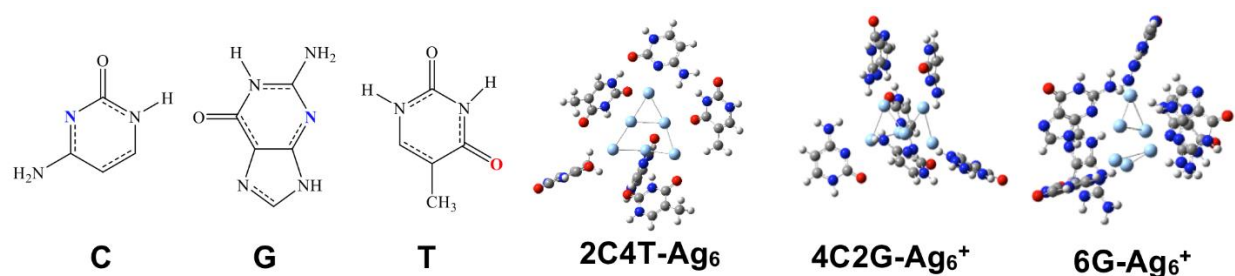


**Figure 3.11**: Chemical structures of three DNA bases: cytosine (C), guanine (G), and thymine (T) and examples of optimized geometries of charged and neutral $Ag_6$ clusters passivated by a different number of C, G and T bases. The colored atoms in schematic representation of bases indicate the atoms coordinated with silver atoms in DNA-AgNCs.

### 3.4.1. Dependence of Base-Cluster Interactions on the Base Type

Since Geom-1 and Geom-3 isomers of charged and neutral **6C**-Ag$_6$ clusters represent two limiting cases for the lowest energy transition being either optically bright or dark, we use both structures as a starting conformation and substitute all six, four, or two cytosines by either guanines (G) or thymine (T) (Table 3.6 and Figure 3.12). Figure 3.13 shows the average binding energy between each base type and Ag$_5$ or Ag$_6$ clusters calculated by equation 3.1 for the most stable isomers of the DNA-AgNC optimized in water. Both Ag$_5$ and Ag$_6$ clusters demonstrate very similar trends in their base-cluster interactions. In the charged clusters, the positive charge is distributed over the metal atoms, which increases the interaction between cationic Ag and electronegative N and O atoms of the bases.[38-39] As a result, the base-AgNC binding energy is typically stronger in charged clusters, compared to their neutral counterparts, Figure 3.12 and Figure 3.13. This trend is the most consistent for cytosines, due to its largest electrostatic dipole moment.[40] Among the considered bases, T-AgNC interaction is the weakest both for neutral and charged clusters, which is rationalized by the smallest dipole moment of T.[40] For the charged clusters, the presence of other base types noticeably reduces the T-AgNC interaction, changing the binding energy from -0.3 eV to -0.05 eV. Such weak binding energy together with high flexibility due to the small size of the thymine, suggest that thymines are likely not contributing to the coordination of AgNC, when strongly interacting cytosines and guanines are available in a DNA strand.

**Table 3.6**: The difference between the total energies of the isomers obtained from the initial Geom-1 and Geom-3 structures of neutral and charged $Ag_6$ clusters passivated by various bases in water. The values are obtained using the formula: $\Delta E_{tot} = E_{tot}(\text{Geom-1}) - E_{tot}(\text{Geom-3})$.

| Passivating Bases | Neutral Clusters | | +1 Charged Clusters | |
|---|---|---|---|---|
| | $\Delta E_{tot}$ (eV) | The Most Stable Isomer | $\Delta E_{tot}$ (eV) | The Most Stable Isomer |
| 6C | 0.30 | Geom-3 | 0.11 | Geom-3 |
| 6G | -0.01 | Geom-1 | 0.29 | Geom-3 |
| 6T | -0.71 | Geom-1 | -0.76 | Geom-1 |
| 4C2G | -0.10 | Geom-1 | 0.16 | Geom-3 |
| 4C2T | -1.05 | Geom-1 | -0.04 | Geom-1 |
| 2C4T | -0.38 | Geom-1 | 0.65 | Geom-3 |
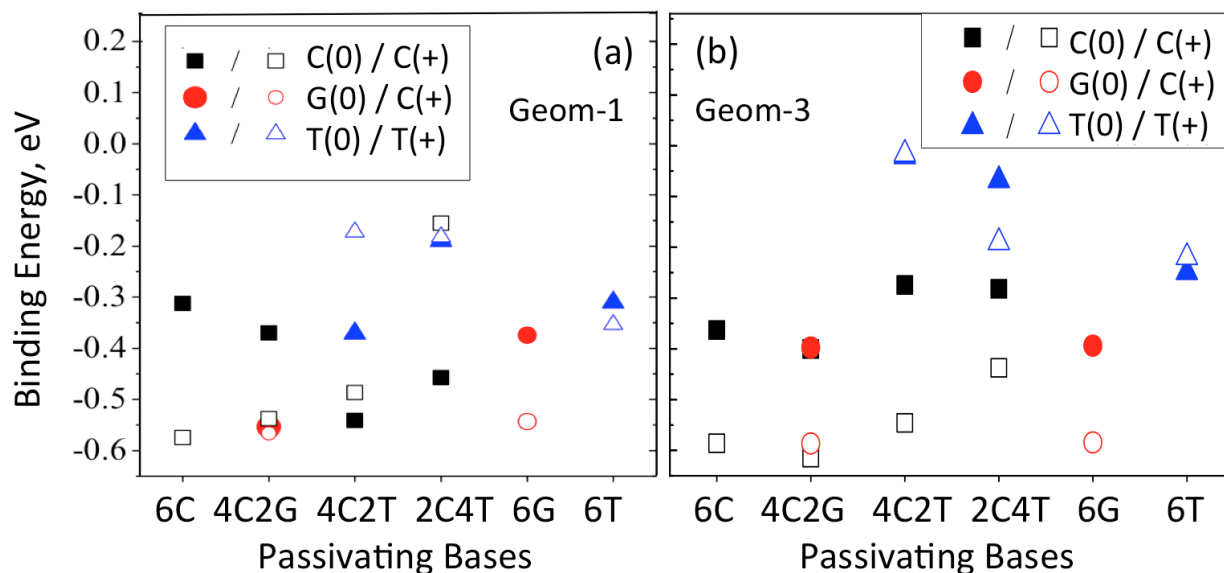


**Figure 3.12:** The binding energies of the cytosine (black squares), guanine (red circles), and thiamine (blue triangles) bases to $Ag_6$ cluster in water. The geometry of each DNA-AgNC is optimized, starting with the Geom-1 **(a)** or Geom-3 **(b)** conformations of **6C-**$Ag_6$ in water with substituted C by T or G bases. Solid and empty symbols correspond to neutral and +1 charged clusters, respectively.
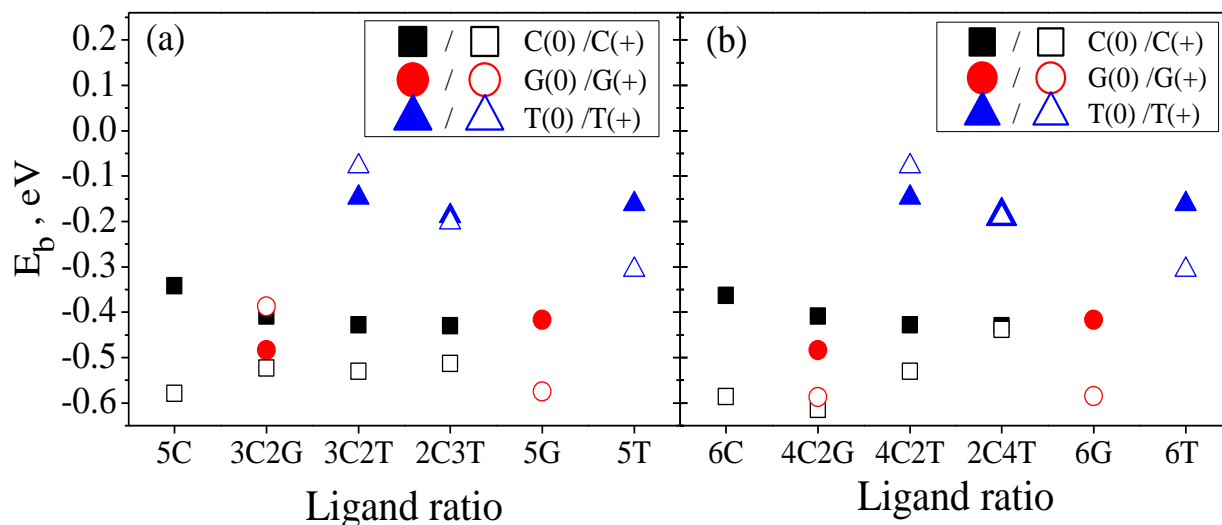
**Figure 3.13:** The binding energy of cytosine, guanine, and thymine to $Ag_5$ **(a)** and $Ag_6$ **(b)** clusters in water. The most stable isomer of each DNA-AgNC is chosen from the optimized geometry started with either the Geom-3 or Geom-1 structures of neutral and charged **6C-**$Ag_6$ and **5C-**$Ag_5$ in water with all or several C substituted by T or G. Neutral cluster are depicted by solid symbols and charged clusters by empty symbols. The X-axis indicates the number and types of bases passivating the cluster.

While strongly interacting (from -0.6 to -0.5 eV), cytosines also show some decrease in their interactions with the AgNC when other bases passivate the charged cluster. This trend can be rationalized by a reduced number of hydrogen bonds between bases of different types, which have larger contributions for charged systems compared to neutral clusters in water, Table 3.3. In contrast, for neutral clusters, the C-AgNC and G-AgNC interactions are enhanced due to other bases. It is known that the dipole moment of a base noticeably changes depending on its location in the DNA sequence or codons[40] and the ionization potential of the nucleotide base pairs.[20] Thus, the dipole moment of G significantly increases when it is paired with C, CC, or CT, compared to GGG. The dipole moment of C also increases when it is paired with T, G, TT, or GG, compared to CCC.[40] By analogy, a presence of other bases at the surface of the AgNC in close proximity to C or G increases the dipole moment of these bases resulting in their stronger interactions with the cluster. Overall, the strength of interactions of cytosines and guanines with

AgNCs is comparable, with a very slight enhancement for guanines. It is important to note that for charged clusters **6G**-$Ag_6^+$ and **4C2G**-$Ag_6^+$, a strong dipole moment along with a relatively larger size of guanines results in the formation of two $Ag_3$ sub-clusters that are held together by weak base-base interactions via hydrogen bonds, Figure 3.11. This result suggests that despite a strong G-AgNC binding energy, the charged clusters coordinated by guanines are less stable compared to those coordinated by cytosines and likely dissociate into several smaller clusters under thermal fluctuations.

### 3.4.2. Effect of Different Bases on Optical Response of Clusters

Absorption spectra of $Ag_6$ and $Ag_6^+$ clusters passivated by various bases for the most stable isomers in water are shown in Figure 3.14. The spectra for all calculated structures are represented in Figures. 3.15-3.17. For all neutral clusters, one can resolve five main absorption bands: (I) a weak peak (or a shoulder) at 2.0-2.5 eV, (II) an intensive peak at ~ 3 eV, (III) another intensive peak at ~3.5 eV, which degree of overlapping with the neighboring peak depends on the passivating bases, (IV) a less intensive and broader band at 4.0-4.7 eV, and (V) a highly intensive peak at ~5.2 eV, Figure 3.14a and b and Figure. 3.15. While the relative intensity, width, and energy of the peak maximum are slightly changing depending on the passivating bases and conformations, the overall spectral shape with these well-resolved bands is consistent for all structures. Interestingly, experimental spectra of bigger $Ag_{10}^{6+}$ cluster formed by repeated CCX sequences where $X \neq C$ show similar lower energy absorption bands with a weak band at 2.25-2.50 eV followed by a strong sub-structured band at 2.75-3.50 eV, with the intensity of the first peak being more sensitive to the sequences and the length of the encapsulated strand.[41]
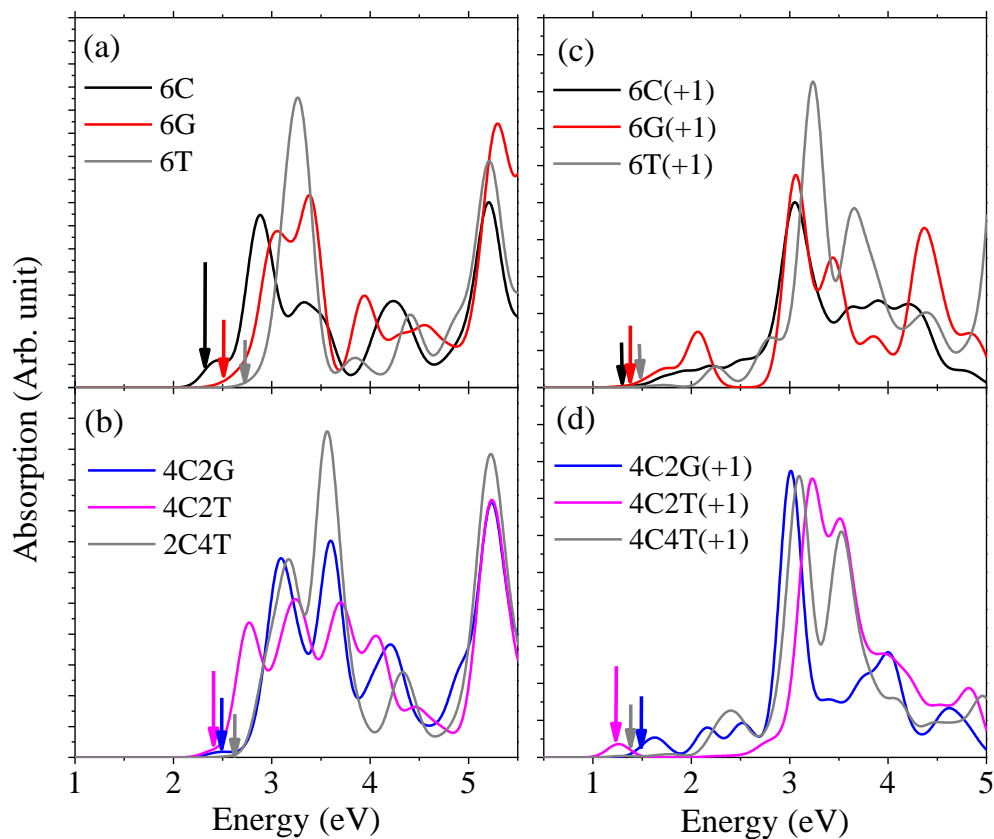
**Figure 3.14:** Absorption spectra of $Ag_6$ and $Ag_6^+$ clusters passivated by various bases in water. For these spectra, the most stable isomer is chosen from the optimized geometry started with either the Geom-3 or Geom-1 structures of $6C$-$Ag_6$ **(a)** and **(b)** and $6C$-$Ag_6^+$ **(c)** and **(d)** in water with all **(a)** and **(c)** or several C **(b)** and **(d)** substituted by T or G. Vertical arrows indicate the lowest energy optical transition. The height of arrows represents the relative intensity of these transitions.
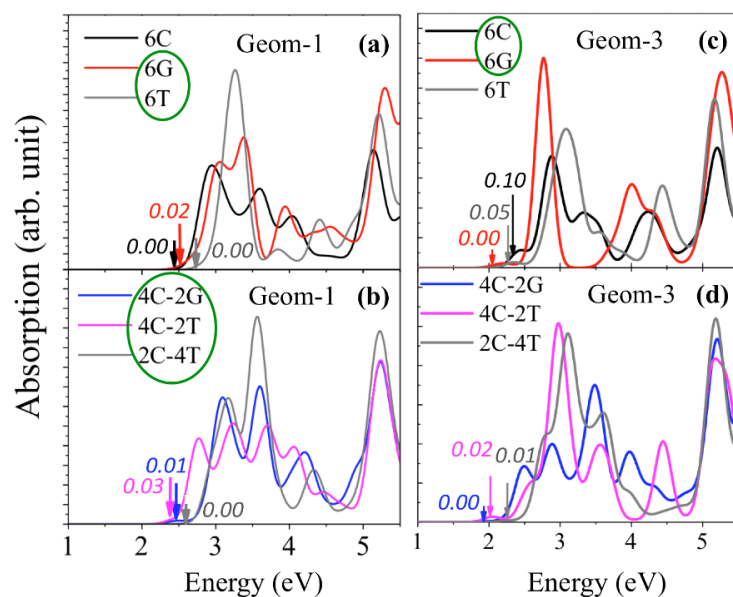
**Figure 3.15:** Absorption spectra of neutral Ag$_6$ clusters passivated by various bases in water using the optimized geometry started with either the Geometry-1 **(a)** and **(b)** or Geometry-3 **(c)** and **(d)** of 6C-Ag$_6$ with all **(a)** and **(c)** or several C **(b)** and **(d)** substituted by T or G. Vertical arrows indicate the lowest energy optical transitions. The height of arrows represents the relative intensity of these transitions. Green ovals indicate the structures with the lowest total energy, according to Table 3.6.
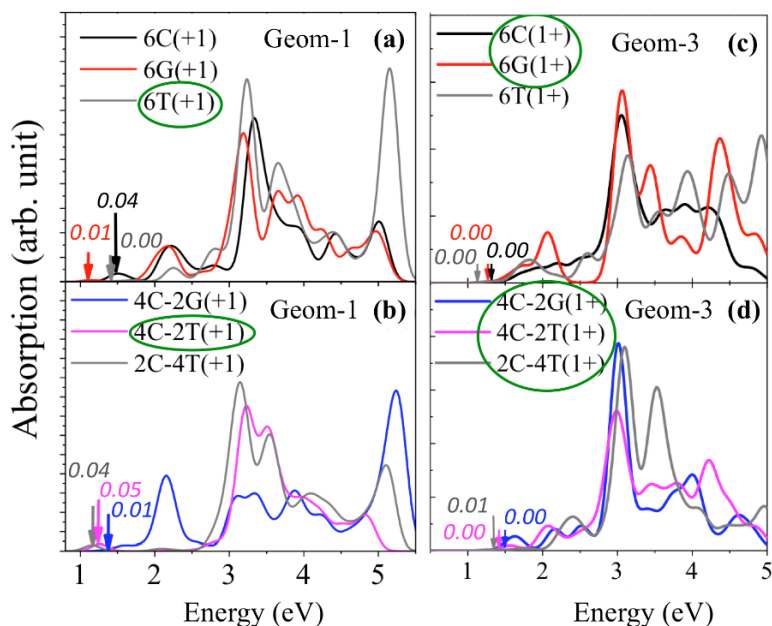


**Figure 3.16:** Absorption spectra of charged Ag$_6^+$ clusters passivated by various bases in water using the optimized geometry started with either the Geometry-1 **(a)** and **(b)** or Geometry-3 **(c)** and **(d)** of 6C-Ag$_6^+$ with all **(a)** and **(c)** or several C **(b)** and **(d)** substituted by T or G. Vertical arrows indicate the lowest energy optical transitions.
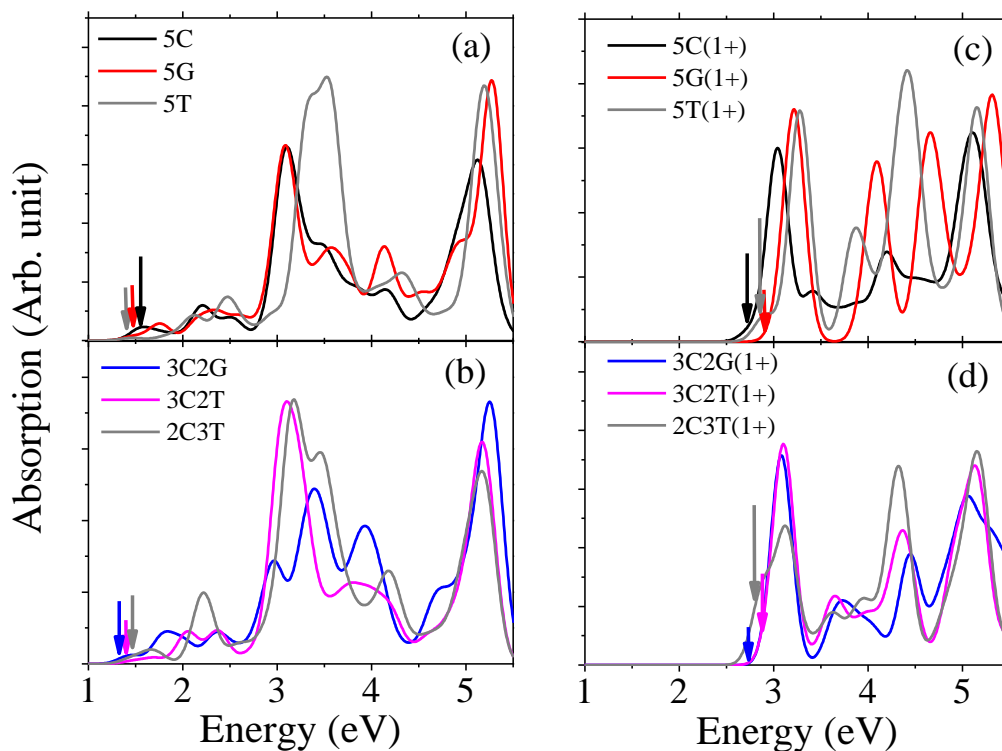
**Figure 3.17**: Absorption spectra of neutral $Ag_5$ **(a)** and **(b)** and charged $Ag_5^+$ **(c)** and **(d)** clusters passivated by different bases in water using the optimized geometries started with Geometry-1 of 5C-$Ag_5$ or 5C-$Ag_5^+$ with all **(a)** and **(c)** or several C **(b)** and **(d)** substituted by T or G. Vertical arrows indicate the lowest energy optical transition.

These bands are also well pronounced in the calculated spectra of charged $Ag_6^+$ clusters, almost independent on the passivated bases and conformations. However, for charged clusters, an additional optically weak band appears at the lower energy range of 1.0-2.0 eV, Figure 3.14c and d and Figure. 3.16. Similar bands nearly at the same energy ranges are observed for spectra of $Ag_5$ and $Ag_5^+$ clusters passivated by various bases, but with the reverse trend for neutral and charged clusters: $Ag_5$ exhibits an additional red-shifted weak peak at 1.0-2.0 eV, while the spectra of $Ag_5^+$ exclude this band, Figure 3.17. This reverse trend of spectra between charged and neutral $Ag_5$ and $Ag_6$ clusters are rationalized by the difference in the spin multiplicity of transitions contributing to these optical bands. The absorption spectra of the closed shell $Ag_5^+$ and $Ag_6$ systems are governed by singlet transitions, while doublet transitions contribute to

spectra of the open shell $Ag_5$ and $Ag_6^+$ clusters. Thus, the doublet transitions of clusters with open shell electronic structure result in the red-shifted optically weak band at the energy $< 2.5$ eV, almost independent of the cluster size (5 or 6 atoms), its conformation, and the passivating bases. However, its intensity and the energy of its peak maximum are sensitive to the base type.

It has been computationally predicted and experimentally detected that the lowest excited states in small emissive AuNCs[42, 43,] and AgNCs[39, 44, 45] passivated by various ligands often have the ligand-to-metal charge transfer (LMCT) or metal-to-ligand charge transfer (MLCT) character. Our calculations demonstrate that the stable isomer of **6C-**$Ag_6$ has the most intensive first optical transition compared to other stable structures of $Ag_6$ passivated by different bases. This difference is rationalized by the highest MLCT character of this transition, with the hole mainly originated from the metal, while electron density is contributed from both metal atoms and cytosines, as evidenced from NTOs depicted in **Table 3.7 and Table 3.8**. Changing all or several cytosines to guanines or thymines reduces ligand contribution to the lowest transition and, thus, decreases the MLCT character, which results in the reduced intensity of these transitions. For higher energy optical transitions contributing to the second and third peaks at the energy range of 2.5-3.5 eV, this trend is the same: optically active transitions with the largest oscillator strength exhibit higher MLCT character with a significant portion of the electron density distributed over the base bearing $\pi^*$ character, **Table 3.7** and **Table 3.9**.

**Table 3.7:** Natural transition orbitals showing the contributions of the electron-hole pair to the transitions with the lowest energy (S₁) and with the largest oscillator strength (*Os. Str.*) at the energy range of 2.5-3.5 eV of the neutral Ag₆ clusters passivated by different bases in water with the most stable conformations.
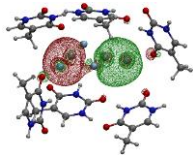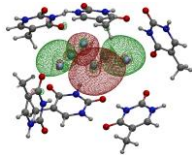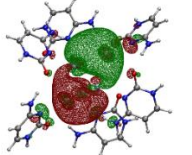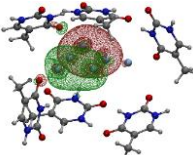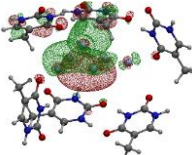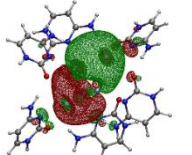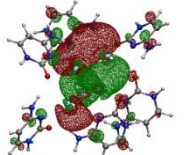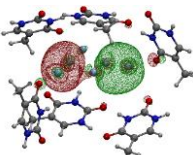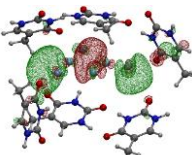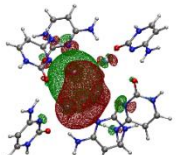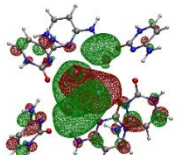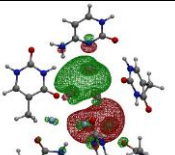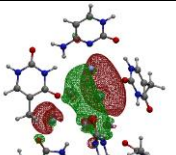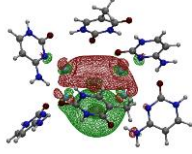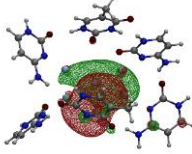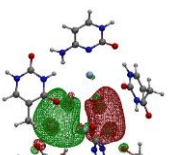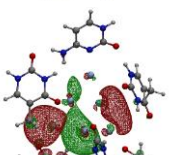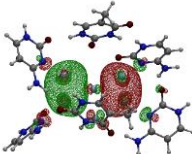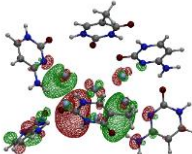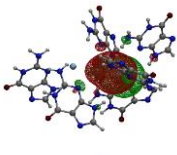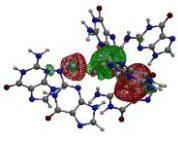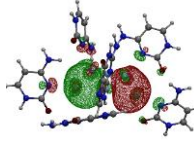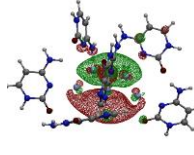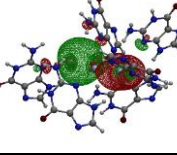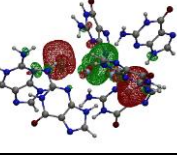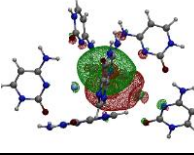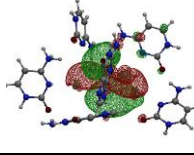
| State E (eV) *Os. Str.* | Hole | Electron | State E (eV) $f_{os}$ | Hole | Electron |
|---|---|---|---|---|---|
| **6T** | | | **6C** | | |
| S₁ 2.64 eV *0.0014* | | | S₁ 2.38 *0.0935* | | |
| S₆ 3.18 eV *0.6339* | | | S₂ 2.50 eV *0.0922* | | |
| S₈ 3.33 eV *1.1471* | | | S₅ 2.82 eV *0.4517* | | |
| **2C4T** | | | **4C2T** | | |
| S₁ 2.56 eV *0.0024* | | | S₁ 2.41 eV *0.0300* | | |
| S₆ 3.20 eV *0.7731* | | | S₈ 3.30 eV *0.4403* | | |
| **6G** | | | **4C2G** | | |
| S₁ 2.51 eV *0.0171* | | | S₁ 2.42 eV *0.0126* | | |
| S₄ 2.98 eV *0.7135* | | | S₆ 3.09 eV *0.7158* | | |

**Table 3.8:** NTOs showing the electron and hole contributions to the first optical transitions of the neutral $Ag_6$ and charged $Ag_6^+$ clusters passivated by different bases in water (only C, G, and T). The structures were obtained either from the optimized Geom-1 or Geom-3.
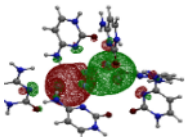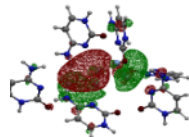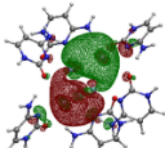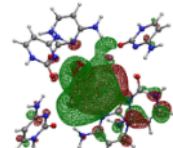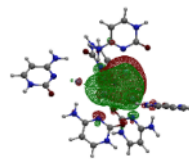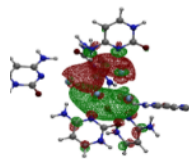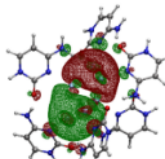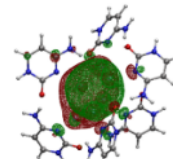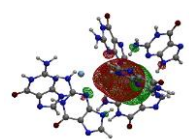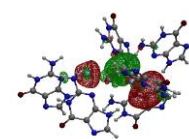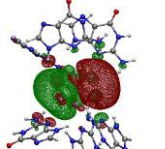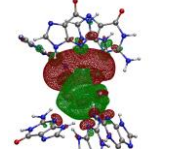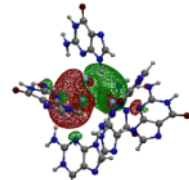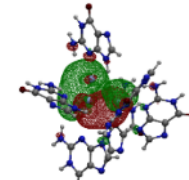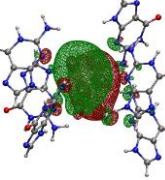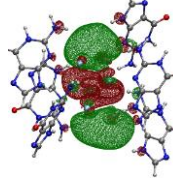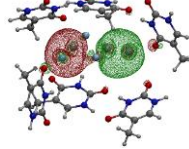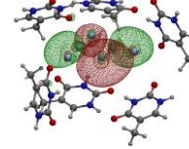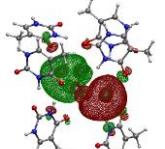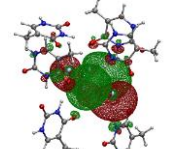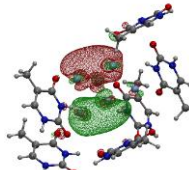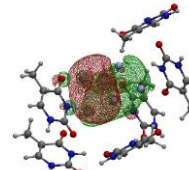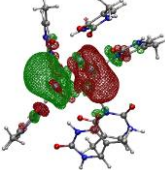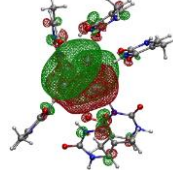
| Geom-1 | | | Geom-3 | | |
|---|---|---|---|---|---|
| State E (eV) $f_{os}$ | Hole | Electron | State E (eV) $f_{os}$ | Hole | Electron |
| **6C** $S_1$ 2.49 eV *0.0034* | | | **6C** $S_1$ 2.38 eV *0.0955* | | |
| **6C(+1)** $S_1$ 1.47 eV *0.0351* | | | **6C(+1)** $S_1$ 1.32 eV *0.0015* | | |
| **6G** $S_1$ 2.51 eV *0.0171* | | | **6G** $S_1$ 2.02 eV *0.0026* | | |
| **6G(+1)** $S_1$ 1.14 eV 0.0098 | | | **6G(+1)** $S_1$ 1.32 eV *0.0042* | | |
| **6T** $S_1$ 2.64 eV *0.0014* | | | **6T** $S_1$ 2.33 eV *0.0448* | | |
| **6T(+1)** S1 1.45 eV *0.0004* | | | **6T(+1)** $S_1$ 1.16 eV *0.0011* | | |

**Table 3.8:** NTOs showing the electron and hole contributions to the first optical transitions of the neutral $Ag_6$ and charged $Ag_6^+$ clusters passivated by different bases in water (Mix passivation of C, G and T) (continued). The structures were obtained either from the optimized Geom-1 or Geom-3.
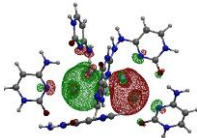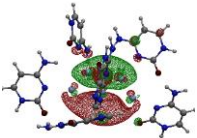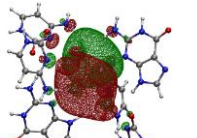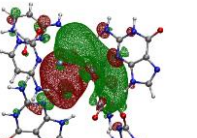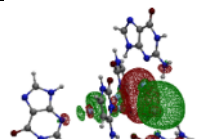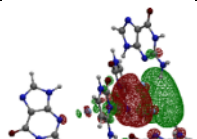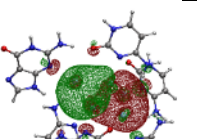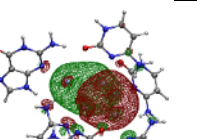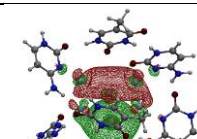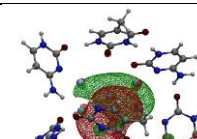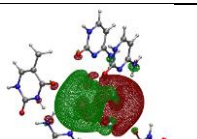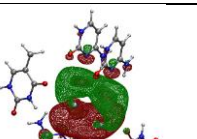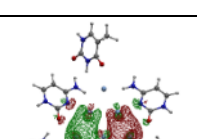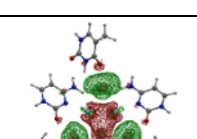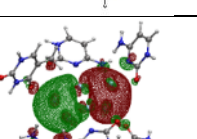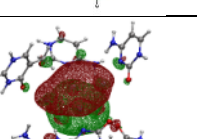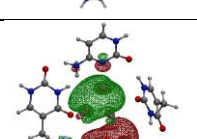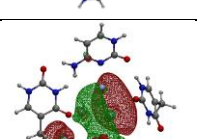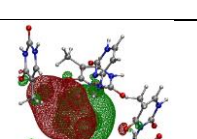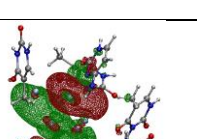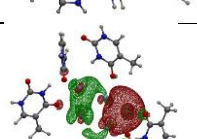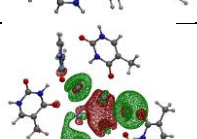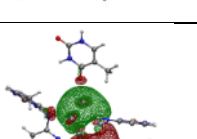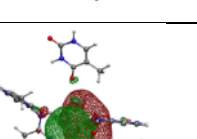
| Geom-1 | | | Geom-3 | | |
|---|---|---|---|---|---|
| State<br>E (eV)<br>$f_{os}$ | Hole | Electron | State<br>E (eV)<br>$f_{os}$ | Hole | Electron |
| **4C2G**<br>$S_1$<br>2.42 eV<br>*0.0126* |  |  | **4C2G**<br>$S_1$<br>1.96 eV<br>*0.0044* |  |  |
| **4C2G(+1)**<br>$S_1$<br>1.37 eV<br>0.0078 |  |  | **4C2G(+1)**<br>$S_1$<br>1.45 eV<br>0.0003 |  |  |
| **4C2T**<br>$S_1$<br>2.41 eV<br>*0.0300* |  |  | **4C2T**<br>$S_1$<br>2.01 eV<br>*0.0176* |  |  |
| **4C2T(+1)**<br>$S_1$<br>1.26eV<br>0.0510 |  |  | **4C2T(+1)**<br>$S_1$<br>1.34 eV<br>0.0011 |  |  |
| **2C4T**<br>$S_1$<br>2.56 eV<br>*0.0024* |  |  | **2C4T**<br>$S_1$<br>2.22 eV<br>*0.0108* |  |  |
| **2C4T(+1)**<br>$S_1$<br>1.16 eV<br>*0.0425* |  |  | **2C4T(+1)**<br>$S_1$<br>1.30 eV<br>0.0054 |  |  |

**Table 3.9**: NTOs showing the electron and hole contributions to the most optically intensive transitions at the energy range of 2.70 - 3.50 eV, of the neutral $Ag_6$ and charged $Ag_6^+$ clusters passivated by different bases in water (C, G, and T). The structures were optimized either from the Geom-1 or Geom-3.

| Geom-1 | | | Geom-3 | | |
|---|---|---|---|---|---|
| State<br>E (eV)<br>$f_{os}$ | Hole | Electron | State<br>E (eV)<br>$f_{os}$ | Hole | Electron |
| **6C**<br>$S_5$<br>2.80 eV<br>*0.5017* |  |  | **6C**<br>$S_5$<br>2.82 eV<br>*0.4517* |  |  |
| **6C(+1)**<br>$S_{17}$<br>3.31 eV<br>0.7090 |  |  | **6C(+1)**<br>$S_{16}$<br>2.99 nm<br>*0.3995* |  |  |
| **6G**<br>$S_4$<br>2.98 eV<br>*0.7135* |  |  | **6G**<br>$S_7$<br>2.77 eV<br>*1.0670* |  |  |
| **6G(+1)**<br>$S_{10}$<br>3.00 eV<br>0.1536 |  |  | **6G(+1)**<br>$S_{10}$<br>3.05 eV<br>*0.7289* |  |  |
| **6T**<br>$S_6$<br>3.18 eV<br>*0.6339* |  |  | **6T**<br>$S_7$<br>3.06 eV<br>*0.8707* |  |  |
| **6T**<br>$S_8$<br>3.33 eV<br>*1.1471* |  |  | | | |
| **6T(+1)**<br>$S_{15}$<br>3.22 eV<br>*0.3383* |  |  | **6T(+1)**<br>$S_{19}$<br>3.14 eV<br>*0.2184* |  |  |

**Table 3.9**: NTOs showing the electron and hole contributions to the most optically intensive transitions at the energy range of 2.70 - 3.50 eV, of the neutral $Ag_6$ and charged $Ag_6^+$ clusters passivated by different bases in water (mix of C, G, and T bases) (continued). The structures were optimized either from the Geom-1 or Geom-3.

| Geom-1 | | | Geom-3 | | |
|---|---|---|---|---|---|
| State<br>E (eV)<br>$f_{os}$ | Hole | Electron | State<br>E (eV)<br>$f_{os}$ | Hole | Electron |
| **4C2G**<br>$S_6$<br>3.09 eV<br>*0.7158* |  |  | **4C2G**<br>$S_7$<br>2.88 eV<br>*0.4228* |  |  |
| **4C2G(+1)**<br>$S_6$<br>2.17 eV<br>0.2609 |  |  | **4C2G(+1)**<br>$S_{15}$<br>3.00 eV<br>*0.8107* |  |  |
| **4C2G(+1)**<br>$S_{13}$<br>3.08 eV<br>0.3475 |  |  | | | |
| **4C2T**<br>$S_8$<br>3.30 eV<br>*0.4403* |  |  | **4C2T**<br>$S_7$<br>2.94 eV<br>*0.6444* |  |  |
| **4C2T(+1)**<br>$S_{13}$<br>3.21 eV<br>0.8059 |  |  | **4C2T(+1)**<br>$S_{16}$<br>2.94 eV<br>*0.4276* |  |  |
| **2C4T**<br>$S_6$<br>3.20 eV<br>*0.7731* |  |  | **2C4T**<br>$S_7$<br>3.04 eV<br>*0.5389* |  |  |
| **2C4T(+1)**<br>$S_{11}$<br>3.17 eV<br>*0.7935* |  |  | **2C4T(+1)**<br>$S_{17}$<br>3.10 eV<br>*0.9352* |  |  |
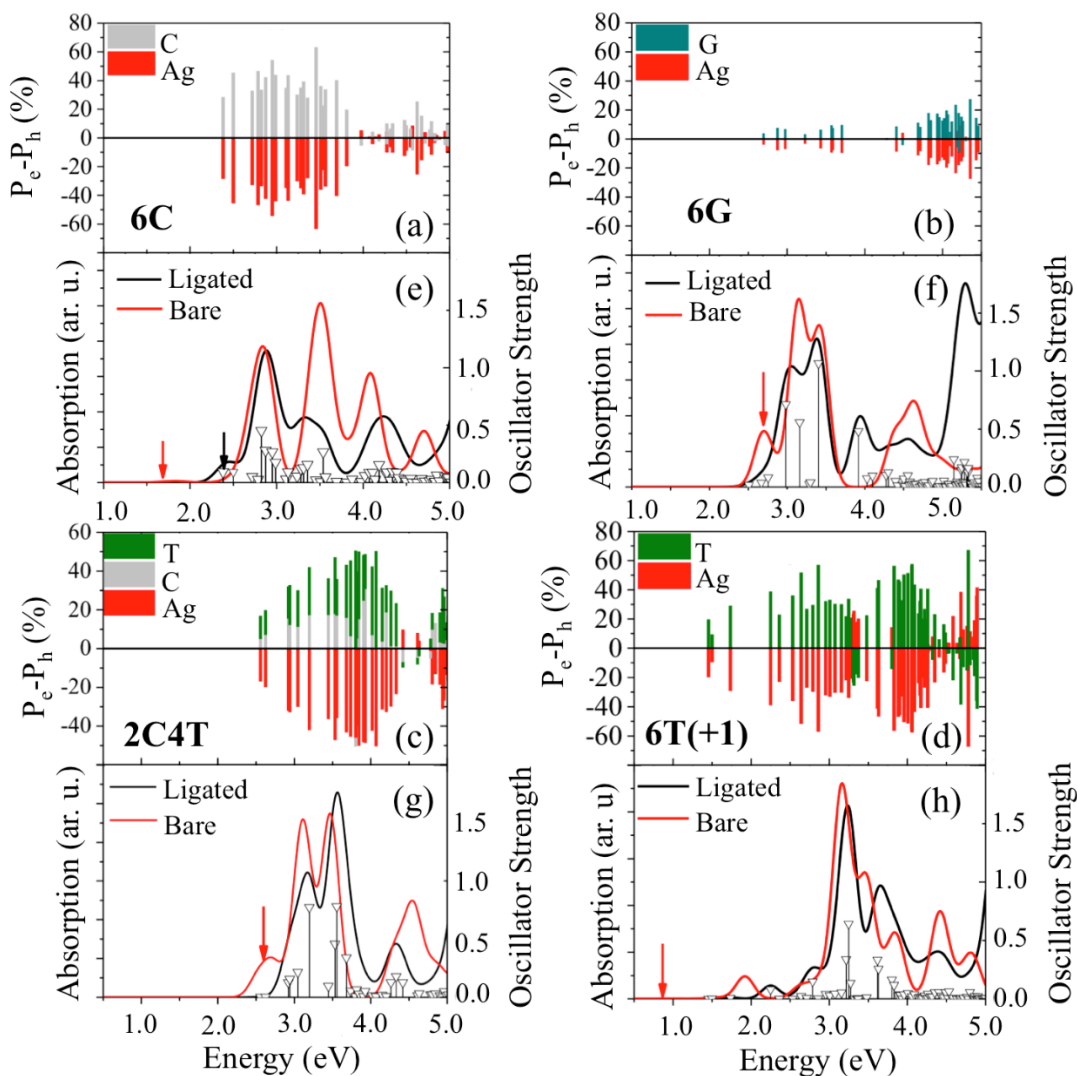
**Figure 3.18**: Absorption spectra and percent of charge transfer in each optical transition of the neutral $Ag_6$ and charged $Ag_6^+$ clusters passivated 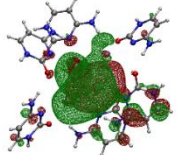by different bases in water with the most stable conformations. **(a)-(d)** The degree of charge transfer, $P_e$-$P_h$, for each optical transition defined as a difference between projections of unoccupied (electron) and occupied (hole) orbitals projected to the base C (grey), G (teal), or T (green) and the Ag cluster (red). *(e)-(h)* Absorption spectra of the optimized clusters passivated by bases (black lines) and the bare cluster with eliminated bases but preserving the same geometry as it has in the passivated structures (red line). Vertical black lines with triangle heads identify the oscillator strength of each optical transition contributing to the absorption spectra of the passivated clusters. The values of the oscillator strength are represented on the right Y-axis. Red arrows indicate the lowest energy transition of the cluster of nucleobases removed.

**Figure 3.18 and Figures 3.19 and 3.20** quantitatively represent the degree of charge

transfer for each transition obtained for the most stable conformations of the charged and neutral

$Ag_6$ clusters passivated by different bases. The degree of charge transfer, $D_m = P_e - P_h$, is

90

identified as a difference between electron and hole orbitals contributing to the excited state $m$ and integrated over the base or the AgNC fragments, as defined by **equation 2.33 and 3.34**. Negative values of $D_m$ indicate the charge transfer from the fragment, and positive $D_m$ indicate the charge transfer to the fragment. As a result, $D_m$ presented as vertical sticks in Figure 5 and Figures S7 and S8 are mirror images of positive and negative values. Very small $|D_m|$ indicates that transitions have negligible CT character and are mainly metal-to-metal or base-to-base ($\pi$-$\pi^*$) transitions.
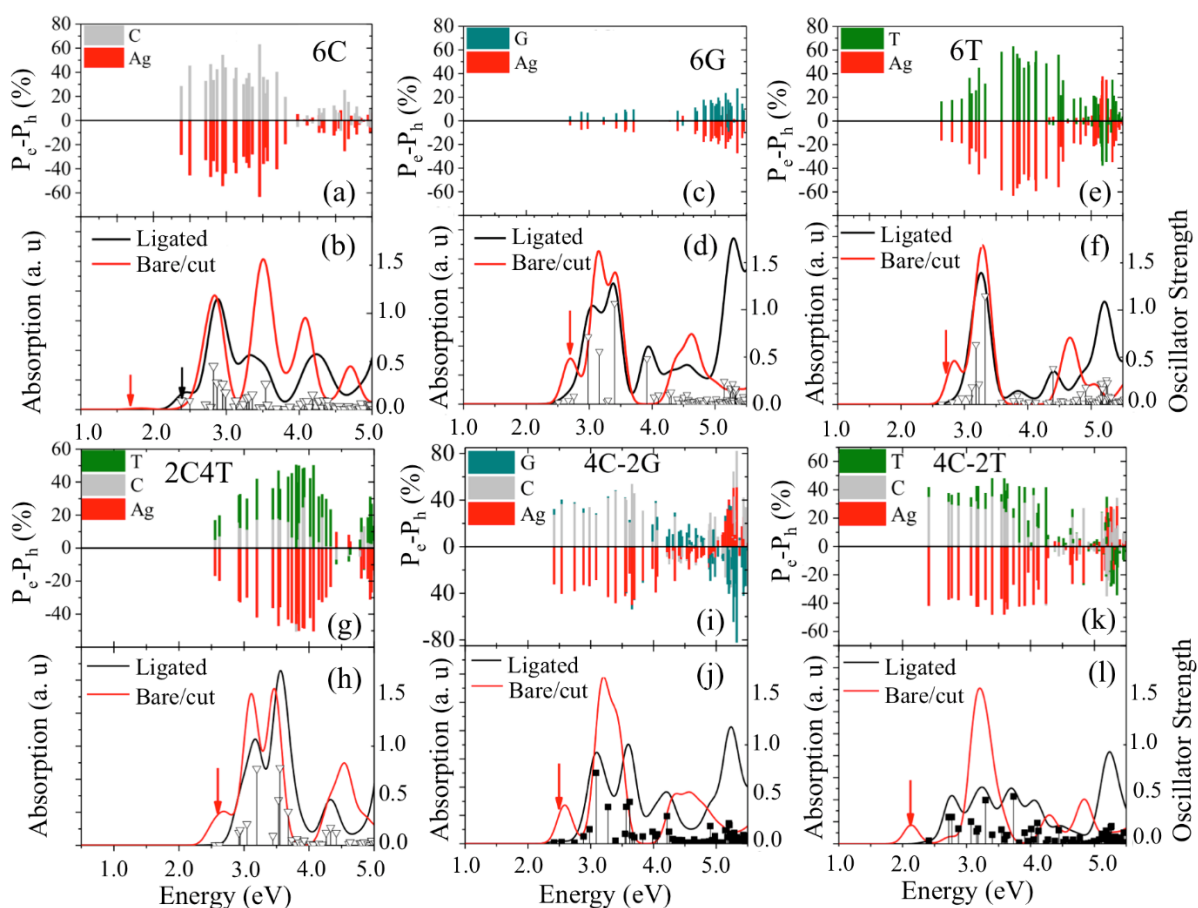


**Figure 3.19:** Absorption spectra and percent of charge transfer in each optical transition of the neutral $Ag_6$ clusters passivated by different bases with the most stable conformations. Panels **(a)**, **(c)**, **(e)**, **(g)**, **(i)**, and **(k)** show the degree of charge transfer, $D_m = P_e - P_h$, for each optical transition projected to the base C (grey), or T (green), or G (teal) and the Ag cluster (red). Panels **(b)**, **(d)**, **(f)**, **(h)**, **(j)**, and **(l)** show absorption spectra of the optimized $Ag_6$ clusters passivated by bases (black lines) and the core $Ag_6$ cluster after removing the bases (red line).
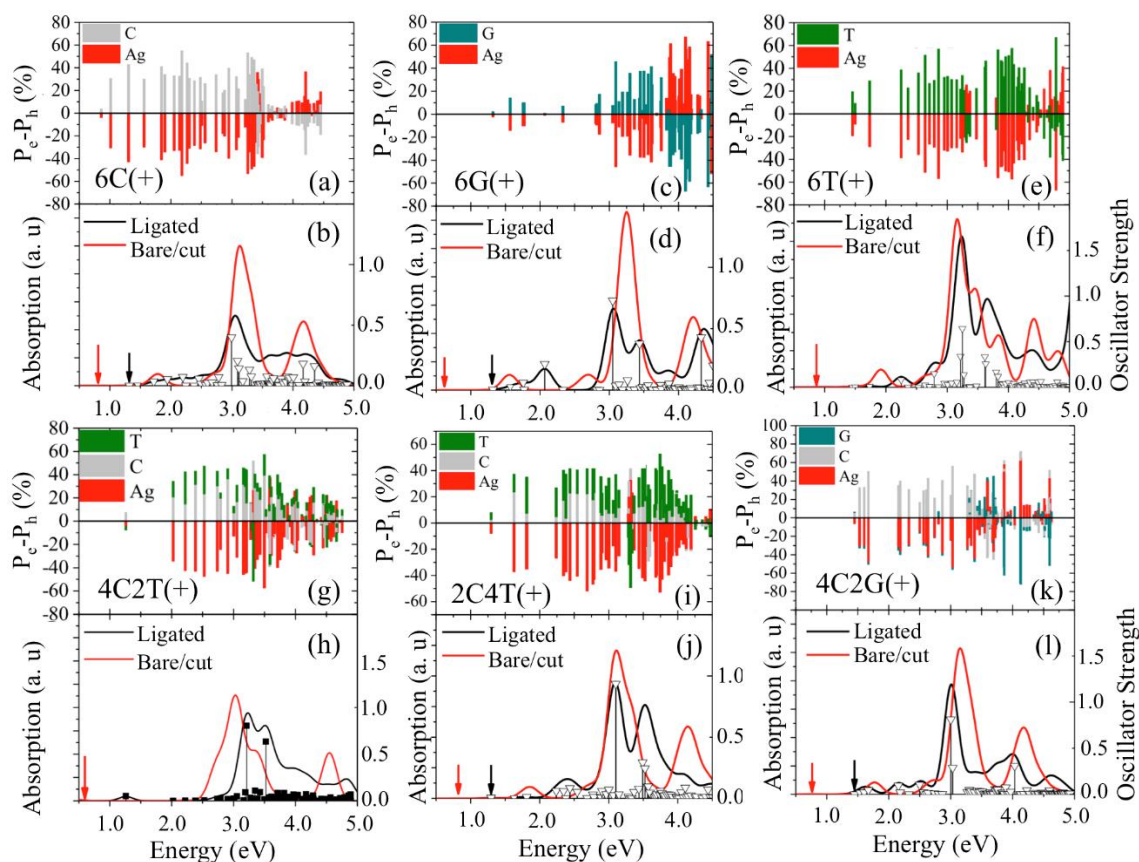
**Figure 3.20:** Absorption spectra and percent of charge transfer in each optical transition of the neutral $Ag_6^+$ clusters passivated by different bases with the most stable conformations. Panels **(a)**, **(c)**, **(e)**, **(g)**, **(i)**, and **(k)** show the degree of charge transfer, $D_m = P_e - P_h$, for each optical transition projected to the base C (grey), or T (green), or G (teal) and the Ag cluster (red). Panels **(b)**, **(d)**, **(f)**, **(h)**, **(j)**, and **(l)** show absorption spectra of the optimized $Ag_6$ clusters passivated by bases (black lines) and the core $Ag_6$ cluster after removing the bases (red line).

For all structures, according to this analysis, optical transitions with energies < 4 eV exhibit a noticeable degree of MLCT character from 20% to 60%. The lowest energy transitions have the largest degree of MLCT (up to ~40%) for **6C-**$Ag_6$ and the smallest for **6G-**$Ag_6$ (<10 %), Figure 3.18a-d. The absorption bands at ~3.5 eV have the largest MLCT character up to 60% for all structures, except **6G-**$Ag_6$ that has the MLCT degree < 20% for all transitions at this energy range, Figure 3.19. In contrast to all other neutral clusters, the optical bands at 2.5-3.5 eV of **6G-**$Ag_6$ are predominantly metal-to-metal transitions, including highly intensive transitions, which is also confirmed by NTOs depicted in Table 3.7. It is important to note that the MLCT character

92

of the lowest transitions increases when guanines or thymines are accompanied by cytosines (**4C2G-** and **4C2T-**Ag$_6$), Figure 3.19. This increase in an MLCT character is reflected in higher intensities of these transitions compared to those of **6G**-, **6T**-, and **2C4T**- Ag$_6$, Figure 3.14a-b. However, the MLCT character mainly originates from cytosines (~30%), with less than 10% contributions from other bases. Thus, cytosines maintain the MLCT character of the lowest energy transitions in a higher degree than other bases.

**3.4.3. Effects of Nucleotide Passivation on the Charge Transfer Characteristics of a Transition**

We also compare the absorption spectra of the passivated Ag$_6$ clusters and the bare cluster in which passivated bases are deleted, while the cluster is preserving the same geometry as it has in the passivated structures, Figure 3.18e-g and Figure 3.19. Interestingly, the lowest energy transitions of the neutral bare clusters are optically active, in contrast to those of the passivated clusters, except **6C-**Ag$_6$ where the passivated cluster has optically active first transition, while it is optically inactive for the bare cluster. This trend points to a change in the optical selection rules of the lowest transitions of AgNCs due to the delocalization of the excited state both over the cluster and the bases bearing MLCT character. In contrast, highly intensive absorption peaks at 3.0-3.5 eV, almost coincide between the bare and the passivated clusters, especially in 6G-,6T and 2C4T-Ag$_6$, despite the admixture of MLCT character in transitions contributing to these peaks, **Figure 3.18e-g** and **Figure 3.19**. As such, transitions at this energy range exhibit the same optical selection rules for both pure metal-to-metal and mixed MLCT states.

Similar to transitions at 3.0-3.5 eV, the lowest energy transitions contributing to the 2.5-3.0 eV band of the ligated clusters also exhibit the *s*-character of holes (50-70%) and *p*-character

93

of electrons (30-50%), but with a more pronounced admixture of *s*-orbitals in the electron states, Table 3. In contrast, the lowest transitions in the bare clusters show smaller contributions of *p*-orbitals to electrons resulting in a predominant *s*-character of both electrons (60-70%) and holes (80-85%). These results agree with literature reports showing that the lower energy transitions in small silver clusters with less than eight atoms in size mainly involve *s*-orbitals, where the hole has predominantly *s*-orbital contribution, and the electron has a more hybridized *s+p* character.[46-47] However, a significantly stronger degree of *s+p* character of electrons in the ligated clusters, compared to their bare counterparts, is responsible for differences in their optical selection rules of the lowest transitions at the 2.0-3.0 eV band.

The absorption band at 4.0-4.5 eV has the smallest MLCT contribution (< 20 %) for all ligated structures, Figure 3.18a-c, and Figure 3.19. NTOs demonstrate either π-π* transitions originated from bases or metal originated transitions with predominant *s*-character of holes and *p*-character with a very small admixture of *s*-orbitals of electrons, similar to the bare clusters, Table 3.7. Notably, there are no *d*-orbital contributions to electron states for both ligated and bare clusters. A lack of *d*-character also reflects on the reduced MLCT character of these transitions in the ligated systems. Due to the reduced hybridization of the electron-hole pairs, the intensity of these transitions is noticeably smaller compared to those in the 3.0-3.5 eV range. Comparing the bare and ligated structures, there is a significant splitting between optical peaks at ~4.0 eV in the bare clusters, which is not present in the ligated clusters. This is the result of minimizing the energy splitting between the bonding and antibonding Ag-associated *p* orbitals due to the perturbation by nucleobases' electrostatic dipole,[47] despite a minimal direct contribution of base orbitals to these states. This explains significant deviations between this band in the bare and passivated clusters, Figure 3.18e-h and Figure 3.19.

For the band at the energy > 4.5 eV, the CT degree increases to 20%-40% for most structures but exhibiting mainly LMCT, rather than MLCT character. For these transitions, the *d*-orbital contribution to holes becomes significant (40-80%). These results well agree with previously reported calculations of DNA-Ag$_4$ clusters, showing that the absorption peaks from red to blue wavelengths are predominantly of MLCT character, while absorption in the blue-violet range are mostly represented by transitions with a mixed character of LMCT or *d-d\**.[11] The similar trends in CT contributions to all absorption bands are observed for charged passivated and bare Ag$_6^+$ clusters, with the difference that the lowest energy optically inactive transition (at ~1.5 eV) has a small contribution of MLCT with a dominant metal-to-metal character associated with *s*-orbitals of both electrons and holes, Figure 3.20 and S10.
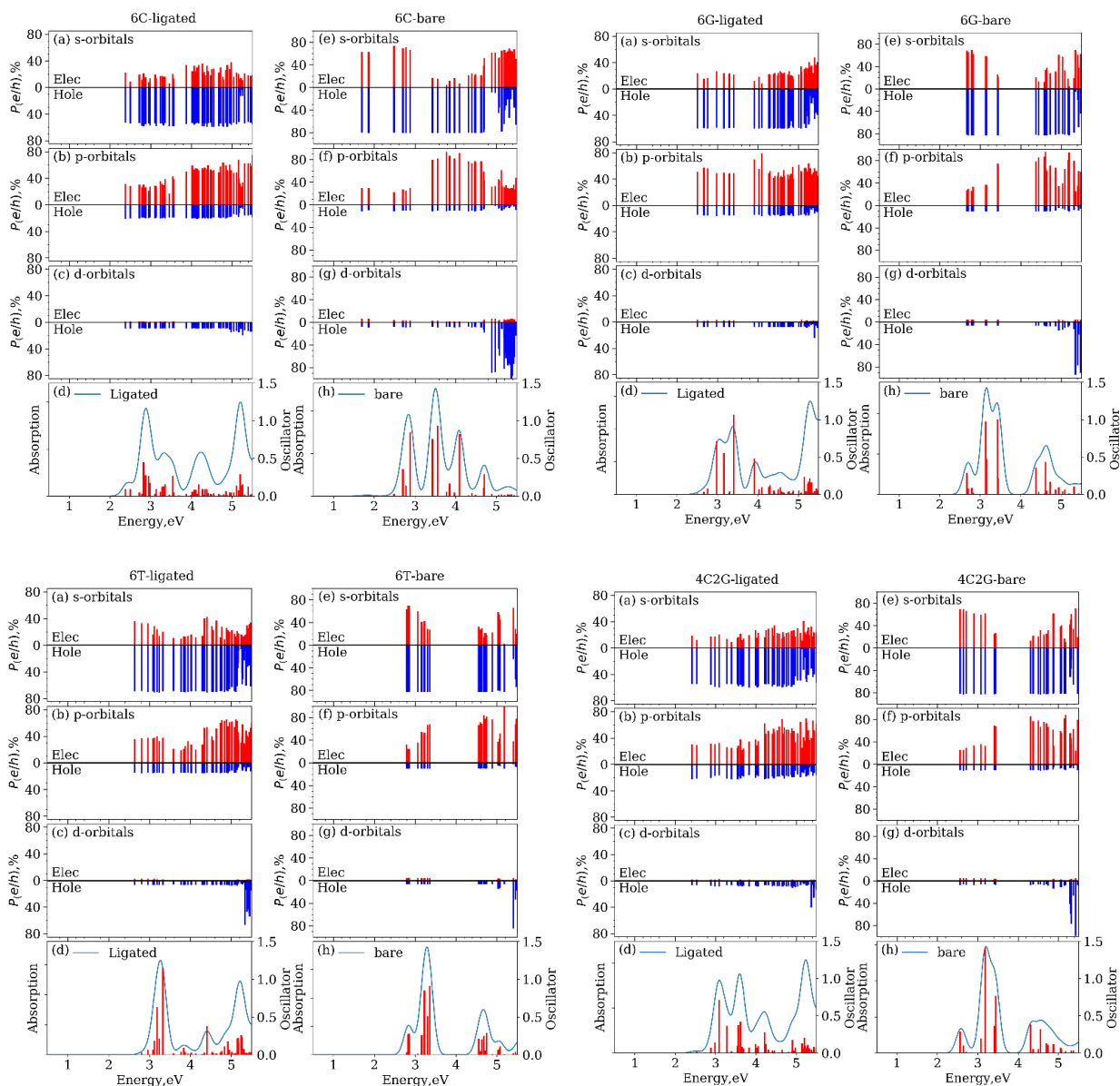
**Figure 3.21:** Absorption spectra and Ag's *s, p, d* angular momentum contribution to the excited states *(hole and electron)* of the all transitions in the most stable nucleobases ligated Ag$_6$ and their bare clusters. All panels are labeled with the name of the clusters. In each panel, *a-c* and *e-g* sub-panel are the contribution of Ag's *s, p, d* angular momentum in the ligated and bare clusters, respectively. Panel *d* and *h* are the absorption spectra of the respective ligated and bare clusters, red vertical line indicates the oscillation strength of the transitions. In case of nucleobase passivated clusters, transitions of oscillator strength > 0.01 are plotted to reduce the overlapping bar plot. The sum of *s, p,* and *d* of the Ag in the hole and electron states indicates the total contribution of the Ag in the respective transition.
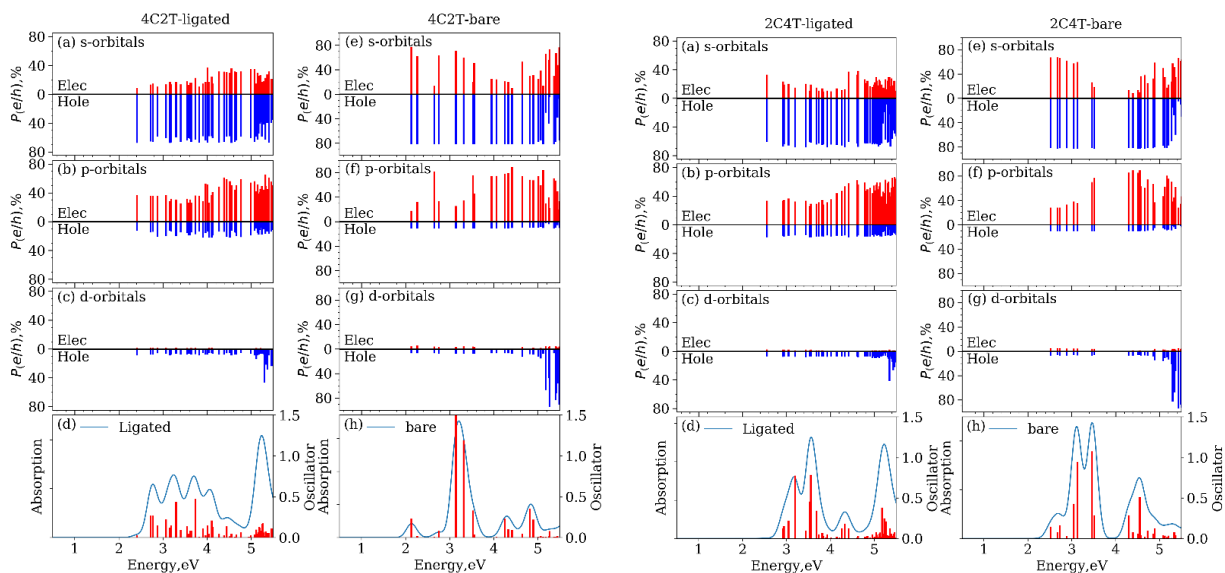
**Figure 3.21:** Absorption spectra and Ag's *s, p, d* angular momentum contribution to the excited states *(hole and electron)* of all transitions in the most stable nucleobases ligated $Ag_6$ and their bare clusters (continued). All panels are labeled with the name of the clusters. In each panel, *a-c* and *e-g* sub-panel are the contributions of Ag's *s, p, d* angular momentum in the ligated and bare clusters, respectively. Panel *d* and *h* are the absorption spectra of the respective ligated and bare clusters; red vertical line indicates the oscillation strength of the transitions. In the case of nucleobase passivated clusters, transitions of oscillator strength > 0.01 are plotted to reduce the overlapping bar plot. The sum of *s, p,* and *d* of the Ag in the hole and electron states indicates the total contribution of the Ag in the respective transition.

## 3.5. The Size and Charge Dependent Absorption Features of Cytosine Passivated Ag Nanoclusters

The next promising feature of silver nanoclusters is the evaluation of absorption spectra with the number of Ag atoms in a cluster and overall charge of the nanoclusters. The molecule like discrete optical transitions and their spectra characteristics are diminished when the Ag clusters grow to a larger size. Instead, larger Ag clusters show a unique absorption band in the UV-vis energy range.[48] It was reported that the red-shifted plasmon like absorption band had been shown in the size of the nanoclusters, about 20 silver atoms.[49-50,] While smaller clusters have shown the absorption band in the range of ≈3.0 eV[51-52]. A note to remember that besides the

cluster size effects, the optical response of a metal nanocluster can be modified by several

factors, as we have shown in section 2.4 of this chapter,

We have considered $Ag_4$-$Ag_{10}$ and $Ag_{17}$-$Ag_{21}$ nanoclusters to study the size effects and

charge of the system. In the previous section, it has been shown that the lowest energy transition

has non-zero oscillator strength, which is tuned in the response of structural and ligand

interactions. Time-dependent DFT (TD-DFT) calculation of the wide range of Ag clusters will

help understand the size effects. The initial geometries were taken from the previous prediction

of the bare silver clusters[1]. The bare clusters are passivated by cytosine with the 1:1 ration up to

9 Ag size nanoclusters. The predicted energetically stable Ag nanoclusters of larger than nine

atoms consist of Ag core; thus, the Ag to cytosine passivation ratio is smaller than 1:1 in the

nanoclusters larger than nine atoms size. Two different types of passivated $Ag_{10}$ clusters are

considered- five and ten cytosine passivation.

### 3.5.1. Size Dependent Structural Change in Ground State Geometries

In section 3.4, we have shown the planner and non-planner structure of the Ag5 and Ag6

cluster dominate the Ag-C interaction, and the Ag-C interactions dominate the charge transfer

nature of the transitions. The lowest energy conformation of the nanoclusters larger than 6 Ag

atom is non-planner. The optimized ground state $Ag_7$ is pentagonal bipyramidal, which has $D_{5v}$

symmetry, comparable to the geom-3 of the 6C (sub-chapter -3.4). $Ag_8$ has a triangular

bipyramidal in the center of $Ag_3$ (figure 3.22). Petty et al. also predicted a core bipyramidal

structure in the $Ag_{10}$ clusters.[53] The larger geometry has shown multiple symmetries or almost

symmetric geometry. Moreover, $Ag_{20}$ preserves an almost perfect pyramidal structure. The

adopted initial geometry of the $Ag_{20}$[1] is covered by eight cytosine due to a smaller surface area

compared to other nanoclusters model. Due to the bulk-like conformation, structural

reorganization by the cytosine passivation is minimum in the $Ag_{20}$ nanocluster (Figure 3.23).

Because of high symmetry, it shows a metal-like brighter absorption peak.
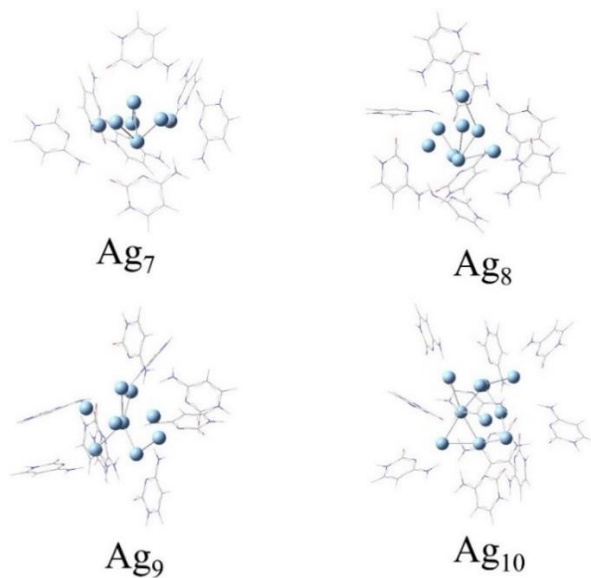


**Figure 3.22:** The optimized neutral ground state structure of the $Ag_7$-$Ag_{10}$. All geometries were optimized in water solvent using DFT ab initio method
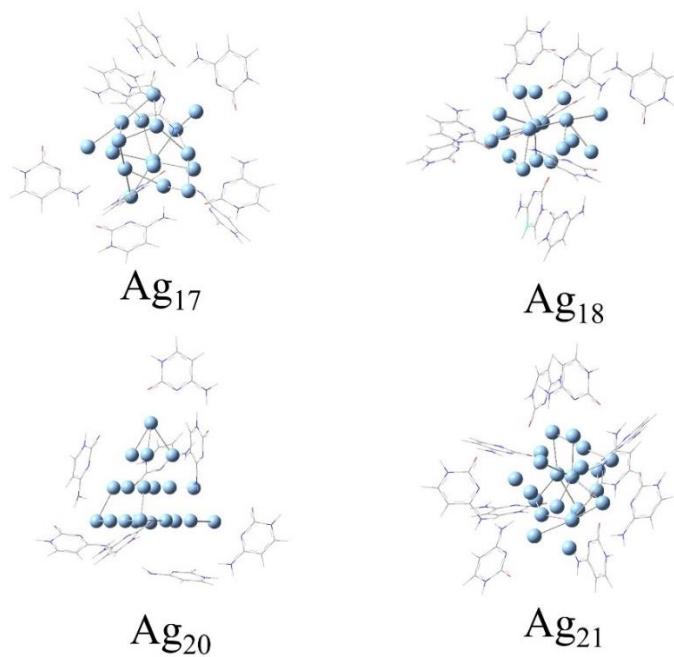


**Figure 3.23:** The optimized neutral ground state structure of the $Ag_{17}$-$Ag_{21}$. All geometries were optimized in water solvent using DFT ab initio method

### 3.5.2. Size Dependent Absorption of the Ag Nanoclusters

Figure 3.24-3.26 are showing the absorption spectra of the neutral and +1 charged Ag nanoclusters from 4 to 10 and 17-21 Ag atom sizes. Overall, Ag clusters have two spin configurations- singlet and doublet spin. The absorption spectra feature in the range higher than 2.5eV is comparable in both spin systems (Figure 3.24-3.25). Ag nanoclusters of smaller than ten atoms have three distinct absorption bands in the range of 2.5-5.00 eV. The discrete energy splitting between the absorption peak decreases with growing cluster size; as a result, the intensity is also increased. Although the absorption peaks at around 3.50-4.75eV are insensitive to the cluster size, the lowest energy absorption peak at 3.00 eV in the singlet spin geometries are red shifted with increasing the cluster size (Figure 3.24-3.25). Because of higher symmetry in the $Ag_5$ and $Ag_6$ clusters, the 3.25eV absorption peak is slightly blue-shifted compared to others.[54] In all clusters, the absorption peak at 5.00eV is consistent mainly due to a similar nucleobase cytosine molecule (This peak is not shown in the larger nanoclusters' absorption spectra due to limitation of required resources in TDDFT calculation for high energy states).

In contrast to the nanoclusters of singlet spin, doublet spin nanoclusters have a lower energy absorption band in the range of 1.00-2.50eV. The overall energy and intensity of the absorption in this range are nanoclusters size and charge sensitivity. It has shown that the intensity of the at the energy range 1.5eV decreases with the increasing neutral clusters size ($Ag_5$, $Ag_7$, and $Ag_9$). In contrast, it increases in the +1 charged clusters (+1 charged 4, 6, 8, and 10 atom size Ag clusters) (Figure 3.24-3.25).
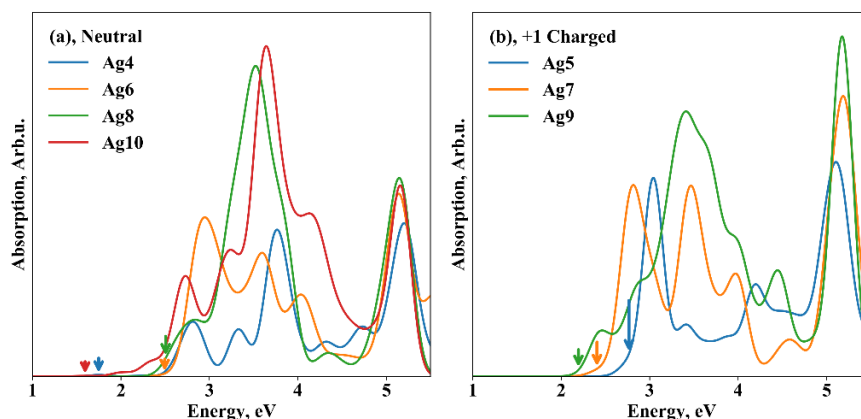
**Figure 3.24:** Absorption spectra of the neutral (panel a) and +1 charged (panel b) Ag clusters. Even and odd number clusters are categorized as singlet spin. All calculation is done in water solvent and Cam-B3LYP functional.
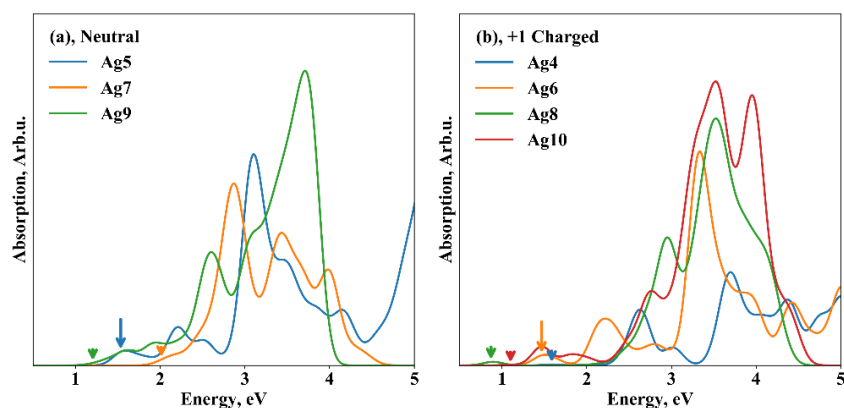


**Figure 3.25:** Absorption spectra of the neutral (panel a) and +1 charged (panel b) Ag clusters. Odd and even number clusters are categorized as doublet spin. All calculation is done in water solvent and Cam-B3LYP functional.
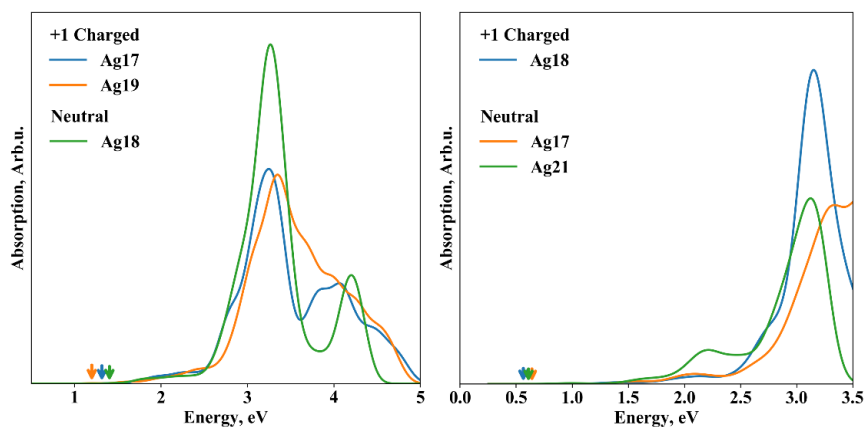


**Figure 3.26:** Absorption spectra of the neutral (panel a) and +1 charged (panel b) of the larger Ag clusters (n>16). Odd and even number clusters are categorized as doublet spin. All calculation is done in water solvent and Cam-B3LYP functional

101

On the other hand, nanoclusters' size and charge have minimum effects on the overall absorption feature of the larger Ag nanoclusters. Both the neutral and +1 charged clusters shown a low energy absorption band in the range of 1.75-2.50eV and high intensity peak at the 3.25eV (Figure 3.26). This absorption feature is comparable with the reported aromatic compounds passivated $Ag_{20}$ nanoclusters, where higher oscillator transitions at the energy 3.25eV are insensitive to the surface passivation molecule.[48]

The lowest energy transition carries the information of size and charges sensitivity of the bandgap and selection rule. The nanoclusters' energy and oscillator strength change over the size of the clusters are shown in Figure 3.27. Overall, smaller metal clusters are shown brighter lowest energy transition compare to larger nanoclusters. The transition energy decreases with increasing the size of the cluster, which is a result of decreasing the confinement energy and increasing the bulk metal like feature. The oscillator strength is very sensitive to the charge and symmetry when nanoclusters are smaller than 20 atoms.
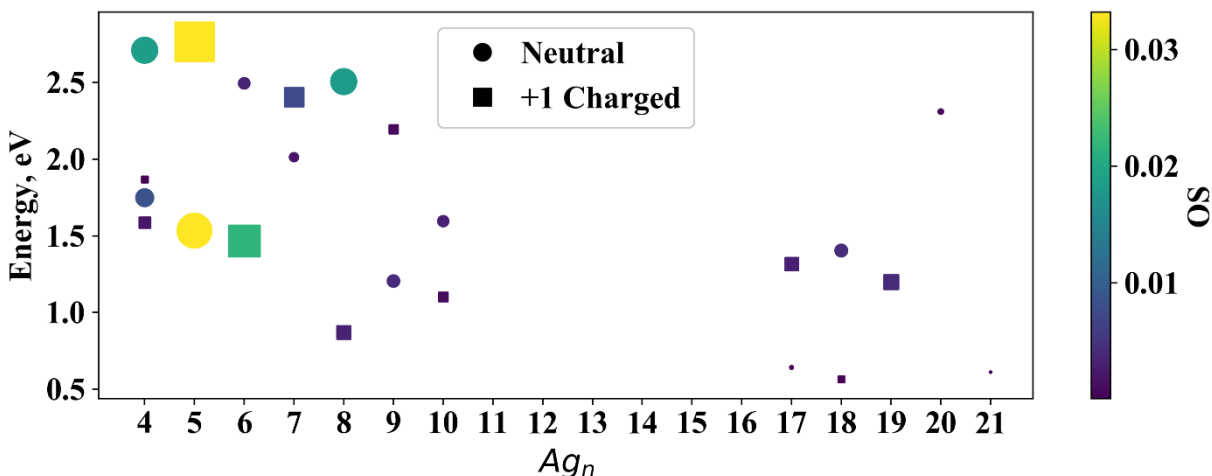


**Figure 3.27:** Energy and oscillator strength of the lowest energy transition in the all neutral and +1 charged clusters ($Ag_4 - Ag_{21}$). The size of the marker represents the brightness of the lowest energy transition. The color bar is also representing the same information-oscillator strength.

## 3.6. Principal Component Analysis of $Ag_5$ and $Ag_6$ Clusters

From the above studies, the electronic structure of Ag nanoclusters is certainly dominated by Ag core structure, surface interaction with the ligand nucleobases, the charge of the systems, etc. Because of several degrees of freedom in determining the overall photophysical properties, a large-scale structural analysis could determine the dominating feature. In this section, we have done principle component analysis (PCA) of the structural descriptor, like Ag-Ag, Ag-N bond, relative energy of the clusters, excitation energy, and oscillator strength of the cytosine passivated Ag nanoclusters.

### 3.6.1. Methodology

We have randomly generated 500 structures for each of cytosine passivated Ag5 and Ag6, charge, and neutral nanoclusters in the first step. We have maintained 1 to 1 Ag and cytosine ration, and all cytosine bound with Ag cluster by Ag-N2 of cytosine bond. All the initial created geometries are optimized using DFT method[55] in water solvent using Cam-B3LYP functional[7] and a mixed basis set of LANL2DZ[8] (for Ag atoms) / 6-31G*[9]. Because of the random creation, some conformations significantly deviate from the chemically realizable structure, and those are excluded from the optimization, which is less than 5% of the total number of conformations. The excited state energy and oscillator strength are obtained using linear response time dependent DFT (TDDFT) using a similar functional, basis set, and solvent. All calculations have been done in the Gaussian software packages.

### 3.6.2. Data Collection and Categorizing

Our goal is to determine the dominating structural feature for the higher oscillator strength. So, all nanoclusters are divided into four categories according to the lowest energy transition's oscillator strength. The four range of oscillator strengths is *<0.01, 0.01- 0.03, 0.03-*

*0.05, >0.05*, and name as dark, bright, brighter, and brighter, respectively. The relative energy is the energy relative to the lowest energy conformation of the considered cluster series ($Ag_5$, $Ag_5^{+1}$, $Ag_6$, $Ag_6^{+1}$). To calculate the Ag-Ag bond length, the Ag-Ag bond is defined by threshold value 3.50Å, and the lowest three are considered here. Ag-cytosine bond is defined by the bond between Ag and N2 of the cytosine ring. Although all initial geometries were prepared by placing on the Ag-N bond, the number Ag-N bond deviates in the optimized structure. We have considered a bond as Ag-N if the value is lower than the threshold distance of 3.50Å. All the Ag-Ag and Ag-N bonds are ordered in ascending order. For example, Ag-Ag1 indicates the strongest Ag-Ag bond.

### 3.6.3. Principal Component Analysis of the Structural Features

In the first step, the two-component analysis of Ag-Ag and Ag-N bond combination are studied. The PCA plots are shown in Figure 3.28. It is shown that Ag-Ag bond length is dominant over the Ag-N bond. We assume that the Ag-N determines the overall structure, which led to modifying the Ag-Ag bond and the final geometry of the nanoclusters dominating the oscillation strength. Ag-Ag bonds also determine the overall energy. Figure 3.29 is showing the two components analysis of the Ag-Ag bond with relative energy. It was noticeable that oscillator strength is predominately dependent on the Ag nanocluster structural feature rather than the system's relative energy. Due to the variation of charge and symmetry in nanocluster, it is also uncertain the basis of the relative energy. In our calculation, the basis is the lowest energy of a series in our considered geometries. Ag-N bond with the relative energies is shown scattered brightest transitions (Figure 3.30). This indicates that Ag-N bond length will not be the best choice as a descriptor. It is also noted that Ag-N bond length is used as unlabeled data, so we have not to tag metal atom to determine the Ag-N bond. In section 3.2 and 3.4., it was shown that

ligand metal interaction plays an important role in determining transition energy and oscillator strength. Our future plan is to explore the correlation between the Ag-Ag and Ag-N bond, including binding side label.
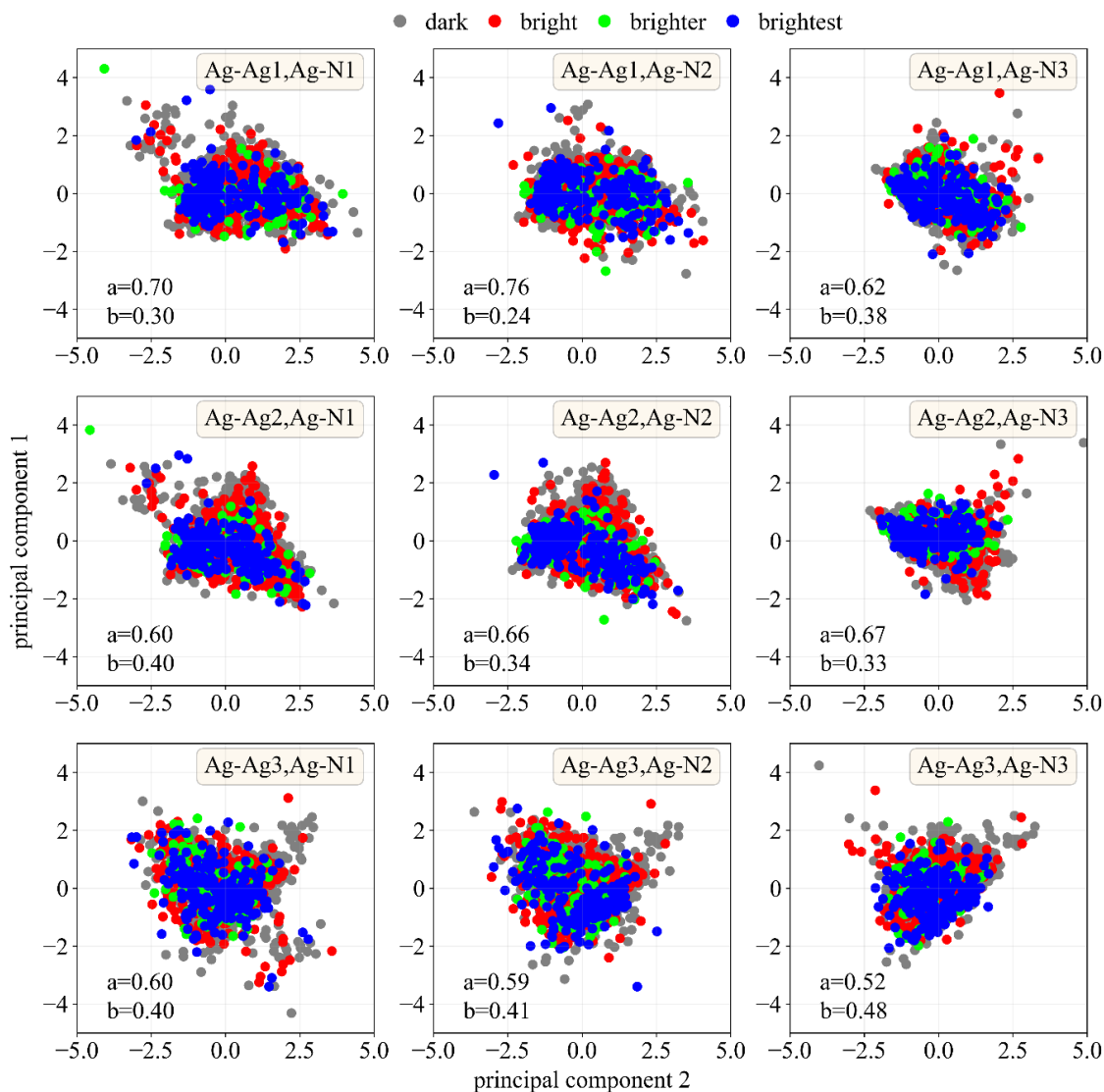


**Figure 3.28:** The correlation between the Ag-Ag bond and Ag-N bond. The data is categorized based on the oscillator strength of the lowest energy transitions. In some clusters, number of Ag-N bond are 3, so maximize the sample pool, three Ag-Ag and three Ag-N bonds are plotted.
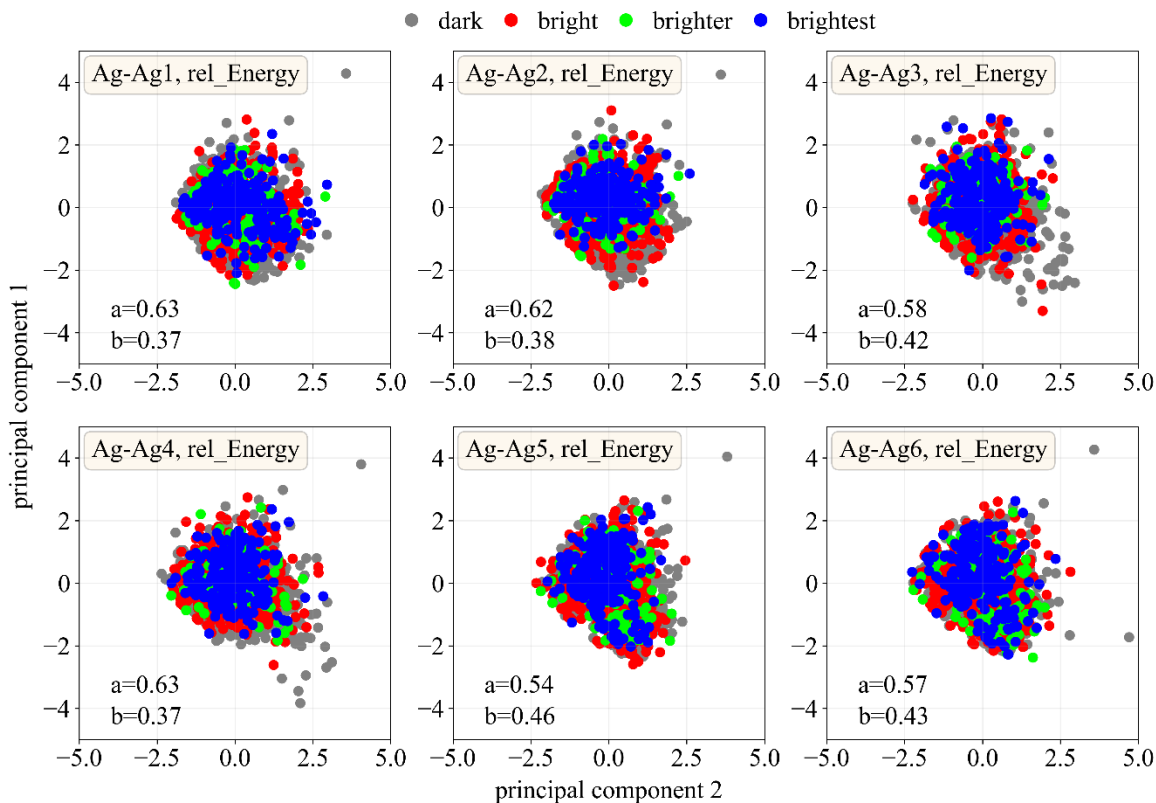
**Figure 3.29:** The two-dimensional (2D) correlation between the Ag-Ag bond and relative energy of the optimized clusters.

Moreover, the three descriptors, Ag-Ag1, Ag-N1, and relative energies, are plotted in a two-dimensional (2D) plot in figure 3.31. The confidence level is 81%, where component 1 is predominant. Another advantageous feature of PCA is the clusterization of the data, which lets us categorize based on the features. Figure 3.31 shows that the brightest oscillator strength is less scattered compared to the lower oscillator strength transition. This indicates that bright transitions can be described using these descriptors. The Gaussian distribution of all the four transitions categories shows significant overlap, which minimizes the probability of accurate prediction using these three descriptors.
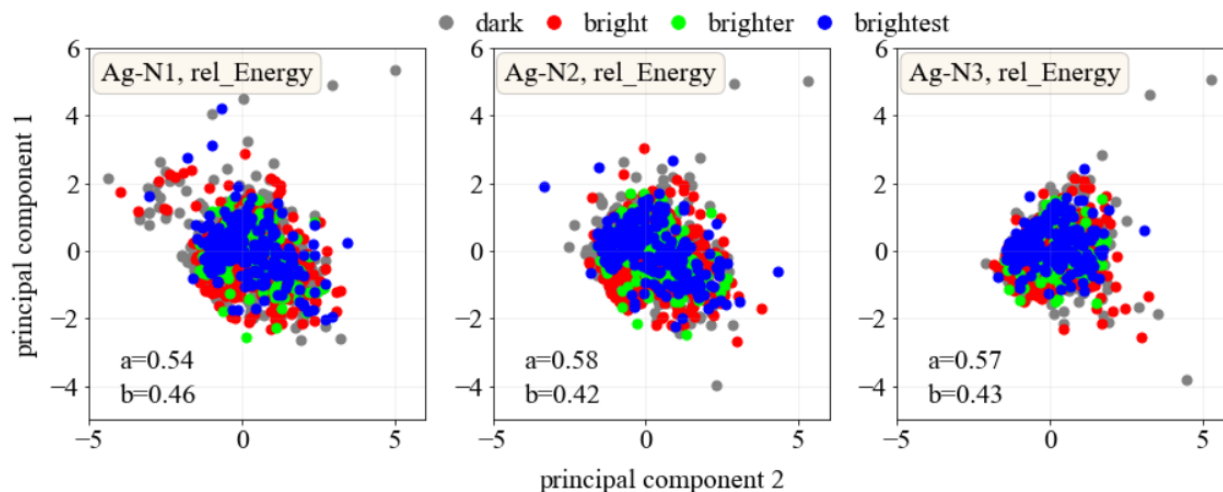
**Figure 3.30**: The two-dimensional (2D) correlation between the three shorted Ag-N bond and relative energy of the optimized clusters.
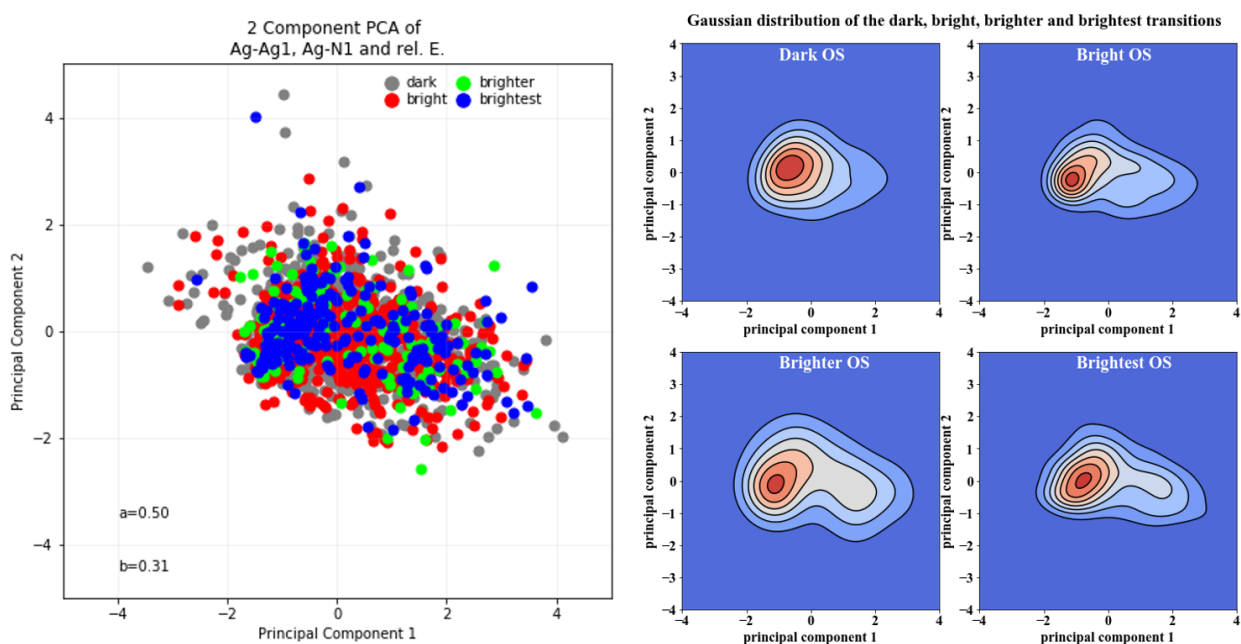


**Figure 3.31**: The two-dimensional (2D) correlation of the three descriptors – the shortest Ag-Ag and Ag-N bond- and the relative energy of the optimized clusters. Gaussian distribution of all transitions shows a significant overlap between the distribution of all target descriptors.

### 3.6.4. Correlation with the Volume of Ag Clusters

The volume of the silver clusters is an important descriptor. We have described the

relative shape of the cluster by counting the number Ag-Ag bond. A single atom thick nanorod

shape Ag nanocluster has a minimum number of Ag-Ag bond. In contrast, an Ag atom should

coordinate with the maximum number of Ag atoms in a compact 3D geometry (**Figure3.32**).



3 Ag-Ag bond     4 Ag-Ag bond     5 Ag-Ag bond
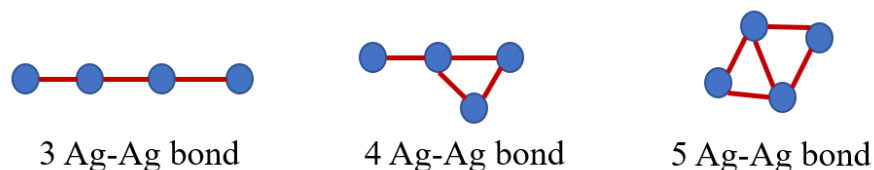
**Figure 3.32:** The number of Ag-Ag bonds in Ag4 nanoclusters based on the Ag nanocluster geometry shape.
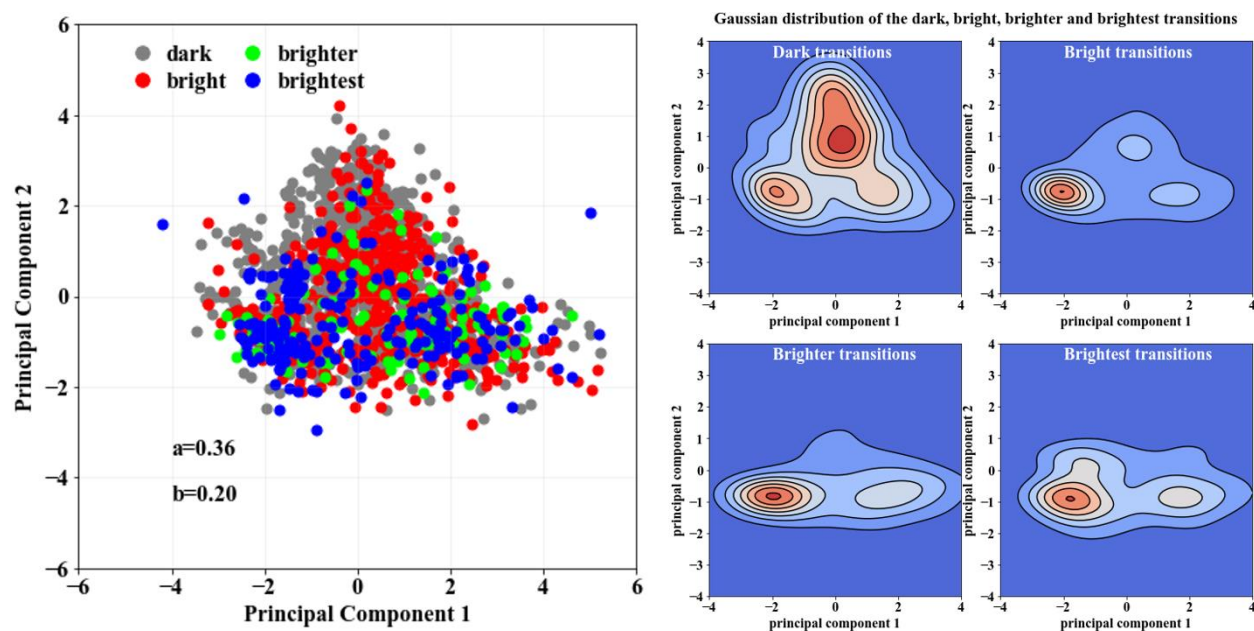


**Figure 3.33:** The two-dimensional (2D) correlation of the three descriptors – the shortest Ag-Ag and Ag-N bond- and the relative energy of the optimized clusters. Gaussian distribution of all transitions shows a significant overlap between the distribution of all target descriptors.

From the previous discussion, certainly, Ag-Ag bond length and Ag-N bond length,

especially the shortest bond, along with relative energy, could be a good descriptor. The 2-D

PCA conversion of the three shortest Ag-Ag bonds, three Ag-N bonds, relative energy of the

optimized geometry, and the number of Ag-Ag bonds are shown in Figure 3.33. Gaussian

distribution of dark and bright-brightest transition shows the significant distribution between

dark and non-dark transitions. These results indicate that the cluster shape is an important

descriptor. Although the inclusion of these descriptors shows a separation of the category, the sum of the principal factors' variance ratio is lower than 60%.

We identified a few important structural descriptors for unsupervised clustering analysis. A larger dataset is needed to increase the confidence label. In summary, the PCA analysis shows that the Ag-Ag bond is a good descriptor, besides Ag-N and relative energy. In addition, overall cluster shape (incorporated by the number of Ag-Ag bond) increases the selectivity.

### 3.7. Summary

We have studied all the conditions and features what impacts the optical and structural feature of the nucleobase passivated Ag nanoclusters. Our calculations demonstrate that a polar solvent like water is an important factor that transforms the geometries of clusters passivated by cytosines from planner 2-D to non-planar 3-D structures, while the planar conformations are the most stable for the non-passivated $Ag_5$ and $Ag_6$ clusters.3 In addition to the cluster-base interactions, the hydrogen bond network between passivating bases significantly impacts the cluster geometry and its stability. Therefore, the most stable isomer is the one preserving the largest number of hydrogen bonds and the strongest base-cluster interactions. On the other hand, the redox potential of an Ag NC would determine the relative stability of the NC. Ag NC has shown alternative redox potential strength against the size of the clusters due to the doublet and singlet spin of the clusters. Reduction potential difference between a consecutive oxidation state is large in a smaller cluster; as such certain oxidation states are preferential. This leads us to calculate the redox potential of the two model redox reactions. According to our calculations, NC of neutral or +2 oxidation states should predominate when the number of Ag atom is even, and the +1 oxidation state should be predominating if the cluster size is odd number Ag atoms.

It suggested that several isomers of base-passivated clusters coexist in polar solvents due to the relatively small energy differences between their conformations ($< 0.2$ eV). Comparing the cluster-based binding energies, cytosines and guanines interact much stronger than thymines even in mixed passivation, due to their larger electrostatic dipole moments, with their interactions increasing in charged clusters. T binding energy is almost half of the C and G binding energy. It suggests that the thymines likely contribute a minimal amount to the coordination of AgNCs, when cytosines and guanines are available in a DNA strand. Despite some variations in energies and intensities of spectral peaks of clusters with different conformations, passivation bases, and charges, the spectral profile with well resolved five main peaks at the range of 2.5-5.5 eV is similar for all studied structures. It was shown that the doublet transitions in base-passivated clusters with the open shell electronic structure ($Ag_5$ and $Ag_6^+$) result in the additional red-shifted ($< 2.5$ eV) and optically weak band. Besides, closed shell electronic structure ($Ag_5^+$ and $Ag_6$) has a higher optical intensity of their lowest energy transitions with a high MLCT contribution providing better conditions for emission. In the energy range of 2.5-4.5 eV, hybridization in s+p+d orbitals facilitate the delocalization, which also modulates the MLCT characters of transitions. The higher energy peak at the range 4.5eV can be explained by the degree of the charge transfer from the Ag to nucleobase ligand. For the optically intensive band at the energy $> 5.0$ eV, the charge transfer character increases but exhibiting mainly LMCT rather than MLCT character. This change is dictated by significantly increased contributions of d-orbitals to hole states leading to delocalization of the hole between metal centers and bases. Overall, our results help to understand the intrinsic properties of DNA-AgNCs chromophores better and complement experimental data.

The brightness of the lowest energy transition decreases in the response of increasing the cluster size. The lowest energy transition becomes dark when the cluster size approaches Ag20. Overall, Ag nanoclusters lose their' lower energy signature absorption feature and approach to a bright abruption at the energy 3.50 eV.

Besides the NC size, we have shown the structure descriptor, which could determine the brightness of the lowest energy transitions. It was shown that Ag-Ag bond length in the small clusters like Ag5 and Ag6 has a strong correlation with the oscillator strength. On the other hand, we did not find such dependence on the relative total energy of the clusters. These results indicate that some higher energy conformation could have brighter lowest energy transitions. In addition, our PCA analysis suggests that machine learning or QSAR models can be used using the structural descriptor like Ag-Ag and Ag-N bond.

### 3.8. References

1.    Chen, M.; Dyer, J. E.; Li, K.; Dixon, D. A., Prediction of Structures and Atomization Energies of Small Silver Clusters, (Ag)n, n < 100. *J. Phys. Chem. A* **2013,** *117* (34), 8298-8313.

2.    Bonačić-Koutecky, V.; Veyret, V.; Mitrić, R., Ab initio study of the absorption spectra of Agn (n=5–8) clusters. *J. Chem. Phys.* **2001,** *115* (22), 10450-10460.

3.    Fernández, E. M.; Soler, J. M.; Garzón, I. L.; Balbás, L. C., Trends in the structure and bonding of noble metal clusters. *Phys. Rev. B.* **2004,** *70* (16), 165403.

4.    Furche, F.; Ahlrichs, R., Adiabatic time-dependent density functional methods for excited state properties. *J. Chem. Phys.* **2002,** *117* (16), 7433-7447.

5.    Casida, M. E.; Jamorski, C.; Casida, K. C.; Salahub, D. R., Molecular excitation energies to high-lying bound states from time-dependent density-functional response theory: Characterization and correction of the time-dependent local density approximation ionization threshold. *J. Chem. Phys.* **1998,** *108* (11), 4439-4449.

6.    Frisch, M. J.; Trucks, G. W.; Schlegel, H. B.; Scuseria, G. E.; Robb, M. A.; Cheeseman, J. R.; Scalmani, G.; Barone, V.; Petersson, G. A.; Nakatsuji, H.; Li, X.; Caricato, M.; Marenich, A. V.; Bloino, J.; Janesko, B. G.; Gomperts, R.; Mennucci, B.; Hratchian, H. P.; Ortiz, J. V.; Izmaylov, A. F.; Sonnenberg, J. L.; Williams; Ding, F.; Lipparini, F.; Egidi, F.; Goings, J.; Peng, B.; Petrone, A.; Henderson, T.; Ranasinghe, D.; Zakrzewski,

V. G.; Gao, J.; Rega, N.; Zheng, G.; Liang, W.; Hada, M.; Ehara, M.; Toyota, K.; Fukuda, R.; Hasegawa, J.; Ishida, M.; Nakajima, T.; Honda, Y.; Kitao, O.; Nakai, H.; Vreven, T.; Throssell, K.; Montgomery Jr, J. A.; Peralta, J. E.; Ogliaro, F.; Bearpark, M. J.; Heyd, J. J.; Brothers, E. N.; Kudin, K. N.; Staroverov, V. N.; Keith, T. A.; Kobayashi, R.; Normand, J.; Raghavachari, K.; Rendell, A. P.; Burant, J. C.; Iyengar, S. S.; Tomasi, J.; Cossi, M.; Millam, J. M.; Klene, M.; Adamo, C.; Cammi, R.; Ochterski, J. W.; Martin, R. L.; Morokuma, K.; Farkas, O.; Foresman, J. B.; Fox, D. J. *Gaussian 16 Rev. B.01*, Wallingford, CT, 2016.

7.      Yanai, T.; Tew, D. P.; Handy, N. C., A new hybrid exchange–correlation functional using the Coulomb-attenuating method (CAM-B3LYP). *Chem. Phys. Lett.* **2004,** *393* (1-3), 51-57.

8.      Hay, P. J.; Wadt, W. R., Ab initio effective core potentials for molecular calculations. Potentials for the transition metal atoms Sc to Hg. *J. Chem. Phys.* **1985,** *82* (1), 270-283.

9.      Ditchfield, R.; Hehre, W. J.; Pople, J. A., Self-Consistent Molecular-Orbital Methods. IX. An Extended Gaussian-Type Basis for Molecular-Orbital Studies of Organic Molecules. *J. Chem. Phys.* **1971,** *54*, 724-728.

10.     Pakiari, A. H.; Jamshidi, Z., Nature and Strength of M−S Bonds (M = Au, Ag, and Cu) in Binary Alloy Gold Clusters. *J. Phys. Chem. A* **2010,** *114* (34), 9212-9221.

11.     Longuinhos, R.; Lúcio, A. D.; Chacham, H.; Alexandre, S. S., Charge-transfer optical absorption mechanism of DNA:Ag-nanocluster complexes. *Physical Review E* **2016,** *93* (5), 052413.

12.     Ramazanov, R. R.; Kononov, A. I., Excitation Spectra Argue for Threadlike Shape of DNA-Stabilized Silver Fluorescent Clusters. *J. Phys. Chem. C* **2013,** *117* (36), 18681-18687.

13.     Cossi, M.; Rega, N.; Scalmani, G.; Barone, V., Energies, structures, and electronic properties of molecules in solution with the C-PCM solvation model. *J. Comput. Chem.* **2003,** *24* (6), 669-681.

14.     Martin, R. L., Natural transition orbitals. *J. Chem. Phys.* **2003,** *118* (11), 4775.

15.     Frisch, M. J.; Trucks, G. W.; Schlegel, H. B.; Scuseria, G. E.; Robb, M. A.; Cheeseman, J. R.; Scalmani, G.; Barone, V.; Mennucci, B.; Petersson, G. A.; Nakatsuji, H.; Caricato, M.; Li, X.; Hratchian, H. P.; Izmaylov, A. F.; Bloino, J.; Zheng, G.; Sonnenberg, J. L.; Hada, M.; Ehara, M.; Toyota, K.; Fukuda, R.; Hasegawa, J.; Ishida, M.; Nakajima, T.; Honda, Y.; Kitao, O.; Nakai, H.; Vreven, T.; Montgomery Jr, J. A.; Peralta, J. E.; Ogliaro, F.; Bearpark, M. J.; Heyd, J.; Brothers, E. N.; Kudin, K. N.; Staroverov, V. N.; Kobayashi, R.; Normand, J.; Raghavachari, K.; Rendell, A. P.; Burant, J. C.; Iyengar, S. S.; Tomasi, J.; Cossi, M.; Rega, N.; Millam, N. J.; Klene, M.; Knox, J. E.; Cross, J. B.; Bakken, V.; Adamo, C.; Jaramillo, J.; Gomperts, R.; Stratmann, R. E.; Yazyev, O.; Austin, A. J.; Cammi, R.; Pomelli, C.; Ochterski, J. W.; Martin, R. L.; Morokuma, K.; Zakrzewski, V. G.; Voth, G. A.; Salvador, P.; Dannenberg, J. J.; Dapprich, S.; Daniels,

A. D.; Farkas, Ö.; Foresman, J. B.; Ortiz, J. V.; Cioslowski, J.; Fox, D. J. *Gaussian 09*, Gaussian, Inc.: Wallingford, CT, USA, 2009.

16.    Humphrey, W.; Dalke, A.; Schulten, K., VMD: Visual molecular dynamics. *J. Mol. Graphics* **1996,** *14* (1), 33-38.

17.    Xiong, R.; Die, D.; Xiao, L.; Xu, Y.-G.; Shen, X.-Y., Probing the Structural, Electronic, and Magnetic Properties of AgnV (n = 1–12) Clusters. *Nanoscale Res. Lett.* **2017,** *12* (1), 625.

18.    Wang, J.; Wang, G.; Zhao, J., Structures and electronic properties of Cu20, Ag20, and Au20 clusters with density functional method. *Chem. Phys. Lett.* **2003,** *380* (5), 716-720.

19.    K. Samanta, P.; Periyasamy, G.; K. Manna, A.; K. Pati, S., Computational studies on structural and optical properties of single-stranded DNA encapsulated silver/gold clusters. *J. Mater. Chem.* **2012,** *22* (14), 6774-6781.

20.    Colson, A. O.; Besler, B.; Sevilla, M. D., Ab initio molecular orbital calculations on DNA base pair radical ions: effect of base pairing on proton-transfer energies, electron affinities, and ionization potentials. *J. Phys. Chem.* **1992,** *96* (24), 9787-9794.

21.    Itoh, M.; Kumar, V.; Adschiri, T.; Kawazoe, Y., Comprehensive study of sodium, copper, and silver clusters over a wide range of sizes 2≤N≤75. *J. Chem. Phys.* **2009,** *131* (17), 174510.

22.    Dale, B. B.; Senanayake, R. D.; Aikens, C. M., Research Update: Density functional theory investigation of the interactions of silver nanoclusters with guanine. *APL Materials* **2017,** *5* (5), 053102.

23.    Weis, P.; Bierweiler, T.; Gilb, S.; Kappes, M. M., Structures of small silver cluster cations (Agn+, n<12): ion mobility measurements versus density functional and MP2 calculations. *Chem. Phys. Lett.* **2002,** *355* (3), 355-364.

24.    Petty, J. T.; Sergev, O. O.; Nicholson, D. A.; Goodwin, P. M.; Giri, B.; McMullan, D. R., A Silver Cluster–DNA Equilibrium. *Anal. Chem.* **2013,** *85* (20), 9868-9876.

25.    Henglein, A., Physicochemical properties of small metal particles in solution: "microelectrode" reactions, chemisorption, composite metal particles, and the atom-to-metal transition. *J. Phys. Chem.* **1993,** *97* (21), 5457-5471.

26.    Núñez, M. E.; Hall, D. B.; Barton, J. K., Long-range oxidative damage to DNA: Effects of distance and sequence. *Chem. Biol.* **1999,** *6* (2), 85-97.

27.    Hua, H.; Liu, Y.; Wang, D.; Li, Y., Size-Dependent Voltammetry at Single Silver Nanoelectrodes. *Anal. Chem.* **2018,** *90* (16), 9677-9681.

28.    Obliosca, J. M.; Liu, C.; Yeh, H.-C., Fluorescent silver nanoclusters as DNA probes. *Nanoscale* **2013,** *5* (18), 8443-8461.

29. Mallick, K.; Witcomb, M.; Scurrell, M., Silver nanoparticle catalyzed redox reaction: An electron relay effect. *Mater. Chem. Phys.* **2006,** *97* (2), 283-287.

30. Jackschath, C.; Rabin, I.; Schulze, W., Electron impact ionization of silver clusters $Ag_n$, n≦36. *Zeitschrift für Physik D Atoms, Molecules and Clusters* **1992,** *22* (2), 517-520.

31. Klacar, S.; Hellman, A.; Panas, I.; Grönbeck, H., Oxidation of Small Silver Clusters: A Density Functional Theory Study. *J. Phys. Chem. C* **2010,** *114* (29), 12610-12617.

32. Henglein, A., Small-particle research: physicochemical properties of extremely small colloidal metal and semiconductor particles. *Chem. Rev.* **1989,** *89* (8), 1861-1873.

33. Ho, J.; Ertem, M. Z., Calculating Free Energy Changes in Continuum Solvation Models. *J. Phys. Chem. B* **2016,** *120* (7), 1319-1329.

34. Ribeiro, R. F.; Marenich, A. V.; Cramer, C. J.; Truhlar, D. G., Use of Solution-Phase Vibrational Frequencies in Continuum Models for the Free Energy of Solvation. *J. Phys. Chem. B* **2011,** *115* (49), 14556-14562.

35. Marenich, A. V.; Cramer, C. J.; Truhlar, D. G., Universal Solvation Model Based on Solute Electron Density and on a Continuum Model of the Solvent Defined by the Bulk Dielectric Constant and Atomic Surface Tensions. *J. Phys. Chem. B* **2009,** *113* (18), 6378-6396.

36. Cossi, M.; Barone, V.; Cammi, R.; Tomasi, J., Ab initio study of solvated molecules: a new implementation of the polarizable continuum model. *Chem. Phys. Lett.* **1996,** *255* (4), 327-335.

37. Miertuš, S.; Scrocco, E.; Tomasi, J., Electrostatic interaction of a solute with a continuum. A direct utilizaion of AB initio molecular potentials for the prevision of solvent effects. *Chem. Phys.* **1981,** *55* (1), 117-129.

38. Negishi, Y.; Nobusada, K.; Tsukuda, T., Glutathione-Protected Gold Clusters Revisited: Bridging the Gap between Gold(I)−Thiolate Complexes and Thiolate-Protected Gold Nanocrystals. *J. Am. Chem. Soc.* **2005,** *127* (14), 5261-5270.

39. K., S. P.; K., M. A.; K., P. S., Structural, Electronic, and Optical Properties of Metallo Base Pairs in Duplex DNA: A Theoretical Insight. *Chem. Asian J.* **2012,** *7* (11), 2718-2728.

40. Berezhnoy, A. Y.; Duplij, S. A., Dependence of nucleotide physical properties on their placement in codons and determinative degree. *J. Zhejiang Univ., Sci., B* **2005,** *6* (10), 948.

41. Petty, J. T.; Ganguly, M.; Rankine, I. J.; Baucum, E. J.; Gillan, M. J.; Eddy, L. E.; Léon, J. C.; Müller, J., Repeated and Folded DNA Sequences and Their Modular Ag106+ Cluster. *J. Phys. Chem. C* **2018,** *122* (8), 4670-4680.

42. Wu, Z.; Jin, R., On the Ligand's Role in the Fluorescence of Gold Nanoclusters. *Nano Lett.* **2010,** *10* (7), 2568-2573.

43. Stamplecoskie, K. G.; Kamat, P. V., Size-Dependent Excited State Behavior of Glutathione-Capped Gold Clusters and Their Light-Harvesting Capacity. *J. Am. Chem. Soc.* **2014,** *136* (31), 11093-11099.

44. Chen, Y.; Yang, T.; Pan, H.; Yuan, Y.; Chen, L.; Liu, M.; Zhang, K.; Zhang, S.; Wu, P.; Xu, J., Photoemission Mechanism of Water-Soluble Silver Nanoclusters: Ligand-to-Metal–Metal Charge Transfer vs Strong Coupling between Surface Plasmon and Emitters. *J. Am. Chem. Soc.* **2014,** *136* (5), 1686-1689.

45. Rodolphe, A.; Thibault, T.; Michel, B.; Philippe, D.; Roland, M.; Vlasta, B.-K., Optical Properties of Gas-Phase Tryptophan–Silver Cations: Charge Transfer from the Indole Ring to the Silver Atom. *ChemPhysChem* **2006,** *7* (2), 524-528.

46. Harb, M.; Rabilloud, F.; Simon, D.; Rydlo, A.; Lecoultre, S.; Conus, F.; Rodrigues, V.; Félix, C., Optical absorption of small silver clusters: Agn, (n=4–22). *J. Chem. Phys.* **2008,** *129* (19), 194108.

47. Grandjean, D.; Coutiño-Gonzalez, E.; Cuong, N. T.; Fron, E.; Baekelant, W.; Aghakhani, S.; Schlexer, P.; D'Acapito, F.; Banerjee, D.; Roeffaers, M. B. J.; Nguyen, M. T.; Hofkens, J.; Lievens, P., Origin of the bright photoluminescence of few-atom silver clusters confined in LTA zeolites. *Science* **2018,** *361* (6403), 686-690.

48. Bousquet, B.; Cherif, M.; Huang, K.; Rabilloud, F., Absorption Spectra of Aryl Thiol-Coated Silver Nanoclusters: A Time-Dependent Density-Functional Study. *J. Phys. Chem. C* **2015,** *119* (8), 4268-4277.

49. Scholl, J. A.; Koh, A. L.; Dionne, J. A., Quantum plasmon resonances of individual metallic nanoparticles. *Nature* **2012,** *483* (7390), 421-427.

50. Haberland, H., Looking from both sides. *Nature* **2013,** *494* (7435), E1-E2.

51. Petty, J. T.; Story, S. P.; Hsiang, J.-C.; Dickson, R. M., DNA-Templated Molecular Silver Fluorophores. *J. Phys. Chem. Lett.* **2013,** *4* (7), 1148-1155.

52. Kasperovich, V.; Kresin, V. V., Ultraviolet photoabsorption spectra of silver and gold nanoclusters. *Philos. Mag. B* **1998,** *78* (4), 385-396.

53. Petty, J. T.; Sergev, O. O.; Ganguly, M.; Rankine, I. J.; Chevrier, D. M.; Zhang, P., A Segregated, Partially Oxidized, and Compact Ag10 Cluster within an Encapsulating DNA Host. *J. Am. Chem. Soc.* **2016,** *138* (10), 3469-3477.

54. Zhao, G. F.; Lei, Y.; Zeng, Z., Absorption spectra of small silver clusters Agn (n=4, 6, 8): A TDDFT study. *Chem. Phys.* **2006,** *327* (2), 261-268.

55. Kohn, W.; Sham, L. J., Self-Consistent Equations Including Exchange and Correlation Effects. *Phys. Rev.* **1965,** *140* (4A), A1133-A1138.

# 4. SURFACE STATES AND TOTAL DIPOLE EFFECTS ON THE ELECTRON TRANSFER IN PBS QD-PDI SYSTEMS

Organic semiconductors-based materials recently get significant attention in optoelectronics applications like photovoltaic,[1] transistor,[2] light-emitting diodes,[3] and sensors.[4] But, despite the promising features, the lower device efficiency limits the uses of these materials commercially. The energy conversion in the semiconductor-organic materials is mostly dependent on the carrier transfer steps. One dominating variable of the photoexcited charge transfer is related electronic state energy alignment of the electron acceptor and donor. Photoexcited electron transfer from QD to dye or dye to QD increases the overall energy conversion rate of dye functionalized QD.[5-6] Therefore, surface passivation is a useful tool to modulate the electronic structure of semiconductor-organic systems.[5, 7]

On the other hand, PDI has a strong reduction potential[8], extensive light absorption[9], and a one-dimensional charge transport promoter.[10] The photoinduced electron can transfer to PDI, and an anionic PDI system can be utilized for catalysis,[8, 11] charge separation. However, the photo-induced electron transfer efficiency is susceptible to electronic structure, $\pi$-$\pi$ stacking of the PDI, and semiconductor-PDI assembly. Motivated by these promising features, we have studied surface passivation and surface state effects on the electronic structure of the PbS-PDI system.
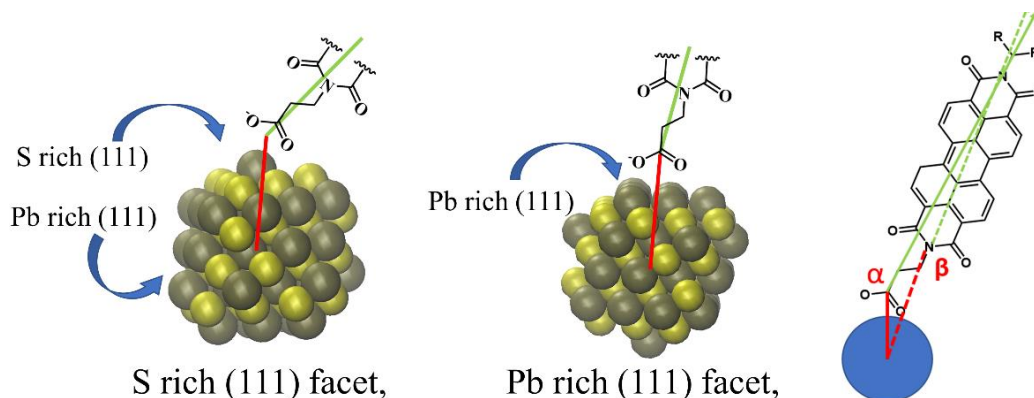
**Figure 4.1**: The PbS QD model what we used in this study. The axis angle is defined from the center of the QDs and N in the top PDI axis.

## 4.1. Methodology

Since we use deprotonated ligands, we have considered non-stoichiometric PbS QDs. A $Pb_{44}S_{40}^{+8}$ QD model is prepared from the bulk PbS rocksalt lattice structure (Figure 4.1). (111) facet is the most reactive side of a Pb chalcogenide material, PbS QD model prepared as larger (111) facets. The calculated PbS model has a total of eight (111) facet, where four Pb and four S rich facet. The excess Pb is attached to the S rich (111) facets. In the first stage of calculations, each of the Pb rich (111) facets are capped with Cl atom ($Pb_{44}S_{40}Cl_4^{+4}$). This let us minimize the computational model size and resources. So, QD is passivated with a total of four ligands. In the second stage of calculations, all the QD surfaces are passivated with different organic molecules – oleic acid, cinnamic acid derivatives, and electron acceptor perylene diimide (PDI) derivatives of variation in linker group. The effects of ligands on the frontier band of the PbS QDs and ligands effects on PDI localized state are studied. PbS quantum dot surfaces are passivated by three different cinnamic acid (CA) derivatives – trans-2,6-Difluoro CA (*DFCA/DFCA26*), trans-3,4-Difluoro CA (*DFCA35*) and trans-4-(Trifluromethyl) CA (*CFCA*) and an oleic acid analog propanoic acid (*OA*) **(Figure 4.2)**.
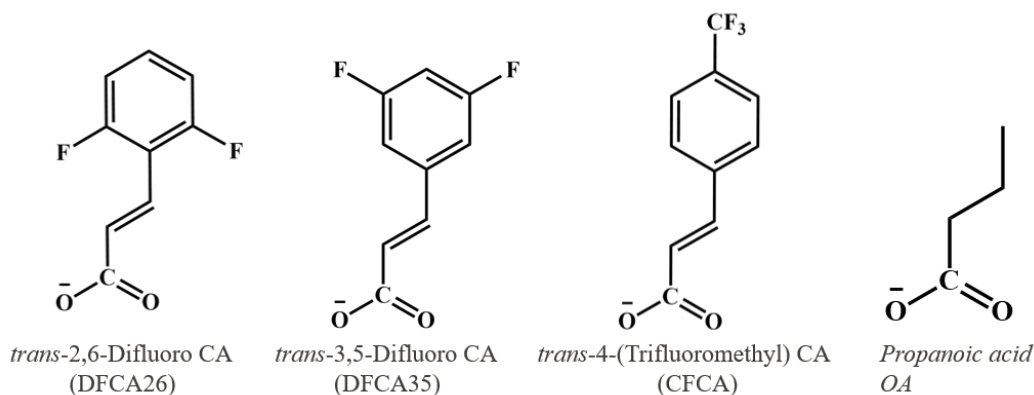
**Figure 4.2:** Cinnamic acid derivative and an oleic acid analog (propanoic acid) are used to passivate the PbS QD surface. The short name we used to describe each of the ligands are given in the parenthesis.

The ground state geometries of all states are optimized using the DFT method (sub-chapter 2.1) using the PBE0 functional and a mixed basis set of LANL2DZ for QD and 6-31g* for the ligands and dye. Dichloromethane is used as a solvent and implemented in DFT calculation using the CPCM solvation method. The density of states (DOS) is obtained by dressing the electronic energies of the molecular orbitals. The projected density of states (PDOS) is plotted by Gaussian broadening the partial occupation of molecular orbitals in a fragment.

$$PDOS_{Frag}(\varepsilon) = \sum_{i=1}^{N} F_{fag,i} e^{-\frac{1}{2}\left(\frac{\varepsilon-\varepsilon_i}{\sigma}\right)^2} \tag{4.1}$$

PDOS of the fragment '$frag$', where partial occupancy of the $i^{th}$ orbitals is $F_{fag,i}$ and $N$ is the total number of electrons. To calculate the PDI ligand axis on the surface of the QDs, the QD surface is considered a spherical surface. The axis angle ($\alpha$) is defined by the angle between the vector of the center of mass of the QD to carbon in the carboxylic group and the vector of the same carbon to N in the PDI core (**Figure 4.1**). The two different conformational isomers can be made by replacing one ligand. PDI can be replaced on the Pb rich or S rich (111) facets (Figure 4.1).

119
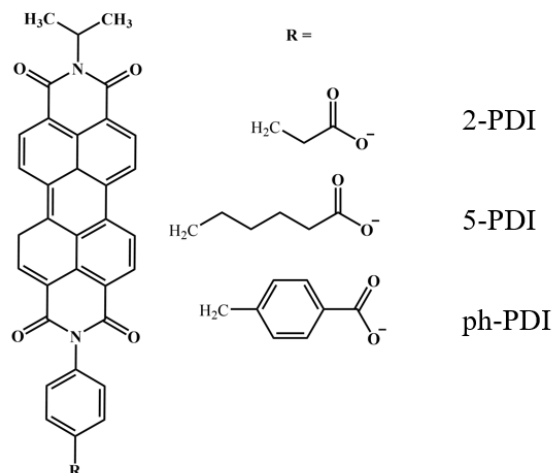
**Figure 4.3:** PDI molecule and its derivatives of a different linker group.

Binding energy is calculated by using the energy of the optimized fragments. To calculate the PDI binding energy of a system, we optimized both fragments – PDI and QD-Ligands. The PDI binding energy, $E_{bind,PDI}$ as follows -

$$E_{bind,PDI} = E_{QD-Ligand-PDI} - (E_{QD-Ligand} + E_{PDI}) \qquad (4.2)$$

$E_{QD-Ligand-PDI}$ is the total energy of ligand and PDI passivated QD, $E_{QD-Ligand}$ is the ligand passivated QD energy, this fragment is cationic and $E_{PDI}$ is the energy of the deprotonated anionic PDI molecule.

## 4.2. Ligand and PDI Linker Group Effects on Electronic Properties of the PbS-PDI

Kroupa et al. have shown a surface ligand engineering pathway to tune the frontier band edge. In the first step, we have calculated the electronic band structure of the eight OA, DFCA and CFCA passivated PbS QDs. Ligand exchange is the common synthesis procedure to make dye sensitize QD. So, one ligand in the passivated QD is substituted and replace with a PDI molecule. Reoptimized the structure and calculated the MO energy. **Figure 4.4** is showing the MO energy of the ligand passivated, and one PDI substitutes QD-PDI systems. It is shown that frontier band states energy increases with increasing the ligand dipole (CFCA < OA < DFCA)

although shifted by >100meV (Black bar in **Figure 4.4**). It is noted that this model is relatively

small in comparison to the experimental condition and is passivated by only four ligands. As

expected, both HOMO and LUMO are localized on the PbS QDs. Substitution of one ligand by

2-PDI and 5-PDI creates another state in the band edge.  The projected density of states (PDOS)

shows that the intermediates states are PDI localized states (Figure 4.5). Relative comparison

with the MO energy of the non-PDI model shown that PDI does not change the QD bandgap, but

the relative energy alignment of the bandgap states and PDI originated states are modulated. The

overall QD-PDI junction is a type-II heterojunction. The type of linker group of PDI (5-PDI vs.

2-PDI) does not alter the PDI bandgap. Figure 4.6 shows the HOMO and LUMO molecular

orbitals localization of the OA passivated and PDI substitute PbS-PDI.  HOMO orbitals are

localized on the PbS core, but in the case of PDI, HOMO localized on the PDI core. Due to the

longer linker group in 5PDI, LUMO is pure PDI core localized state, but LUMO in the 2-PDI is

partially hybridized with the QD surface states. In the photoexcited carrier transfer process in the

PbS-PDI model, the photoexcited electron from the QD transfer to the PDI molecules. So, the

energy offset between the LUMO and LUMO+1 is a driving force. If the geometry

reorganization energy is minimum, the adiabatic energy offset could be considered to get a

qualitative electron transfer rate. Therefore, in the following section, we have investigated the

structural effect on the unoccupied states' energy offset in the PbS-2PDI system.
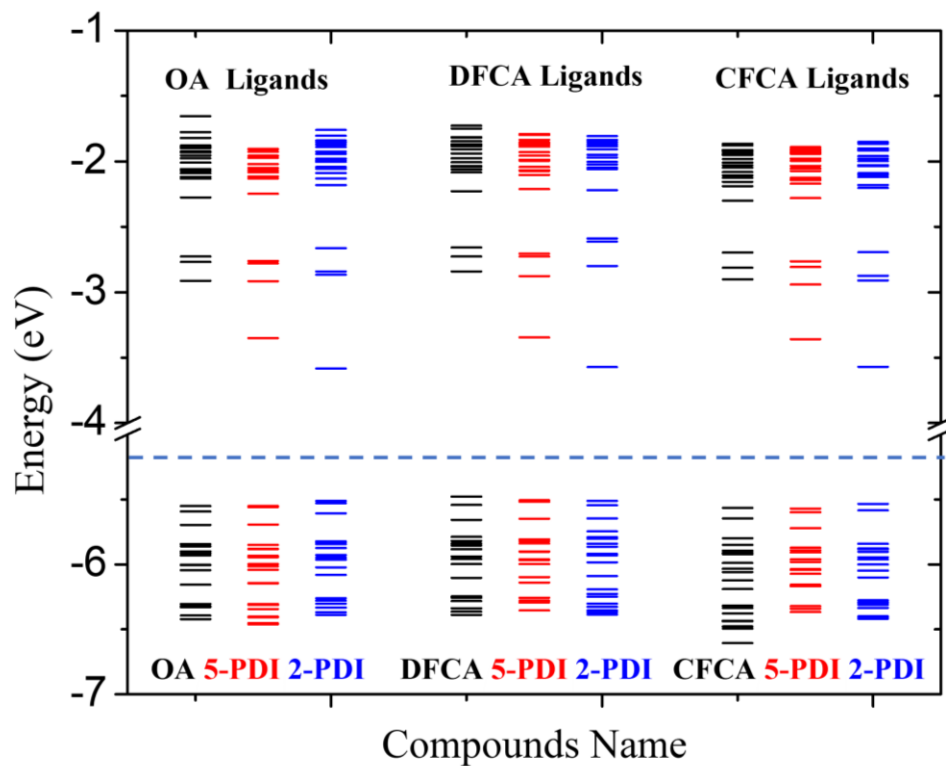
**Figure 4.4:** Molecular orbitals energies of three different ligands passivated and with the two different PDI derivatives. The horizontal dotted line indicates the separation of occupied and unoccupied orbitals.
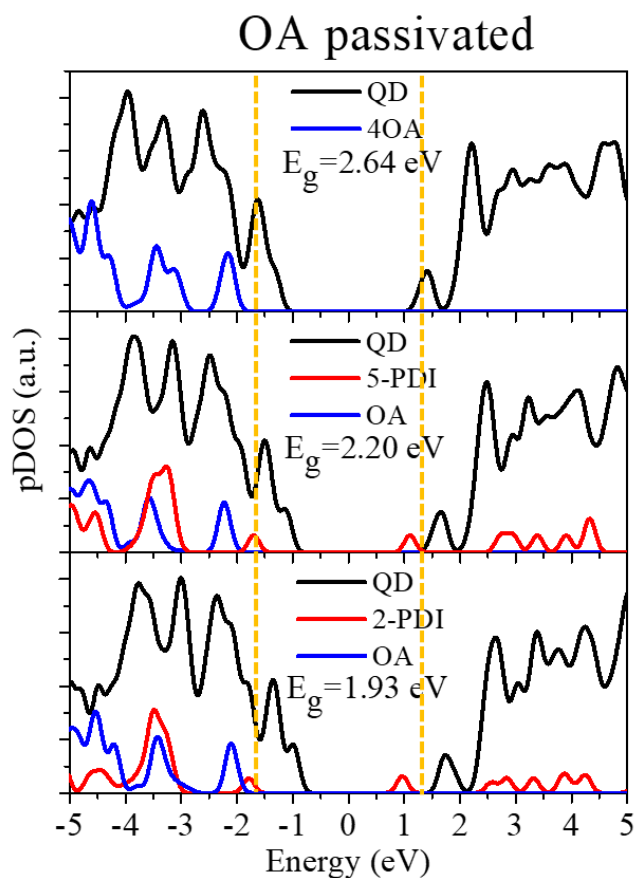
**Figure 4.5:** Projected density of State (PDOS) of the OA (propanoic acid) passivated PbS QDs. Two other models are on OA substitute by 5PDI and 2PDI.
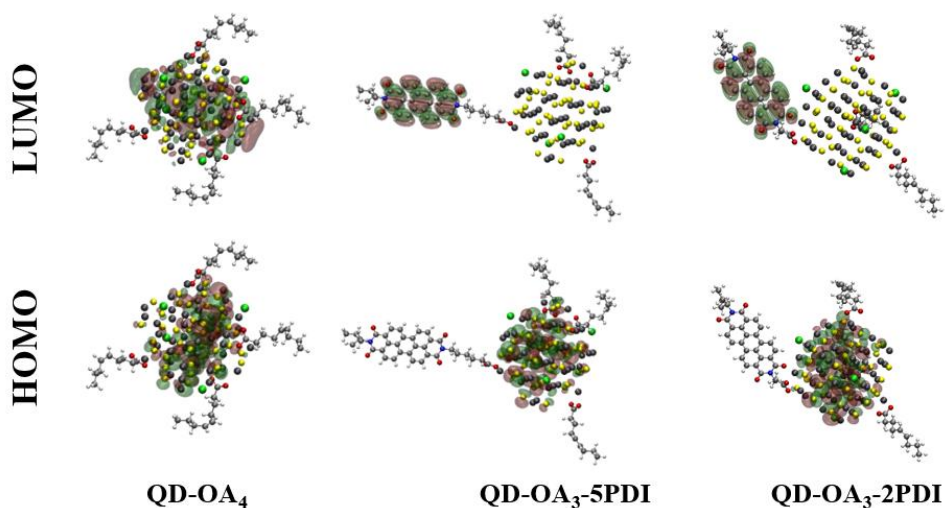


**Figure 4.6:** Frontier orbitals of the OA passivated, and 5PDi and 2PDI substituted models.

## 4.3. Structural Isomers and its' Effects on the Surface State of QD-2PDI

In continuation of studies with a different linker, we studied the factor influence the structural feature, hence the overall electronic structure. We considered the $Pb_{40}S_{44}^{+8}$ PbS QD and passivated by seven ligands and one 2-PDI on the Pb rich (111) facet. The optimized structure is shown in Figure 4.7. Optimized structures show a qualitative trend between the ligand dipole and PDI molecule interaction with the QD surface interactions. The optimized structure shows a correlation between the energy offset to the total dipole of the optimized structures.

On the other hand, the qualitative trend on the structure is also presented. The PDOS is shown that ligands do not contribute to the electronic frontier states (Figure 4.8). Our collaborator at the University of Texas at Austin prepared the PbS-PDI model and measured the intrinsic electron transfer rate (Results not published yet). The Calculated binding energy of the PDI and total dipole is also shown a linear relationship with the intrinsic electron transfer rate (Figure 4.9). All these linear correlations suggest that structural features would dominate the overall electron transfer rate, and that could be a result of overall dipole change in response to structural variation.



**DFCA26**
$\mu = 22.4843\ D$

**OA**
$\mu = 14.98\ D$

**DFCA35**
$\mu = 8.6444\ D$

**CFCA**
$\mu = 3.3943\ D$
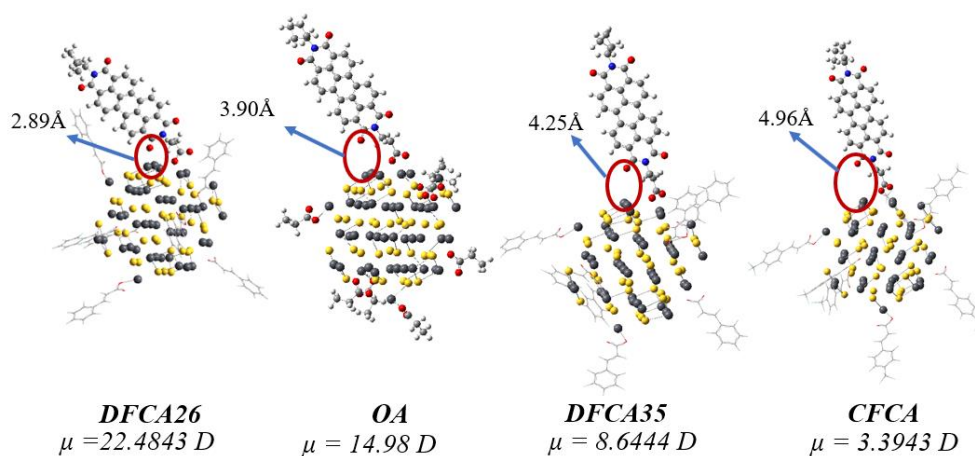
**Figure 4.7:** The optimized structure of the PbS-2PDI with different ligand passivated. The structure features are correlated with the total dipole of the QD-PDI system.
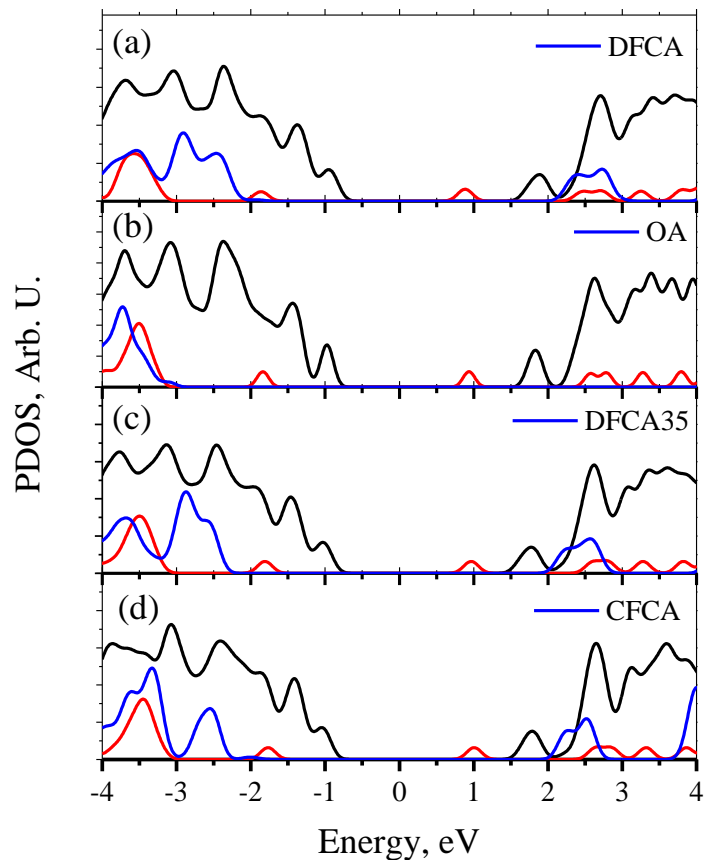
**Figure 4.8:** Projected density of states (PDOS) PbS-2PDI model with the different ligand passivation on the surface. 2PDI is attached on the Pb rich (111) facet of the PbS QD.
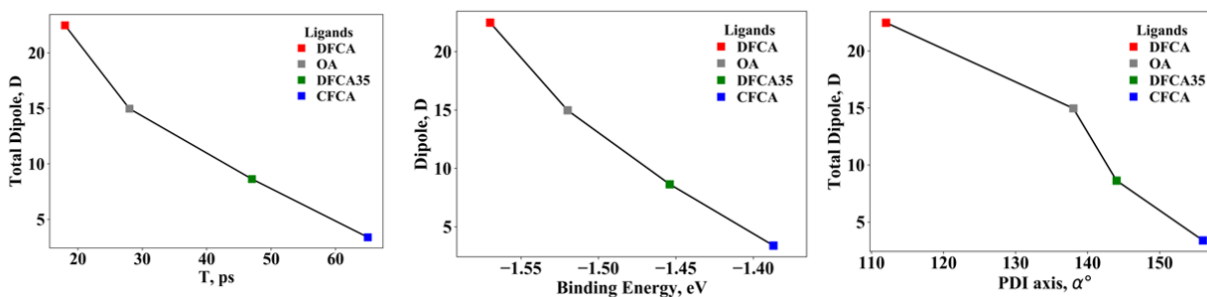


**Figure 4.9**: Intrinsic electron transfer rate from the PbS to PDI, PDI binding energy and PDI axis angle (α) dependence on the total dipole of the systems.

To Investigate the structural isomers, we have created a systematic variation of the initial QD-2PDI geometries. We used the DFCA, DFCA35, CFCA passivated geometry (Figure 4.7) and replaced the ligand with the other two ligands (Scheme 4.1). The new initial geometries are

optimized using the DFT method. This procedure shows the effects of ligands on structural variation. Due to the structural similarities between the CA derivative, only CA derivatives ligand passivated model are used to make structural isomers; The OA passivated QD geometry is not used to make isomers.
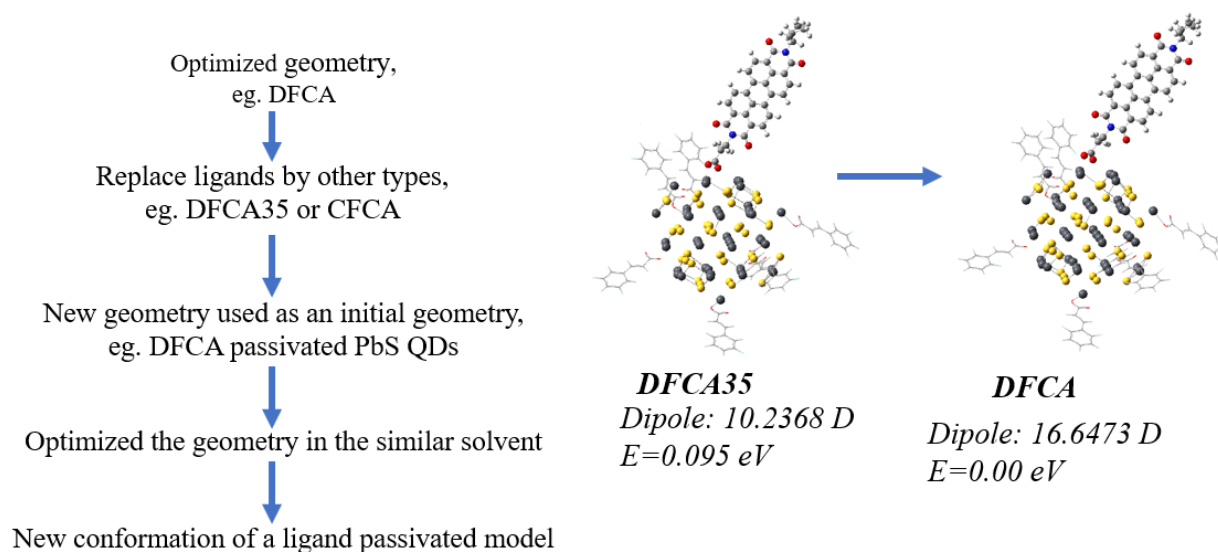


**Scheme 4.1:** A scheme to create the different initial geometry of a particular CA derivative passivated model from the other ligand passivated optimized geometries. We have skipped OA passivated structure due to the significant structural dissimilarity with CA derivative ligand.

Figure 4.10 is showing the PDI binding energy and intrinsic electron transfer rate with the total dipole of the systems. It is noticed that geometry reorganization is minimum in the geometry optimization after the ligand modification. We assume that geometries were relaxed in the local minima in the potential surface, which is not overcome by ligand modification. These structural isomers' variations are comparable with the colloidal QD environment where ligand exchange can create different structural isomers. The axis angle α measures the orientation of the PDI on the QD surface. The α value of 180° indicates the vertical PDI on the QD surface, and 90° indicates the lying on the surface. 2PDI is the most tilted on the surface in DFCA passivated QD. As such, PDI has the highest binging energy in the structure obtained from the initial DFCA

passivated model (solid circle marker in figure 4.10). The PDI binding energy strength is correlated with the surface interaction of the QD-PDI. It is shown that the DFCA passivated system has the highest dipole in all three series of conformations (Figure 4.10). In each series of conformations, PDI binding energy increases with decreasing the total dipole moment, while binding energy increases from one series to another series with increasing the total dipole. It suggests that PDI's stronger binding minimizes the total dipole of the systems, but the structural change would increase the total dipole despite the stronger PDI bond.
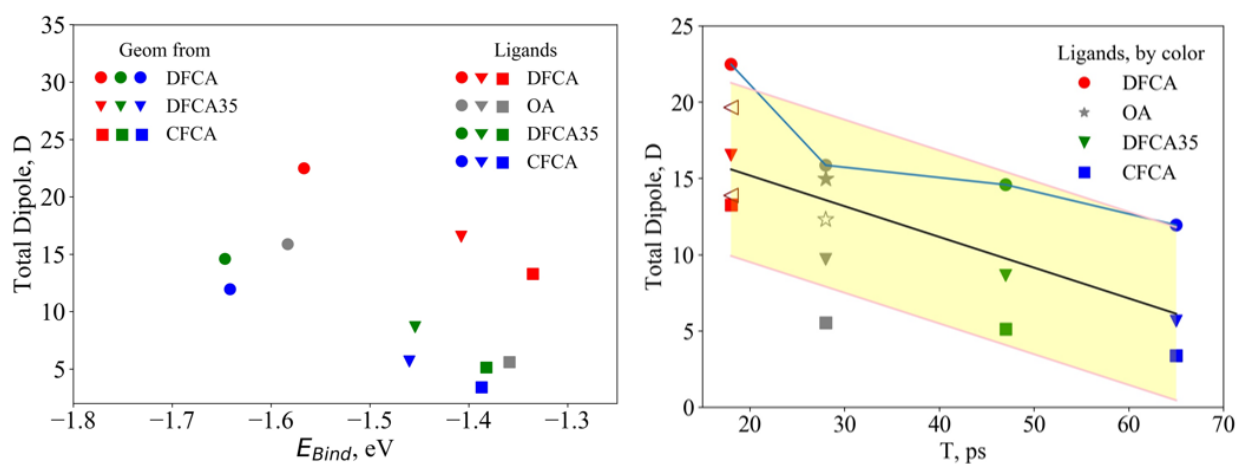


**Figure 4.10**: The binding energy and intrinsic electron transfer rate relationship with the total dipole of the ligand passivated PbS-2PDI systems. The total dipole of all structural isomers shown a linear statistical relationship.

The total dipole is linearly correlated with the intrinsic electron transfer rate (Figure 4.9). The correlation is shown considering the total dipole of all clusters. Besides the structural conformation created by ligand exchange, we have made a model where PDI is on S rich (111) facets, with different orientations in initial geometries. The total dipole of the all Ligand-PbS-2PDI model is plotted with the experimental electron transfer rate in **figure 4.10**. The conformation which is created from the optimized DFCA passivated model is the lowest in total energy in the all ligand series. It indicates that the stronger binding energy and QD-PDI interaction through the surface state would increase the stability of the QD-PDI systems (cyan

line in **Figure 4.10**). The electron transfer rate shows linearly dependent on the statistical

average of the total dipole of all considered models (yellow shaded area represents the 95%

confidence level).
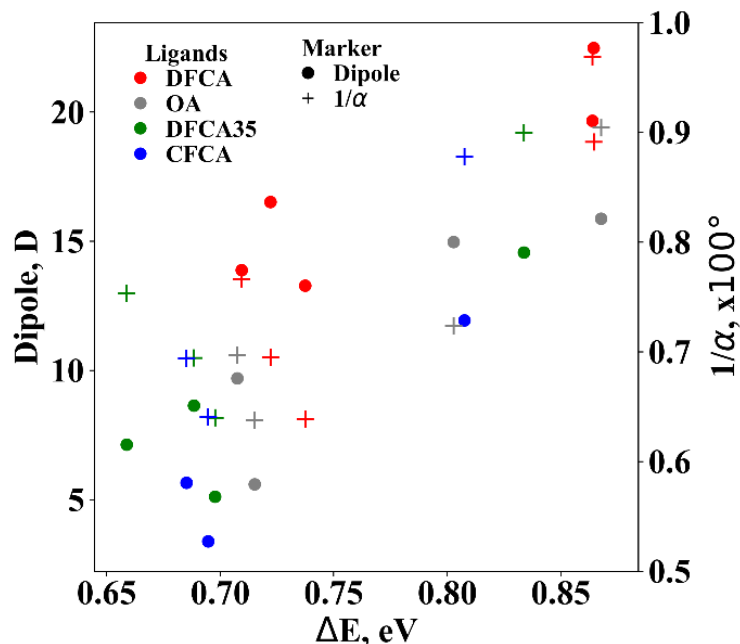


**Figure 4.11**: The plot of the total dipole (D) and inverse alpha (α) as a function of the energy offset between the LUMO and LUMO+1. All the isomers of the all different ligand passivated PbS-2PDI are included in this chart.

Therefore, one of the driving forces for the QD to PDI photoexcited electron transfer is

the energy offset between the LUMO and LUMO+1. The total dipole and axis angle both

dominate the overall electron transfer rate. Figure 4.11 shows that the energy ($\Delta E$) linearly

increases with increasing dipole moment and inverse of α. It is noted that smaller α or larger

inverse α indicates stronger QD surface – PDI interaction. Despite sparse data points, the overall

qualitative correlation suggests that experimental electron transfer would be comparable with the

ensemble average of the computational results. On the other hand, PDI -QD surface interaction

in the DFCA passivated cluster could have two effects. The redox potential of PDI is a suitable

core modification. QD surface and PDI core hybridization influence the redox potential of the

PDI core,[12] which increases the rate of electron-accepting of PDI.[13] On the other hand, QD surface-PDI interaction would initiate the through-space electron transfer pathway. In a QD-PDI system, a photoexcited electron from the QD transfer to the PDI molecule through the bond. In addition to this, the through-the-space pathway can be activated by the QD surface-PDI core interactions (Figure 4.12). A similar mechanism is suggested in the CdSe-viologens[14] and dye-sensitized CsPbI$_3$ perovskite materials.[15]
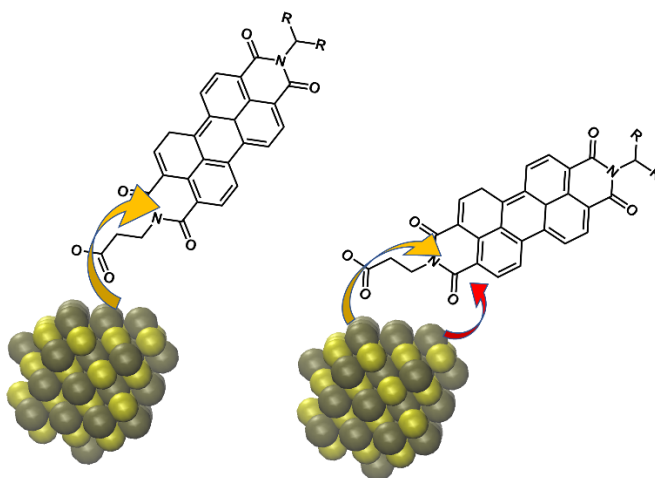


**Figure 4.12:** Schematic diagram of the two possible photoexcited electron transfer pathways. Depending on the PDI molecule's bond on the PbS QD surface, a photoexcited electron can transfer to the PDI only through the bond pathways or both- through the bond and the space pathways.

## 4.4. Summary

In summary, our studies have shown the dependence of the excited state electron transfer rate on the structure-dependent surface state hybridization. The higher dipole moment of a surface passivated ligand would tune the frontier band alignment, but PDI localized LUMO states energy dominated by the feature of PDI-QD surface interaction. We hypothesize that it increases the PDI core's electron-accepting capability, and besides, it also initiates an additional electron transfer pathway, which could significantly increase the electron transfer rate. Although the non-adiabatic and photoexcited electron transfer process is not studied in this study, we able

129

to show a structural relationship with the electronic characteristic of the system. Our result will

help rationalize the experimental results and design the methodology for the non-adiabatic

electron transfer process, which is our future plan of study.

## 4.5. References

1.  Maity, P.; Debnath, T.; Ghosh, H. N., Ultrafast Hole- and Electron-Transfer Dynamics in CdS–Dibromofluorescein (DBF) Supersensitized Quantum Dot Solar Cell Materials. *J. Phys. Chem. Lett.* **2013,** *4* (23), 4020-4025.

2.  Mei, J.; Diao, Y.; Appleton, A. L.; Fang, L.; Bao, Z., Integrated Materials Design of Organic Semiconductors for Field-Effect Transistors. *J. Am. Chem. Soc.* **2013,** *135* (18), 6724-6746.

3.  Chen, Y.; Ma, D., Organic semiconductor heterojunctions as charge generation layers and their application in tandem organic light-emitting diodes for high power efficiency. *J. Mater. Chem.* **2012,** *22* (36), 18718-18734.

4.  Li, L.; Gao, P.; Baumgarten, M.; Müllen, K.; Lu, N.; Fuchs, H.; Chi, L., High Performance Field-Effect Ammonia Sensors Based on a Structured Ultrathin Organic Semiconductor Film. *Adv. Mater.* **2013,** *25* (25), 3419-3425.

5.  Kroupa, D. M.; Arias, D. H.; Blackburn, J. L.; Carroll, G. M.; Granger, D. B.; Anthony, J. E.; Beard, M. C.; Johnson, J. C., Control of Energy Flow Dynamics between Tetracene Ligands and PbS Quantum Dots by Size Tuning and Ligand Coverage. *Nano Lett.* **2018,** *18* (2), 865-873.

6.  Chang, J.; Ogomi, Y.; Ding, C.; Zhang, Y. H.; Toyoda, T.; Hayase, S.; Katayama, K.; Shen, Q., Ligand-dependent exciton dynamics and photovoltaic properties of PbS quantum dot heterojunction solar cells. *Phys. Chem. Chem. Phys.* **2017,** *19* (9), 6358-6367.

7.  Kroupa, D. M.; Vörös, M.; Brawand, N. P.; McNichols, B. W.; Miller, E. M.; Gu, J.; Nozik, A. J.; Sellinger, A.; Galli, G.; Beard, M. C., Tuning colloidal quantum dot band edge positions through solution-phase surface chemistry modification. *Nat. Commun.* **2017,** *8* (1), 15257.

8.  Ghosh, I.; Ghosh, T.; Bardagi, J. I.; König, B., Reduction of aryl halides by consecutive visible light-induced electron transfer processes. *Science* **2014,** *346* (6210), 725-728.

9.  Gosztola, D.; Niemczyk, M. P.; Svec, W.; Lukas, A. S.; Wasielewski, M. R., Excited Doublet States of Electrochemically Generated Aromatic Imide and Diimide Radical Anions. *J. Phys. Chem. A* **2000,** *104* (28), 6545-6551.

10.     Yang, J.; Miao, H.; Wei, Y.; Li, W.; Zhu, Y., π–π Interaction between self-assembled perylene diimide and 3D graphene for excellent visible-light photocatalytic activity. *Applied Catalysis B: Environmental* **2019,** *240*, 225-233.

11.     Zeng, L.; Liu, T.; He, C.; Shi, D.; Zhang, F.; Duan, C., Organized Aggregation Makes Insoluble Perylene Diimide Efficient for the Reduction of Aryl Halides via Consecutive Visible Light-Induced Electron-Transfer Processes. *J. Am. Chem. Soc.* **2016,** *138* (12), 3958-3961.

12.     Huang, C.; Barlow, S.; Marder, S. R., Perylene-3,4,9,10-tetracarboxylic Acid Diimides: Synthesis, Physical Properties, and Use in Organic Electronics. *The Journal of Organic Chemistry* **2011,** *76* (8), 2386-2407.

13.     Abdelhameed, M.; Aly, S.; Lant, J. T.; Zhang, X.; Charpentier, P., Energy/Electron Transfer Switch for Controlling Optical Properties of Silicon Quantum Dots. *Sci. Rep.* **2018,** *8* (1), 17068.

14.     Morris-Cohen, A. J.; Peterson, M. D.; Frederick, M. T.; Kamm, J. M.; Weiss, E. A., Evidence for a Through-Space Pathway for Electron Transfer from Quantum Dots to Carboxylate-Functionalized Viologens. *J. Phys. Chem. Lett.* **2012,** *3* (19), 2840-2844.

15.     Forde, A.; Kilin, D., Hole Transfer in Dye-Sensitized Cesium Lead Halide Perovskite Photovoltaics: Effect of Interfacial Bonding. *J. Phys. Chem. C* **2017,** *121* (37), 20113-20125.

# 5. THE EFFECTS OF INTERFACE AND CONFINEMENT ON HOT CARRIER DYNAMICS IN PBSE NPL AND QD

PbSe NPL synthesized by oriental attachment of PbSe QD by Cl-Pb-Cl bridging on (110) facet and grown in (100) lattice direction[1]. The effects of the $PbCl_2$ bridging molecules on the hot carrier relaxation process is still unknown, although this method gives more control on the orientation of the lateral dimension and thickness. Despite the promising feature of PbSe NPL, no detailed study on the excited carrier dynamics in PbSe NPL and confinement effects on carrier relaxation are reported yet. Moreover, we have discussed in chapter 1 that how carrier relaxation rate would dominate the CM rate in the confined nanocrystals. So, an ab-initio method based excited state study would be able to predict the confinement effects and carrier relaxation dynamics. Therefore, in this chapter, we have studied $PbCl_2$ bridged PbSe NPL and $PbCl_2$ passivated PbSe QDs to investigate the effects of the confinement and $PbCl_2$ bridging molecule on the hot carrier dynamics. Due to the 1D confinement and symmetry breaking in NPL, degenerate frontier states of the bulk PbSe are split and form a frontier band in NPL. Hot carrier relaxation rate is slower in NPL compare to 0-D QD, especially the hot electron. High energy electronic states of NPL are coupled with optical phonon in the range of 150 cm$^{-1}$ to 225 cm$^{-1}$, while QDs states are mainly couple with acoustic phonon.

## 5.1. NPL and QD Model and Methodology

### 5.1.1. Preparation and Consideration of the NPL and QD Models

The initial structure was made by cutting $(PbSe)_{68}$ from the bulk PbSe rocksalt structure, and then 12 $PbCl_2$ molecules are added to the 12 (110) facets of the $Pb_{68}Se_{68}$ unit. It was reported that PbSe QD's (110) and (111) facets are the most reactive surface. $PbCl_2$ molecules are attached on the (110) surface and form a network between the PbSe QDs. Experimental results

show the consistent formation of approximate 2 nm thick NPL[1], which is equivalent to 6 layers thick of the PbSe rocksalt crystals. Previous theoretical reports are also suggested that considerable accurate experimental results can be predicted by using six layers $Pb_{68}Se_{68}$ QD. The periodic cell for the three dimensionally confined QD calculation is prepared by adding an 8Å vacuum in all three directions. On the other hand, the NPL model is prepared by maintaining periodicity in the X and Y axis and 20 Å vacuum in the Z-direction.[1] Z-direction is meant to the confined direction of the NPL in all the results in this chapter. Both structures are optimized by DFT method[2] (details *in subsection 2.1*) using a GGA functional PBE[3] and projector-augmented wave (PAW) pseudopotentials[4] in VASP software packages[5]. NPL calculations are performed with 2x2x1 and QD in 1x1x1 k-point in Monkhorst pack mesh. NPL has a direct gap of 1.26 eV at Gamma point and the lowest direct bandgap of 0.96 eV at the L high symmetry point of the first Brillouin zone. Previous experimental study and hyperbolic band model[6] suggested that 2nm thick PbSe NPL bandgap is ~1.20 eV[1]. Considering the very large Bohr radius of PbSe (~46nm) while the finite dimension of the synthesized NPL, the calculated bandgap (0.96 eV) of the infinitely elongated PbSe NPL model is considered as a reasonable agreement. Moreover, it is already established from the previous studies that the hybrid and range separated functional, eg. PBE0[7], HSE06[8] does not change the ground state electronic structure and the wavefunction localization of the Pb and Cd chalcogenide nanomaterials. However, hybrid functional increases the bandgap compare to the GGA functional[9]. Spin-orbit correction is not included since it was reported that the inclusion of spin-orbit has less than 1% correction in lattice parameters and negligible effects on the electronic structure.[10-11]
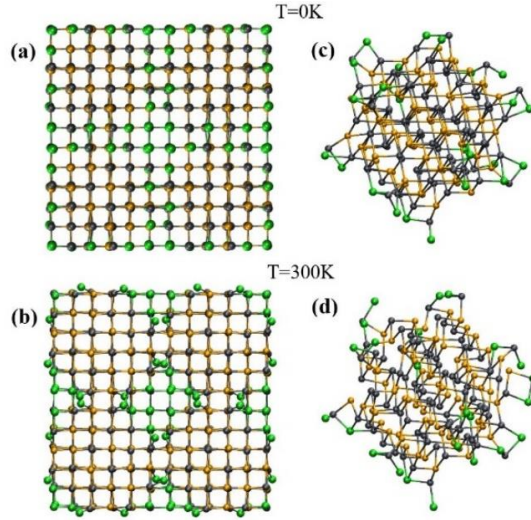
**Figure 5.1:** Geometries of the PbCl$_2$ bridged PbSe nanoplatelets and PbCl$_2$ passivated PbSe QDs. Image a and c are the nanoplatelets and QD, respectively optimized at 0K. Optimized NPL and QD geometries are heated up to 300K and shown in b and d, respectively. Color scheme: dark gray – Pb, yellow – Se, green – Cl
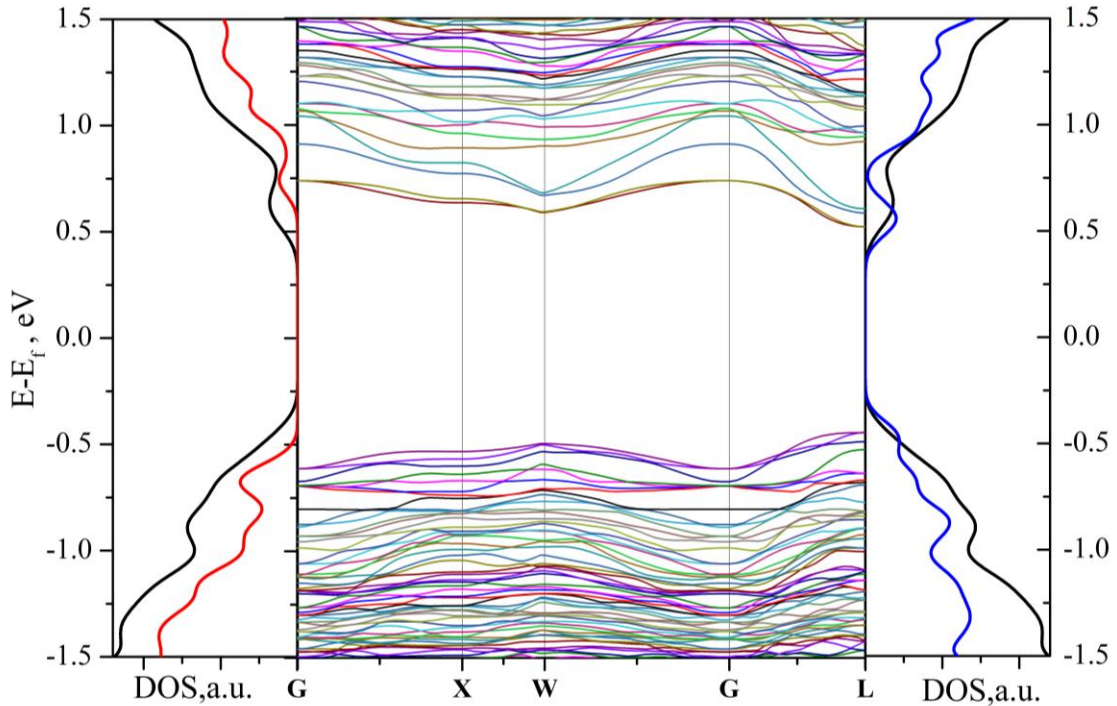


**Figure 5.2:** The energy band over the first Brillouin zone of the Cl-bridged PbSe NPL. The right and left panels are the density of states (DOS) at Gamma (G) and L high symmetry points, respectively. The energy band calculations are done at 2x2x1 K-point mesh, with a minimal number of K-point along with the NPL thickness. The NPL has the 0.96 eV direct bandgap at the high symmetry point L while the direct gap 1.26 eV at the Gamma point. Black lines in the left and right panel are the average density of states over the G, X, W, and L high symmetry points.

134

### 5.1.2. Thermalization and Molecular Dynamics

We have run a molecular dynamics simulation at room temperature (300K). To attain the equilibrium ionic kinetic energy, the optimized geometries are thermalized at 300K by velocity scaling for 1.0 ps long with similar functional and other parameters. The structure of NPL optimized at 0 K shows that $PbCl_2$ molecules form an in-lattice bridging between the QD units, but $PbCl_2$ acts as Cl terminated surface passivated molecule in the 3-D confined QD structure (Figure 5.1). Due to relaxing the confinement energy in X and Y directions, surface reconstructions are minimum in NPL compare to the $PbCl_2$ passivated QD. Increasing the kinetic energy in NPL at 300K, $PbCl_2$ is shown the maximum atomic displacement. However, Cl-Pb-Cl is shown only in-plane vibration over the adiabatic trajectory (one snapshot in Figure Ab). On the other hand, QD has a minimum overall average surface modification at 300K compared to the optimized structure at 0K. The obtained geometry from the thermalization step is used to calculate the adiabatic trajectory using molecular dynamics calculation in the VASP software package[5]; the complete theory is given in the sub-chapter 2.5. Although there has no computational study on the excited state lifetime of the similar model, the study of the comparable PbSe QDs model predicted ≈3.0ps electron lifetime.[12] Therefore, we have simulated 5.0ps and 4.0ps long adiabatic trajectories for the NPL and QD respectively.

## 5.2. Ground State Electronic Structure of NPL and QD

### 5.2.1. Consideration of the Band Structure and Initial Condition of the Simulation

We have calculated the NPL's electronic band structure over G, X, W, and L high symmetry points in the first Brillouin zone and 20 points in between each point (Figure 5.2). The overall band structure is comparable with the bulk PbSe, but higher energy splitting due to the confinement. NPL has a minimum direct bandgap at L high symmetry points. Electronic

structure, especially band-edge states, is sparse with a sub-gap at L-point compared to the

gamma point. Characteristics of the band edge states of materials are more important for

optoelectrical devices because the hot carrier relaxed to the band edge state, and recombination

or separation takes place from the band edge states. As such, in the case of NPL, all the

following calculations are done based on the electronic states at L high symmetry point.
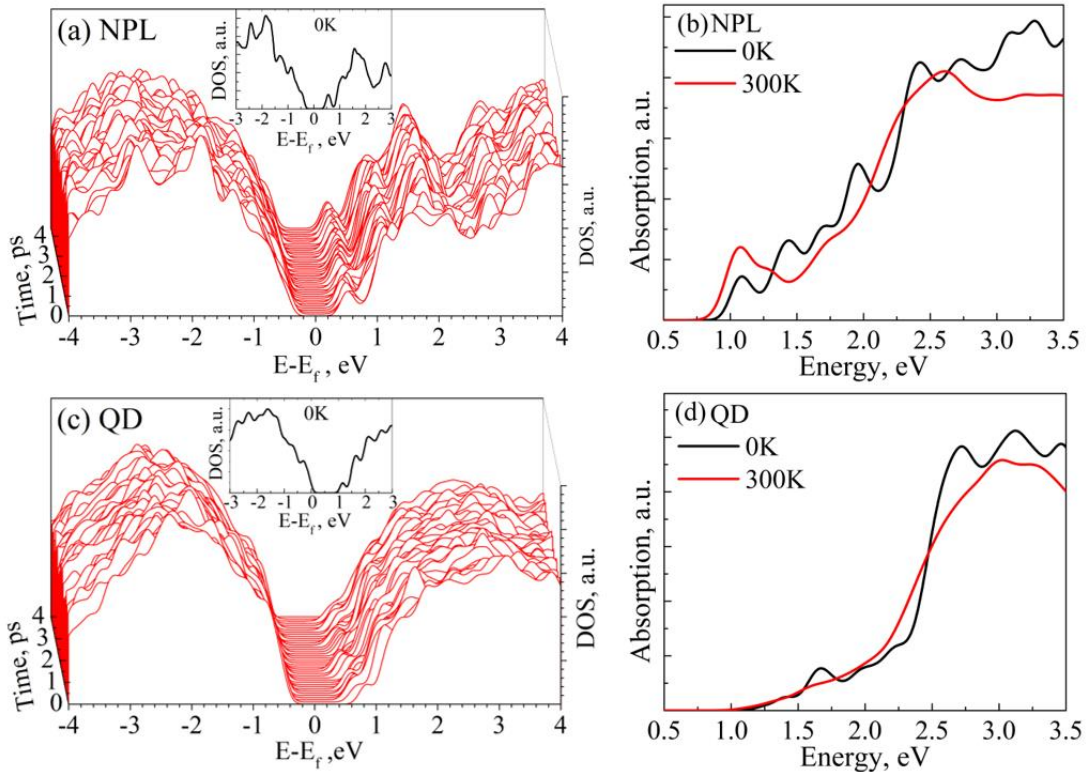


**Figure 5.3:** Time-dependent total density of states (DOS) of the PbCl$_2$ bridged NPL(a), and QD (c) at 300K. DOS of the NPL and QD at 0K is shown in the insets of the respective panels. The highest occupied molecular orbital (HOMO) energy is close to the Fermi energy in QD at 0K. Absorption spectra of both NPL and QD are shown in the panel (b) and (d), respectively. Absorption spectra at 300K are the average absorption spectra of the 100 fs interval over the adiabatic trajectory.

**Figure 5.3** is showing the total density of states (DOS) of the PbSe NPL and QD. Ground

state electronic structure of the NPL at the room temperature has a minimum variation over the

time while the 3-D confinement leads to the bandgap fluctuation at the room temperature

(**Figure 5.3 a, c**), as such effective mass of the band edge electrons and holes in the NPL are

136

comparable in the whole adiabatic trajectory. Strong confinement effect in QD results in almost homogeneous and discrete unoccupied states, while NPL has shown a sub-gap in the unoccupied band. To understand the effects of the $PbCl_2$ in the PbSe lattice, we have calculated the projected density of states (pDOS) of both NPL and QD (Figure 5.4 and 5.5). The occupied band is dominated by the Se and unoccupied band Pb. The overall PDOS structure agrees with the previously reported PbSe band structure.[13] The discrete feature of the NPL in the unoccupied band is the result of the Pb localized state. Most importantly, Cl contribution on the band edge states is minimum, which implies that $PbCl_2$ bridges do not create any trap state in the frontier occupied and unoccupied band.
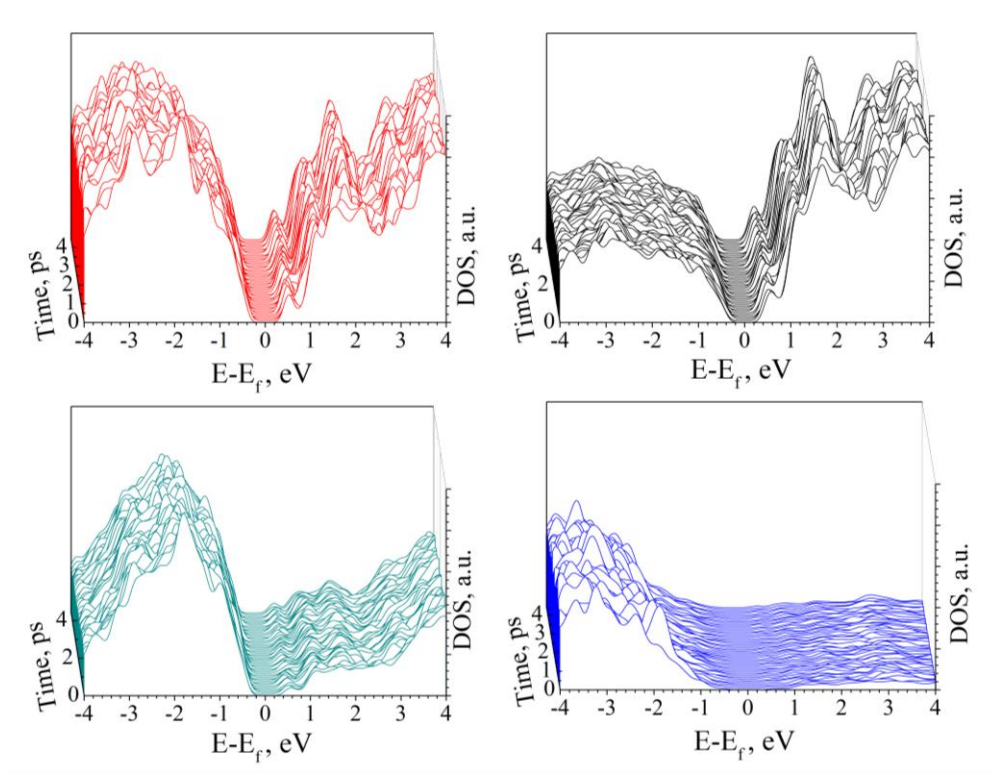


**Figure 5.4:** Total density of states (DOS) (a) and the projected density of states (pDOS) of the Pb (b), Se (c), and Cl (d) of the $PbCl_2$ bridged NPL.
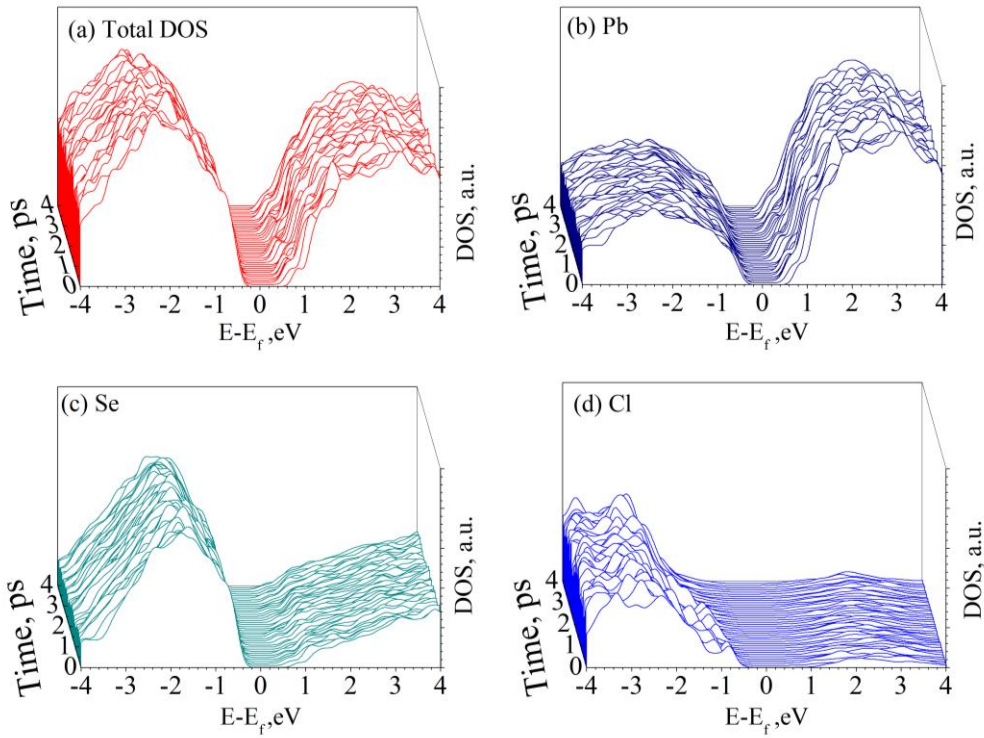
**Figure 5.5:** Total density of states (DOS) (a) and the projected density of states (pDOS) of the Pb (b), Se (c), and Cl (d) of the PbCl$_2$ passivated PbSe QD over time.
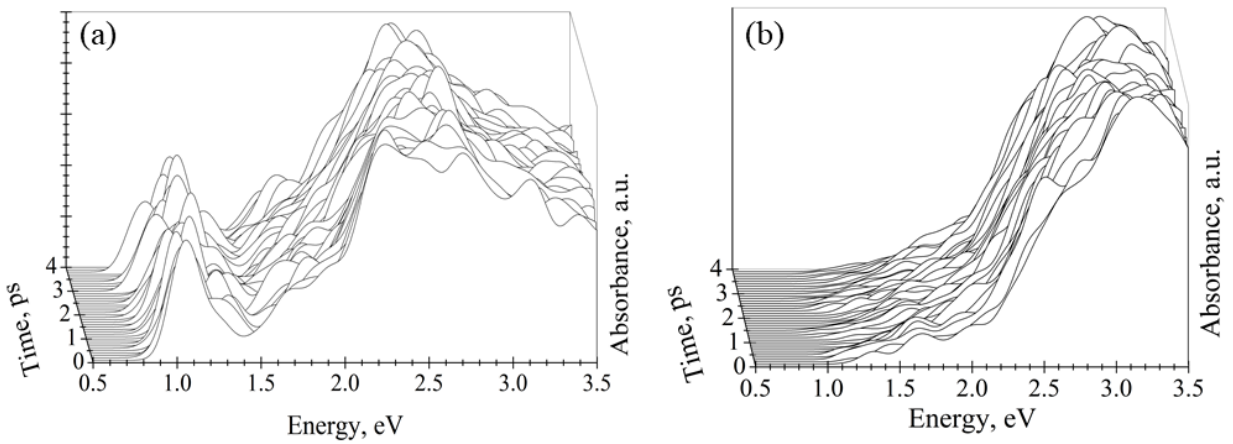


**Figure 5.6:** Time-dependent absorption spectra of the NPL (a) and QD (b). Absorption spectra of every 100 fs time steps of the adiabatic trajectory of the NPL and QD.

## 5.2.2. Absorption of the NPL and QD Characteristics of the Transitions

The overall DOS features reflect on the absorption spectra of both NPL and QD. The **figure 5.3-b, d** shows the absorption spectra of the NPL and QD calculated at the 0K, and the average absorption spectra at 300 K. NPL shows featured absorption spectra (**Figure 5.3** and **Figure 5.7**) due to the sub-gap. Increasing temperature to 300K, the absorption peaks are broadened, and the discrete lowest energy absorption peak is visible. The time-dependent absorption spectra are shown that the lowest energy is consistent over time (**Figure 5.6-a**). On the other hand, due to the homogenous broadening of the occupied and unoccupied band, $PbCl_2$ passivated PbSe QD shows broader absorption spectra. The lowest energy transition peak is also fluctuating over the adiabatic time (Figure 5.6-b). Despite three-dimensional confinement, QD has shown the comparatively lower degree of discrete featured absorption spectra because of the rocksalt lattice symmetry breaking and surface reorganization on the PbSe QD surface.
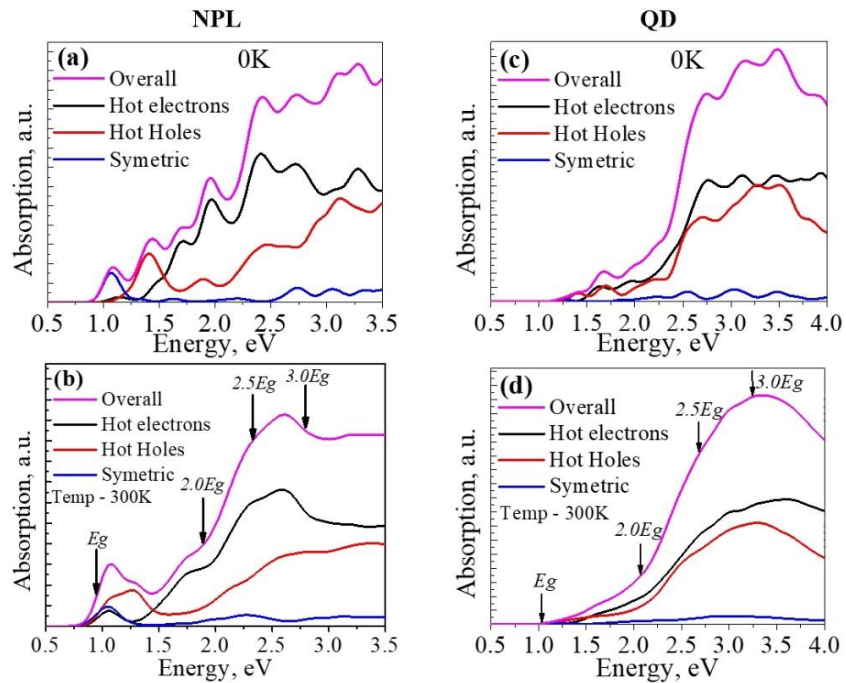


**Figure 5.7:** Analysis of the nature of the NPL and QD transitions at 0K and 300K temperature. All transitions are divided as hot-electron, hot-hole, and symmetric transition according to the electron (e) and hole (h) energy differences.

139

To understand the nature of the transition, we have categorized all the transitions into three categories, asymmetric transitions – hot hole and hot electron, and symmetric transitions. Hole and electron energies are defined relative to the HOMO and LUMO energy ($E_h = E_{HOMO} - \varepsilon_k$ and $E_e = \varepsilon_l - E_{LUMO}$) where $E_{HOMO}$ is the highest occupied molecular orbital (HOMO) energy and $E_{LUMO}$ are the lowest unoccupied molecular orbitals (LUMO) energy, $\varepsilon_k(\varepsilon_l)$ is the excited occupied state (unoccupied state) energy of a transition. Based on the electron and hole energy, transitions are categorized to the symmetric and asymmetric transition based on the electron ($e$) and the hole ($h$) energy of a transition, where $|E_h - E_e| \leq \Delta\varepsilon$ is denoted as symmetric transition and $|E_h - E_e| \geq \Delta\varepsilon$ is asymmetric transitions, where $\Delta\varepsilon = 0.10 eV$. Among the asymmetric transitions, a transition is denoted as a hot hole transition if $E_h - E_e \geq \Delta\varepsilon$ and hot electron transition if $E_h - E_e \leq -\Delta\varepsilon$. The ground state absorption spectra of both NPL and QD at and 0K and average spectra at 300K are decomposed to the hot electron (*hot-e*), hot hole (*hot-h*), and symmetric transitions in **Figure 5.7**. In the NPL, the first two peaks originated from the transition of the two unoccupied bands to the frontier occupied band (*L-L+3*) (**Figure 5.7**). Nature of homogeneous distribution of occupied and unoccupied bands in QD results in broadened absorption spectra (**Figure 5.3**), where the hot hole ($E_h > E_e$) and hot electron ($E_h < E_e$) transitions are almost equally dominated over the whole energy range (**Figure 5.7**). NPL has shown the featured absorption peak (**Figure 5.3**) due to the sparse unoccupied bands. Because of this, optical transitions of *hot-e* are dominated at the energy range of $2.5xE_g$ ($E_g = E_{LUMO} - E_{HOMO}$), but both *hot e-h* are equally dominated at the energy range of 3.0xEg (**Figure 5.7 a, b**).

## 5.3. Relaxation Dynamics in NPL and QD

### 5.3.1. Initial Condition

A 5.0ps and 4.0ps long ground state MD trajectories are calculated for the NPL and QD, respectively, by using the 2fs nuclear time steps. The first 300 initial trajectories are considered as an initial condition to simulate hot carrier relaxation, and it ensures trajectory branching.[14] Phonon mediated relaxation dynamics are calculated using the Fewest Switching Surface Hopping (FSSH) method[15] with the single-particle approximation for the hole and the electron. FSSH gives a time-dependent probability of the carrier transition between the states, which is correlated with the Non-Adiabatic Coupling (NAC) term $\boldsymbol{d}_{km} \cdot \dot{\boldsymbol{R}} = -i\hbar \left\langle \tilde{\varphi}_k \left| \frac{\partial}{\partial t} \right| \tilde{\varphi}_m \right\rangle$, where $\tilde{\varphi}_m$ is the adiabatic Kohn-Sham (KH) basis, and the thermal equilibrium of the hot carrier is achieved by ensuring the detail balance[16] with considering the Boltzmann factor (Detail in sub-chapter 2.5). Since the hot carrier relaxation dynamics could be different in different energy ranges, the degree of *hot-h* and *hot-e* is important because depending on it, the energy dissipation mechanism could be varied. In the case of the CM process, the minimum photon energy when carrier generation is more than unity is known as the CM threshold energy of that certain materials[17]. The threshold energy for CM of a material can be tuned by structure and materials composition, which is 6 -7 times the bandgap (*Eg*) in bulk PbSe and 2.2-2.7xEg in QDs[18]. Reducing the confinement to along one dimension (1D nanorods), threshold energy slightly improved, 2.6Eg[19]. Considering the threshold energy in QD and NR, two initial excitation energy constrain – 2.5xEg and 3.0xEg are considered in the phonon mediated hot carrier dynamics simulation. It was shown in **Figure 5.7** that both *hot-e* and *hot-h* transitions dominate the optical transition in the 2.5xEg and 3.0xEg energy range. To get the full understanding, we have studied the hot carrier relaxation dynamics with the initial constrain - the inclusion of all transitions and

selectively all symmetric transitions only. Besides, two limiting cases are also considered, the inclusion of selectively all *hot-e* and *hot-h* transitions.

## 5.3.2. Phonon Mediated Relaxation in NPL and QD
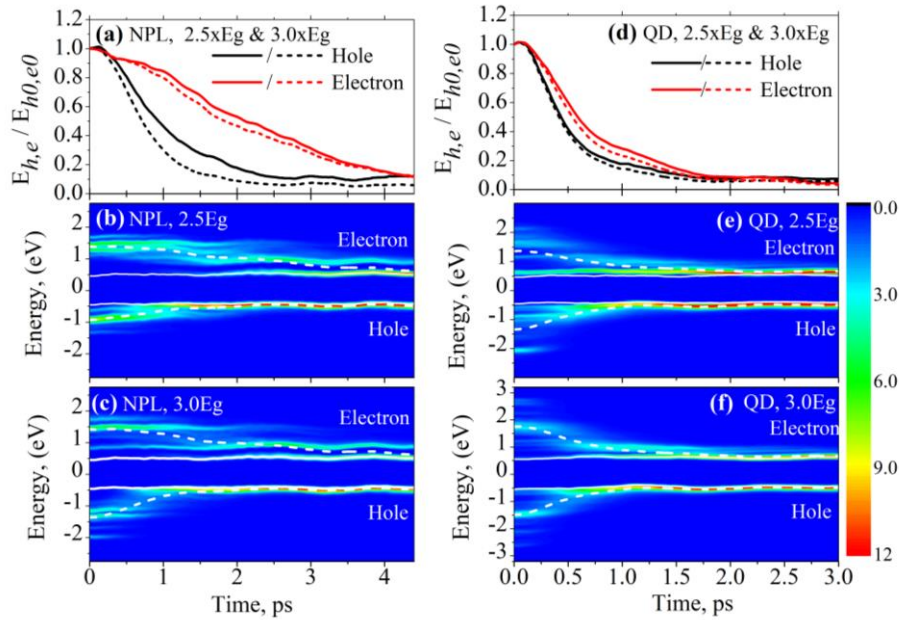


**Figure 5.8:** Phonon mediated electron and hole relaxation over time of the PbCl$_2$ bridged NPL and PbCl$_2$ passivated QD, calculated by initial condition of all symmetric transitions and transition energy of 2.5xEg and 3.0xEg. Panels *a, e* are the time-dependent normalized average electron and hole energy over the time in NPL and QD where solid and dash lines represent the 2.5xEg and 3.0xEg initial excitation energy. Panel *b, c*, and *e, f* is showing the time-defendant evaluation of the (hot-e) and hot-hole (hot-h) wavepacket of initial excitation of energy 2.5xEg and 3.0xEg in NPL and QD, respectively. Solid white lines represent the ensemble average HOMO and LUMO states, and dotted white lines represent the ensemble average hot-e and hot-h energy over time.

Figure 5.8 -5.12 shows the phonon mediated relaxation dynamics of the excited electron-hole of the initial condition of 2.5xEg and 3.0xEg excitation energy. Surface plots show the DOSxpopulation of the hole and electron states over the 4.40ps (NPL) and 3.00ps (QD) long trajectories. Overall, the hole relaxation rate in QD is about 1ps faster than the hot electron relaxation. This result is showing a good agreement with the previous PbSe QD results[12]. On the other hand, relaxation time in NPL is much slower, especially the *hot e*, independent of the initial *hot-h* and *hot-e* energy. Since the ratio of the *hot-e* and *hot-h* in optical transitions is higher in

3.0xEg excitation energy compare to the 2.5xEg (**figure 5.7**), only hole energy is increased by increasing the initial excitation energy constrain (**Figure 5.8 a, b, c**). Although the overall rate is not affected by initial excitation energy constrain, the energy dissipation rate of the initial high energy hot-*h* and hot-*e* states are high at 3xEg constrain because of the denser unoccupied states (**Figure 5.8a**). The fast continuous intraband relaxation of the excited hole can be realizable from the higher average NAC term and smaller intraband splitting in the unoccupied band, which is even pronounced in the 3xEg excitation (**Table 5.1**). On the other hand, hole relaxation dynamics of the NPL shows a discontinuity in the initial condition of selective *hot-h* excitation and symmetric excitation (**Figure 5.9e, 5.10b**), which indicates a multiphoton relaxation dynamic. Due to the strong confinement and surface reconstruction, the density of occupied and unoccupied states of the QD are widely distributed, as such initial wavepacket is also widely distributed, and average *hot-e* and *hot-h* energy are symmetric in energy in both initial excitation energy constraints (**Figure 5.8 d, e, f**). In both models, electron and hole energy dissipation follow the exponential decay where intermediate states don't affect the overall relaxation mechanism. Exponential fitting of the depopulation of the initial hot *e-h* and population of the final band (*L to L+3 / H to H-3*) are shown in **figure 5.13**. Except for the electron in NPL, higher energy *e-h* has a smaller average intraband energy splitting and a larger average coupling term in both NPL and QD (Table 1). Therefore, the initial hot carrier relaxation rate is fast in the 3.0xEg excitation condition. In contrary, the average coupling term is unchanged, and average intraband energy splitting is higher in the case of an electron in NPL in 3.0xEg excitation because of more hot-hole ($E_h \gg E_e$) and sparse band-edge state.
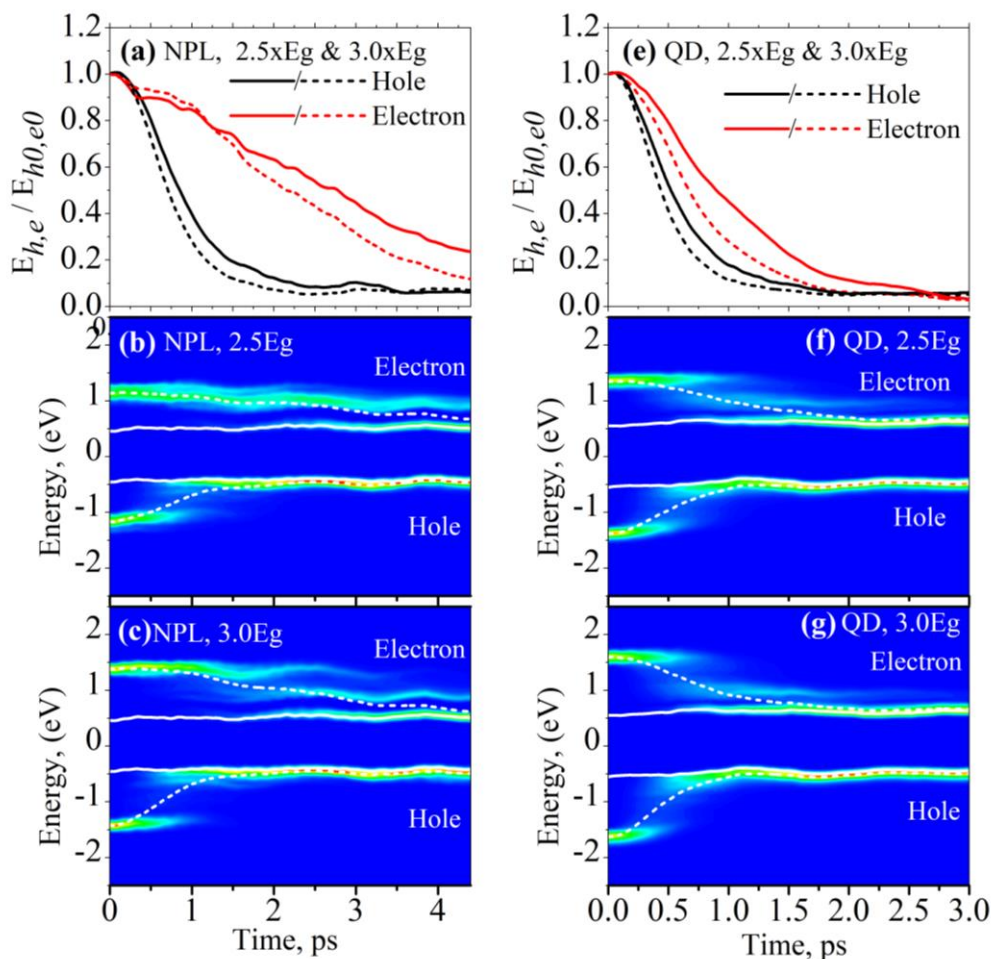
**Figure 5.9:** Phonon mediated electron and hole relaxation over time of the PbCl$_2$ bridged NPL and PbCl$_2$ passivated QD, calculated by initial condition of all symmetric transitions and transition energy of 2.5xEg and 3.0xEg. Panel *a* and **e** are the time-dependent normalized average electron and hole energy over the time in NPL and QD where solid and dash lines represent the 2.5xEg and 3.0xEg initial excitation energy. Panel *b, c,* and *f, g* is showing the time defendant evaluation of the (hot-e) and hot-hole (hot-h) wavepackets of initial excitation of energy 2.5xEg and 3.0xEg in NPL and QD, respectively. Solid white lines represent the ensemble average HOMO and LUMO states, and the dotted white line represent the ensemble average *hot-e* and *hot-h* energy over time.

144
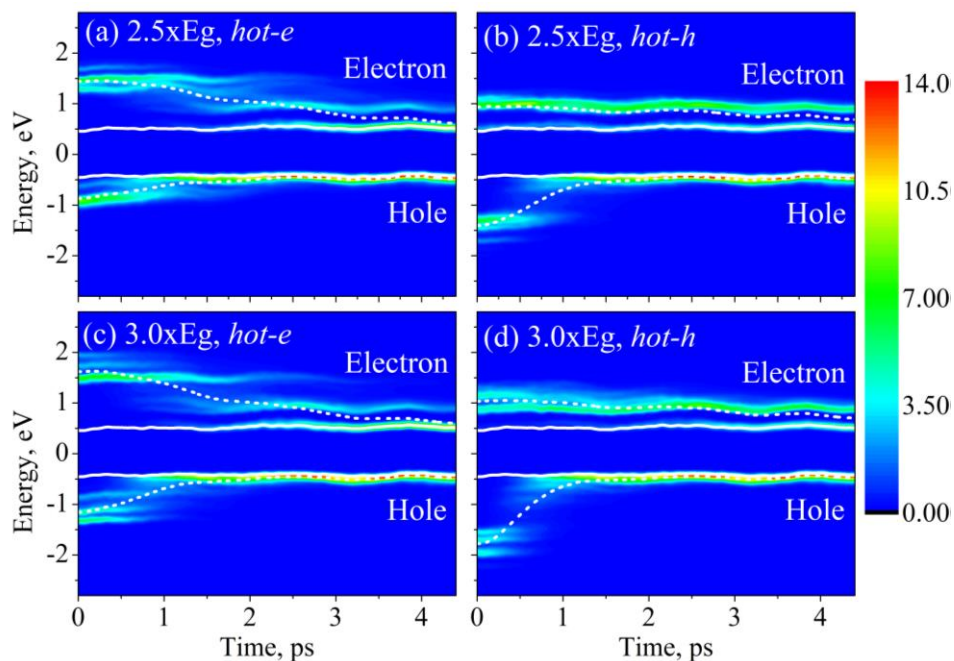
**Figure 5.10**: Phonon mediated electron and hole relaxation of the PbCl₂ bridged NPL overtime where (*panel a, c*) hot electron (*hot-e*) and (*panel b, d*) hot hole (*hot-h*) transitions are selected as an initial condition. Solid white lines represent the ensemble average HOMO and LUMO states.
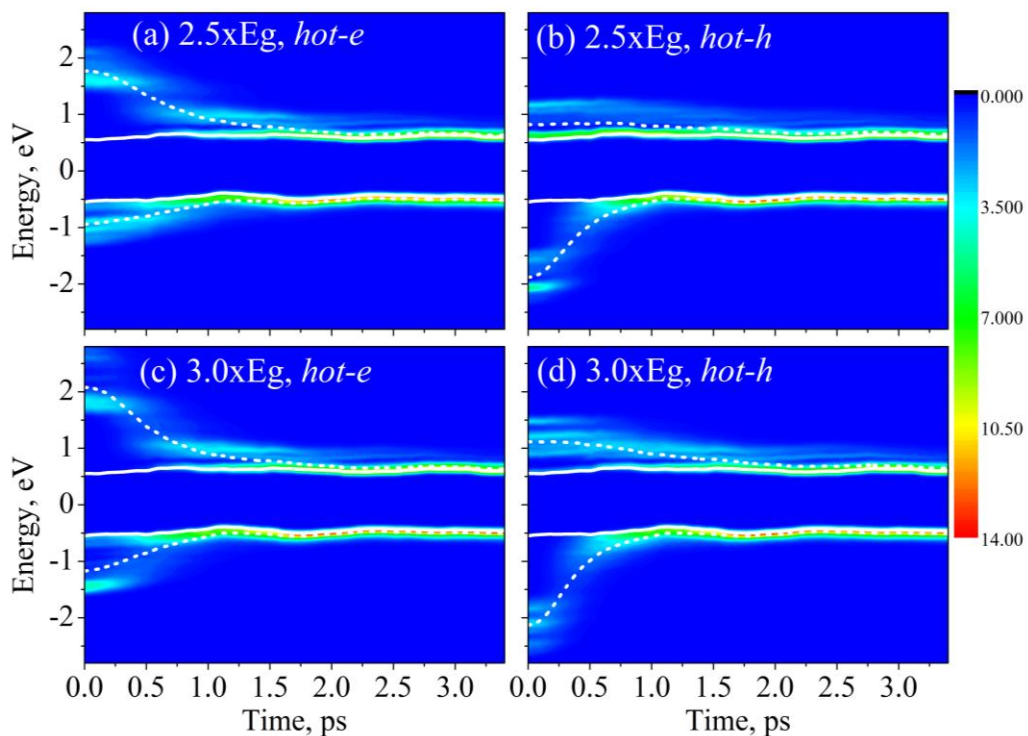


**Figure 5.11:** Electron and hole relaxation where (panel *a, c*) hot electron (*hot-e*) and (panel *b, d*) hot hole (hot-h) transitions are selected as an initial condition. The dotted white line represent the ensemble average hot-e and hot-h energy over time.

145
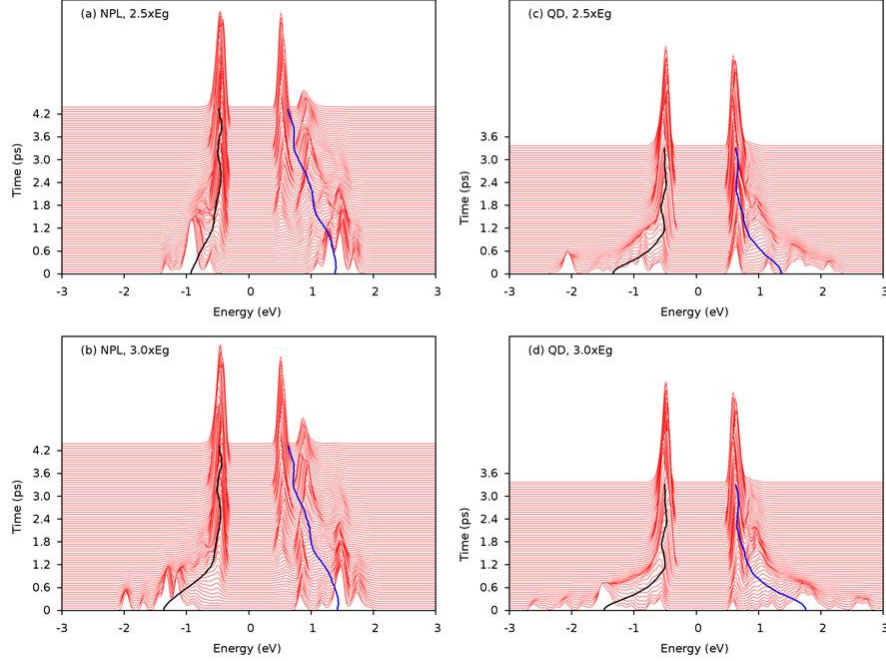
**Figure 5.12:** Waterfall graph of the phonon mediated electron and hole relaxation of PbCl$_2$ bridged NPL and PbCl$_2$ passivated QD with the initial condition of 2.5xEg and 3.0xEg transition energy. Black and blue line represent the ensemble average hot-h and hot-e energy over time. Figure 3 of the main article is another representation of similar calculations.

**Table 5.1:** Nonadiabatic Coupling (NAC) constant, intra-band splitting, and e-h relaxation rate constant of the NPL and QD. $d_{i,i+1}$ and $d_{i,i+2-n}$ are the ensemble average NAC constant between the nearest states and between all other states, respectively, $\Delta E_{NN}$ is the average energy difference between the states and average over the ensemble. $\tau$ is the hot carrier relaxation rate constant calculated by the exponential fitting.

|  |  | Hole | | Electron | |
|---|---|---|---|---|---|
|  |  | 2.5xEg | 3.0xEg | 2.5xEg | 3.0xEg |
| NPL | $d_{i,i+1}$, meV | 13.11 | 17.07 | 11.67 | 11.69 |
|  | $\Delta E_{NN}$, meV | 28.33 | 21.21 | 37.78 | 41.40 |
|  | $d_{i,i+2-n}$, meV | 1.86 | 1.56 | 1.03 | 0.96 |
|  | $\tau$, fs | 1.18 | 0.81 | 2.40 | 2.22 |
| QD | $d_{i,i+1}$, meV | 20.53 | 22.98 | 15.86 | 21.71 |
|  | $\Delta E_{NN}$, meV | 23.07 | 20.67 | 32.74 | 27.72 |
|  | $d_{i,i+2-n}$, meV | 2.26 | 2.27 | 1.71 | 1.89 |
|  | $\tau$, fs | 0.58 | 0.51 | 0.75 | 0.66 |

### 5.3.3. Phonon Modes Coupled with Electron and Hole States

Overall, PbCl$_2$ passivated Pb$_{68}$Se$_{68}$ QD shows a similar relaxation mechanism of Pb$_{68}$Se$_{68}$ QD[12] and the absence of the phonon bottleneck. *Hot-h* relaxes slightly faster than *hot-e*, and occupied band edge states get 80% populated by 1ps (**Figure 5.13**). **Figure 5.14** shows the ensemble-average spectra of phonon coupled with initial hot-e (hot-h) and the final LUMO (HOMO) states in both initial conditions. The spectra are obtained by the fast Fourier transform (FFT) of an electronic state over the adiabatic trajectories.

$$A_k = \sum_{n=0}^{N-1} a_n \, e^{-i\frac{2\pi}{N}kn} \tag{5.1}$$

Where N is the number of discrete data ($a_n$), k is known as the Nth roots of unity and *k=0.......N-1*
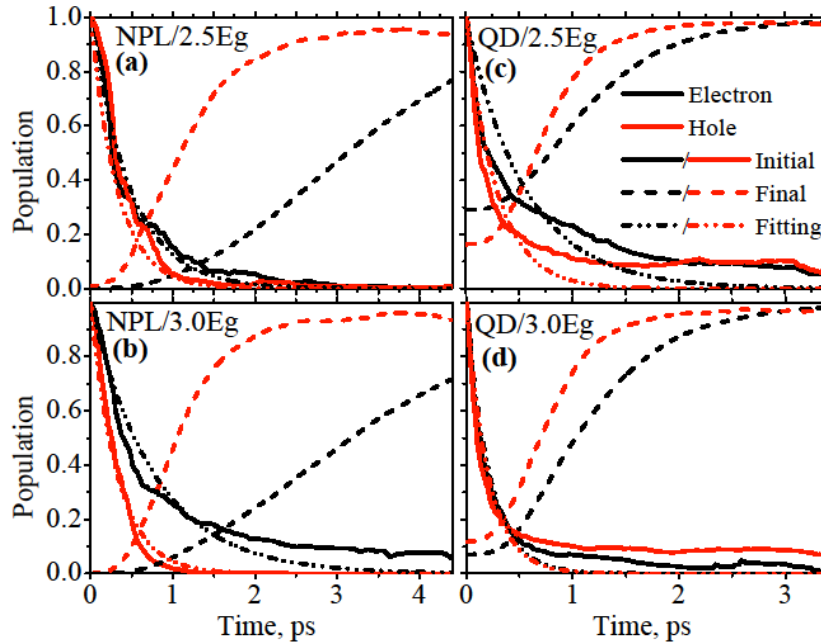


**Figure 5.13:** Ensemble average population of the initial excited state and final band (LUMO to LUMO+3, and HOMO to HOMO+3) over the time, when initial excitation energy was constrained to 2.5xEg (a & c) and 3.0xEg (b & d). dash-dotted lines are the exponential fitting line of the initial decay of the hot carrier. In few trajectories of the ensemble in 2.5xEg excitation constrain in QD, ground state electron is excited to the frontier unoccupied states, which is considered the final state, as such exponential function is not fitting correctly.

Independent of initial hot *e-h* states, initial hot *e-h* states of both NPL and QDs are coupled with weaker acoustic phonons (**Figure 5.14**). Similar hot carrier acoustic phonon coupling reported in the experimental and computational study of Pb chalcogenide nanomaterials.[9, 20] Spectral density of the acoustic phonon in QD are dominating due to the symmetry breaking in spherical 3D confined QD and substantial surface reconstruction by $PbCl_2$ passivation, which results in smaller energy gap, leads to the hot e-h relaxation by coupling with weak acoustic phonon. On the other hand, *e-h* of NPL is coupled with both acoustic phonon and optical phonon in the range 100-250 cm$^{-1}$ frequency, where an initial *hot-e* couple with 75 cm$^{-1}$ and 150 cm$^{-1}$ while *hot-h* is coupled with 55 cm$^{-1}$ and 110 cm$^{-1}$. Coupling with the phonon of 55 cm$^{-1}$ and 110 cm$^{-1}$ governed the hot hole relaxation dynamics; as such, its' spectral density increases with increasing excitation energy (**Figure 5.14 a, b**), resulting in faster energy dissipation (**Figure 5.9a**). The final state, homo-lumo, in both NPL and QD has noticeable acoustic phonon coupling. In addition to coupling with phonon in the range of 100-250cm$^{-1}$, NPL's HOMO-LUMO is predominantly coupled with the phonon 200cm$^{-1}$. Considering the average energy gap between the states, NPL should have the phonon bottleneck or multi-phonon relaxation process, especially for the electron relaxation. A smaller surface to volume ratio and relatively rigid surface should decrease the electron-phonon interaction[21]. Hot electron is relaxed to the sub-gap edge states, and electrons are distributed according to Boltzmann distribution.
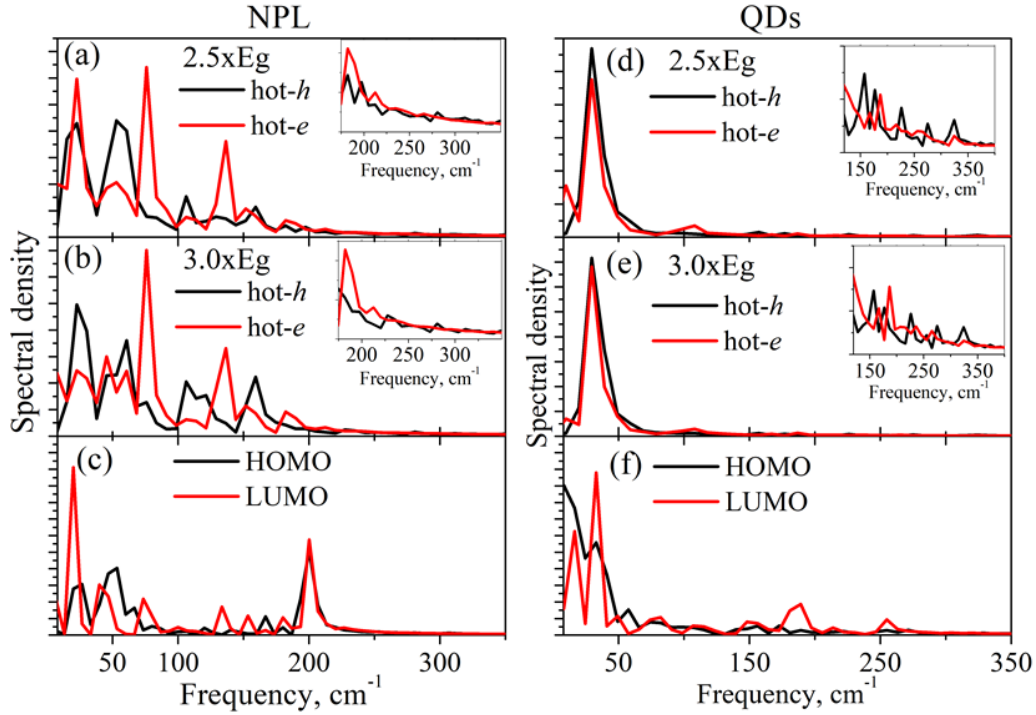
**Figure 5.14:** Spectral density of the autocorrelation function of the hot-e and hot-h energies over time (average over ensemble) of the both 2.5xEg and 3.0xEg initial condition in the panel a, b and d, e of the NPL and QD respectively. Panel c and f is the Fast-Furrier transform (FFT) of the final state (homo and lumo) of the NPL and QD.

## 5.4. The Spatial Separation of Electron and Holes

In the sub-chapter 1.3, we have discussed how the initial and final states' population and spatial separation dominates the overall Auger process. We have studied the spatial distribution of the hot carrier over time. Despite relaxing the momentum conservation and higher Coulomb interaction, PbS QD does not show the expected very high CM efficiency because of sparse electronic states and very fast energy dissipation rate[22], as we observe the ps range relaxation in PbCl$_2$ passivated PbSe QD. But as reported in the 1D nanorods (NR) [23], 1-D confinement and spatial separation of hot carriers could enhance the CM process.[24-25]

**Table 5.2:** Four examples of the charge density of PbCl$_2$ bridged NPL from the adiabatic trajectories. All images are viewing from the Z-X plane (The vacuum in the unite cell along Z-axis is omitted). In the following row, charge density is projected to Z-axis (black line), and the projected wave function of Pb, Se, and Cl are projected on Z-axis (green, red, and blue for Pb, Se, and Cl, respectively).

| | T=0.0ps | T=2.0ps | T=4.0ps | T=5.0ps |
|---|---|---|---|---|
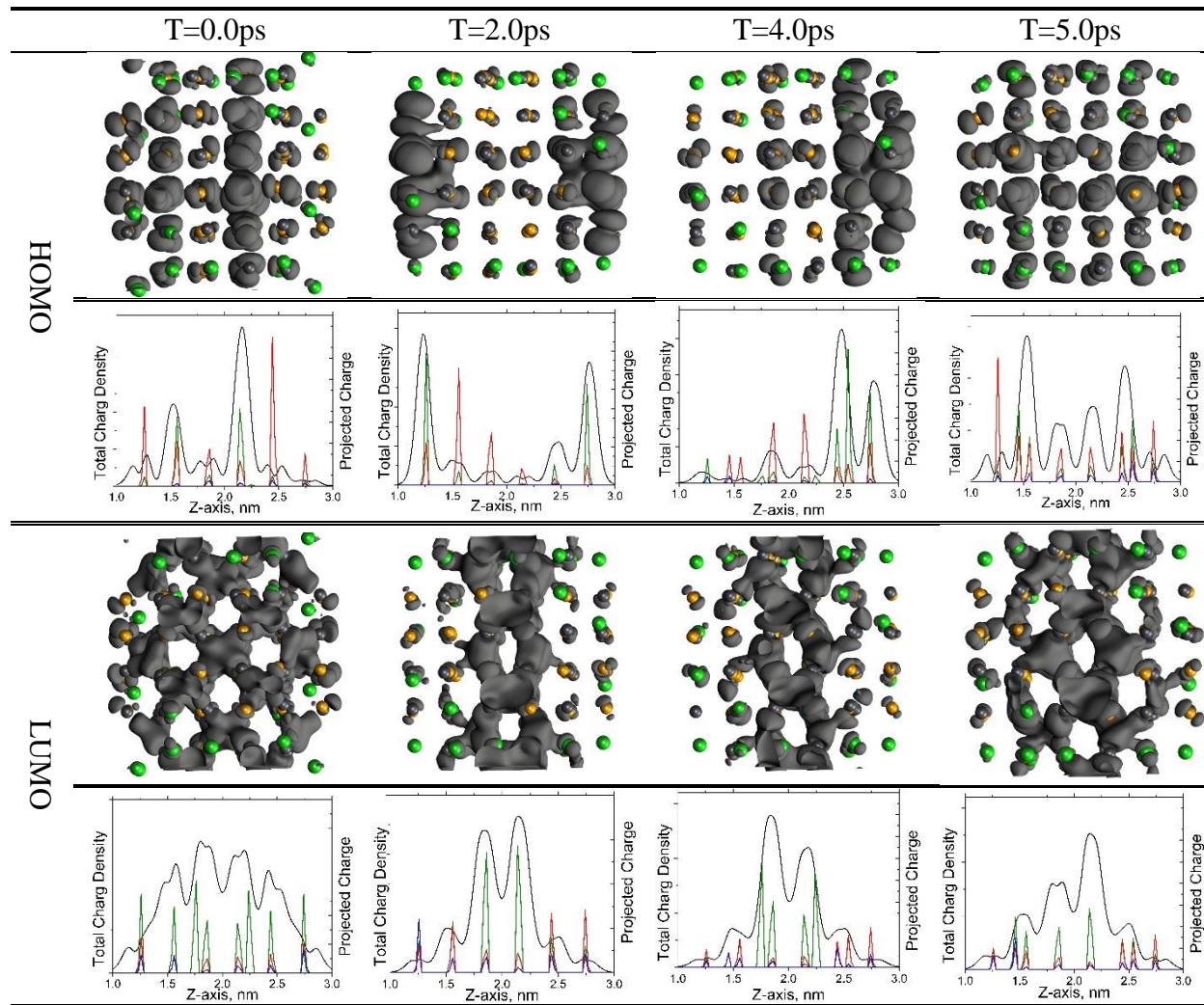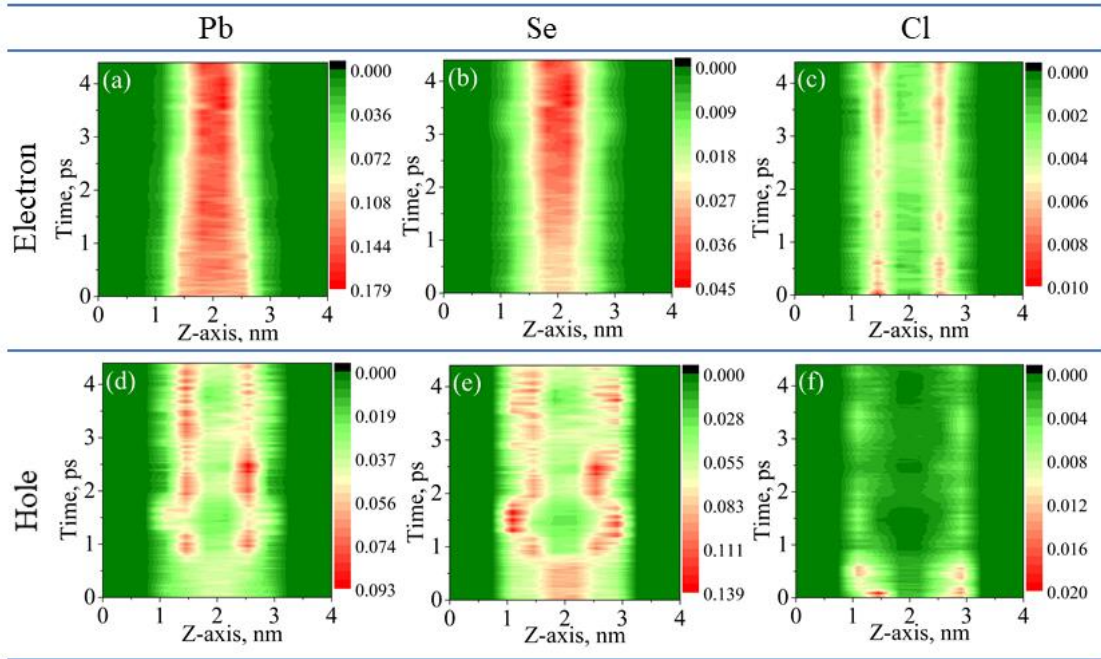
**Figure 5.15**: Ensemble average of the Pb, Se, Cl projected charge density of the electron and hole and plotted by projecting in Z-axis. The Z-axis of the unit cell is 4 nm, where 1nm vacuum on both sides along the Z-axis of the cell. All calculations were done with the initial condition of 3.0xEg eV optical transition energy.
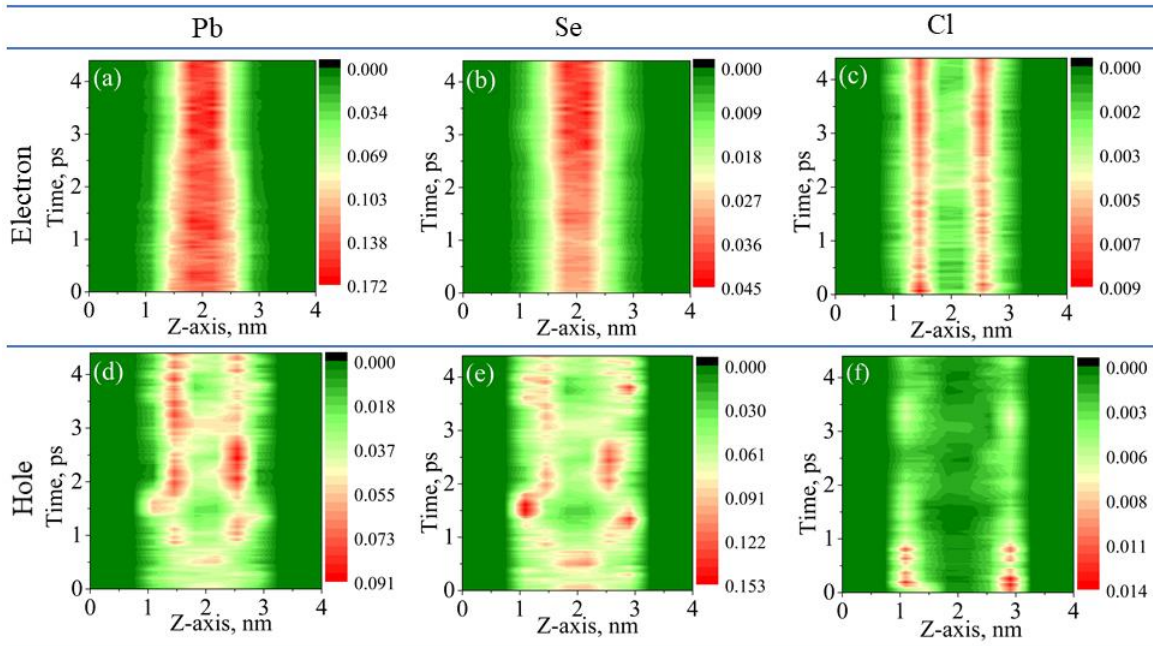


**Figure 5.16:** Ensemble average of the Pb, Se, Cl projected charge density of the electron and hole and plotted by projecting in Z-axis. The Z-axis of the unit cell is 4 nm, where 1nm vacuum on both sides along the Z-axis of the cell. All calculations were done with the initial condition of 2.5xEg eV transition energy.

The charge density of the final states (HUMO/LUMO) are mainly delocalized over the entire unit or occupied, and unoccupied states are partially delocalized on the core and surface layer of NPL, respectively (few snapshots of the HOMO and LUMO from the Adiabatic trajectory are shown in **Table 5.2**). We have calculated the ensemble average sum of the Kohn-Sham wave function norm $|\Psi_i(r)|^2$ of the highest populated state at a certain time ($t$) in the X and Y direction and projected on the Z direction over NAMD time (**Figure 5.15, 5.16**). Independent of initial excitation energy constrain, both the initial hot hole and electron mainly delocalized on the core layer of the NPL. But the hole is delocalized over the surface layer (**Figure 5.15, 5.16**) after the dissipation of energy. Hot hole and hot electron confined in the core layers would increase the Coulomb interaction and hence intraband relaxation rate[26]. Smaller intraband spacing and intraband coupling of the occupied states facilitate the decoherence of the *e-h* at the initial moment of time, and electron and holes are spatially separated by about 1.0 ps. Delocalization of the hot *h* to the surface by 1ps increases the coupling with surface acoustic phonon, and decreases electron-hole Coulombic interaction. On the other hand, a core layer confined electron relaxation rate is much slower than the phonon mediated relaxation rate. Despite relaxed *e-h* spatial separation in QD, Coulomb interaction leads to faster electron energy losses through the Auger process. But due to the larger volume of NPL, spatial separation minimizes the rate of the electron's energy loss, which indicates that NPL could have an optimal condition of Coulomb interaction for slower relaxation and higher CM.

### 5.5. Summary

The electronic structure and excited state relaxation dynamics of the $PbCl_2$ bridged NPL and QDs are studied using the DFT based FSSH method. NPL has a direct bandgap at the L high symmetry in the first Brillion zone. NPL has shown symmetric density of the states in

conduction and valance band but sparse valance band. On the other hand, $PbCl_2$ passivated PbSe QD has broadened and symmetric valance and conduction band due to the surface reconstruction and 3D confinement. The electronic transitions of the hot-e are dominated in the NPL in the range 2.5xEg while *hot-h* and *hot-e* are symmetric in the QD.

The hot carrier relaxation rate is relatively slower in the NPL compared to QDs. Stronger coupling and dense electronic states in QD lead to faster hot carrier relaxations. The valance band of NPL has wider average energy splitting, and weaker coupling results in slower hot electron relaxation dynamics. Increasing the initial excitation energy increases the hot hole energy in NPL. As a result, initial excitation energy doesn't change the electron dynamics significantly. In contrast, the energy dissipation rate of the hole increases in the initial condition of 3.0xEg excitation. Hot electron and hot hole states are coupled with lower energy acoustic phonon in QD, while NPL shows the coupling with the phonon mode in the range of 150-250cm$^{-1}$. Discontinuity in the energy dissipation of hole in QD suggested that hole energy dissipated via multiphonon processes. Our calculations are also shown that the initial hot holes and electrons are predominately NPL core localized. The hot hole dissipates the energy and transfers to surface layers by 1ps. The spatial separation of the hole and electron would minimize the Auger process, and which is favorable for the CM process.

## 5.6. References

1.     Koh, W.-k.; Dandu, N. K.; Fidler, A. F.; Klimov, V. I.; Pietryga, J. M.; Kilina, S. V., Thickness-Controlled Quasi-Two-Dimensional Colloidal PbSe Nanoplatelets. *J. Am. Chem. Soc.* **2017,** *139* (6), 2152-2155.

2.     Kohn, W.; Sham, L. J., Self-Consistent Equations Including Exchange and Correlation Effects. *Phys. Rev.* **1965,** *140* (4A), A1133-A1138.

3.     Perdew, J. P.; Burke, K.; Ernzerhof, M., Generalized Gradient Approximation Made Simple. *Phys. Rev. Lett.* **1996,** *77* (18), 3865-3868.

4.      Blöchl, P. E., Projector augmented-wave method. *Phys. Rev. B.* **1994,** *50* (24), 17953-17979.

5.      Kresse, G.; Hafner, J., Ab initio molecular dynamics for liquid metals. *Phys. Rev. B.* **1993,** *47* (1), 558-561.

6.      Kang, I.; Wise, F. W., Electronic structure and optical properties of PbS and PbSe quantum dots. *J. Opt. Soc. Am. B* **1997,** *14* (7), 1632-1646.

7.      Ernzerhof, M.; Scuseria, G. E., Assessment of the Perdew–Burke–Ernzerhof exchange-correlation functional. *J. Chem. Phys.* **1999,** *110* (11), 5029-5036.

8.      Krukau, A. V.; Vydrov, O. A.; Izmaylov, A. F.; Scuseria, G. E., Influence of the exchange screening parameter on the performance of screened hybrid functionals. *J. Chem. Phys.* **2006,** *125* (22), 224106.

9.      Lystrom, L.; Tamukong, P.; Mihaylov, D.; Kilina, S., Phonon-Driven Energy Relaxation in PbS/CdS and PbSe/CdSe Core/Shell Quantum Dots. *J. Phys. Chem. Lett.* **2020,** *11* (11), 4269-4278.

10.     Romero, A. H.; Cardona, M.; Kremer, R. K.; Lauck, R.; Siegle, G.; Serrano, J.; Gonze, X. C., Lattice properties of PbX (X = S, Se,Te): Experimental studies and ab initio calculations including spin-orbit effects. *Phys. Rev. B.* **2008,** *78* (22), 224302.

11.     Zhang, Y.; Ke, X.; Chen, C.; Yang, J.; Kent, P. R. C., Thermodynamic properties of PbTe, PbSe, and PbS: First-principles study. *Phys. Rev. B.* **2009,** *80* (2), 024304.

12.     Kilina, S.; Kilin, D.; Prezhdo, O., Breaking the Phonon Bottleneck in PbSe and CdSe Quantum Dots: Time-Domain Density Functional Theory of Charge Carrier Relaxation. *ACS Nano* **2009,** *3* (1), 93-99.

13.     Wehrenberg, B. L.; Wang, C.; Guyot-Sionnest, P., Interband and Intraband Optical Studies of PbSe Colloidal Quantum Dots. *J. Phys. Chem. B* **2002,** *106* (41), 10634-10640.

14.     Tully, J. C., Molecular dynamics with electronic transitions. *J. Chem. Phys.* **1990,** *93* (2), 1061-1071.

15.     Tully, J. C., Mixed quantum–classical dynamics. *Faraday Discuss.* **1998,** *110* (0), 407-419.

16.     Parandekar, P. V.; Tully, J. C., Mixed quantum-classical equilibrium. *J. Chem. Phys.* **2005,** *122* (9), 094102.

17.     Beard, M. C.; Midgett, A. G.; Hanna, M. C.; Luther, J. M.; Hughes, B. K.; Nozik, A. J., Comparing Multiple Exciton Generation in Quantum Dots To Impact Ionization in Bulk Semiconductors: Implications for Enhancement of Solar Energy Conversion. *Nano Lett.* **2010,** *10* (8), 3019-3027.

18. Kim, S. J.; Kim, W. J.; Sahoo, Y.; Cartwright, A. N.; Prasad, P. N., Multiple exciton generation and electrical extraction from a PbSe quantum dot photoconductor. *Appl. Phys. Lett.* **2008,** *92* (3), 031107.

19. Padilha, L. A.; Stewart, J. T.; Sandberg, R. L.; Bae, W. K.; Koh, W.-K.; Pietryga, J. M.; Klimov, V. I., Aspect Ratio Dependence of Auger Recombination and Carrier Multiplication in PbSe Nanorods. *Nano Lett.* **2013,** *13* (3), 1092-1099.

20. Krauss, T. D.; Wise, F. W., Coherent Acoustic Phonons in a Semiconductor Quantum Dot. *Phys. Rev. Lett.* **1997,** *79* (25), 5102-5105.

21. Bozyigit, D.; Yazdani, N.; Yarema, M.; Yarema, O.; Lin, W. M. M.; Volk, S.; Vuttivorakulchai, K.; Luisier, M.; Juranyi, F.; Wood, V., Soft surfaces of nanomaterials enable strong phonon interactions. *Nature* **2016,** *531* (7596), 618-622.

22. Stewart, J. T.; Padilha, L. A.; Qazilbash, M. M.; Pietryga, J. M.; Midgett, A. G.; Luther, J. M.; Beard, M. C.; Nozik, A. J.; Klimov, V. I., Comparison of Carrier Multiplication Yields in PbS and PbSe Nanocrystals: The Role of Competing Energy-Loss Processes. *Nano Lett.* **2012,** *12* (2), 622-628.

23. Htoon, H.; Hollingsworth, J. A.; Dickerson, R.; Klimov, V. I., Effect of Zero- to One-Dimensional Transformation on Multiparticle Auger Recombination in Semiconductor Quantum Rods. *Phys. Rev. Lett.* **2003,** *91* (22), 227401.

24. Krahne, R.; Zavelani-Rossi, M.; Lupo, M. G.; Manna, L.; Lanzani, G., Amplified spontaneous emission from core and shell transitions in CdSe/CdS nanorods fabricated by seeded growth. *Appl. Phys. Lett.* **2011,** *98* (6), 063105.

25. Oron, D.; Kazes, M.; Banin, U., Multiexcitons in type-II colloidal semiconductor quantum dots. *Phys. Rev. B.* **2007,** *75* (3), 035330.

26. Klimov, V. I.; Mikhailovsky, A. A.; McBranch, D. W.; Leatherdale, C. A.; Bawendi, M. G., Mechanisms for intraband energy relaxation in semiconductor quantum dots: The role of electron-hole interactions. *Phys. Rev. B.* **2000,** *61* (20), R13349-R13352.

# 6. INTERFACIAL PROPERTIES OF THE PBSE|CDSE JANUS QDS

The importance of the interfacial layers is discussed detailed in the sub-chapter 1.2. An interfacial layer is used and tuned for minimizing the surface reorganization and tuning the multi-carrier process as well. It also dominates the carrier transport process. An interfacial layer plays a dominating role in overall device efficiency[1-3], along with the electronic properties of the semiconductor materials in the Janus type heterostructure.[1, 4-5] Kroupa et al. predicted that the high energy holes (*hot-h*) are trapped in the interfacial layer, which slows down the hole's energy dissipation.[1] Subsequently, a higher CM yield was predicted. In the core-shell structure, the Auger process is tuned by smoothening interfacial layer potential.[2, 6-7] Considering the importance of an interfacial layer, we have studied the interfacial states and overall geometrical parameters in PbSe|CdSe Janus type heterostructure. PbSe has the rocksalt lattice structure, while the most stable crystal lattice of the CdSe is Wurtzite type. So, the degree of mismatch between the PbSe and CdSe lattice and surface reconstruction is needed to consider before making a model for the computational calculations. Most recent syntheses reported that PbSe|CdSe Janus QDs are synthesized by cation exchange of CdSe QD, and PbSe continue to grow in the presence of $PbCl_2$ solution. The lattice structure after the cation exchange or the lattice of extended PbSe needs to be explored first to evaluate the electronic properties of QD. We have considered three common chalcogenide lattice – rocksalt and wurtzite to identify the most probable Janus structure and their electronic properties.

## 6.1. Methodology

We have used PbSe Rocksalt, CdSe Wurtzite structure for Janus QD structure. The previous theoretical calculation was reported about 2.00 nm in diameter six layers $Pb_{68}Se_{68}$ are optimal big QD model which can predict considerably accurate electronic and photophysical

properties.[8-10] Three different Janus QD models were prepared by cutting the $Pb_{68}Se_{68}$ QD in (100) and (111) facets and replaced one half of the Pb by Cd. Dividing along (100) facet generates a symmetric QD. On the other hand, (111) facets create an asymmetric QD, so two types of Janus QD are considered- Pb rich ($Pb_{37}Cd_{31}Se_{68}$) and Cd rich ($Pb_{31}Cd_{37}Se_{68}$). The next considered model prepared by replacing half of the Cd by Pb in CdSe wurtzite lattice QD, Since Janus QD synthesis is reported as cation exchange of the CdSe QD in the presence of $PbCl_2$ precursor. Considering the result from both types of models, the third type model is made by placing wurtzite and rocksalt structure in a position of minimum lattice mismatch. This non-stoichiometric QDs are passivated by the 8 Cl to balance the charge. All the models are optimized by using the DFT method[11] in Gaussian software[12] with using the functional PBE1PBE[13] and LANL2DZ basis set[14]. LANL2DZ pseudopotentials are used for the core electron. To investigate the characteristics of the electronic states, the projected density of states is calculated by considering fragments – Pb, Cd, Se in Pb, and Se in Cd.

Absorption spectra are simulated by using the line response Time-Dependent DFT (TD-DFT).[15] We have calculated a total of 150 excited state transitions energy and oscillator strength. Due to the limitation of the required resources and dense electronic state, we have simulated absorption spectra up to ≈3.00 eV. Absorption spectra are simulated by Gaussian dressing of the excited energy and oscillator strength with the 0.07 eV thermal broadening. Natural transition orbitals (NTOs)[16] are generated to visualize the special localization of the electron and hole particle of the higher oscillator strength transitions. All NTOs are visualize using 0.20 iso value using the VMD visualization software.
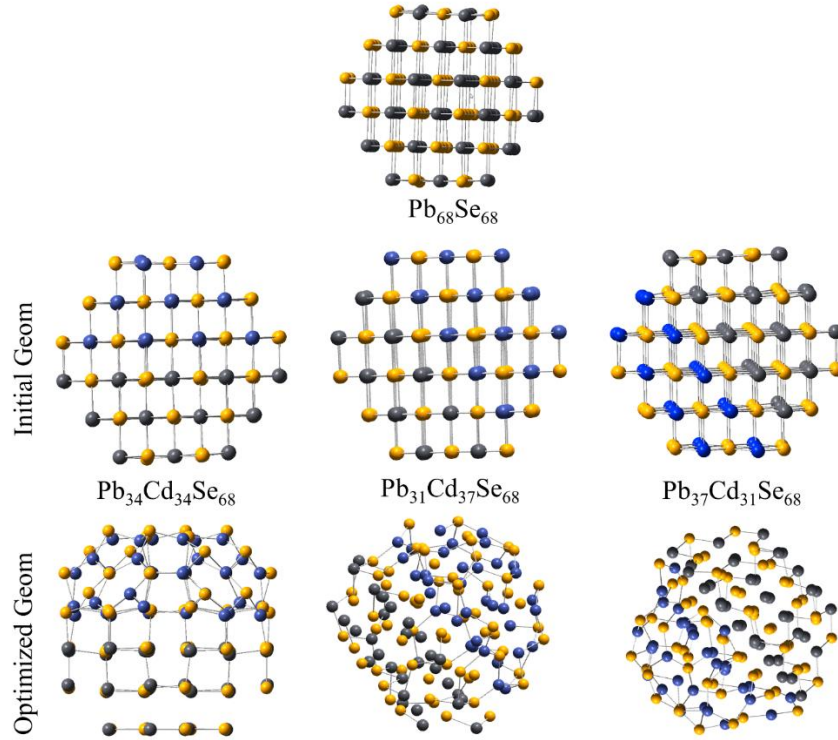
**Figure 6.1**: The initial and optimized structure of the PbSe|CdSe Janus clusters made from the PbSe rocksalt crystal lattice structure, prepared by replacing Cd in one part along (100) and (111) plane in $Pb_{68}Se_{68}$ QD.

## 6.2. Result and Discussion

Figure 6.1 is showing the preparation of the PbSe|CdSe Janus QD from the rocksalt QDs. Although (100) facets make symmetric Pb and Cd parts, the CdSe fragment has significant surface reconstruction. Due to the formation of the wurtzite type surface in the CdSe part, the core part of the CdSe part has less density of metal atoms. In contrast, the PbSe part of the Janus QD retained the rocksalt lattice structure. Consequently, $Pb_{34}Cd_{34}Se_{68}$ Janus QD has a significant lattice mismatch in the core interfacial layer. On the other hand, the Cd surface in the (111) facet in Pb and Cd rich Janus QS has minimal surface reorganization in comparison to the (100) facets in $Pb_{34}Cd_{34}Se_{68}$ QDs. Because of only two layers in $Pb_{31}Cd_{37}Se_{68}$ QD, the Pb part has significant distortion from the rocksalt lattice structure, which is minimum in $Pb_{37}Cd_{31}Se_{68}$.

158
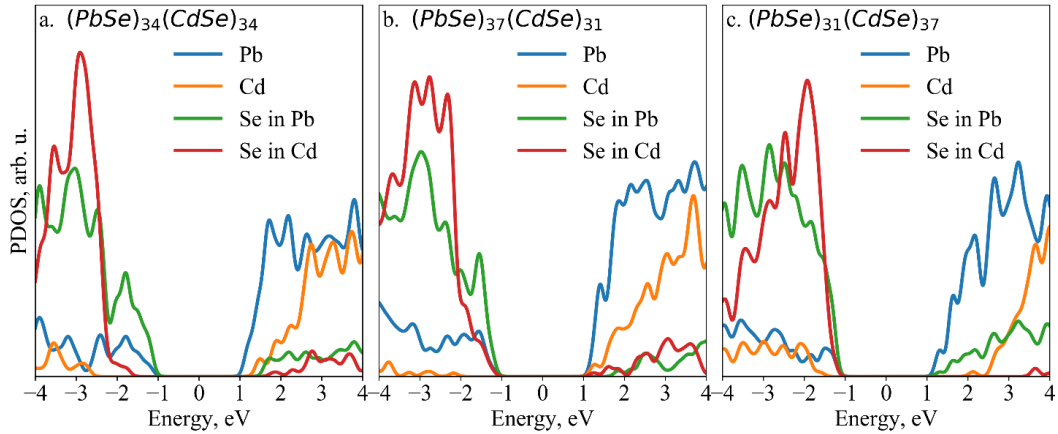
**Figure 6.2:** Projected Density of the State (PDOS) of the PbSe|CdSe Janus QD obtained from the PbSe rocksalt crystal lattice. (a) Symmetric stoichiometric, (b) Pb rich, and (c) Cd rich asymmetric QDs.

All three types of Janus QD from rocksalt lattice have a ≈2.00 eV bandgap (Figure 6.2). The occupied states are dominantly Se localized, and unoccupied states are metal (Pb and Cd) localized. In all cases, the frontier bands are localized on the PbSe part of the QD, which agrees on the previously predicted results. On the other hand, the energy offset between the unoccupied Cd localized and Pb localized states are minimum in Pb rich Janus structure, which is a result of interfacial Se in the both Pb and Cd rich QDs. Because of comparable electronic structure in all three Janus QDs, absorption spectra show the comparable features. The frontier band is localized on the Pb part of the QD in all three Janus QDs. As such lowest energy absorption peak is brighter, where electron and hole both are localized on the PbSe part of the QDs. Qualitative features of the absorption spectra are well agreed with the experimental absorption spectra.[1] The lowest energy absorption peak is localized in the PbSe part, although energy is blue-shifted due to the smaller size of our model.
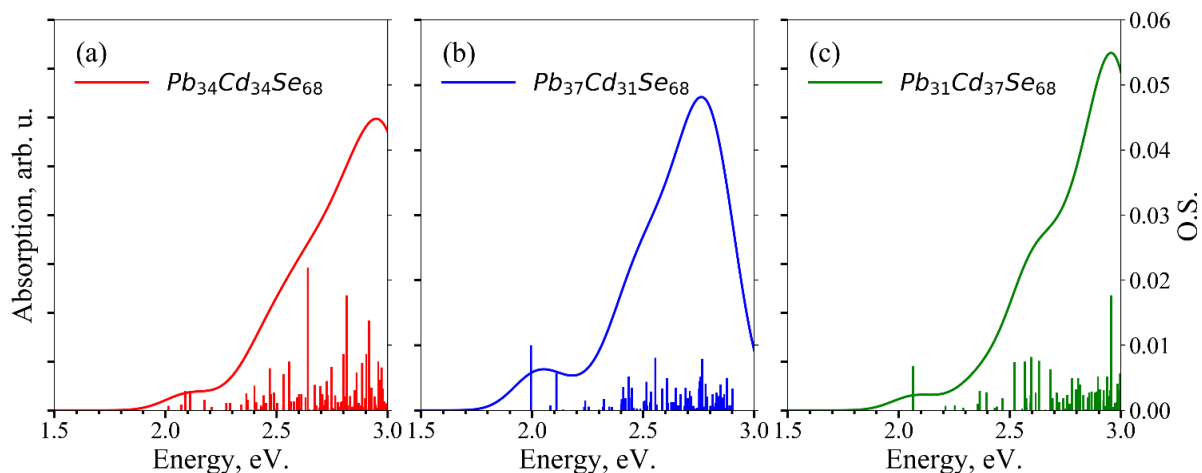
**Figure 6.3:** Absorption spectra of PbSe|CdSe Janus QD obtained from the PbSe rocksalt crystal lattice. (a) Symmetric stoichiometric, (b) Pb rich and (c) Cd rich asymmetric QDs
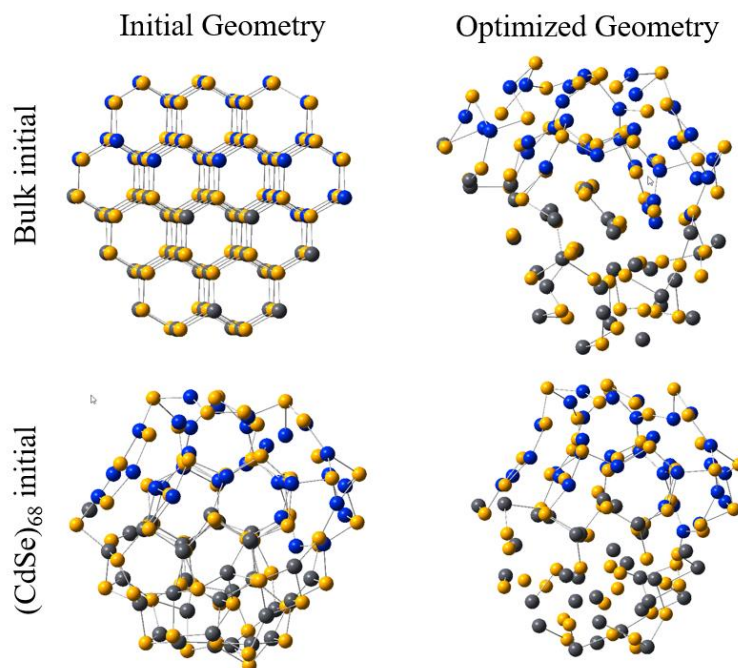


**Figure 6.4:** Janus QD from the CdSe Wurtzite lattice. Janus QD models are prepared by two methods, replacing half of Cd by Pb in bulk pristine Wurtzite lattice and half of Cd in optimized $Cd_{68}Se_{68}$ Wurtzite lattice.

Considering the cation exchange synthesis procedure,[5] the next possible lattice structure is growing from the wurtzite lattice since it the energetically favorable lattice structure of the CdSe QDs. We have prepared PbSe|CdSe Janus QD from the Wurtzite lattice in two different methods. In the first method, we have cut an "almost spherical" size $Cd_{68}Se_{68}$ QD from the bulk

CdSe Wurtzite lattice. We have cut through (1120) plane, and Cd is replaced by Pb. The resulting geometry is optimized (It is labeled as '*bulk initial*' in the figure) (Figure 6.4). In the second method, $Cd_{68}Se_{68}$ is optimized using a similar condition in the DFT method, and half of the Cd is replaced by Pb (this geometry is labeled as '*(CdSe)$_{68}$ initial*') (Figure 6.4). *w*-PbSe|CdSe Janus QD has significant reorganization, especially in the Pb part due to the surface tension and lattice mismatch. Both clusters have shown the trap state localized in the interfacial layer (Figure 6.5). PDOS shows that both clusters have trap states in the band edge or between the frontier band (Figure 6.5). Due to the lowest energy discrete conduction band in the Janus QD from the bulk initial, absorption spectra show a redshifted discrete absorption peak compare to the Janus QD from (CdSe)$_{68}$ initial geometry. The transition to the trap state in both models is optically bright, creating the lowest energy discrete absorption peaks (NTOs in Table 6.1).
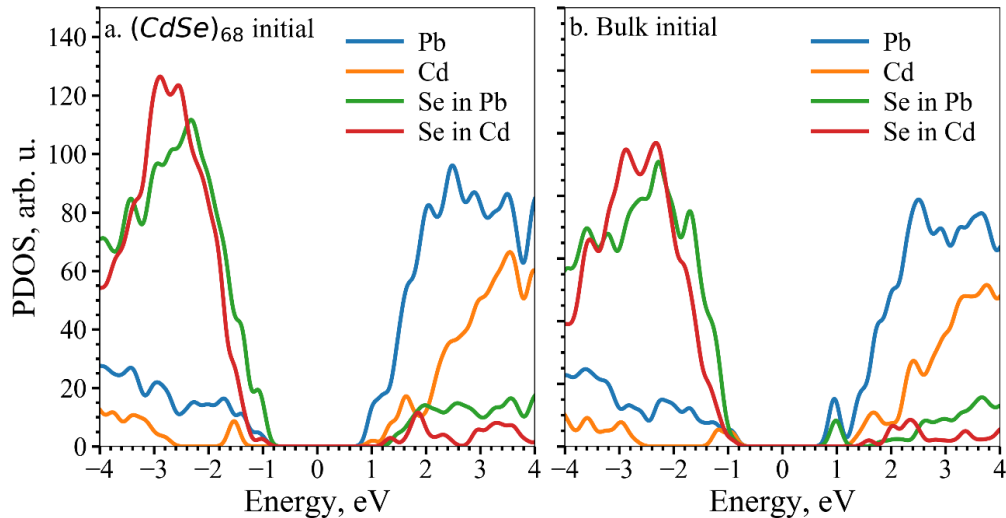


**Figure 6.5**: PDOS of the PbSe|CdSe Janus QD, where Janus QD models are prepared from the CdSe Wurtzite lattice.
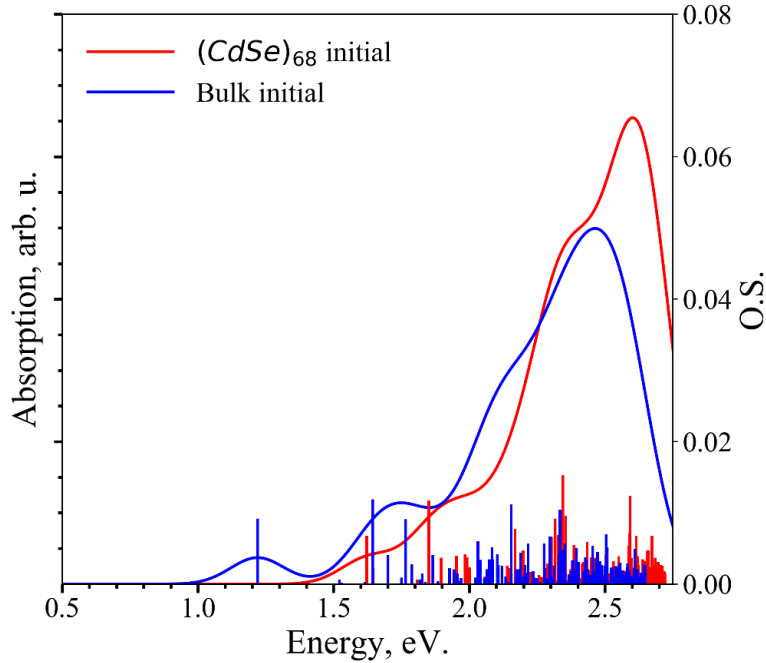
**Figure 6.6**: Absorption spectra of the two models which are prepared from the CdSe Wurtzite structure.

**Table 6.1:** NTOs of the dominant transition of the two lowest absorption peaks in the PbSe|CdSe Janus QD prepared from the CdSe Wurtzite lattice structure. NTOs are calculated in Gaussian software and visualize in the VMD.

| Bulk initial | | | $(CdSe)_{68}$ initial | | |
|---|---|---|---|---|---|
| Energy OS | HOLE | Electron | Energy OS | HOLE | Electron |
| $S_1$ 1.23 eV 0.0092 |  |  | $S_1$ 1.62eV 0.0068 |  |  |
| $S_5$ 1.64 eV 0.0119 |  |  | $S_4$ 1.85 eV 0.0092 |  |  |

To avoid the lattice transformation during the optimization, the next model we studied are

prepared from the combination of both wurtzite and rocksalt lattice for the CdSe and PbSe part,

respectively Figure 6.7. A larger model is needed to consider minimizing the lattice mismatch and capped with 8 Cl atoms to balance the stoichiometric charge – $Pb_{52}Cd_{52}Se_{100}Cl_8$. Capping Cl is added on the three Pb rich (111) facet of the PbSe part of the QDs. Due to the different lattice parameters of Wurtzite and rocksalt crystal, the lattice mismatch is not completely avoided; as a result, a trap state is formed in the PbSe part of the Janus QDs (Figure 6.8). PDOS of this model shown that frontier unoccupied are localized in PbSe and energy offset between the PbSe and CdSe are minimum.

On the other hand, due to the smaller bandgap of the PbSe semiconductor materials, the highest energy states of CdSe and PbSe localized has higher energy offset. Without the consideration of the trap states, overall, this Janus QD model has a type-I electronic structure, where the valance band has a larger energy difference. This electronic structure agrees with the predicted result from the experimental results[1]. Table 6.2 is showing the spatial localization of the four frontiers occupied and unoccupied states. The modeled Janus QD is not perfectly symmetric in space. As a result, the trap states are formed in the thin PbSe layer and the QD's interfacial area. We suggest that more capping would eliminate the trap states, but it will make the model unfeasible for an ab initio computational calculation.
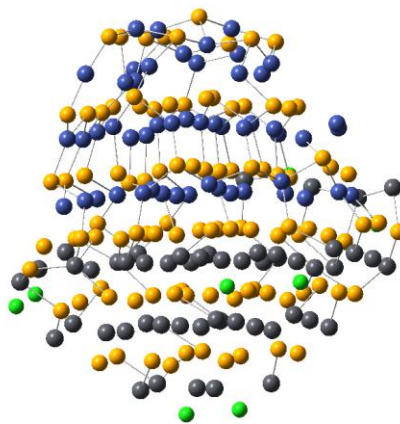


**Figure 6.7:** PbSe|CdSe Janus QDs prepared by the PbSe rocksalt and CdSe Wurtzite lattice structure. QD is capped with 8 Cl atom on the 8 Pb rich (111) facet to make it stoichiometric structure.
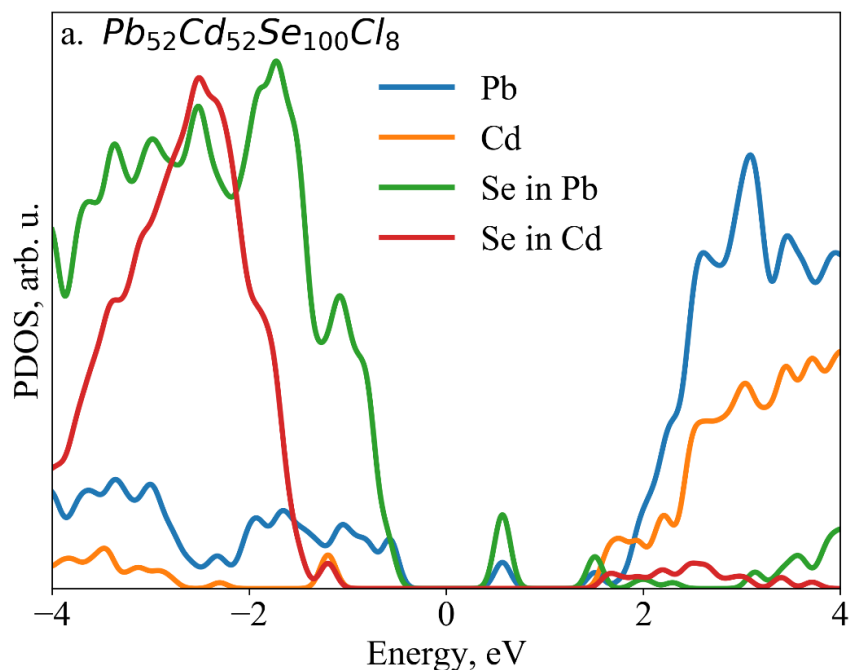
**Figure 6.8**: Projected density of state (PDOS) of the rocksalt -wurtzite PbSe|CdSe Janus QDs. The electronic structure showed strong agreement with the experimental result suggested.

### 6.3. Summary

We have studied the effects of structure and lattice symmetry on the electronic structure and photophysical properties of the Janus QDs. We have shown that wurtzite to rocksalt lattice transformation of PbSe would create an unfeasible electronic structure, and this model won't predict the acceptable results. On the other hand, a model from the PbSe rocksalt lattice suggested that the interfacial layer in Janus QD is in (111) facets. It has a type-I electronic band between the two parts of Janus QD, where higher energy offset in the Pb and Cd unoccupied states. A larger model is needed to consider simulating the acceptable result, and an interfacial surface atom needs to be capped with a ligand. It minimizes the trap states. Independent of Pb and Cd chalcogenide lattice, PbSe|CdSe Janus QD has type-I electronic structure, where Pb and Cd localized valance band shows higher energy offset than conduction band. This observation suggested that high energy hole dynamics would dominate the overall energy relaxation rate. Our

future plan is to study the hot carrier dynamics in the Janus QD. This study elucidates the

electronic properties of the Janu QD and presentative model to excited state process calculations.

## 6.4. References

1.      Kroupa, D. M.; Pach, G. F.; Vörös, M.; Giberti, F.; Chernomordik, B. D.; Crisp, R. W.; Nozik, A. J.; Johnson, J. C.; Singh, R.; Klimov, V. I.; Galli, G.; Beard, M. C., Enhanced Multiple Exciton Generation in PbS|CdS Janus-like Heterostructured Nanocrystals. *ACS Nano* **2018**.

2.      Bae, W. K.; Padilha, L. A.; Park, Y.-S.; McDaniel, H.; Robel, I.; Pietryga, J. M.; Klimov, V. I., Controlled Alloying of the Core–Shell Interface in CdSe/CdS Quantum Dots for Suppression of Auger Recombination. *ACS Nano* **2013,** *7* (4), 3411-3419.

3.      Lin, Q.; Makarov, N. S.; Koh, W.-k.; Velizhanin, K. A.; Cirloganu, C. M.; Luo, H.; Klimov, V. I.; Pietryga, J. M., Design and Synthesis of Heterostructured Quantum Dots with Dual Emission in the Visible and Infrared. *ACS Nano* **2015,** *9* (1), 539-547.

4.      Pradhan, S.; Xu, L.; Chen, S., Janus Nanoparticles by Interfacial Engineering. *Adv. Funct. Mater.* **2007,** *17* (14), 2385-2392.

5.      Zhang, J.; Chernomordik, B. D.; Crisp, R. W.; Kroupa, D. M.; Luther, J. M.; Miller, E. M.; Gao, J.; Beard, M. C., Preparation of Cd/Pb Chalcogenide Heterostructured Janus Particles via Controllable Cation Exchange. *ACS Nano* **2015,** *9* (7), 7151-7163.

6.      Supran, G. J.; Song, K. W.; Hwang, G. W.; Correa, R. E.; Scherer, J.; Dauler, E. A.; Shirasaki, Y.; Bawendi, M. G.; Bulović, V., High-Performance Shortwave-Infrared Light-Emitting Devices Using Core-Shell (PbS-CdS) Colloidal Quantum Dots. *Adv. Mater.* **2015,** *27* (8), 1437-1442.

7.      Climente, J. I.; Movilla, J. L.; Planelles, J., Auger Recombination Suppression in Nanocrystals with Asymmetric Electron–Hole Confinement. *Small* **2012,** *8* (5), 754-759.

8.      Isborn, C. M.; Kilina, S. V.; Li, X.; Prezhdo, O. V., Generation of Multiple Excitons in PbSe and CdSe Quantum Dots by Direct Photoexcitation: First-Principles Calculations on Small PbSe and CdSe Clusters. *J. Phys. Chem. C* **2008,** *112* (47), 18291-18294.

9.      Kilina, S.; Kilin, D.; Prezhdo, O., Breaking the Phonon Bottleneck in PbSe and CdSe Quantum Dots: Time-Domain Density Functional Theory of Charge Carrier Relaxation. *ACS Nano* **2009,** *3* (1), 93-99.

10.     Kilina, S. V.; Kilin, D. S.; Prezhdo, V. V.; Prezhdo, O. V., Theoretical Study of Electron–Phonon Relaxation in PbSe and CdSe Quantum Dots: Evidence for Phonon Memory. *J. Phys. Chem. C* **2011,** *115* (44), 21641-21651.

11. Mafuné, F.; Kohno, J.-y.; Takeda, Y.; Kondow, T.; Sawabe, H., Structure and Stability of Silver Nanoparticles in Aqueous Solution Produced by Laser Ablation. *J. Phys. Chem. B* **2000,** *104* (35), 8333-8337.

12. Frisch, M. J.; Trucks, G. W.; Schlegel, H. B.; Scuseria, G. E.; Robb, M. A.; Cheeseman, J. R.; Scalmani, G.; Barone, V.; Petersson, G. A.; Nakatsuji, H.; Li, X.; Caricato, M.; Marenich, A. V.; Bloino, J.; Janesko, B. G.; Gomperts, R.; Mennucci, B.; Hratchian, H. P.; Ortiz, J. V.; Izmaylov, A. F.; Sonnenberg, J. L.; Williams; Ding, F.; Lipparini, F.; Egidi, F.; Goings, J.; Peng, B.; Petrone, A.; Henderson, T.; Ranasinghe, D.; Zakrzewski, V. G.; Gao, J.; Rega, N.; Zheng, G.; Liang, W.; Hada, M.; Ehara, M.; Toyota, K.; Fukuda, R.; Hasegawa, J.; Ishida, M.; Nakajima, T.; Honda, Y.; Kitao, O.; Nakai, H.; Vreven, T.; Throssell, K.; Montgomery Jr, J. A.; Peralta, J. E.; Ogliaro, F.; Bearpark, M. J.; Heyd, J. J.; Brothers, E. N.; Kudin, K. N.; Staroverov, V. N.; Keith, T. A.; Kobayashi, R.; Normand, J.; Raghavachari, K.; Rendell, A. P.; Burant, J. C.; Iyengar, S. S.; Tomasi, J.; Cossi, M.; Millam, J. M.; Klene, M.; Adamo, C.; Cammi, R.; Ochterski, J. W.; Martin, R. L.; Morokuma, K.; Farkas, O.; Foresman, J. B.; Fox, D. J. *Gaussian 16 Rev. B.01*, Wallingford, CT, 2016.

13. Ernzerhof, M.; Scuseria, G. E., Assessment of the Perdew–Burke–Ernzerhof exchange-correlation functional. *J. Chem. Phys.* **1999,** *110* (11), 5029-5036.

14. Hay, P. J.; Wadt, W. R., Ab initio effective core potentials for molecular calculations. Potentials for the transition metal atoms Sc to Hg. *J. Chem. Phys.* **1985,** *82* (1), 270-283.

15. Stratmann, R. E.; Scuseria, G. E.; Frisch, M. J., An efficient implementation of time-dependent density-functional theory for the calculation of excitation energies of large molecules. *J. Chem. Phys.* **1998,** *109* (19), 8218-8224.

16. Martin, R. L., Natural transition orbitals. *J. Chem. Phys.* **2003,** *118* (11), 4775.

# 7. CONCLUSION

In the disquisition, we have studied how the photophysical properties are affected by the surface passivation and interface in metal nanoclusters and chalcogenide nanocrystal. We used ab initio method like DFT and TDDFT to study the ground state and excited state electronic properties, and semi-classical method DFT based FSSH to study the excited hole and electron dynamics. We have focused on the two classes of materials, nucleobase passivated Ag nanoclusters, and Pb and Cd chalcogenide nanocrystals like PbX (X=S, Se) QDs, $PbCl_2$ incorporated PbSe NPL, and CdSe|PbSe Janus QD.

In chapter 3, it was shown that the inclusion of polar solvent in calculations significantly change the nucleobases' hydrogen bond network. In response to it, a nanoclusters structure and optical response are significantly modified. Besides, the redox potential of an Ag nanocluster determines the most probable oxidation states in the reaction mixture. Ag nanoclusters have alternative high-low reduction potential, where the difference in reduction potential decreases with increasing the cluster size. Accurate prediction of redox potential helps to determine the thermodynamically favorable cluster size and oxidation states. On the other hand, different structural isomers from the different nucleobase passivation have smaller energy difference, which suggests that they can coexist in a solution. Among the three nucleobases C, G, and T, cytosine (C) has stronger binding energy. Despite the different binding energy and structural differences, all $Ag_6$ clusters shown the characteristic three absorption peaks in the energy range of 2.5-4.5 eV. The lowest energy transition of open-shell nanoclusters is always dark, while it can be bright in a closed shell structure depending on the structure and nucleobase type. The absorption peaks' intensities are shown a correlation with the charge transfer to the cytosine and $s+p+d$ hybridization. The optically active transitions of energy higher than >5.0 eV are

predominately ligand to metal type transitions and which are mainly Ag-*d* orbital localized states. Besides the effects of nucleotide passivation, the effect of the size of the clusters is explored in the next sub-chapter. It was found that the three characteristics absorption bands become dark while size increases to 18-20 atom.

In chapter 4, we have explored the surface passivation and surface bond effects on the photoexcited electron transfer to the perylene diimides (PDI). The frontier electronic states' energies can be tuned by ligand dipole. Besides, the total dipole of the PbS-PDI system is PDI axis angle-dependent. PDI linker group and attached PbS facet lead to a different structural isomer. Our study hypothesizes that the PDI core and PbS QD surface interaction would increase the PDI redox potential and initiate an additional electron transfer pathway, which could increase the photoexcited electron transfer rate.

The excited carrier dynamics of the $PbCl_2$ incorporated PbSe NPL and $PbCl_2$ passivated PbSe QD are studied in chapter 5. PbSe NPL has a direct bandgap at L high symmetry point in the first Brillion zone, where the conduction band has sub-gap in the conduction band. The density of states (DOS) of the valance band and conduction band of QDs are homogeneously distributed due to the confinement and high degree of surface reorganization. In both NPL and QD, the frontier bands are mostly distributed on Pb and Se. The overall relaxation rate is slower in NPL than QDs because of smaller coupling terms and wider intraband energy splitting. It was shown that increasing the initial excitation in NPL increases the ensemble average hot hole energy. The hole energy dissipation rate is higher due to the denser valance band, in result stronger coupling and smaller average intraband energy difference. It is also shown that the initial excited hole and electron state energy in QD dissipated via coupling with lower energy acoustic phonon mode while NPL states show coupling with 150-250 $cm^{-1}$ phonon mode. We

have found that the initial hot *e-h* states are localized on the core layer of the NPL. *e-h* are separated by 1 ps where the hole states are predominately localized on the surface layers, which should increase the hole relaxation state. The separation of electron and hole would prevent the Auger process and could increase the CM process in QDs.

The interface and lattice structure-dependent electronic properties of the Janus QD are studied in chapter 6. Interface along (100) facet of the rocksalt lattice has a higher lattice mismatch due to stoichiometric Pb and Se balanced interface. On the other hand, (111) interface creates Pb or Cd enriched Janus QDs where frontier states are PbSe part originated and shows energy offset between Pb and Cd originated valance band states. The interfacial mismatch is minimum in the model prepared from the wurtzite and rocksalt lattice despite it shows a trap state localized on the interface on the QD surface. Capping the surface could prevent the trap states.